

UNCLASSIFIED

AD NUMBER

AD878050

LIMITATION CHANGES

TO:

Approved for public release; distribution is unlimited.

FROM:

Distribution authorized to U.S. Gov't. agencies and their contractors; Critical Technology; SEP 1970. Other requests shall be referred to U.S. Army Aviation Materiel Laboratories, Fort Eustis, VA 23604. This document contains export-controlled technical data.

AUTHORITY

USAAML ltr, 28 Jun 1971

THIS PAGE IS UNCLASSIFIED

AD878050

AD No. _____

FILE COPY

AD

USAAVLABS TECHNICAL REPORT 70-50

FLIGHT TEST EVALUATION OF A SUPERCRITICAL-SPEED SHAFT

By

Robert J. Baier

September 1970

**U. S. ARMY AVIATION MATERIEL LABORATORIES
FORT EUSTIS, VIRGINIA**

**CONTRACT DA 44-177-AMC-353(T) *new*
THE BOEING COMPANY
VERTOL DIVISION
PHILADELPHIA, PENNSYLVANIA**

This document is subject to special export controls, and each transmittal to foreign governments or foreign nationals may be made only with prior approval of U.S. Army Aviation Materiel Laboratories, Fort Eustis, Virginia 23604.



DDC
RECEIVED
DEC 28 1970
A

DISCLAIMERS

The findings in this report are not to be construed as an official Department of the Army position unless so designated by other authorized documents.

When Government drawings, specifications, or other data are used for any purpose other than in connection with a definitely related Government procurement operation, the United States Government thereby incurs no responsibility nor any obligation whatsoever; and the fact that the Government may have formulated, furnished, or in any way supplied the said drawings, specifications, or other data is not to be regarded by implication or otherwise as in any manner licensing the holder or any other person or corporation, or conveying any rights or permission, to manufacture, use, or sell any patented invention that may in any way be related thereto.

DISPOSITION INSTRUCTIONS

Destroy this report when no longer needed. Do not return it to the originator.

100-100000
100-100000
100-100000

2



DEPARTMENT OF THE ARMY
HEADQUARTERS US ARMY AVIATION MATERIEL LABORATORIES
FORT EUSTIS, VIRGINIA 23604

This report represents a part of a USAAVLABS program to develop design criteria and to conduct experimental and developmental tests on power transmission shafts that operate safely at or above many of their lateral critical speeds. The report explores and defines the problems associated with successfully manufacturing and balancing a full-size aircraft-type supercritical-speed shaft system.

Task 1G162203D14414
Contract DA 44-177-AMC-353(T)
USAAVLABS Technical Report 70-50
September 1970

Flight Test Evaluation of a Supercritical-Speed Shaft

Final Report

D210-10082-1

By

Robert J. Baier

Prepared by

**The Boeing Company
Vertol Division
Philadelphia, Pennsylvania**

for

**U. S. ARMY AVIATION MATERIEL LABORATORIES
FORT EUSTIS, VIRGINIA**

This document is subject to special export controls, and each transmittal to foreign governments or foreign nationals may be made only with prior approval of U.S. Army Aviation Materiel Laboratories, Fort Eustis, Virginia 23604.

SUMMARY

This report presents the effort by The Boeing Company, Vertol Division on the bench testing and analytical description of a full-size supercritical-speed shaft designed for installation in the CH-47 helicopter.

The program objective was to demonstrate a supercritical system for installation in the aircraft.

The phases of the program were:

- Detail design the shaft system and aircraft support structure.
- Develop an aircraft-type damper.
- Bench test the complete system.
- Check shaft performance in the aircraft under ground and flight conditions.

The noncoplanar nature of shaft deflections, observed during the bench test phase of the program, complicated the dynamic balancing of the shaft. The flight test portion was then re-directed to:

- Provide an analytical description of supercritical phenomena as an aid for future drive system design.

The full-size supercritical shaft was built utilizing design information developed under this and previous programs. A shaft damper was developed to meet the requirements of the system as installed in an aircraft, and the splined adapter fittings were redesigned. The bench test program included tests of the damper, torsional fatigue testing of the redesigned adapter fittings, and dynamic tests of the full-size supercritical shaft.

The dampers successfully controlled the deflections of the shaft when the design criteria were not exceeded. The tests indicated the damper could be improved by increasing the stiffness of the elastomer.

Previous balance methods proved to be unsatisfactory for a shaft of this size. A new technique had to be developed to successfully balance the shaft throughout the desired speed range because of the noncoplanar nature of the shaft deflection at higher speeds.

The variable-schedule endurance runs were not completed. The difficulty encountered in balancing the system resulted in the accumulation of an equivalent time of 50 hours under loading conditions more severe (unbalanced) than those originally intended for the tests. No difficulty is anticipated for endurance tests with a balanced shaft.

The ground and flight test portion of the program has been replaced by an analytical description of the phenomena of multiple-mode bending identified during the bench test program. This analytical description includes variables anticipated in future supercritical shaft system designs.

Supercritical-speed-shaft performance has been demonstrated with adequate substantiating data, so that the future of this drive system can be predicted with confidence. The relative weight, reliability, safety, and economics of the system can be compared with more conventional drives since the unknowns have been identified.

FOREWORD

This report discusses the design, fabrication, bench testing, and analytical description of a full-sized supercritical-speed shaft and associated components for a flight test evaluation in a helicopter.

The work was authorized under USAAVLABS Contract DA 44-177-AMC-353(T), Task IG162203D14414. The effort was redirected to account for factors uncovered in the course of the investigation.

The principal investigators were:

R. J. Baier	—	Vertol Division; Project Engineer
D. Reed	—	Vertol Division; Senior Dynamist
R. L. Wesson	—	Vertol Division; Development Manager
Dr. Robert G. Loewy	—	Dynamics Consultant, Dean of the College of Engineering and Applied Sciences, University of Rochester
J. Gorndt	—	Lord Manufacturing Company

The author wishes to thank the USAAVLABS representatives, Mr. J. N. Daniel and Mr. Wayne Hudgins, for their aid in this program.

TABLE OF CONTENTS

	<u>Page</u>
Summary	iii
Foreword	v
List of Illustrations	ix
List of Tables	xvii
Introduction	1
Current Program	1
Future Development	7
Problem Statement	7
Problem Solution	8
Supercritical-Speed Shaft Design	10
Design Criteria Based on Aircraft Requirements	10
Design Analysis for the Dynamic System	13
Analysis Without Damping	14
Analysis With Damping	23
Structural Design Criteria	28
Shaft Torsional Loads	31
Bending Loads	31
Fatigue Conditions	31
Dampers and Support Structure	33
Determination of Maximum Bending Stress	33
Determination of Orbiting End Loads	34
Damper Test	35
Test Maching and Instrumentation	35
Test Procedure	35
Test Results	38
Summary	56
Conclusions	57
Torsion Test	58
Test Machine and Instrumentation	58
Test Procedure	58
Test Results	60
Summary	61
Conclusions	61
Full-Size Supercritical-Speed Shaft Test	63
Shaft Specimen	63
Balance Weights	68

	<u>Page</u>
The Bench Test Machine	68
Damper Supports	77
Instrumentation	78
List of Instruments	78
Optical Pick-Up	79
Test Procedure	79
Test Results	83
Effectiveness of Balance Weights	132
Effectivity Data	132
Test Results With Effectivity Data	152
Test Data From Balanced Shaft	164
Summary	178
Conclusions	178
Interpretation and Analysis of Test Results	180
General Observations	180
Comparison of Test and Initial Design Analysis	180
Noncircular Whirling Motion	180
Multiple Mode Response	184
Analysis of the D-10 Computer Balancing Program	184
Generalized Coordinate Analysis of Test Data and Balancing System	190
Graphic Isolation of Modes	200
Influence Coefficient Balancing Method	209
Analytical Simulation of a Rotating System	216
Analytical Model and Cases Analyzed	216
Results of Analysis	218
Conclusions	221
Literature Cited	222
Selected Bibliography	223
Appendix I. Development of an Analysis for a Rotation Shaft, Program C-58	225
Appendix II. Assembly Drawings	240
Distribution	244

LIST OF ILLUSTRATIONS

<u>Figure</u>		<u>Page</u>
1	Supercritical-Speed Test Shaft	3
2	Aircraft-Type Shaft Damper	4
3	Comparisons Between Subcritical, Supercritical, and Projected Systems	5
4	Drive System Development	6
5	Subcritical-Shaft Installation	11
6	Supercritical Test-Shaft Installation	12
7	Shaft Coordinates and Basic Analytical Model	14
8	Test and Calculated Undamped Frequencies	15
9	Effect of Damping on Critical Speed With Single Support at Station 32	17
10	Effect of Center Support on Undamped Critical Speed (End Damper at Station 32)	18
11	Effect of Damper Stiffness on Undamped Critical Speed	20
12	Effect of Damper Mass on Undamped Critical Speed	21
13	Theoretical Undamped Mode Shapes	22
14	Comparison of Test and Calculated Natural Frequencies With Support at Station 32	24
15	Comparison of Calculated Damped and Undamped Natural Frequencies With Supports at Stations 16 and 32	25
16	Effect of Damping on Shaft Response	26
17	Station 4 Displacement Versus Frequency (Calculated)	27
18	Comparison of Damped Quadrature Shapes and Undamped Mode Shapes	29
19	Mode-Shape Information With Locations for Dampers, Balance Pads, and Strain Gages	30
20	Typical Mode Shapes	32
21	Bending Stress From Shaft Whirling	33

<u>Figure</u>		<u>Page</u>
22	Damper – Sectional View	36
23	Damper Test Setup	37
24	Damper Test Vee-Belt Drive	37
25	Damper Load Versus Deflection (Spring Rate)	39
26	Force Versus Speed to 60 CPS at 70°F	40
27	Force Versus Speed to 100 CPS at 70°F	41
28	Force Versus Speed to 140 CPS at 70°F	42
29	Force Versus Speed to 60 CPS at 32°F	43
30	Force Versus Speed to 100 CPS at 32°F	44
31	Force Versus Speed to 140 CPS at 32°F	45
32	Force Versus Speed to 60 CPS at 160°F	46
33	Force Versus Speed to 100 CPS at 160°F	47
34	Force Versus Speed to 140 CPS at 160°F	48
35	Stabilized Temperature Versus Speed at 70°F	50
36	Stabilized Temperature Versus Speed at 32°F	51
37	Stabilized Temperature Versus Speed at 160°F	52
38	One Chamber Damping Force Versus Speed at 70°F	53
39	One Chamber Stabilized Temperature Versus Speed at 70°F	54
40	Temperature and Force Versus Time – Endurance Test at 160°F	55
41	Disassembled Damper	56
42	Torsion Test Torque Arm	59
43	Torsion Test Failure Analysis	60
44	Test Specimen and Location of Dampers	64
45	Calibration Test Shaft	65

<u>Figure</u>		<u>Page</u>
46	Shaft Adapter - Sectional View	66
47	Splined Adapter Details	67
48	Splined Adapter Assembly Procedure	67
49	Initial Bend as Manufactured – Serial 2	69
50	Initial Bend After Straightening – Serial 2A	70
51	Initial Bend After Straightening and Machining – Serial 2B	71
52	Polar Deflection Initial Bend – Serial 2B	72
53	Time History of Initial Deflection for 180 Degrees of Shaft Rotation	73
54	Balance Weight Assembly	74
55	Balance Weight Chart	75
56	Bench Test Machine	76
57	Bench Test Damper Structure	77
58	Schematic and Calibration of Solar Cell Transducer	80
59	Optical Pickup Trolley	81
60	Standard Format for Presenting Deflection Data Versus Rotational Speed	84
61	Displacement Versus Frequency (Vibrated)	85
62	Vibrated Mode Shapes	86
63	Test 5 – No Balance Weights – Serial 2	87
64	Summary Data From Test 10 With Balance Weights – Serial 2	89
65	Test 12 – Calculated Weights – Serial 2	90
66	Optimum Phase and Weight	91
67	Tests 35 and 42 – Serial 2	92
68	Initial Mode Shapes for Balance Purposes	94
69	Revised Mode Shapes for Balance Purposes	95

<u>Figure</u>		<u>Page</u>
70	Summary Data From Test 35 – Serial 2	96
71	Tests 45 and 46 – Serial 2 (Damper Failure)	97
72	Damper Failure – External	98
73	Damper Failure – Internal	98
74	Tests 66, 67, and 68 – Serial 2A	100
75	Tests 69, 70, and 71 – Serial 2A	101
76	Summary Data From Tests 71 and 72 – Serial 2A	102
77	Optimum Angle Tests 94 through 99 – Serial 2A	103
78	Optimum Weight Tests 97, 100, 101, and 102 – Serial 2A	104
79	Rotated Mode Shapes – Serials 2 and 2A	105
80	Rotated Mode Shapes – Serial 2A	106
81	Rotated Mode Shapes – Serial 2A	108
82	Deflection in Two Planes – Serial 2B	109
83	Polar Deflection at 5,982 and 6,562 RPM – Serial 2B	110
84	Deflection Versus Speed to 8,300 RPM – With Weights	111
85	Deflection Versus Speed to 8,300 RPM – Without Weights	112
86	Deflection and End Load Versus Speed	113
87	Deflection, End Load, and Strain Versus Speed	114
88	Effect of Balance Weight Phase on Deflection and End Load	115
89	Delta Phase of End Load Links	117
90	Horizontal and Vertical Deflection at Station 4	118
91	Effect of Torque	119
92	Deflection in Four Planes at Station 4	120
93	Damper Motion in Two Planes at Station 16	121

<u>Figure</u>		<u>Page</u>
94	Damper Motion in Two Planes at Station 32	122
95	Mode Recorded by the Optical Pickup at 7,300 RPM	123
96	Polar Deflection at 5,400 RPM for Repeatability	124
97	Polar Deflection at 6,000 RPM for Repeatability	125
98	Polar Deflection at 7,300 RPM for Repeatability	126
99	Deflection in Two Planes for Modes at 5,400, 6,000, and 7,300 RPM	127
100	Mode Shapes With Second Component Removed	128
101	Time History of Response for 180 Degrees of Shaft Rotation at 7,300 RPM	129
102	Model of Shaft Deflection at 7,300 RPM	130
103	Acoustic Investigation – Serial 2B	131
104	Balance End Load Test Series	133
105	Deflection and Load Versus Speed After Balancing	134
106	Deflection Versus Speed With Trial Weight at Station 5	136
107	Polar Plot of Trial Weight at Station 5	137
108	Deflection Versus Speed With Trial Weight at Station 8	138
109	Polar Plot of Trial Weight at Station 8	139
110	Deflection Versus Speed With Trial Weight at Station 10	140
111	Polar Plot of Trial Weight at Station 10	141
112	Deflection Versus Speed With Trial Weight at Station 11	142
113	Polar Plot of Trial Weight at Station 11	143
114	Deflection Versus Speed With Trial Weight at Station 21	144
115	Polar Plot of Trial Weight at Station 21	145
116	Deflection Versus Speed With Trial Weight at Station 24	146
117	Polar Plot of Trial Weight at Station 24	147

<u>Figure</u>		<u>Page</u>
118	Deflection Versus Speed With Trial Weight at Station 27	148
119	Polar Plot of Trial Weight at Station 27	149
120	Developed Modes From Effectivity Tests	151
121	Effectivity Data Balance for 5,300 RPM	153
122	Effectivity Data Used for Balance at 7,300 and 8,300 RPM	154
123	Polar Deflection at 5,300 and 7,300 RPM	155
124	Deflection Shapes in Two Planes	156
125	Time History of Shaft Deflection for 180 Degrees of Shaft Rotation at 5,300 RPM	157
126	Time History of Shaft Deflection for 180 Degrees of Shaft Rotation at 7,300 RPM	158
127	Stiffened Versus Flexible Damper Structure	159
128	Intentionally Unbalanced to Hit the Guard	161
129	Substitution of Permanent Balance Weights	162
130	Effect of Under- and Overbalance on the Fifth Critical	163
131	Deflection Versus Speed at Station 3.5	165
132	Bending Stress Versus Speed at Station 4.0	165
133	End Load Versus Speed at Station 1.0	165
134	Damper Motion Versus Speed at Station 15.5	166
135	Damper Motion Versus Speed at Station 31.5	166
136	Deflection Versus Speed at Station 24.0	166
137	Polar Deflection at 8,300 and 7,300 RPM	167
138	Polar Deflection at 5,250 and 3,570 RPM	168
139	Polar Deflection at 2,280 and 1,150 RPM	169

<u>Figure</u>		<u>Page</u>
140	Time History of Shaft Deflection for 180 Degrees of Shaft Rotation at 8,300 RPM	170
141	Time History of Shaft Deflection for 180 Degrees of Shaft Rotation at 7,300 RPM	171
142	Time History of Shaft Deflection for 180 Degrees of Shaft Rotation at 5,250 RPM	172
143	Time History of Shaft Deflection for 180 Degrees of Shaft Rotation at 3,570 RPM	173
144	Time History of Shaft Deflection for 180 Degrees of Shaft Rotation at 2,280 RPM	174
145	Time History of Shaft Deflection for 180 Degrees of Shaft Rotation at 1,300 RPM (Interpolated)	175
146	Polar Plot of Final Balance Weights	176
147	Time History of Final Balance Weight Effectiveness for 180 Degrees of Shaft Rotation	177
148	Comparison of Rotating Test and Calculated Nonrotating Response .	182
149	Whirl Pattern Types	183
150	Generalized Coordinate Analysis of Theoretical Response – Modal Amplitude	192
151	Generalized Coordinate Analysis of Theoretical Response – Modal Phase	193
152	Generalized Coordinate Analysis of Unbalanced Shaft – Modal Amplitude	195
153	Generalized Coordinate Analysis of Unbalanced Shaft – Modal Phase .	196
154	Vector Response of Unbalanced Shaft at the n th Critical Speed . . .	201
155	Vector Response to Trial Weight at the n th Critical Speed	203
156	Shaft Response at First and Second Modes	204
157	Typical Polar Plot Characteristics for Two Modes	205
158	Response to Trial Weight at First and Second Modes	206
159	Shaft Response at Fifth Mode	207

<u>Figure</u>		<u>Page</u>
160	Response to Trial Weight at Fifth Mode	208
161	Analytical Model for Test Configuration	217
162	Unbalance Distribution – Analytical Cases	219
163	Calculated Response – Rotating Analysis	220
164	Analytical Model for Rotating System	226
165	Idealization at Intermediate Support	227
166	Mass Motions at Intermediate Support	228
167	Mass Matrix	231
168	Damping Matrix	233
169	Dynamic Stiffness Matrix	235
170	Forcing Function Matrix	237
171	Program Flow Diagram	238

LIST OF TABLES

<u>Table</u>		<u>Page</u>
I	Total Damper Motion Percent of Maximum Normal Mode Amplitude	19
II	Comparison of Calculated Nonrotating Natural Frequencies and Rotating Critical Speeds	181
III	Comparison of Actual and Calculated Balance Weights From D-10 Analysis	185
IV	List of Symbols for D-10 Analysis	186
V	Comparison of Derived and Measured Initial Deformity	189
VI	Summary of Results: Generalized Coordinate Analysis With Undamped Modes	197
VII	Summary of Results: Generalized Coordinate Analysis With Damped Response Shapes	198
VIII	Experimentally Determined Influence Coefficients at Station 4 With Stiffened Damper Support Structure	212
IX	Comparison of Calculated Balance Configurations Obtained by The Influence Coefficient Method	213
X	Comparison of Initial Weight Distributions for Calculated Balance Configurations	214
XI	Suggested Balance Arrangement	215
XII	List of Symbols for Appendix I	239

INTRODUCTION

This report summarizes the design, bench test, and analytical effort on a program by the Vertol Division of Boeing to develop and flight test a supercritical-speed interconnect shaft for the CH-47 helicopter. This program was undertaken to establish the design criteria necessary for the installation of a supercritical-speed drive system in a CH-47 aircraft, and to determine the effect the aircraft and its environment would have on the system. The object of the program was to evaluate the performance of the shaft by comparing bench test data with data obtained with this shaft installed in an aircraft.

Vertol Division's interest in the field of supercritical-speed drive systems resulted in a proposal early in 1959 to study, build, and test such a system. Actual testing was under way on a company-funded program in 1961. The early work indicated a need for a more satisfactory damper to allow continuous operation at critical speeds. Battelle Memorial Institute of Columbus, Ohio contributed significant progress in this area between 1961 and 1964. Their report, DESIGN CRITERIA FOR HIGH SPEED POWER TRANSMISSION SHAFTS,¹ concludes that damping is the most significant variable in the control of supercritical-speed shafts.

In 1964 Vertol Division, in collaboration with Battelle Memorial Institute, embarked on a program to relate Battelle's model work to a full-size shaft for an actual aircraft (DESIGN AND TEST EVALUATION OF A SUPERCRITICAL SPEED SHAFT, USAAVLABS Technical Report 66-49²). The CH-47 Chinook tandem-rotor helicopter was chosen because the configuration requires the transmittal of a large amount of power over the considerable distance between the rotors. The object of this program was to determine if a full-size shaft would perform as predicted by the smaller model shafts. A full-size shaft was designed and manufactured for test. The test specimen operated successfully only after dynamic balancing. Two methods of balancing were investigated. Battelle's experimental method produced satisfactory results, and it was used for the test specimen. An analytical method was also investigated, with limited success. Three conclusions were drawn from this work: the modeling equations developed under the previous program did not correctly predict full-size performance; variations of the characteristics of the damper would not, by themselves, produce satisfactory performance; and supercritical shafts will have to be balanced.

CURRENT PROGRAM

The success achieved with the full-size shaft prompted expansion of the effort to include a flight test evaluation of the system. This report covers the design, bench test effort, and a mathematical analysis under such a program, including the development of a damper suitable for installation in an aircraft. It presents the design philosophy for a supercritical-speed shaft system and presents the results of the test programs used to evaluate the system. The analytical description based on a rotating system was developed to permit a thorough study of supercritical systems including additional phenomena revealed during the tests.

The supercritical-speed shaft investigated is of the same diameter and turns at the same speed as the existing subcritical shaft system. Diameter, length, and shaft speeds are dictated by present transmission ratios and torque requirements and, in this regard, are the same as those

in the previous program.² Changes from the previous design include the addition of a center damped support (see Figure 1) and the substitution of a new aircraft damper for the laboratory damper. There is very little clearance between the interconnect shaft and the structure on the CH-47. The center damper was added to prevent interference with the rotating shaft if it deflects due to aircraft accelerations or when passing through the lower critical speeds. The aircraft damper (see Figure 2) has fixed characteristics that have been optimized in the previously conducted program; the laboratory dampers had variable characteristics for this purpose. The damping chamber is sealed to make it more suitable for installation in the environment of the aircraft.

The advantages of a successful system are:

- Reduction in weight
- Reduction in parts
- Saving in cost
- Increased reliability

Eliminating the shaft adapter fittings and structural supports which are required at each joint of the subcritical system would reduce weight, and weight saving has an almost direct relationship to the number of critical speeds the system operates through. Moreover, the weight, cost, number of parts, and reliability of a design are all related to one another in a general way, and any increase or decrease of one will affect the others as well. Figures 3 and 4 show the results of a study of these factors for the subcritical system, the supercritical system, and a projected system as applied to the CH-47 helicopter. For purposes of this comparison, the following definitions and limits were used:

Subcritical system – This system consists of the existing drive train between the combining transmission and the forward transmission of the CH-47B Chinook helicopter. All items which are affected by the substitution are included in the comparisons.

Supercritical system – This system could replace the *subcritical system* with no change in the transmissions or attach points at the transmissions. It will turn at the same speeds and carry the same torque loading.

Projected system – This system is a one-piece steel shaft, splined directly to the end transmissions, with misalignment capability provided by the flexibility of the shaft itself. The advantage of this system is the elimination of the number and the weight of the adapters for the dampers and for the ends of the shaft.

A truly optimum system would consider other materials and turn at much higher speeds, thereby affecting further improvements in the drive and probably in the transmissions as well.

Number of Parts – The shaded section in Figure 3 shows only the number of special parts required for a complete drive system. The clear section combined with the shaded section shows the total number of parts required, including shelf items such as bolts, nuts, and bearings. Structural items beyond the immediate drive train supports are not included in this study.

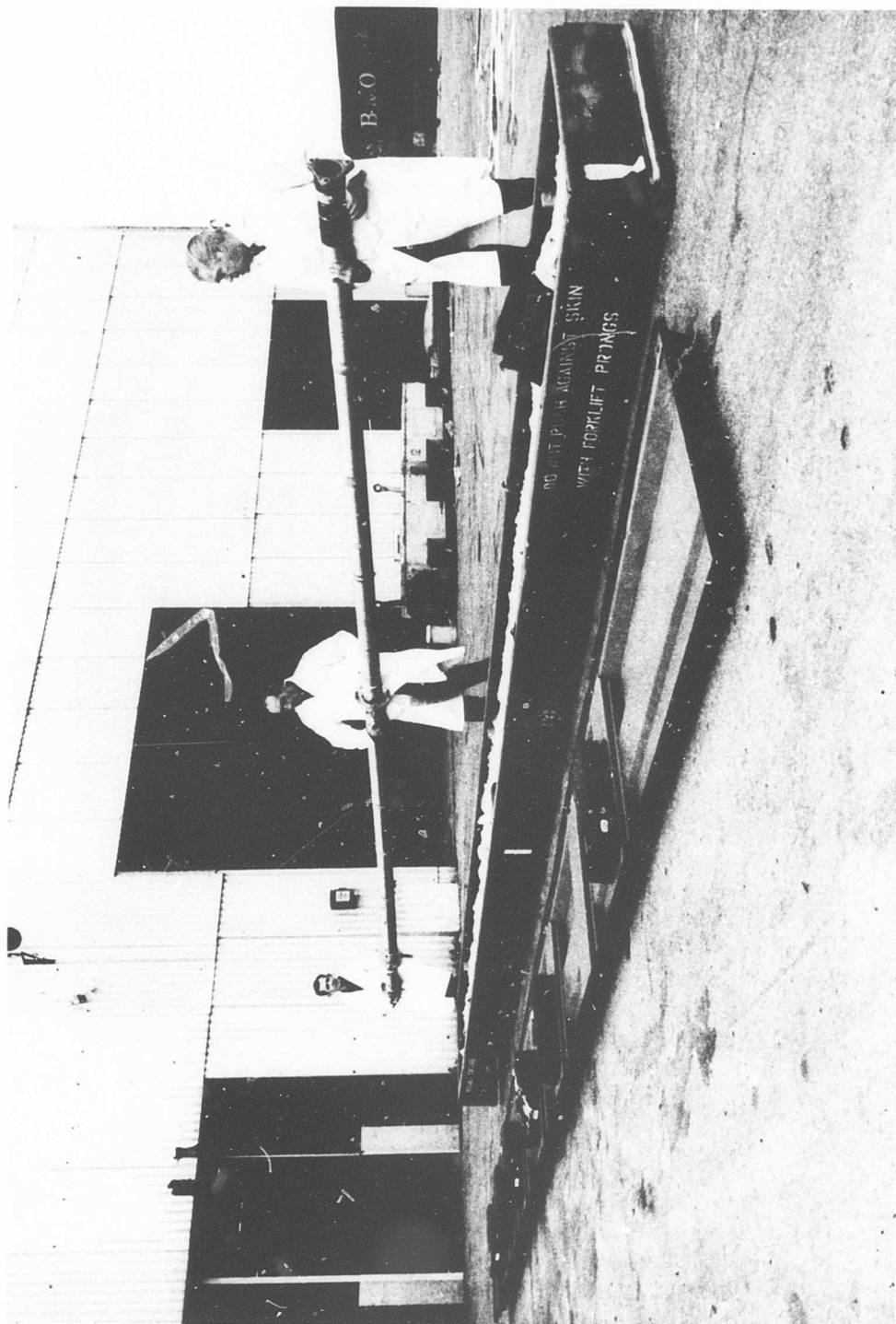


Figure 1. Supercritical-Speed Test Shaft.

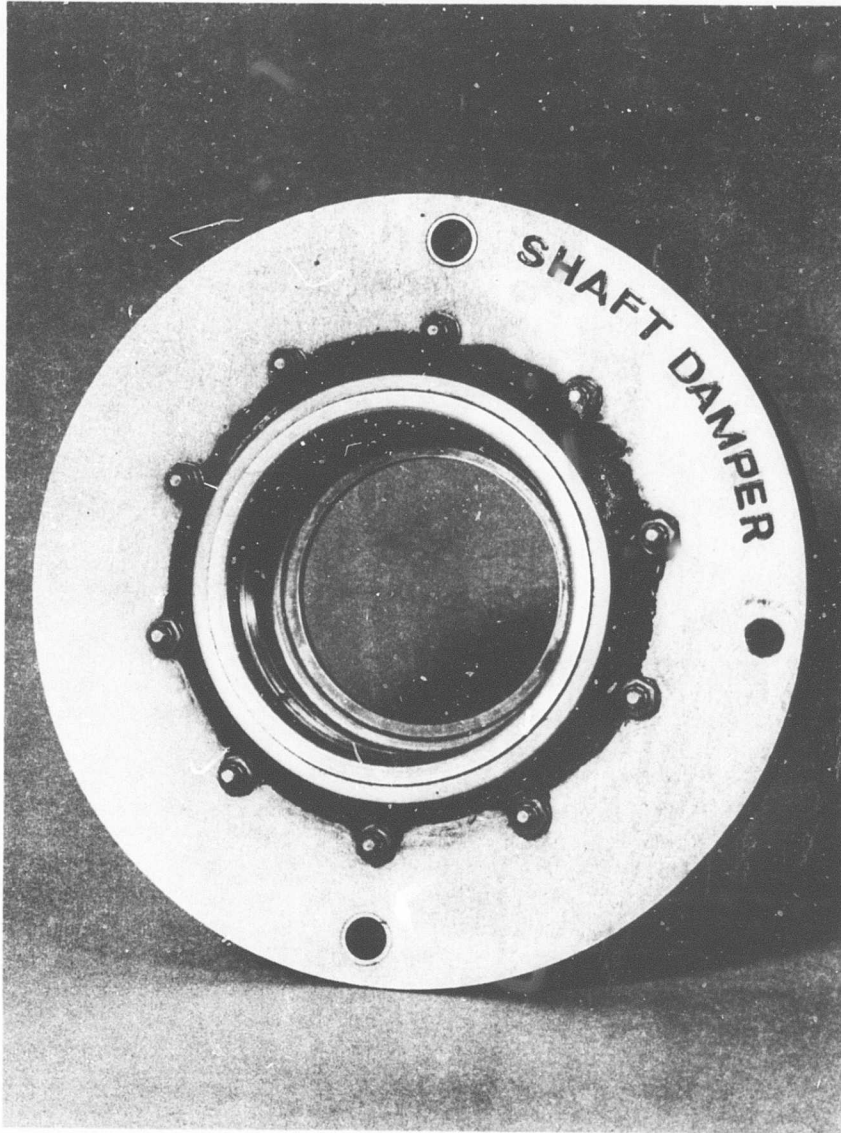
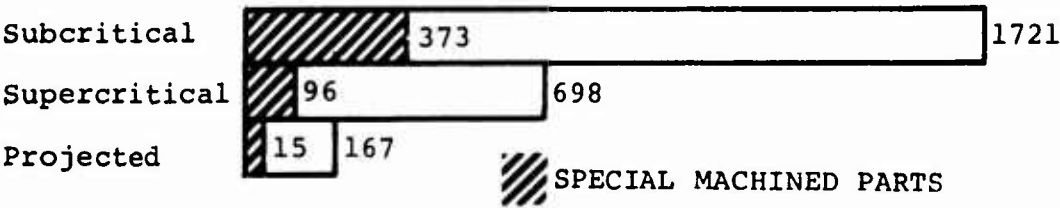
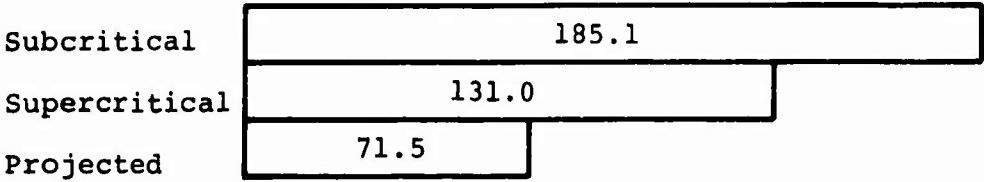


Figure 2. Aircraft-Type Shaft Damper.

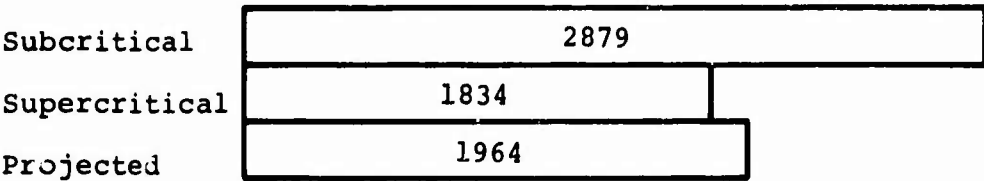
NUMBER OF PARTS



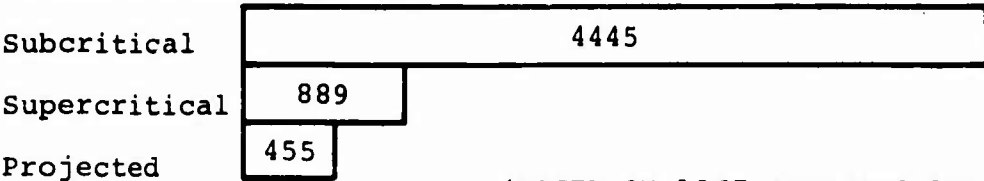
WEIGHT OF SYSTEM, POUNDS



INITIAL PRODUCTION COST FOR 100 AIRCRAFT, DOLLARS *



FUNCTIONAL FAILURES PER MILLION FLIGHT HOURS *



*BASED ON 1967 ANALYSIS AND DATA.

Figure 3. Comparisons Between Subcritical, Supercritical, and Projected Systems.

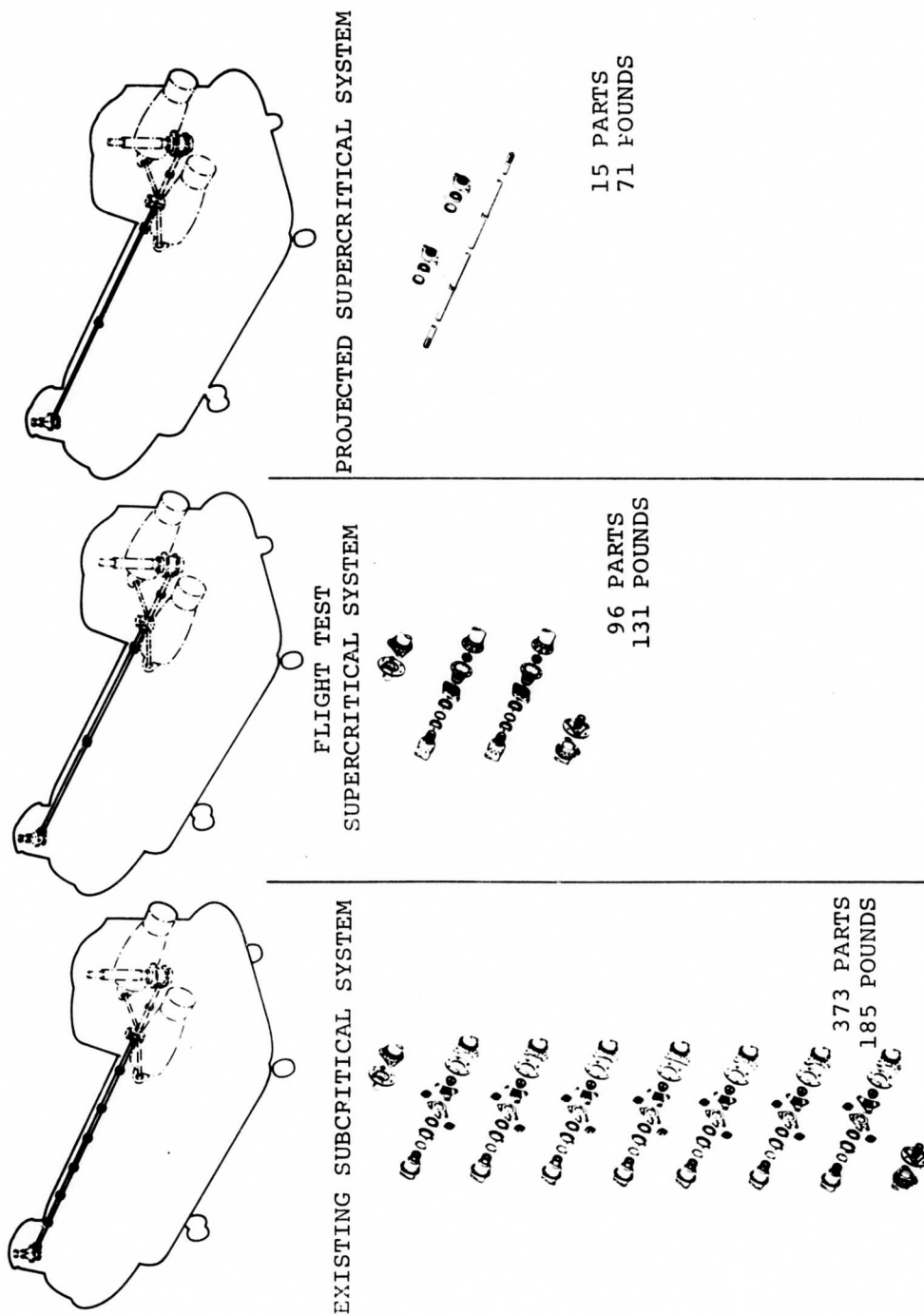


Figure 4. Drive System Development.

Weight of the System – Weights were calculated for the systems described. An optimum system would show further improvement in this area.

Initial Production Cost – The cost study was based on production cost and tooling for 100-ship sets. The projected system cost reflects roll-forge dies which constitute a substantial part of the cost.

Functional Failure – This chart is an indication of reliability. Functional failures per million flight hours are based on actual records for the subcritical system and are projected for the supercritical systems. The comparison represents the value of reducing the number of parts for increased reliability.

FUTURE DEVELOPMENT

The potential advantages of supercritical-speed shafts will be realized when other intangible factors are considered. Appreciable weight saving can be realized when the supercritical drive system is used in a thin structure such as a wing because of the elimination of the inspection holes and covers which are required for a subcritical system. The potential advantages of supercritical-speed drive systems are now limited by transmissions. Current transmissions are not developed for very large ratios of reduction (such as 100 to 1) because the most efficient speed for present drive trains seem to be 8,000 to 10,000 rpm. Higher speeds would require drive shafts with larger diameters or shorter lengths between couplings to keep the sections operating in the subcritical range. Either solution would increase the weight, the complexity, and the cost of the drive system. Supercritical-speed shafts on the other hand can operate at higher speeds without these disadvantages.

PROBLEM STATEMENT

The object was to design and build a supercritical-speed shaft and to install and test it in an existing aircraft to ensure that it meets all design requirements and safely provides the desired test information for evaluation.

Problems were encountered in the following areas:

- Insufficient clearance between the shaft and the aircraft structure under all ground and flight conditions.
- Development of a suitable aircraft damper.
- Detail design of the adapter joint at the dampers to eliminate fretting observed on previous tests and to provide disassembly capability without disturbing the balance of the unit.
- Dynamic balancing of the specimen
- Analytical description of the shaft as a rotating system.

PROBLEM SOLUTION

The clearance problem between shaft and structure was resolved by adding a damped center support which changes the speeds at which the criticals occur. Since the operational ranges, both ground idle and flight range, should be clear of the critical speeds, the location of the center support was varied and the critical speeds were calculated. The location which permitted the operational ranges to be free of critical frequencies was then investigated.

Because of the limitation imposed by designing for the existing speeds and torques and because of variations between calculated performance and actual performance, both ground idle and flight ranges contained a critical speed. The choice was between a well damped critical (the sixth) near the top or autorotational speed and a poorly damped critical (the fifth) in the low range of hover speed. System characteristics which contained a well damped sixth critical speed were preferred, and the design was initiated.

A secondary factor in locating the center support was to locate it clear of major aircraft structure so that extensive modification would not be necessary. This objective was accomplished.

The aircraft-type damper was developed in collaboration with Lord Manufacturing Company. The damper requirements were established by calculation, and the damper was then constructed to the resulting specification. A dual-chamber damper was designed to provide a redundancy for operation in case of fluid loss from one of the chambers. The damper bearing is the same as the one used in the standard drive system at the adapter and flex coupling joint. It is grease lubricated.

The prior test program disclosed the problem of fretting at the damper-adapter joint. The fittings for that program were designed to transmit torque and were not specifically designed for bending. A new joint was designed with special attention directed to maintaining the bending stiffness through the adapter area. Alignment of the joint is provided by tapered washers at each end of the spline. The tapered washers are held in place with a standard type bearing-retainer nut and lock washer. The joint is torqued to a point where bending expected in service will not exceed the initial tension applied at assembly (see Appendix II).

Dynamic balancing proved to be more troublesome than expected. The experimental and analytical methods developed under the previous programs could not be used; a new approach was necessary. Mode shape investigation disclosed bending in more than one plane and mode at any given time. This fact alone was sufficient to make previous balance techniques ineffective.

A new approach was required to determine the actual mode shape. The most effective phase angle of a trial weight at each balance station was used as an indication of the mode at speeds of interest; the noncoplanar nature of the optimum angle was apparent, especially at higher speeds, when the responses from all stations were compared. The angular relationship of trial weights to modes was used as the basis for locating weights to experimentally balance the test shaft.

A computer program based on the trial-weight-effectiveness approach is available and has been used successfully to check the experimental results.

The analytical description, developed for further study of the variables associated with a rotating system, is intended to adequately predict the performance of any supercritical-shaft system. The analytical approach can be used to optimize the independent variables and aid in a complete understanding of the problems.

SUPERCritical-SPEED SHAFT DESIGN

The rotor interconnect shaft of the CH-47 helicopter was chosen as the subject of investigation (see Figure 5) because:

- The present subcritical-speed shaft can be used for comparison of performance, cost analysis, weight, reliability, etc.
- A demonstration vehicle is available for complete evaluation of the final design.
- This shaft is the longest and has the highest continuous horsepower capacity of any high-speed shaft in the military aircraft inventory.
- This program is a continuation of the previous effort.

Design requirements based on an existing subcritical system allow evaluation of a supercritical-speed system without major and costly changes in the drive train. In a new supercritical design it may prove to be advantageous to run the shafting at much higher speed, without intermediate gear reduction from engine speed. Supercritical-speed operation can be achieved either by running at higher speeds or by removing some of the supports. Since shaft speed is dictated by the present transmission, removing the supports was the approach followed (see Figure 6). The center support was added to prevent interference with the structure due to the natural sag of the shaft. Normal sag would become much greater under flight or landing accelerations, and adequate clearance must be provided under these conditions as well. The shaft is continuous through the damped supports and is capable of taking bending through these joints. The shaft extends from the flexible plate coupling on the forward transmission to a similar flexible plate coupling near the tail of the helicopter, where power from the engines is introduced through a combining transmission.

DESIGN CRITERIA BASED ON AIRCRAFT REQUIREMENTS

The design and test program was based on the following requirements of the system as it exists in the helicopter and on the environmental requirements expected for the aircraft in service.

- This data from the operational helicopter will be used in the design of the supercritical system.

Dimensions

Shaft length between gearboxes	338.8 inches
Shaft outside diameter (maximum)	4.50 inches

Operating speed range - minimum to maximum

Ground idle	2763 to 3070 rpm
Normal flight range	7061 to 7460 rpm
Extended flight range	6600 to 8289 rpm

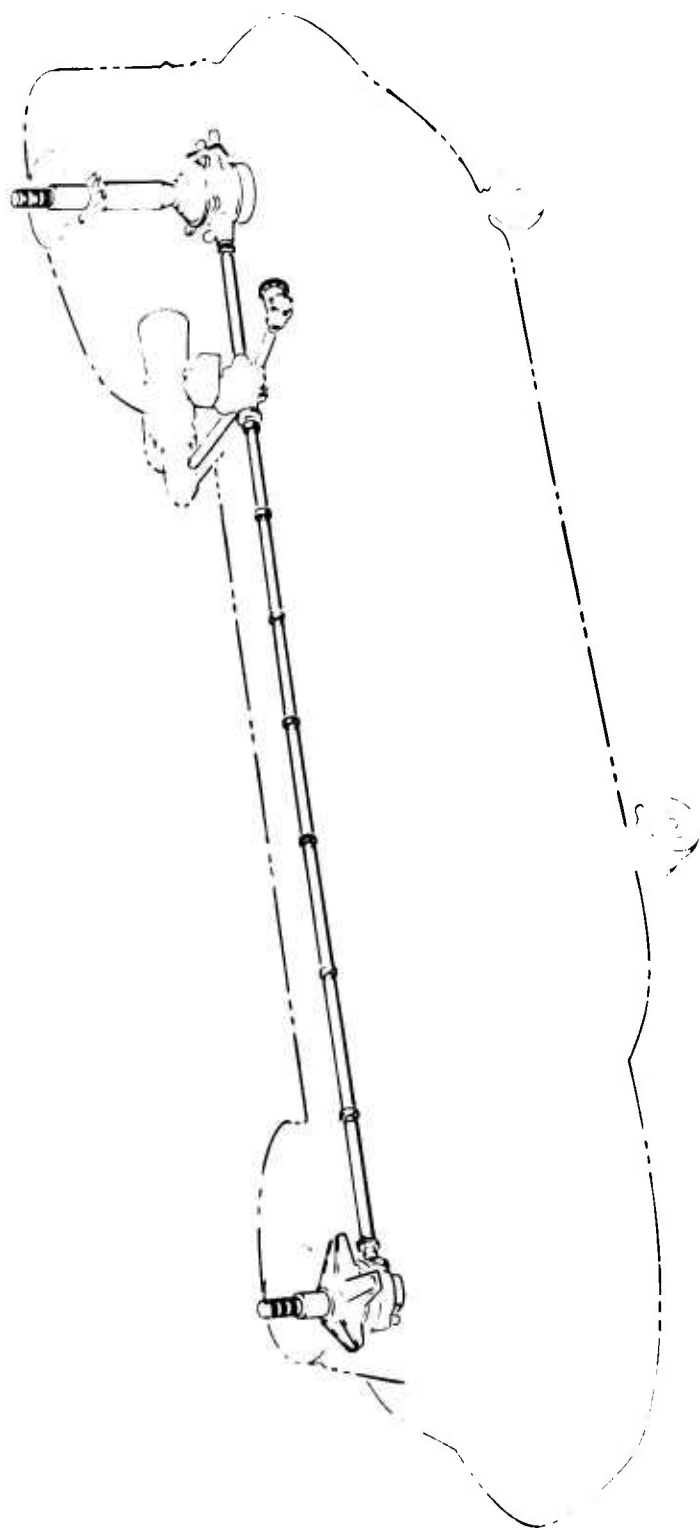


Figure 5. Subcritical-Shaft Installation.

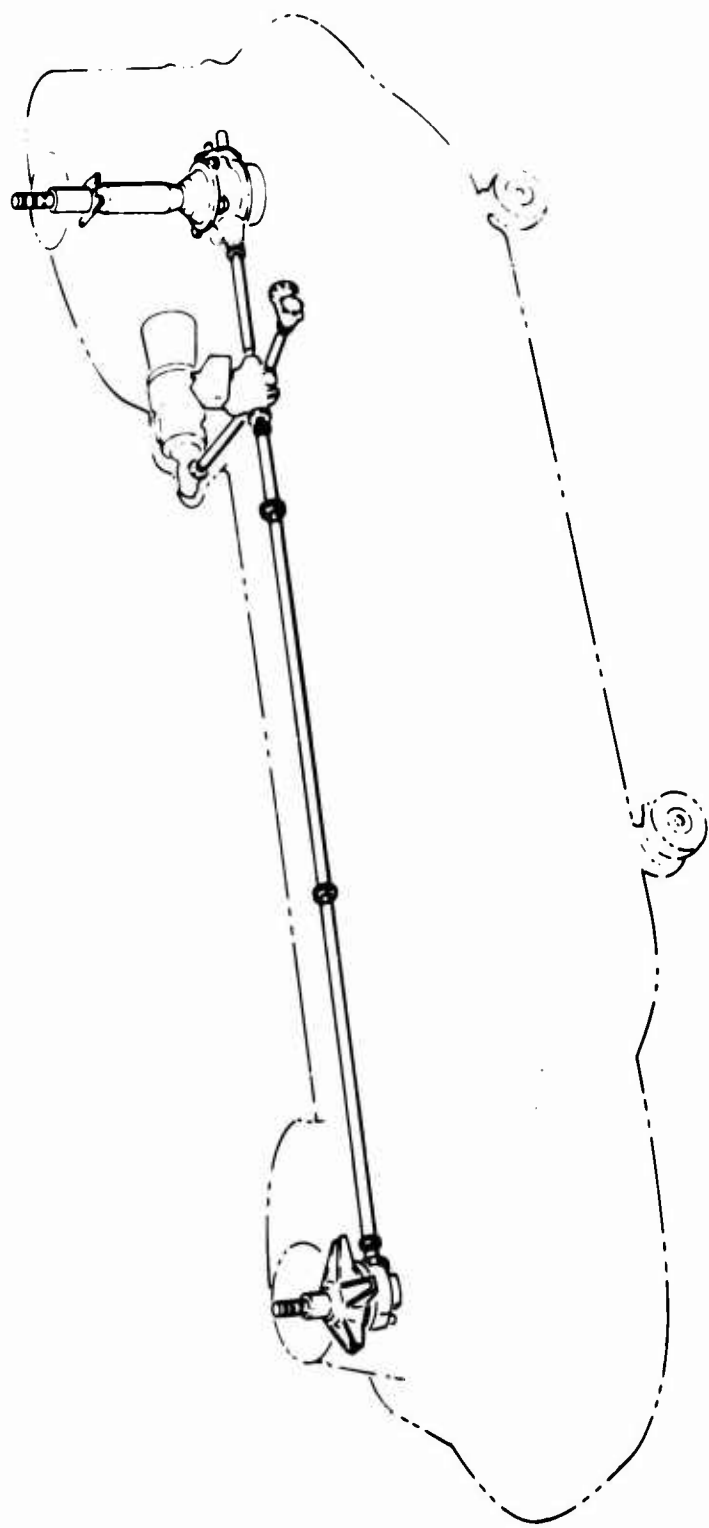


Figure 6. Supercritical Test-Shaft Installation.

Torque

Normal operational torque	15,000 inch-pounds
Design fatigue torque	26,500 \pm 4000 inch-pounds
Ultimate torque	60,000 inch-pounds

Relative motions from fuselage at limit load

Angular	$\pm 0^{\circ} 4$ minutes
Length	± 0.216 inch

Angular tolerance on blade phasing	$\pm 1^{\circ}$ at rotor
------------------------------------	--------------------------

Time to accelerate (approximate)

0 to 3,200 rpm (ground idle)	7 seconds
3,200 rpm to design speed	4 seconds

G Loadings

Flight	+2.67g to -0.50g
Landing	+2.80g
Crash	8g all directions, acting separately

- Environmental temperature range will be restricted to a minimum operational temperature of 32°F and a maximum of 100°F for a standard hot day.
- There will be two dampers. The design will be redundant in that each damper will contain a dual chamber for fail-safe operation.

The torque capacity requirement was met by designing the supercritical tube to the same torsional stress criteria as the present subcritical tube. Restrictions on outside diameter resulted in identical tube diameter and wall thickness. Length between transmissions also duplicates the CH-47 shaft system length.

Restricting the environmental temperature range to +32°F instead of the usual -65°F reduced the number of problem areas associated with the dynamics of the supercritical-shaft system, and a reduced cost for the program was reflected.

DESIGN ANALYSIS FOR THE DYNAMIC SYSTEM

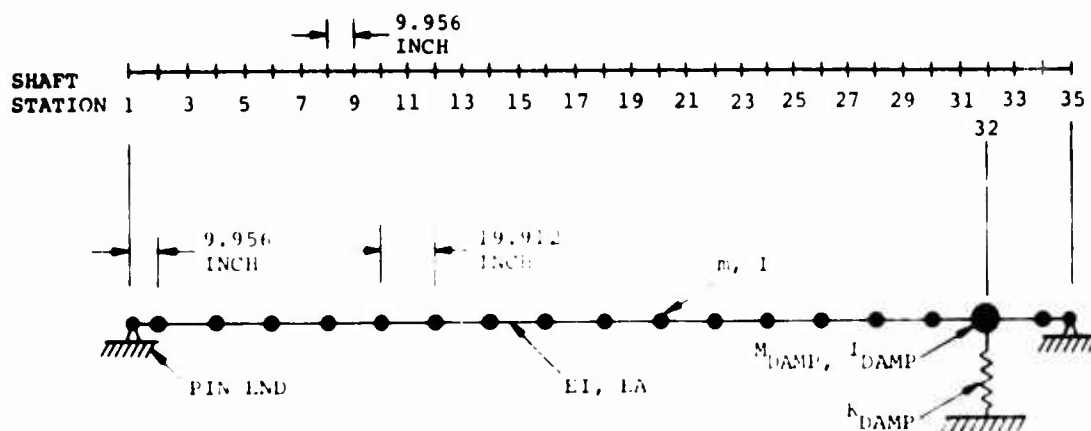
Data to be derived for design of the supercritical shaft were damper variables, damper positions, and critical speeds. The previous test program, which used a similar shaft but contained a single damped support, was used as a starting point for the analytically-derived data.

Analysis Without Damping

For the case of a synchronous forward whirl, the fact is well established that the critical speeds correspond to the natural frequencies in lateral vibration of the stationary (non-rotating) shaft. In order to establish confidence in the analytical method, undamped natural frequencies and modes were first computed for comparison with the following stationary-shake-test configurations from the previous test program:

- Undamped shaft with an elastic support at station 32
- Undamped shaft with an elastic support at station 32 and a rigidly-supported bearing at station 16

Calculations were performed with a digital computer program (Boeing-Vertol Program D-29) which employed Myklestad's method in which the shaft is represented as a series of concentrated masses connected by weightless beam elements. The basic analytical model with a single support is illustrated in Figure 7. Results of the calculations are summarized in Figure 8; excellent correlation with the previous shake-test data is indicated for both frequency and mode shape.



$$m = 0.00855 \text{ LB-SEC}^2/\text{IN.}$$

$$K_{\text{DAMP}} = 100 \text{ LB/IN.}$$

$$I = 0.305 \text{ LB-IN.-SEC}^2$$

$$EI = 4.18 \times 10^7 \text{ LB-IN.}^2$$

$$M_{\text{DAMP}} = 0.0552 \text{ LB-SEC}^2/\text{IN. (1)}$$

$$EA = 1.73 \times 10^7 \text{ LB}$$

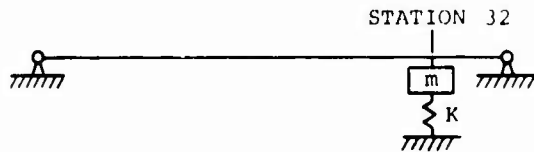
$$I_{\text{DAMP}} = 0.444 \text{ LB-IN.-SEC}^2$$

NOTE:

(1) 18-LB DAMPER WEIGHT PLUS WEIGHT OF SHAFT SEGMENT

Figure 7. Shaft Coordinates and Basic Analytical Model.

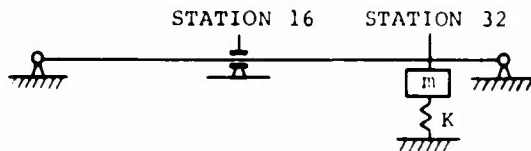
SINGLE ELASTIC SUPPORT



$K = 100 \text{ LB/IN.}$
 $M = 18 \text{ LB}$

MODE	SHAKE TEST FREQUENCY (CPS) (1)	CALCULATED FREQUENCY	MODE SHAPE CORRELLATION
	5.3	5.2	EXCELLENT, WITHIN EXPERIMENTAL ACCURACY
	16.4	16.9	EXCELLENT, WITHIN EXPERIMENTAL ACCURACY
	33	33.8	EXCELLENT, WITHIN EXPERIMENTAL ACCURACY
	58	58.8	EXCELLENT, WITHIN EXPERIMENTAL ACCURACY
	93	91	EXCELLENT, WITHIN EXPERIMENTAL ACCURACY
	135	133.4	EXCELLENT, WITHIN EXPERIMENTAL ACCURACY

ONE ELASTIC AND ONE RIGID SUPPORT



$K = 100 \text{ LB/IN.}$
 $M = 18 \text{ LB}$

MODE	SHAKE TEST FREQUENCY (CPS) (1)	CALCULATED FREQUENCY	MODE SHAPE CORRELLATION
	14.2	14.4	NO TEST DATA AVAILABLE
	30.3	27.6	NO TEST DATA AVAILABLE
	44	47.5	NO TEST DATA AVAILABLE
	92.5	89.9	NO TEST DATA AVAILABLE
	115	110.1	NO TEST DATA AVAILABLE

NOTE: BATTELLE SHAKE TEST DATA

Figure 8. Test and Calculated Undamped Frequencies.

From test data of the shaft with a single elastic support, the plot of Figure 9 has been constructed to determine the effect of damping on the location of the natural frequencies. This plot shows mixed results for the lower modes, while the frequency of the modes above the fourth is essentially the same as the undamped frequency. Since the higher modes are the modes which fall in the operating range, determining the required position and stiffness of the shaft supports using an undamped analysis appears to be justified. Once the geometry of the shaft configuration is established, the damping requirements may be investigated independently.

To minimize the structural modifications required for installation of the shaft in a CH-47 helicopter, the best location for the center support is at approximately station 16, and the best location for the end damper is approximately station 31 or 32. During the previous test program, station 32 was experimentally established as the best overall location for the end damper. The following discussion will show that this result is still valid.

Figure 10 shows the variation in undamped critical speed as a function of the center support location with the end damper at station 32 and a support spring rate of 1,000 pounds per inch. Based on the previous design, a damper mass of 18 pounds was used in the calculations. The GROUND IDLE, NORMAL FLIGHT, and EXTENDED FLIGHT operating ranges are as indicated. The sixth critical is within the extended flight operating range for all practical locations of the center support and within the NORMAL FLIGHT range for all locations between station 10 and station 17.5. Of less significance is the fact that the fourth critical is within the GROUND IDLE range for center support locations between stations 12.5 and 17.5. For the fourth, fifth, and sixth modes, the critical speeds without the center support have been identified; the critical speed with the additional support is always lower due to the added mass of the center support. The importance of the damper mass is further emphasized by comparison of the critical speeds of the shaft with the station 32 damper only and the critical speeds of the unsupported shaft. This comparison shows that the damper mass would have to approach zero in order to raise the sixth critical above the operating range and that the damper weight required to reduce the sixth critical to a point below the flight range would be prohibitive.

One further useful piece of information may be deduced from the curves of Figure 10. In the areas where the critical speed is highest and approaches the value obtained without the center support (station 32 damper only), the center support has no mass effect and must therefore be a node point. Conversely, the areas where the critical speed is lowest indicates large motion of the center support mass and the support point must coincide with an antinode. These observations lead to the important conclusion that a well damped fourth and sixth mode will be obtained if the center support is located at station 16, since the center damper will lie close to an antinode. Similarly, the center damper will contribute no effective damping in the fifth mode due to the near nodal location. Since the sixth mode is within the operational range while the fifth mode is not, location of the center support at station 16 appears to be an acceptable compromise.

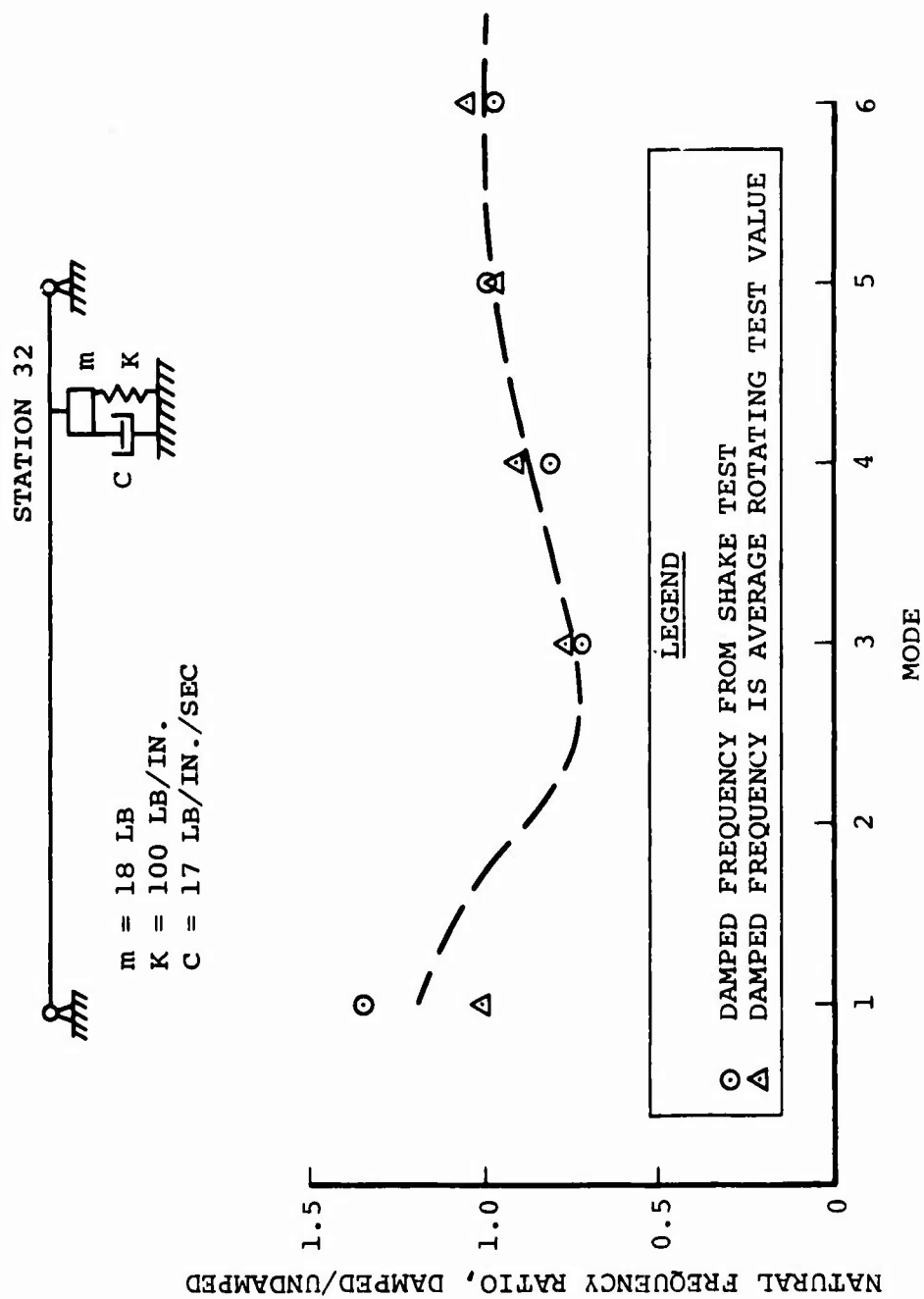


Figure 9. Effect of Damping on Critical Speed With Single Support at Station 32.

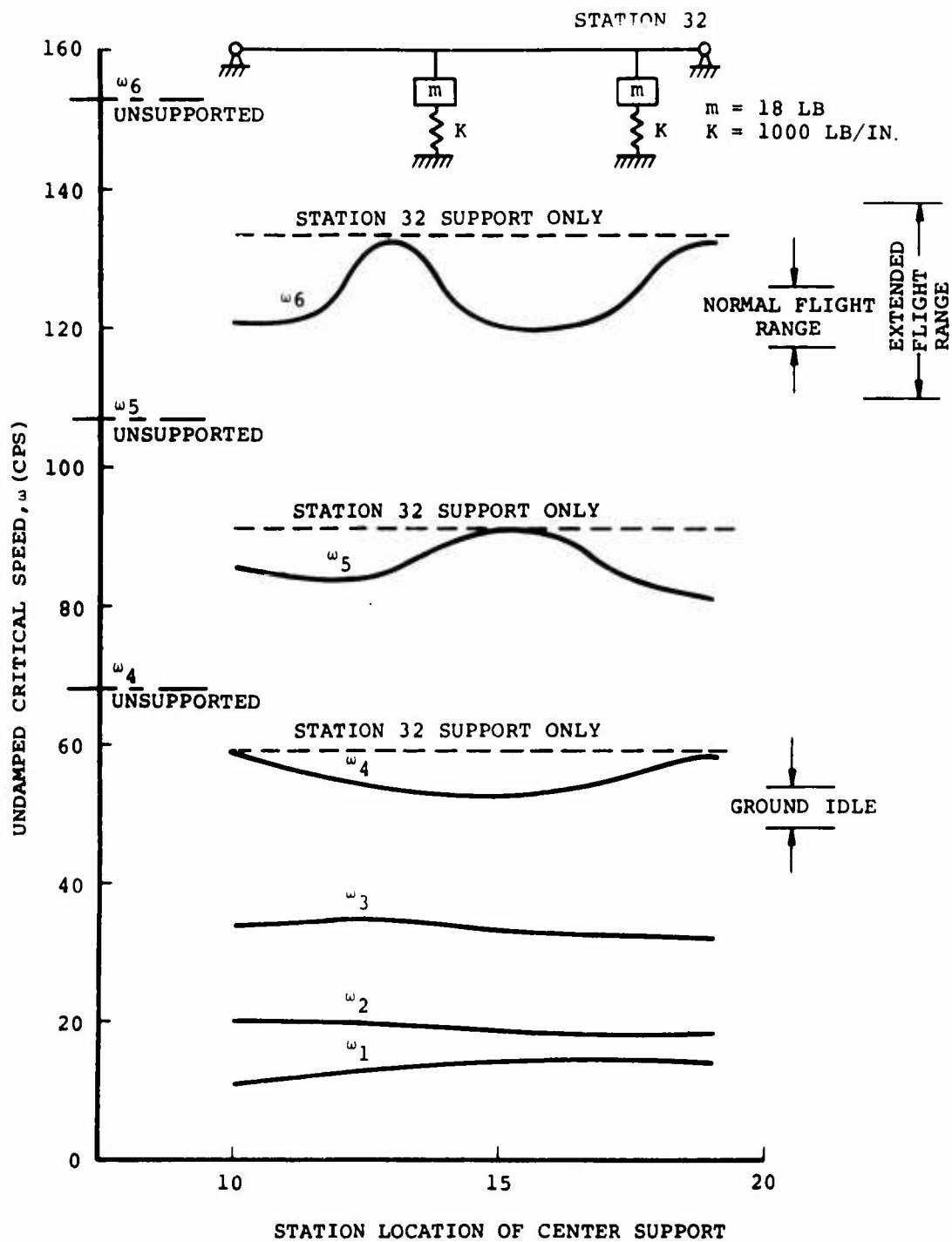


Figure 10. Effect of Center Support on Undamped Critical Speed, End Damper at Station 32.

For a shaft with supports at stations 16 and 32, the effect of damper stiffness on critical speeds is shown in Figure 11, which indicates that the damper stiffness influences only the modes below the fifth critical. In order to minimize loads transmitted to the structure and to obtain the maximum damper effectiveness, the damper spring rate should be as low as possible. Final choice of the spring rate was based on practical damper design considerations and allowable deflections under static and flight loads. A spring rate of 1,000 to 2,000 pounds per inch was considered adequate for these purposes.

The effect of practical variations in damper mass on the critical speeds is shown in Figure 12. It is evident from the plot that small changes in damper mass are of no significance.

In Figure 13, undamped mode shapes for the shaft with two supports are compared with the mode shapes for the shaft with a single support. For the fifth and sixth modes, the station 32 damper motion and the location relative to the adjacent node point are unchanged, indicating that the damper effectiveness at this location is not influenced by the additional support. To a somewhat lesser extent the same conclusion applies to the third and fourth modes. In the case of the third through the sixth modes, therefore, the previous experimental optimization of the end damper location (station 32) is still valid as stated earlier. Total support point motion, which is an indicator of the overall damper effectiveness, is compared in Table I. This comparison shows that the combined damper effectiveness with two supports is equal to or greater than that for a single support, provided that the damper force itself does not seriously alter the mode shapes.

TABLE I. TOTAL DAMPER MOTION PERCENT OF MAXIMUM NORMAL MODE AMPLITUDE		
Mode	One Support	Two Supports
1	20	63
2	53	52
3	69	133
4	53	104
5	37	47
6	27	60

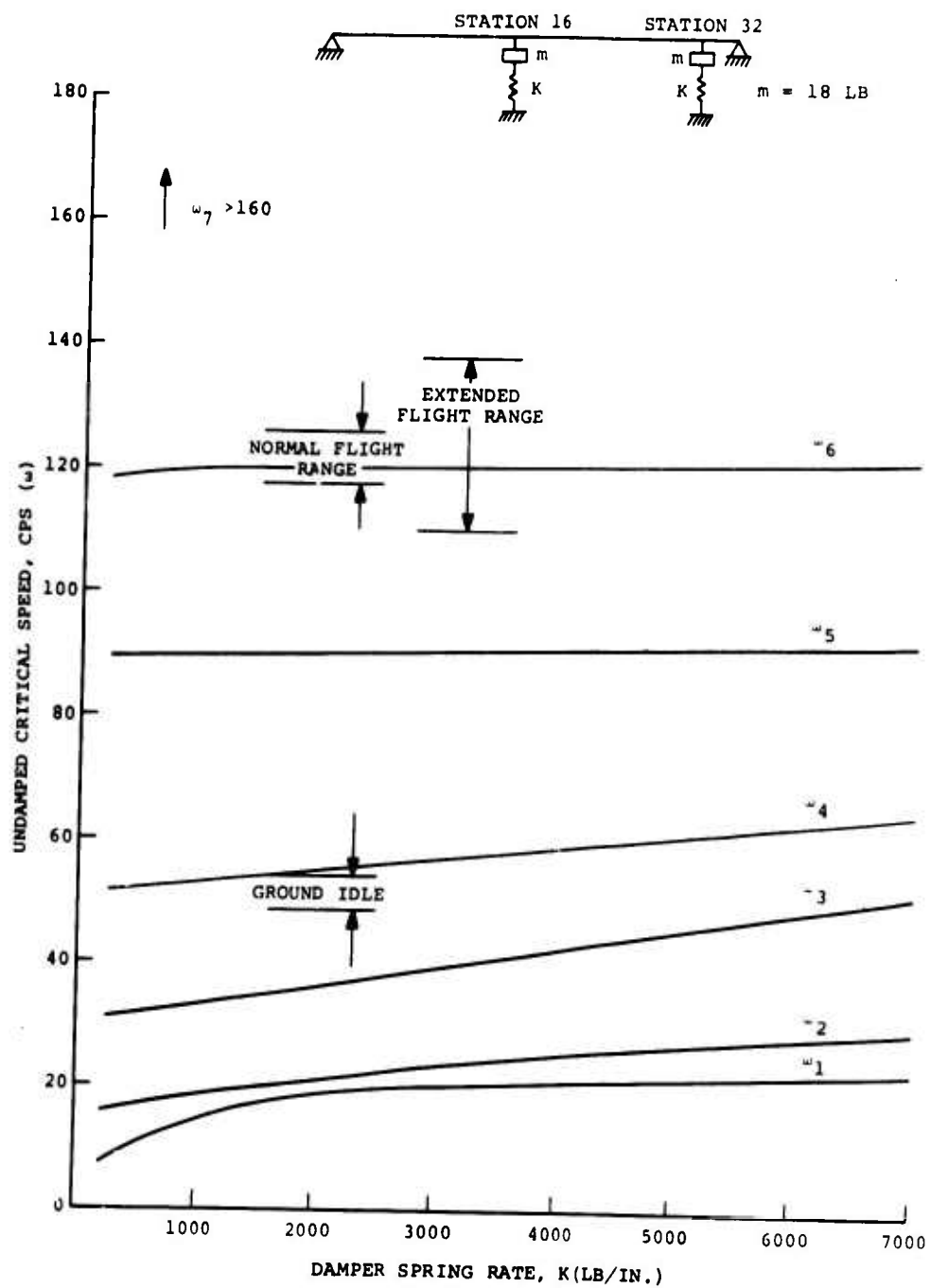


Figure 11. Effect of Damper Stiffness on Undamped Critical Speed.

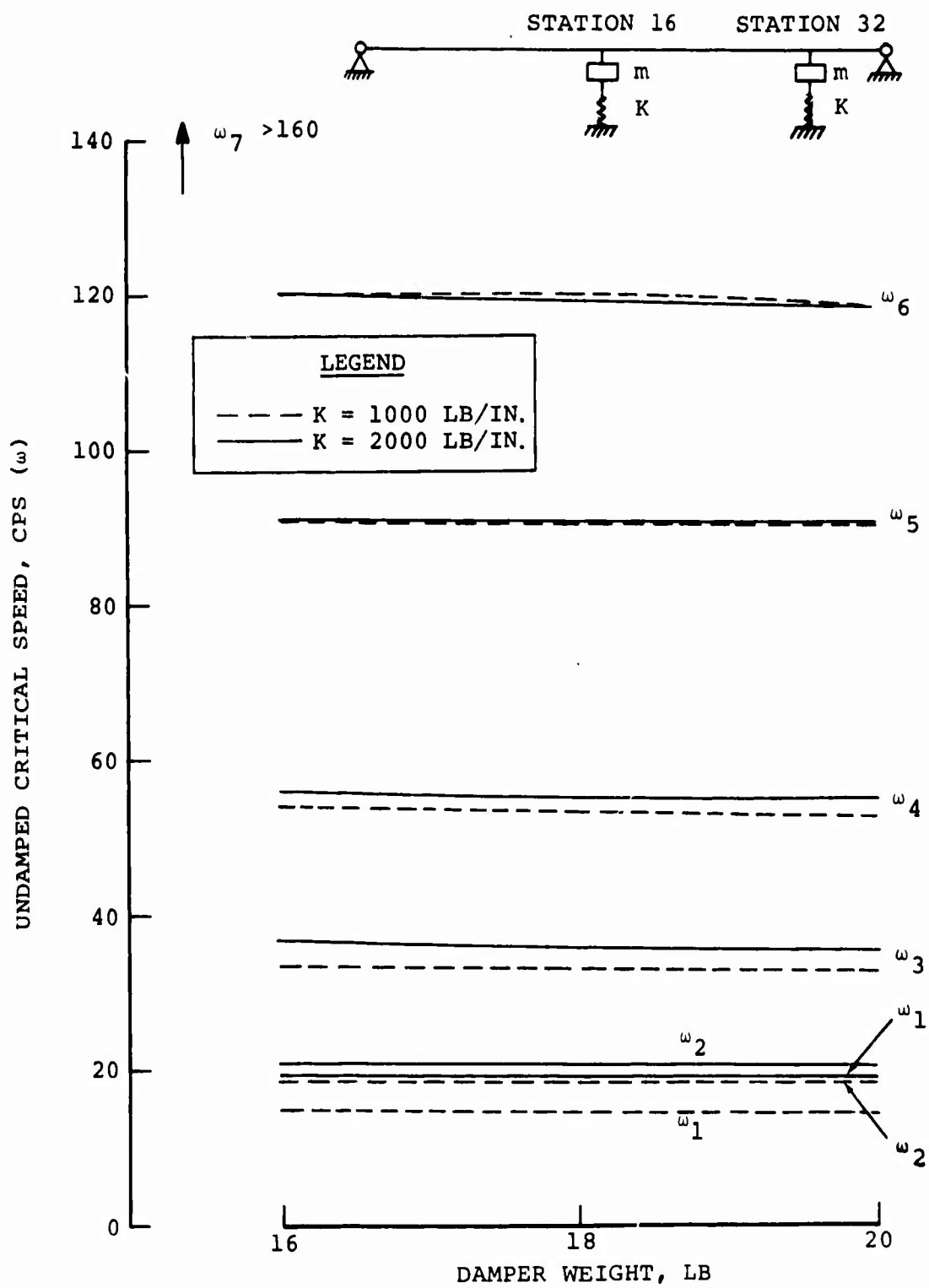


Figure 12. Effect of Damper Mass on Undamped Critical Speed.

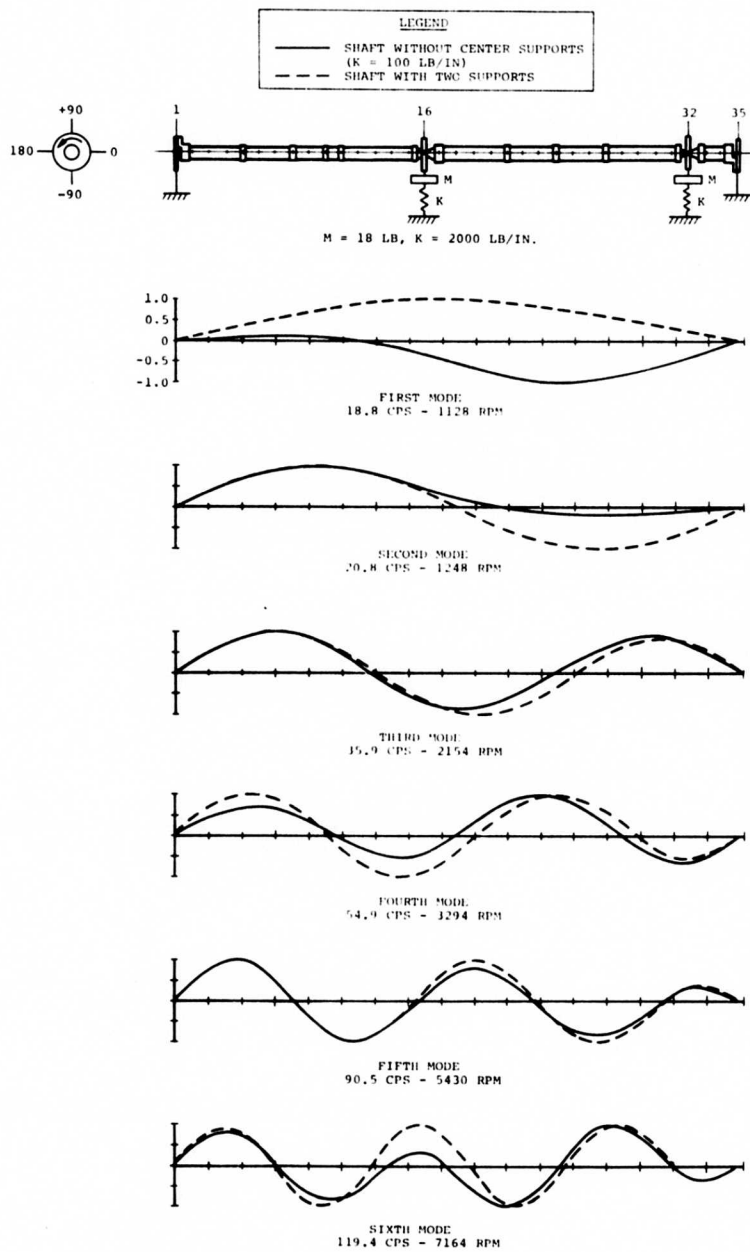


Figure 13. Theoretical Undamped Mode Shapes.

Analysis With Damping

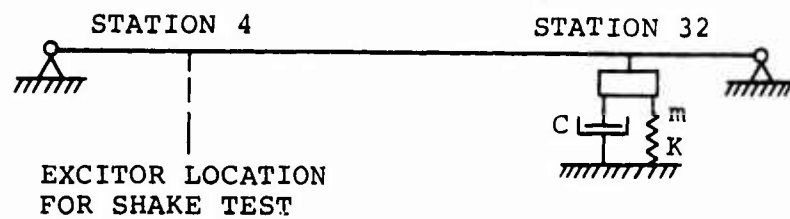
In order to investigate the damping requirements, forced response analyses with damping were performed for the stationary shaft. The analytical model was similar to that used in the undamped analyses except that a viscous damper is assumed to act in parallel with the supporting spring. Calculations were carried out using a digital computer program (Boeing-Vertol program D-97) which is a general-purpose lumped-parameter dynamic-analysis program similar to the General Motors Dynamic Analyzer Program (DYANA).

As in the case of the undamped analysis, calculations were first performed for comparison with available test data from the previous shaft configuration (damper at station 32) in order to establish the credibility of the analysis. Results of these calculations are presented in Figure 14. With minor exceptions, the calculated damped frequencies compare favorably with the test values. The calculated second mode does not appear in the test results probably because this mode is responsive only to a concentrated exciting force near the damper. In general, the results of the damped calculation tend to be slightly higher than the test frequencies. Furthermore, the calculated values for the fifth and sixth modes with damping are higher than the undamped values; this trend is contrary to the trend of the test data.

Calculated natural frequencies with and without damping are compared in Figure 15 for the shaft with supports at stations 16 and 32. Damped calculations were performed using the same damping coefficient ($C = 17$ lb/in./sec) as for the shaft with a single support. In order to compare the damped and undamped frequencies on a common basis, the undamped frequencies from a D-97 forced-response analysis without damping ($C = 0$) are presented in addition to the results from the previous undamped analysis (program D-29). The damped and undamped D-97 results appear consistent throughout with the third, fourth, and fifth modes displaying a slight decrease in frequency due to damping. Above the third mode, the D-29 undamped frequencies are lower (5.6 percent at the sixth mode) than the corresponding frequencies from the D-97 analysis. Investigation of the accuracy of the two methods indicates that the difference is due principally to a small computational error in the D-29 analysis.

On the basis of the undamped natural frequencies, the presence of a damped first mode at approximately 19 cps has been indicated in Figure 15. However, the first and second modes are very tightly coupled and difficult to isolate in the forced response due to the similarity in the normal (undamped) modes (see Figure 13). In this regard, the existence of the first mode is academic since the response of the rotating shaft will, in all likelihood, display only a single-peak response which may be treated as one mode.

Steady-state forced response was computed for damping coefficients of 8.5, 17, 25, and 30 lb/in./sec, and the results are compared in Figure 16, which shows maximum shaft deflection versus excitation frequency. Below 20 cycles per second, a damping coefficient of 17 lb/in./sec appears adequate, since a further increase in the damping shows no real improvement. In the high-frequency range, damping coefficients above 25 lb/in./sec produce no further reduction in the peak responses and values between 17 and 25 lb/in./sec appear adequate. As predicted from the undamped mode shapes, the peak response in the flight operating range due to the sixth mode is well damped. Calculated response at station 4 for later comparison with test data is shown in Figure 17.



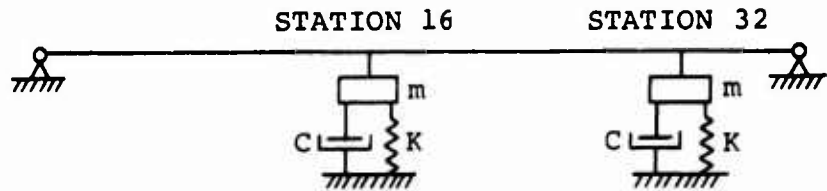
$m = 18 \text{ LB}; K = 100 \text{ LB/IN.}; C = 17 \text{ LB/IN./SEC}$

UNDAMPED NATURAL FREQUENCY, CPS			DAMPED NATURAL FREQUENCY, CPS		
MODE	SHAKE TEST (1)	D-29 CALCULATED	SHAKE TEST (1)	D-97 CALCULATED (2)	ROTATING TEST
1	5.3	5.2	7.1	4-5	5-5.8
2	16.4	16.9	-	15-19 (3)	-
3	33	33.8	24	28-33	24-26
4	58	58.8	47	56-59	53-54
5	93	91	92	94	89-91
6	135	133.4	132	140-141	133-137
7	-	-	182	196	NO DATA

NOTES:

- (1) SHAKER AT STATION 4
- (2) RANGE OF CALCULATED FREQUENCIES FOR FOUR DIFFERENT SHAKER LOCATIONS
- (3) MODE EXCITED ONLY WHEN EXCITING FORCE IS NEAR THE DAMPER

Figure 14. Comparison of Test and Calculated Natural Frequencies With Support at Station 32.



$$m = 18 \text{ LB}; K = 2000 \text{ LB/IN.}; C = 17 \text{ LB/IN./SEC}$$

MODE	NATURAL FREQUENCIES, CPS		
	UNDAMPED		DAMPED
	D-29 CALCULATED	D-97 CALCULATED (1)	D-97 CALCULATED (2)
1	18.8	18.1	19 (3)
2	20.8	20.9	20.5-22.5
3	35.9	36.3	30-32
4	54.9	56.4	54-55
5	90.5	94.2	93-94
6	119.4	126.5	126-130
7	NOT CALCULATED	195.4	195-196

NOTES:

- (1) From forced response without damping
- (2) Range of calculated frequencies for four excitation locations
- (3) Approximate frequency; first and second mode responses are very tightly coupled by damping, making first mode frequency difficult to identify.

Figure 15. Comparison of Calculated Damped and Undamped Natural Frequencies With Support at Stations 16 and 32.

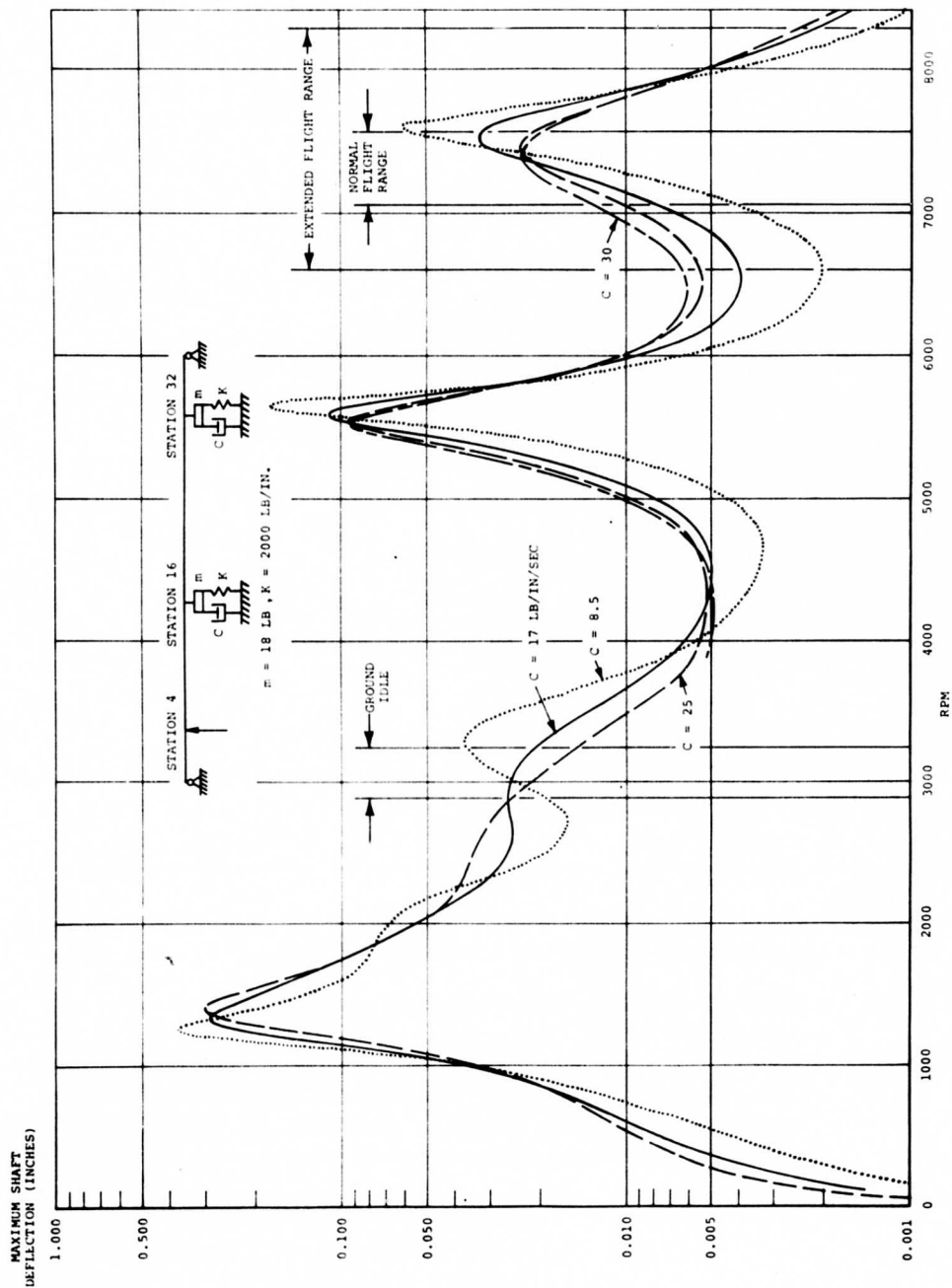


Figure 16. Effect of Damping on Shaft Response.

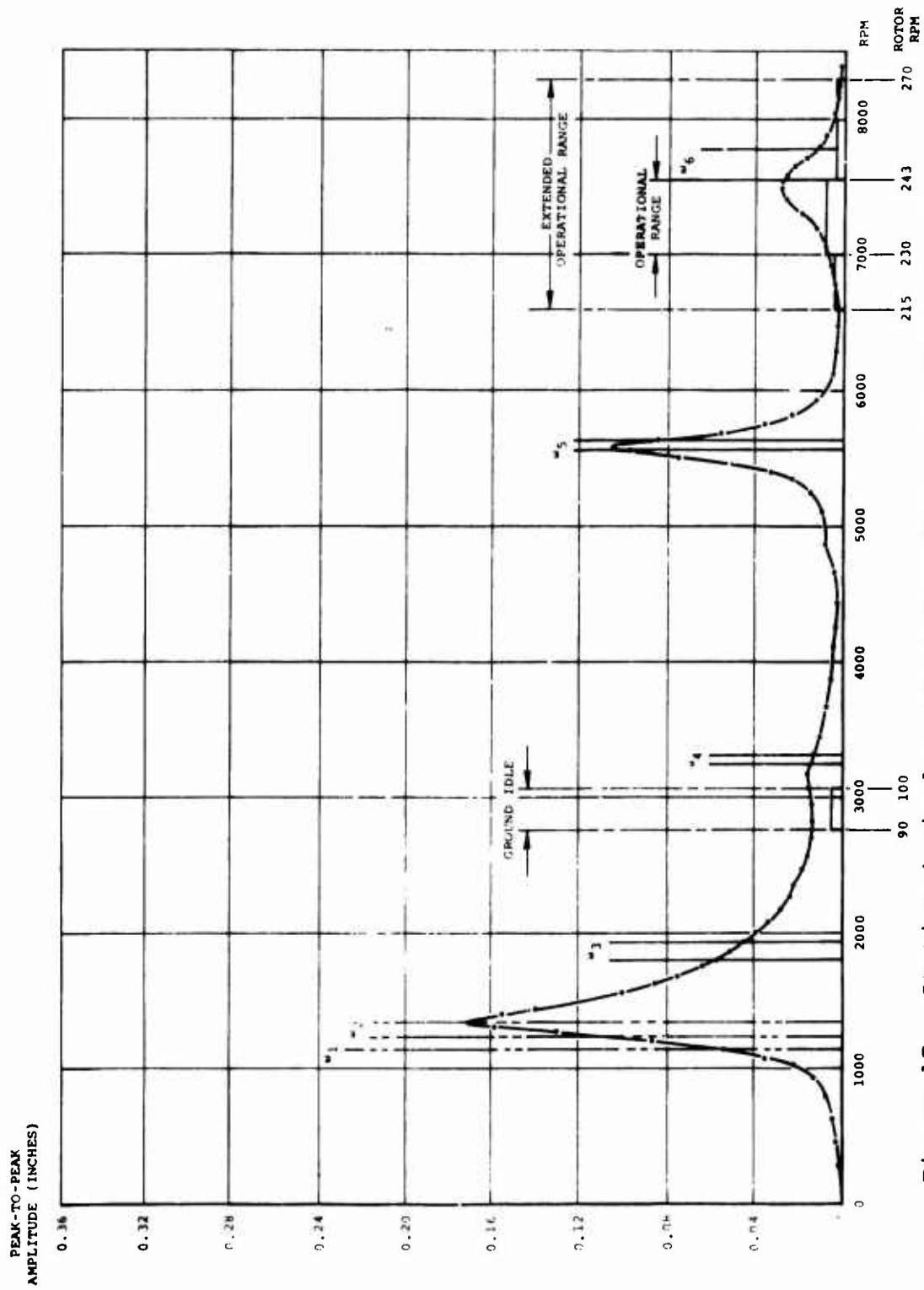


Figure 17. Station 4 Displacement Versus Frequency (Calculated).

The forced response with damping is a complex quantity composed of a real component, in phase with the exciting force, and a quadrature component which is 90 degrees out of phase with the exciting force. The quadrature component is of interest because at resonance it is this component which dominates the response. For a given natural frequency, the shape defined by the quadrature response is relatively constant and can be loosely considered as the damped mode shape. Figure 18 presents quadrature shapes for excitation at station 4 compared with the undamped mode shapes. Since a discrete first mode was not excited, the quadrature shape for the exciter location (station 32), which appeared to best define the first mode, has also been shown. For the third and fourth modes, the characteristic 90-degree exciting-point phase lag was not obtained with the exciting force at station 4. In these cases, the quadrature shapes for the exciter location which did produce a 90-degree phase lag are shown for comparison. Examination of Figure 18 indicates that for the fifth, sixth, and seventh modes, there is no essential difference between the quadrature and undamped shapes. Below the fifth mode, the quadrature shapes strongly resemble the undamped modes; however, the distorting effect of the damping is evident. In the case of the first and fourth modes, a variation in the quadrature shape with exciter location is readily observable.

Figure 19 shows the damper positions selected and superimposes all modes calculated for the proposed design. It also shows the balance planes selected to correct deflections in the various modes. Stations 8 and 24 were selected to balance the lower critical speeds (1, 2, 3 and 4) without affecting the higher ones (5 and 6). Stations 8 and/or 24 are near the antinodes of the lower critical speeds and at the same time near the nodes of the higher critical speeds. Stations 5 and 10 or stations 21 and 27 were selected to balance the higher critical speeds (5 and 6) while having relatively little effect on the lower critical speeds. Weights at station 5 and station 11 are near the antinodes of the higher critical speeds but would have opposite sign to be most effective at these speeds. The opposite sign, however, would make them counterbalance each other at the lower speeds; therefore, they would have little effect at these speeds. Weights at stations 21 and 27 react in the same way.

Figure 19 also identifies the location of the strain gages installed on the test shaft. A bending bridge was installed at shaft station 4 to measure shaft bending. Station 4 will contain some bending stress if there is deflection in any of the modes shown. Other stations may not show bending in some modes. For example, station 3 would not show bending in the fifth mode, and station 7 would not show it for the sixth mode. The bending bridges located at stations 15, 17, 31, and 33 are located one station on each side of the dampers to show the bending carried through the adapter joint at these points. A torsion bridge was installed at station 34 to measure actual shaft torque either in the bench test or in the aircraft.

STRUCTURAL DESIGN CRITERIA

The structural design criteria and the loading conditions for the supercritical-speed shaft are specified in Vertol report D8-0939.³ The primary source of loading on the supercritical-speed shaft system is engine torque. The CH-47A and B are powered by two Lycoming T55-L-7 engines each capable of operating at the transmission limit of 2,485 horsepower at 15,160 rpm. The engines have this capability for both single-engine and twin-engine operation. All components of the supercritical-speed shaft system are designed for the most critical loading conditions during single- or twin-engine operation.

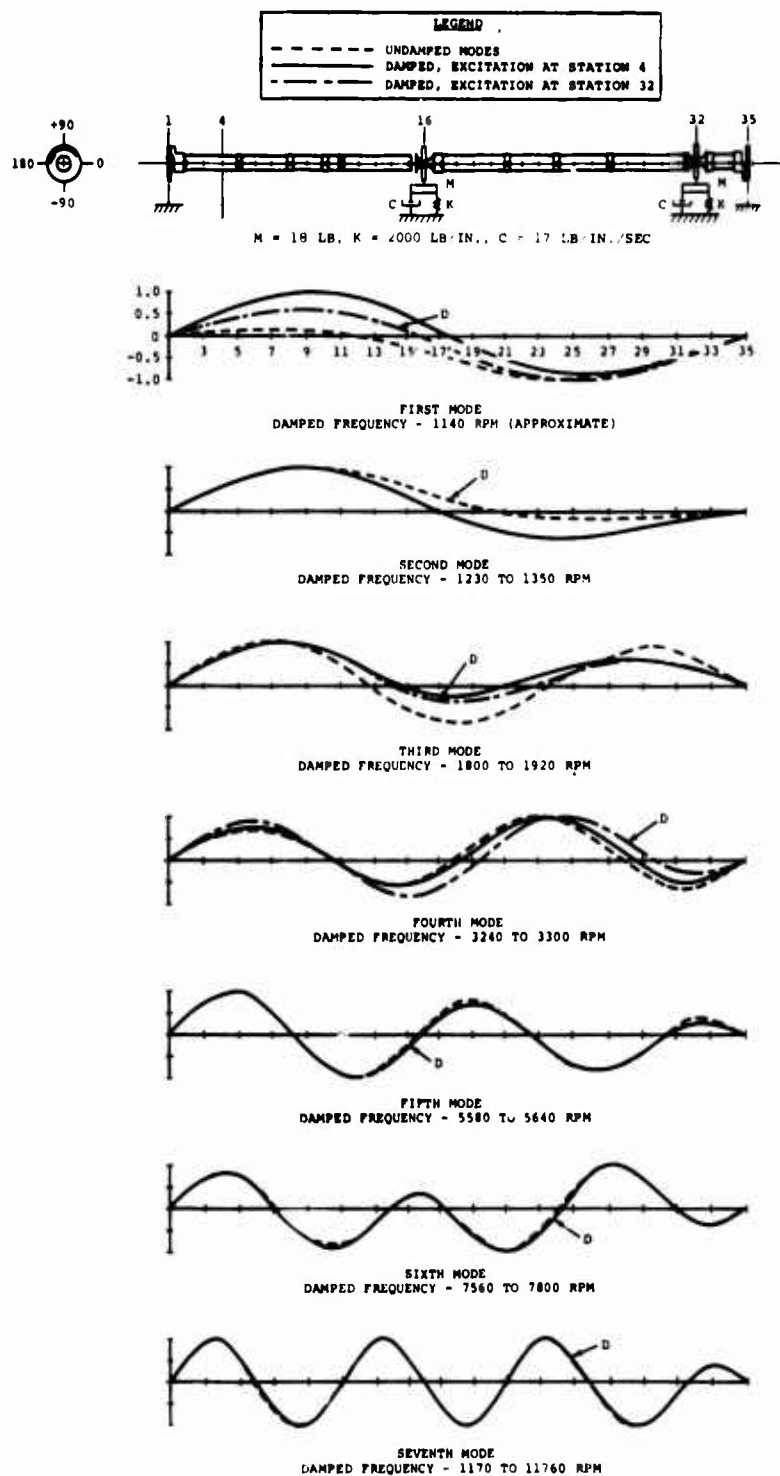
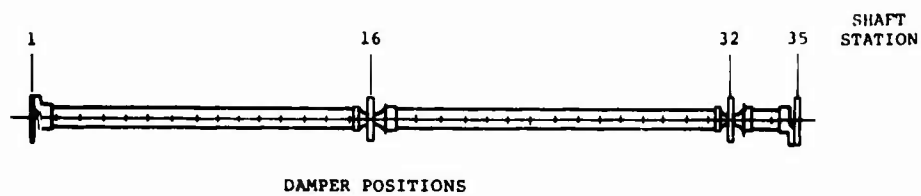


Figure 18. Comparison of Damped Quadrature Shapes and Undamped Mode Shapes.



MODE SHAPES

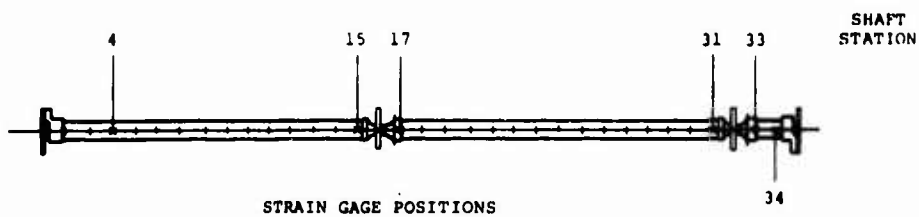
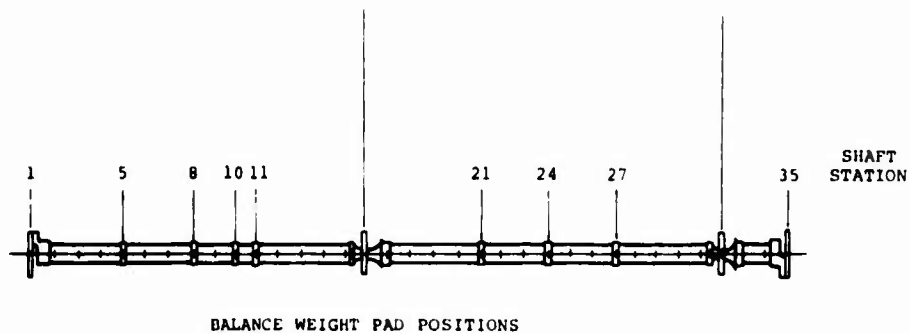


Figure 19. Mode-Shape Information With Locations for Dampers, Balance Pads, and Strain Gages.

In addition to the primary load, the shaft system is also subjected to secondary loads arising from deflections and misalignments. These secondary loads are considered in both limit and fatigue stress analysis.

Ultimate allowable stresses are taken from METALLIC MATERIALS AND ELEMENTS FOR AEROSPACE VEHICLE STRUCTURES, MIL-HDBK-5A.⁴ Allowable fatigue stresses are based on values obtained from Vertol STRUCTURES DESIGN BOOK 86L1 OF THE BOEING COMPANY ENGINEERING DESIGN MANUAL⁵ and from Vertol experience with similar components and materials.

Shaft Torsional Loads

Limit and Ultimate Conditions—All components of the shaft system are designed to withstand momentary applications of ultimate loads without failure. The maximum steady operating torque equals 60 percent of twin-engine torque based on 4,970 horsepower at 230 rotor rpm. The ultimate torque is obtained by multiplying the steady torque by a 1.5 limit factor and a 1.5 ultimate factor of safety. These torque values are:

$$\begin{aligned} T_{\text{max operating}} &= 26,700 \text{ inch-pounds} \\ T_{\text{limit}} &= 40,000 \text{ inch-pounds} \\ T_{\text{ultimate}} &= 60,000 \text{ inch-pounds} \end{aligned}$$

Fatigue Condition—Superimposed on the maximum steady torque is a cyclic torque equal to ± 15 percent of the steady torque.

$$T_{\text{alternating}} = \pm 0.15 (26,700) = \pm 4,000 \text{ inch-pounds}$$

Bending Loads

Limit and Ultimate Conditions—The maximum bending of the shaft system under combined axial compressive force due to the fuselage deflection and transverse load under 3g flight condition is 2,450 inch-pounds. The maximum whirling of the shaft due to the unbalance has a calculated value of 400 inch-pounds. Both of these bending loads take place at the forward damper of the shaft system. The limit bending occurring in the shaft during any operating condition is thus obtained by adding these two bending loads.

The ultimate bending moment is determined by multiplying this limit bending by a 1.5 ultimate factor of safety. These bending loads are:

$$\begin{aligned} M_{\text{limit}} &= 2,850 \text{ inch-pounds} \\ M_{\text{ultimate}} &= 4,280 \text{ inch-pounds} \end{aligned}$$

Fatigue Condition

All components of the shaft system, except bearings, are designed with the objective of attaining a minimum service life of 3,600 hours under the basic fatigue loading schedule in

STRUCTURAL DESIGN CRITERIA, CH-47B AND C.⁶ Bearings will be designed for a minimum B-10 life of 1,200 hours under the same schedule.

The nature of the normally-encountered bending stress experienced by a shaft operating at supercritical speeds in 1g level flight is shown by Figure 20. With the specified mode shapes associated with a given frequency, a strain gage located on the surface of the shaft at point 1 would indicate the stresses shown in Figure 21. From these diagrams it can be seen that the bending stresses are expected to be steady while operating at a constant rpm. Stress reversals occur only when the direction of the bend in the shaft changes between modes. This has been demonstrated by test (see Figure 132).

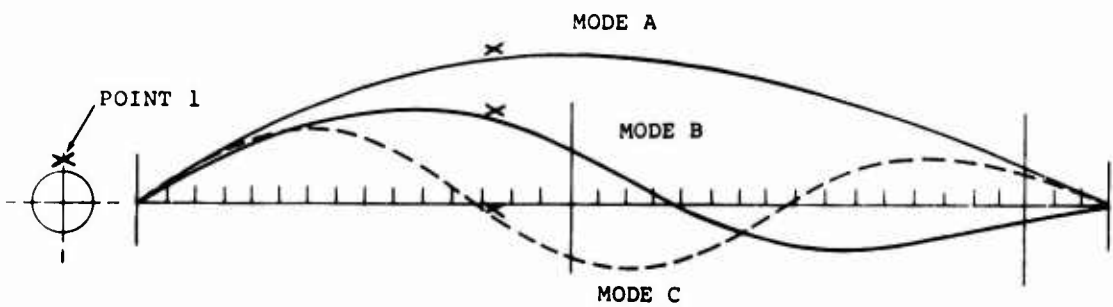


Figure 20. Typical Mode Shapes.

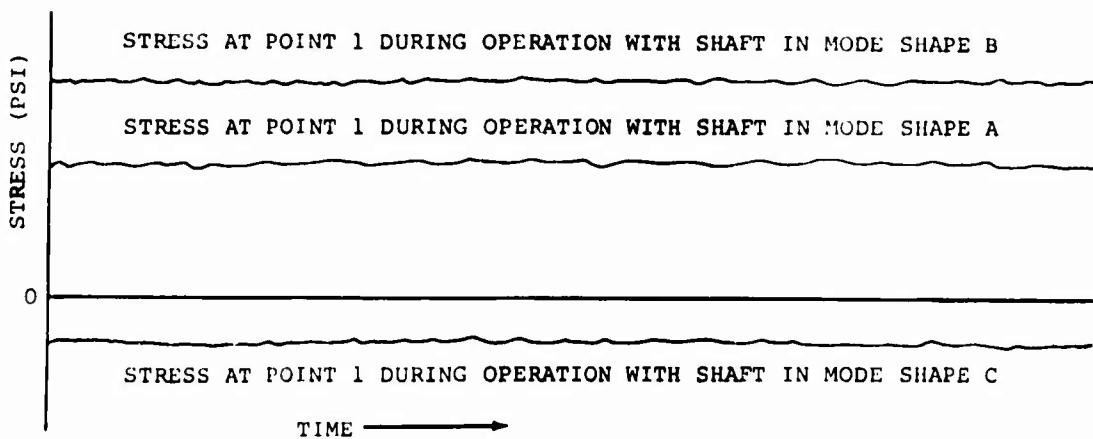


Figure 21. Bending Stress From Shaft Whirling.

Alternating bending occurring in the shaft at the frequency of rotation is a result of fuselage bending and gravity. Alternating bending at twice the frequency of rotation comes from elliptical whirling. This is a transient condition, and it is believed proper balancing will reduce or eliminate it.

Dampers and Support Structure

The dampers and support structure are designed to operate at the bending of the shaft due to unbalance which causes ± 15 pounds alternating load at end bearing supports. Amplitude for use in determining damper-to-structure loads is consistent with allowable alternating lateral bending deflections of the shaft for unlimited life. All mode shapes within or adjacent to the flight range have been considered. This shaft is considered to be deflected sinusoidally.

Actual stress is a function of the mode-shape deflection determined by analysis of the dynamic response of the system.

Secondary loads arising from deflections and misalignments will be considered for both limit and fatigue conditions.

DETERMINATION OF MAXIMUM BENDING STRESS

Maximum bending stress in the supercritical speed shaft system is measured at its whirling speeds. First, the theoretical mode shape is selected whose whirling speed falls in the identified operational ranges. Next, the maximum deflection in the shaft system is determined by assuming that an unbalance in the shaft system causes a ± 15 -pound load at the end supports. The equation for the maximum deflection is a sinusoidally deflected shaft, expressed in terms of the loads at end supports, is

$$Y_{\max} = \frac{\pi g R}{w \omega^2 l} \quad (1)$$

where Y_{\max} = maximum shaft deflection, in.

g = acceleration of gravity, 386 in./sec²

R = load at end support, lb

w = weight of shaft per unit length, lb/in,

ω = shaft speed, rad/sec

l = shaft length between nodes, in.

The maximum bending stress in the shaft system is determined by using the maximum shaft deflection obtained from the above calculation. The equation for the maximum bending stress in a sinusoidally deflected shaft is

$$\sigma_{\max} = \frac{\pi^2 D E Y_{\max}}{2 l^2} \quad (2)$$

where σ_{\max} = maximum bending stress, lb/in.²

D = outside diameter of shaft, in.

E = modulus of elasticity, lb/in.²

Y_{\max} = maximum deflection, in.

l = shaft length between nodes, in.

The maximum shaft bending stress is found at the fifth whirling speed of the shaft system (see Figure 18).

For R = 15 lb

w = 0.165 lb/in.

ω = 568 rad/sec

l = 70.7 in.

D = 4.50 in.

E = 10.5×10^6 lb/in.²

Substituting these values into Equations (1) and (2) gives the maximum bending stress in the shaft system, which is

$$\sigma_{\max} = 230 \text{ lb/in.}^2$$

As previously explained, the above stress is a steady value. It can be used conservatively as an alternating value to cover all possibilities of shaft mode shapes and deflections for the extended operational speed range.

DETERMINATION OF ORBITING END LOADS

Based on the theoretical mode shapes of the undamped shaft system and a maximum allowable bending stress, the maximum shaft deflection of interest for each mode shape can be determined by Equation (2). A maximum allowable bending stress of 2,500 lb/in.² was selected for the bench test program.

With the shaft deflection known for each mode shape, the orbiting end loads can be computed by using Equation (1).

DAMPER TEST

The damper is an immersion body type and displays characteristics of viscous dampers in general. Drawings of the damper are included in Appendix II. Damping force is related to velocity. The damper is composed of several concentric metal sections joined by bonding an elastomeric member between them. When the parts are joined, a circular concentric chamber is formed which is filled with a silicone fluid (see Figure 22). The shaft is supported on a bearing pressed into the inner metal section. When the shaft is deflected, the center moves in relation to the outer metal section and causes the chamber to distort in an eccentric manner. Fluid in the chamber flows from the smaller area to the larger area. When the shaft rotates in the deflected position, the fluid in the chamber is forced to flow ahead of the deflection. Viscous resistance to the flow causes damping. The outer section of the damper is attached to the aircraft structure when installed.

TEST MACHINE AND INSTRUMENTATION

The damper test machine consisted of a belt-driven rotating shaft running in bearings with an eccentric mounted at one end to impose a positive displacement across the damper (see Figure 23). Various eccentrics could be installed to change the displacement as desired (see Figure 24). The entire test machine was mounted on a base which could be placed in an oven or cold box for the desired environmental control during testing. Frequency was controlled by a variable-speed motor driving the unit.

Measurements for the damper test included the damper force output, frequency of rotation, phase of the eccentric, rpm counter, and temperature of the damper elements.

The damper force output was measured by a Kistler quartz load cell which drove a Kistler charge amplifier. The final display appeared on a Tektronix storage oscilloscope. The oscilloscope force traces were photographed at each test condition for analysis.

The frequency was measured with a photoelectric pickoff driving a digital counter. The photoelectric pickoff also triggered a stroboscope when the eccentric was 90 degrees from the load cell location, or at the point of peak velocity of the eccentric in the vertical direction. This test setup provided a force trace with a blip at the point of peak velocity to determine the force component of pure damping for the test unit. This setup was also used to determine the dynamic spring rate of the damper.

The temperature of the inner and outer members of the damper was measured and recorded during all tests by copper-constantan thermocouples and a Leeds and Northrup temperature potentiometer.

TEST PROCEDURE

The damper test machine has three eccentric offsets (0.025, 0.015, and 0.005 inch) for use at different frequencies.

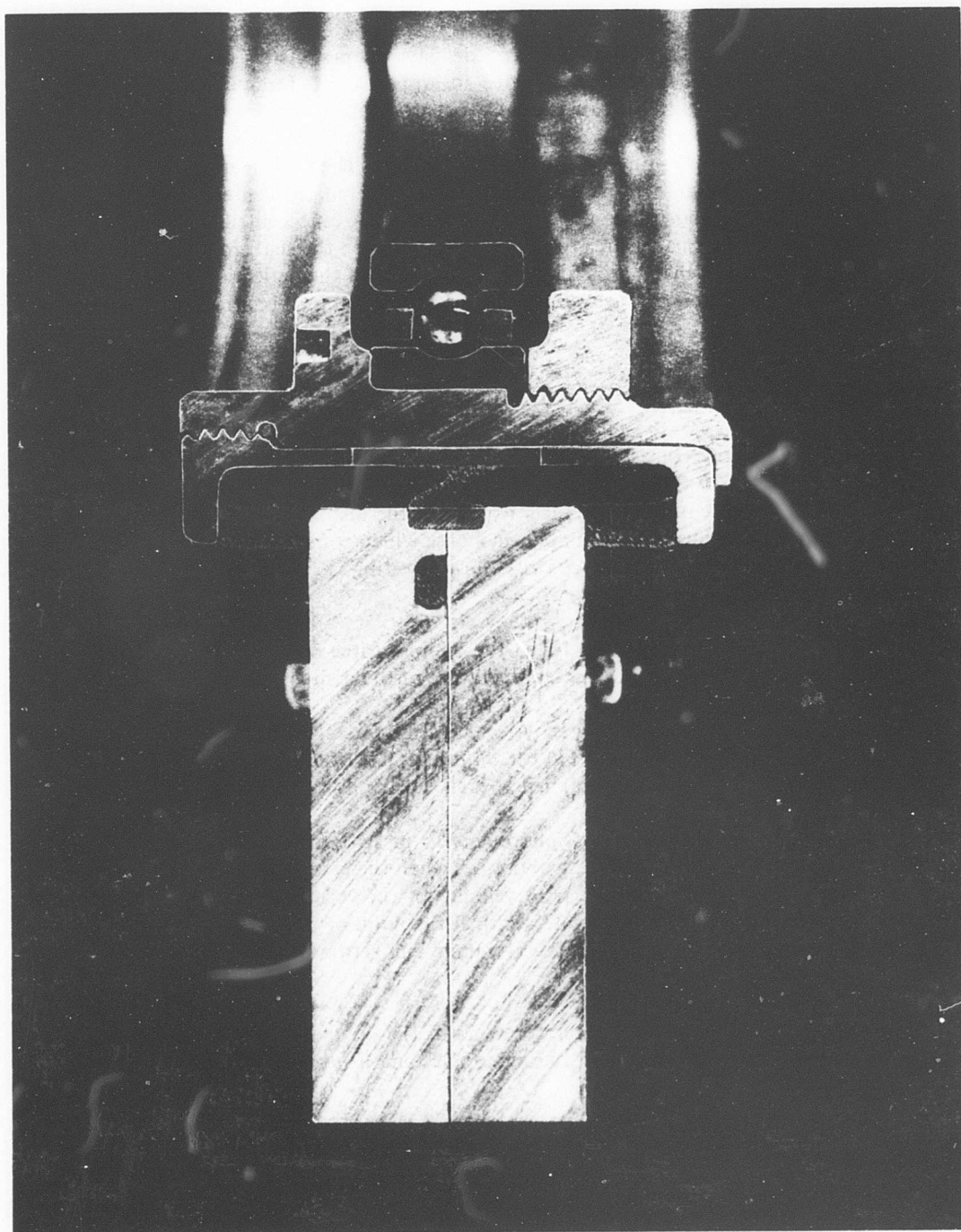


Figure 22. Damper - Sectional View.

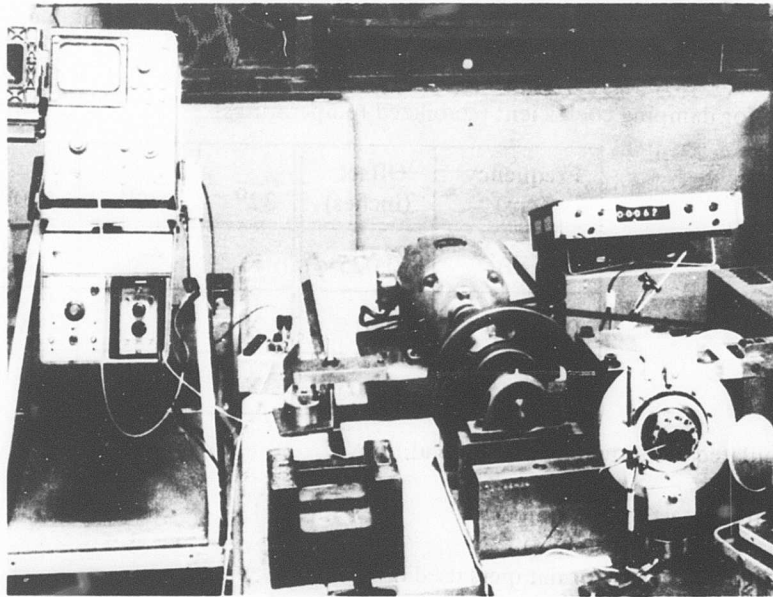


Figure 23. Damper Test Setup.

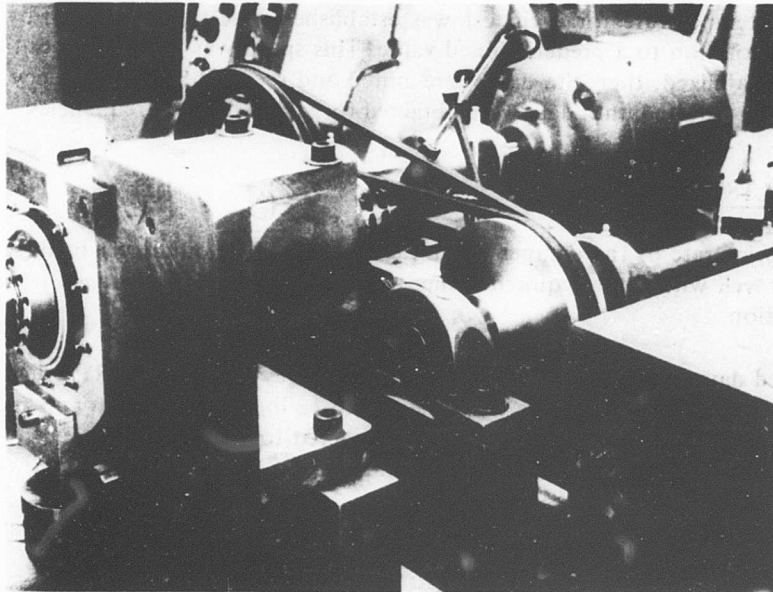


Figure 24. Damper Test Vee-Belt Drive.

The tests were run at +32° F, +70° F, and +160° F. Temperature was maintained by enclosing the test machine in a box or chamber where necessary.

- Test for damping coefficient (stabilized temperatures)

Frequency (cps)	Offset (inches)	32°	70°	160°
0 to 60	0.025	X	X	X
0 to 100	0.015	X	X	X
0 to 145	0.005	X	X	X

- Simulated shutdown from hot condition
- Fluid loss test (one chamber)
- Calibration check for dampers used on shaft test
- Fatigue test at 160° F (to maintain approximately 200° F on inner member)

The physical displacement was established by the eccentric installed on the shaft. The damper was installed in the test machine so that the horizontal damper force reacted against horizontal links to the structure. The vertical force was measured by the Kistler quartz load cell.

The ambient temperature for each test was established. The test was begun by bringing the frequency of rotation to a predetermined value. This speed was maintained until the damper temperature stabilized; then the data were noted and recorded. The frequency was changed and the process repeated until data were obtained for all the desired frequencies.

TEST RESULTS

The radial spring rate of the damper was measured at 1,650 pounds per inch (see Figure 25). This value is well within the required spring rate of 1,000 to 2,000 pounds per inch given in the specification.

The measured damping at room temperature (see Figures 26, 27, and 28) is slightly above the upper design limit of the tolerance envelope (12 to 18 lb/in/sec) at input amplitudes of 0.005 and 0.015 inch. However, the damping was considered to be acceptable, and no attempt was made to adjust the damping force into the tolerance band by changing the fluid viscosity.

Figures 29, 30, and 31 show the damping characteristics at an ambient temperature of 32°F. Similarly, Figures 32, 33, and 34 show the damping characteristics at 160°F. Data derived from comparing these figures with information recorded at room temperature are similar (up to frequencies near 80 Hertz) to the expected change of viscosity with temperature (average damper temperature recorded during the test) for a silicone fluid.

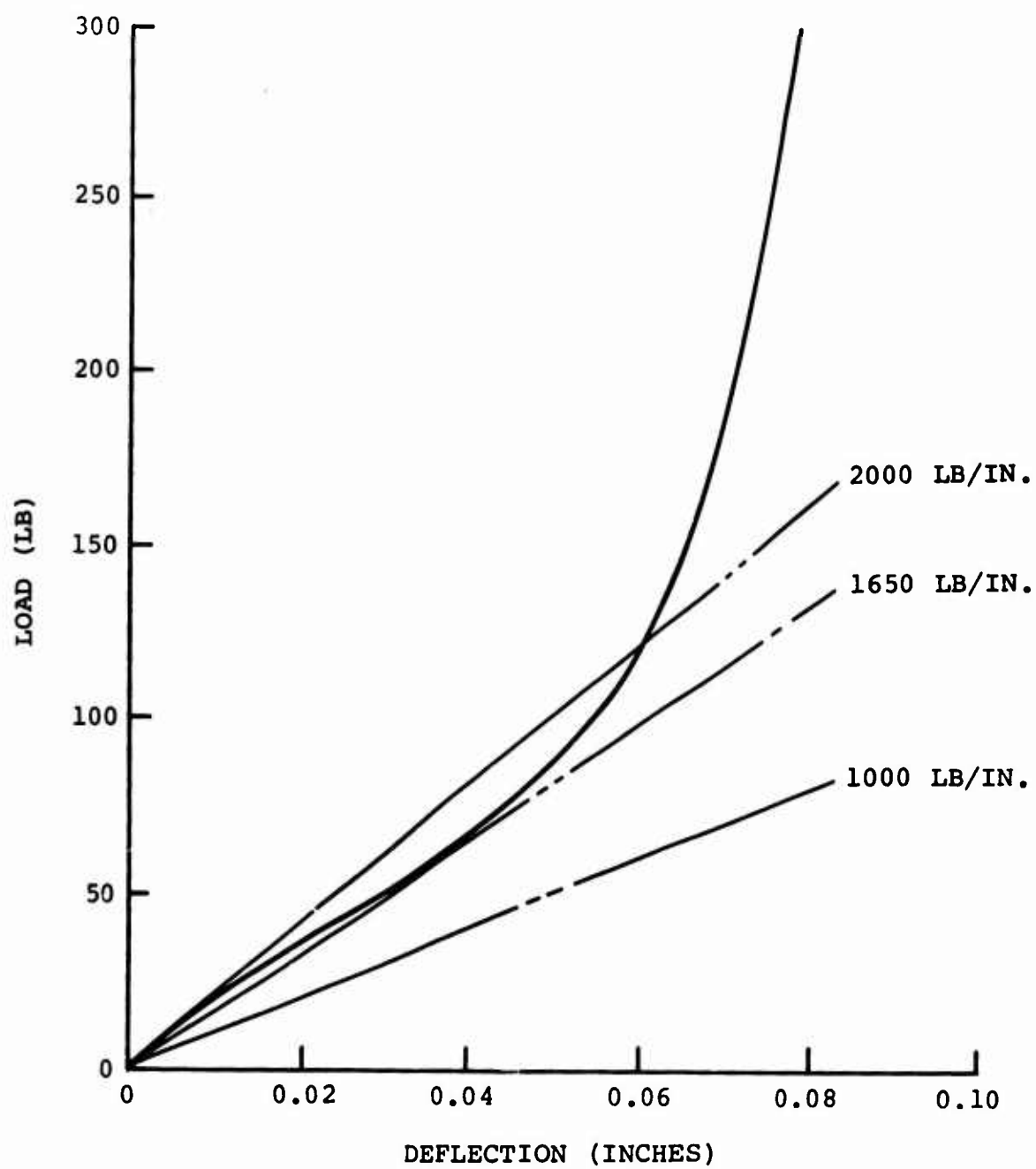


Figure 25. Damper Load Versus Deflection (Spring Rate).

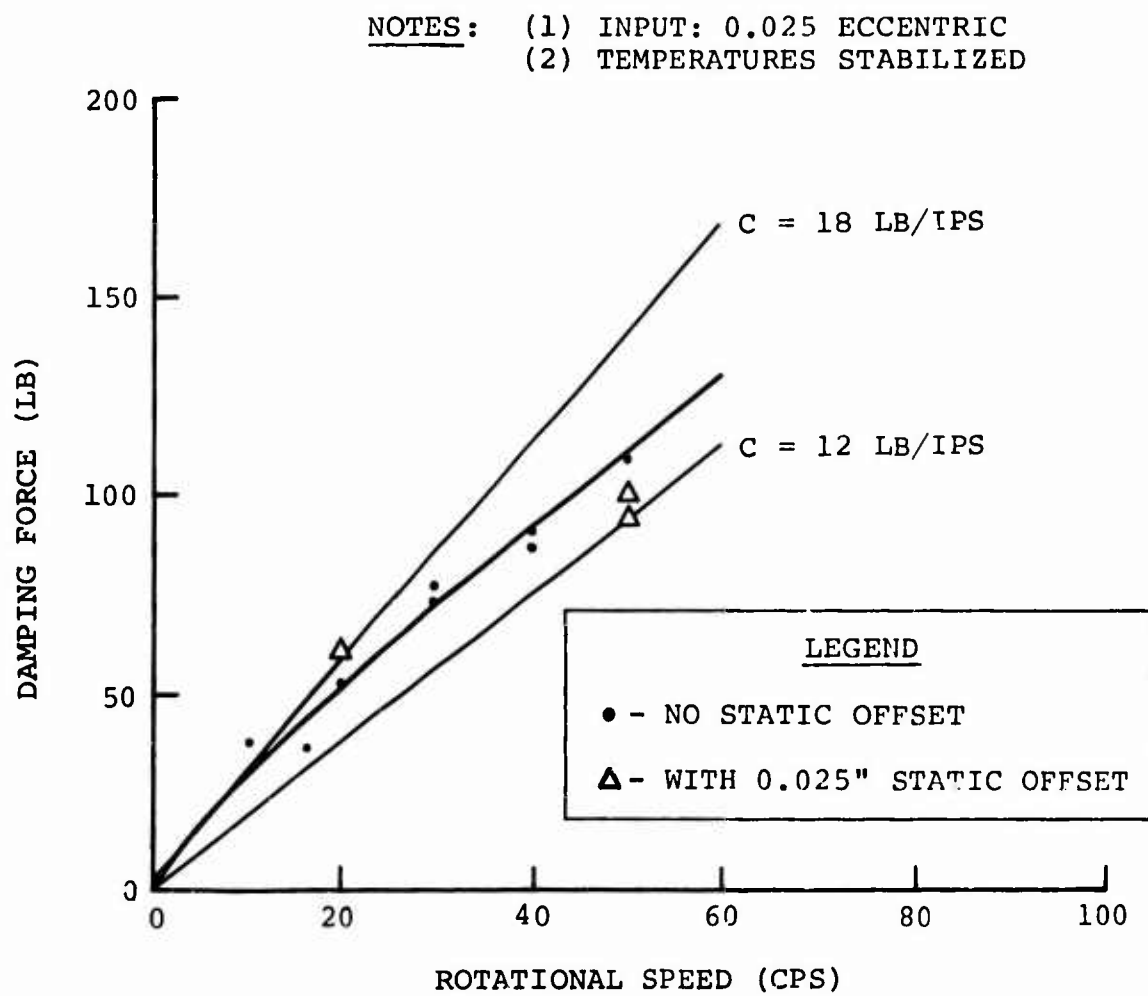


Figure 26. Force Versus Speed to 60 CPS at 70°F.

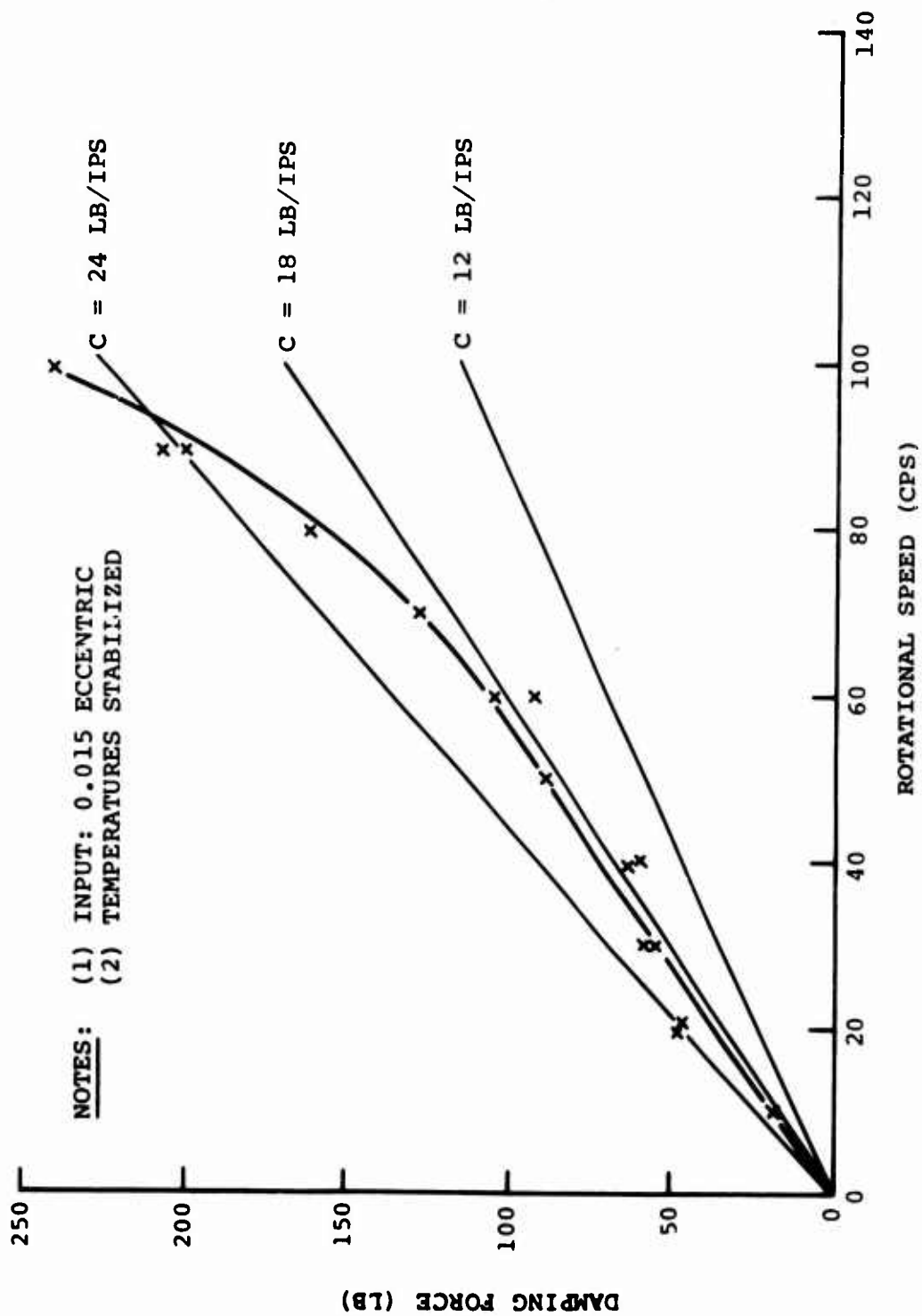


Figure 27. Force Versus Speed to 100 CPS at 70°F.

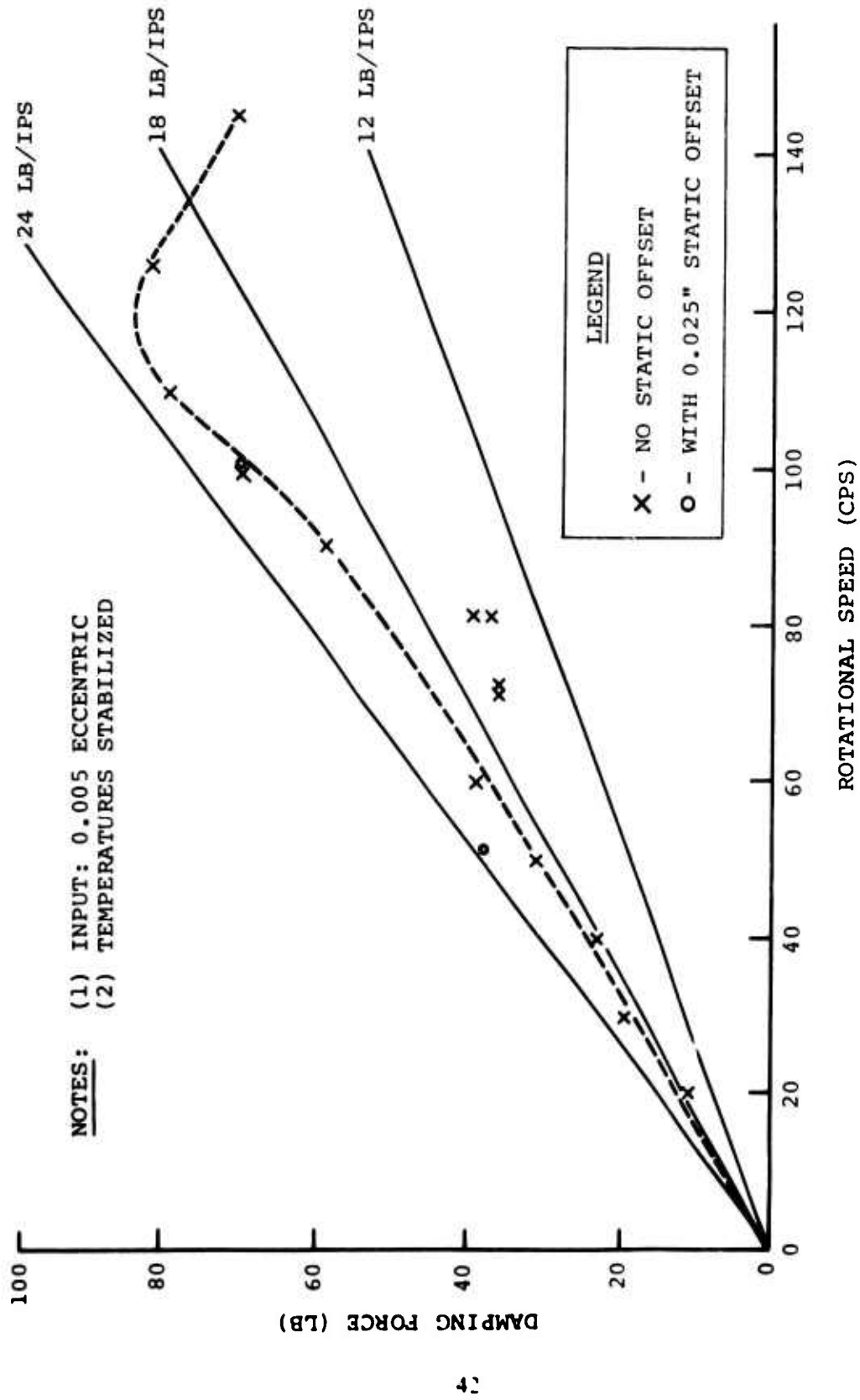


Figure 28. Force Versus Speed to 140 CPS at 70°F.

NOTES: (1) INPUT: 0.025 ECCENTRIC
(2) TEMPERATURES STABILIZED

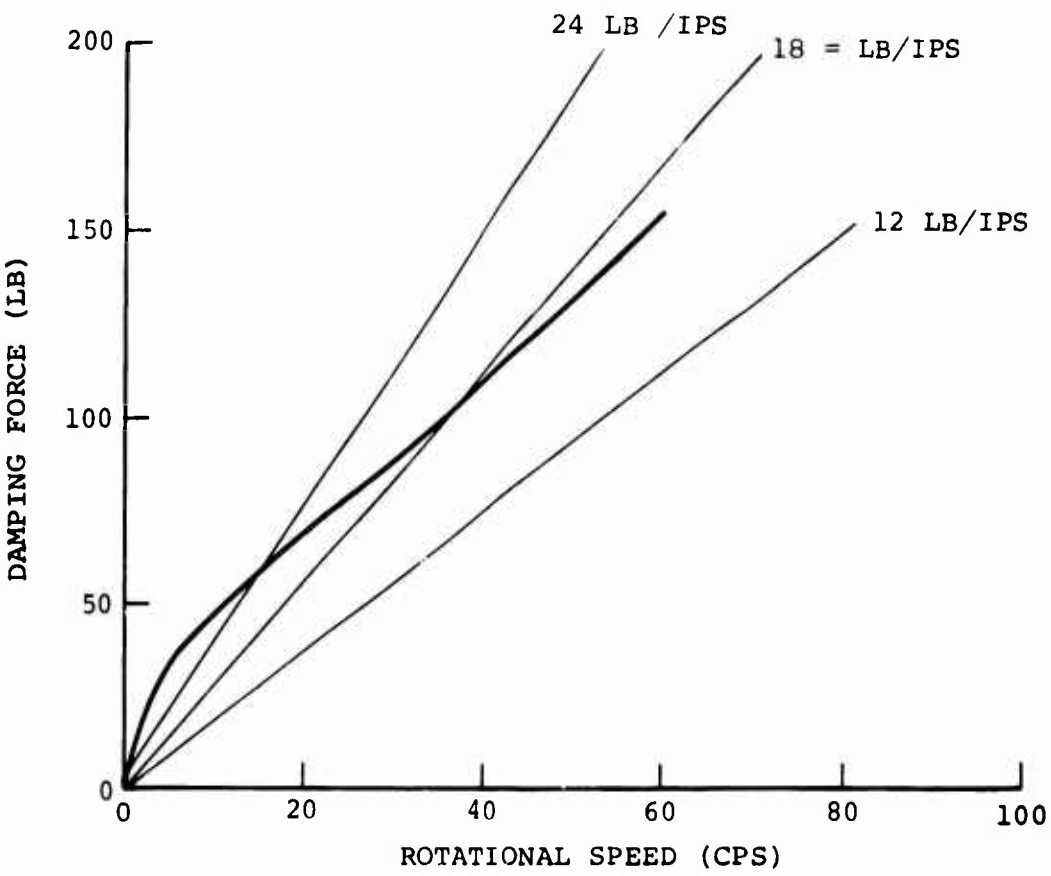


Figure 29. Force Versus Speed to 60 CPS at 32°F.

NOTES: (1) INPUT: 0.015 ECCENTRIC
(2) TEMPERATURES STABILIZED

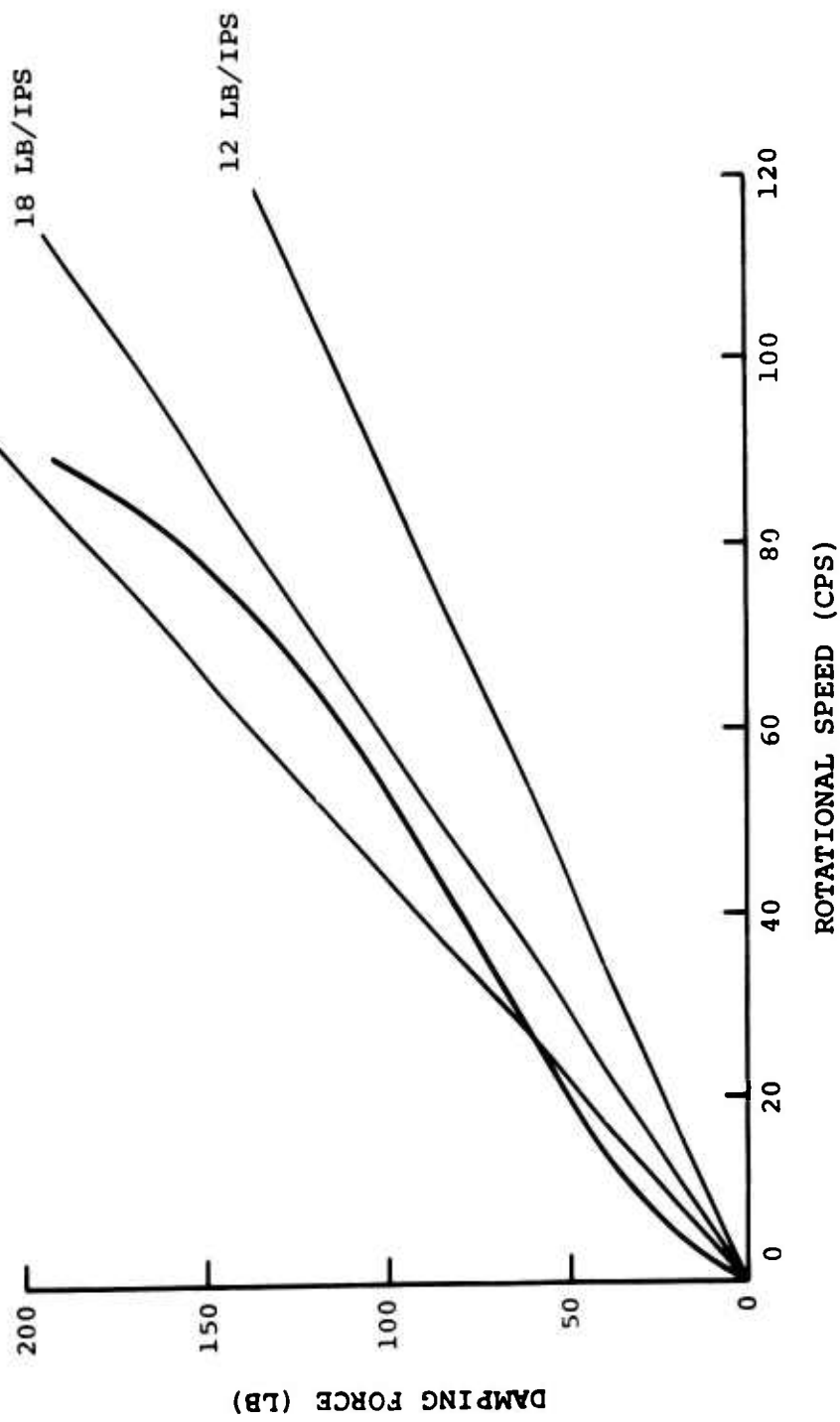


Figure 30. Force Versus Speed to 100 CPS at 32°F.

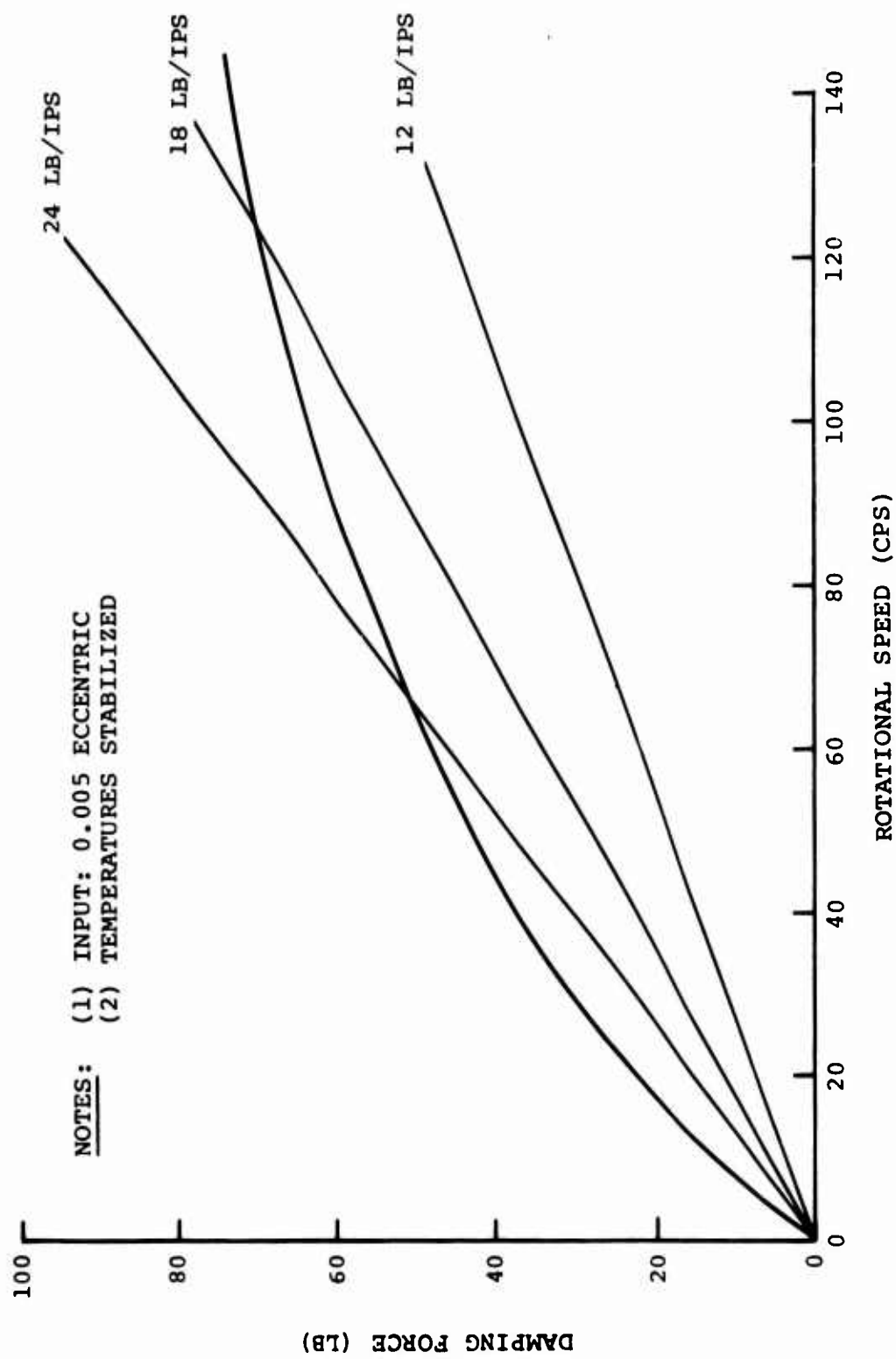


Figure 31. Force Versus Speed to 140 CPS at 32°F.

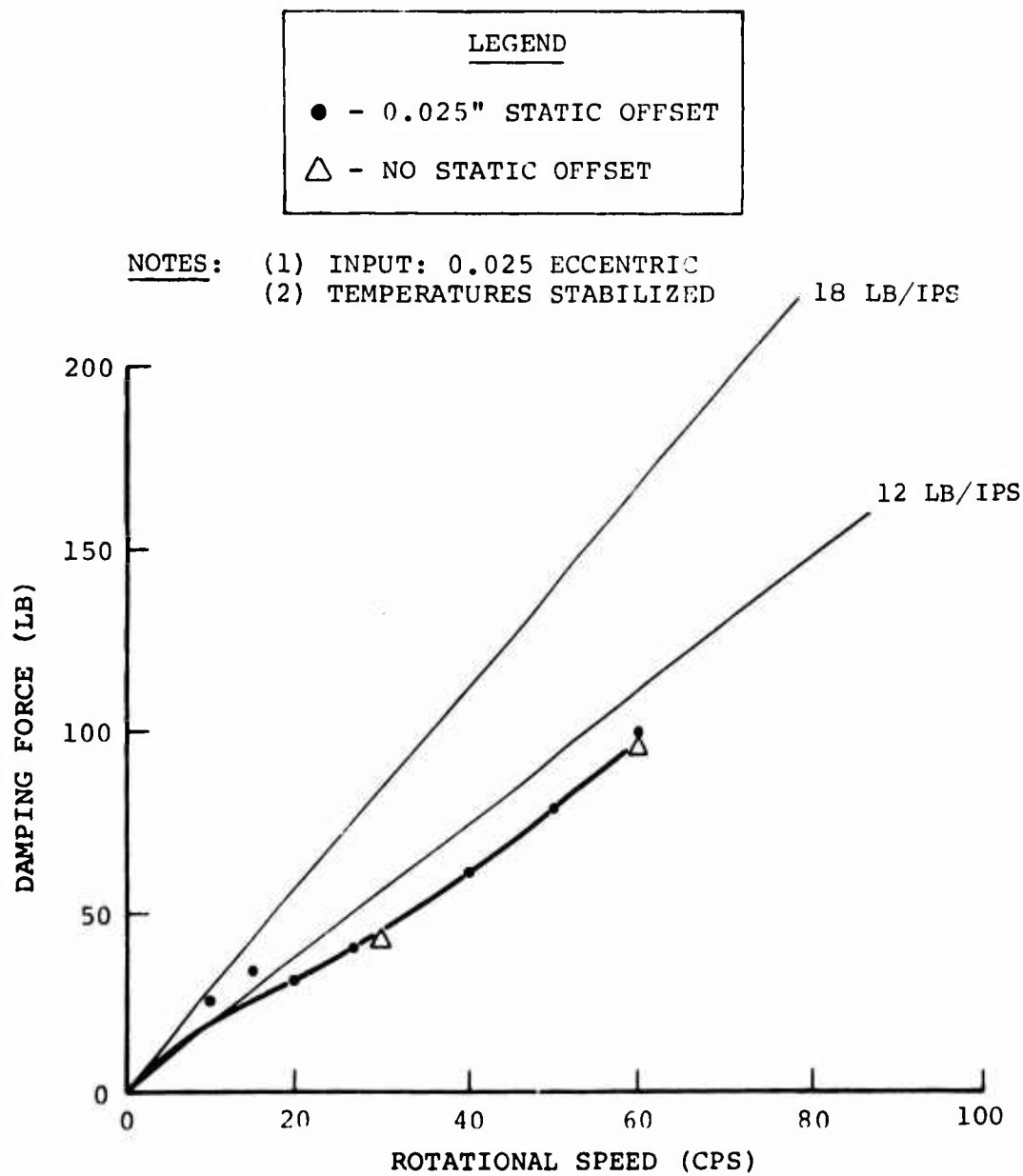


Figure 32. Force Versus Speed to 60 CPS at 160°F.

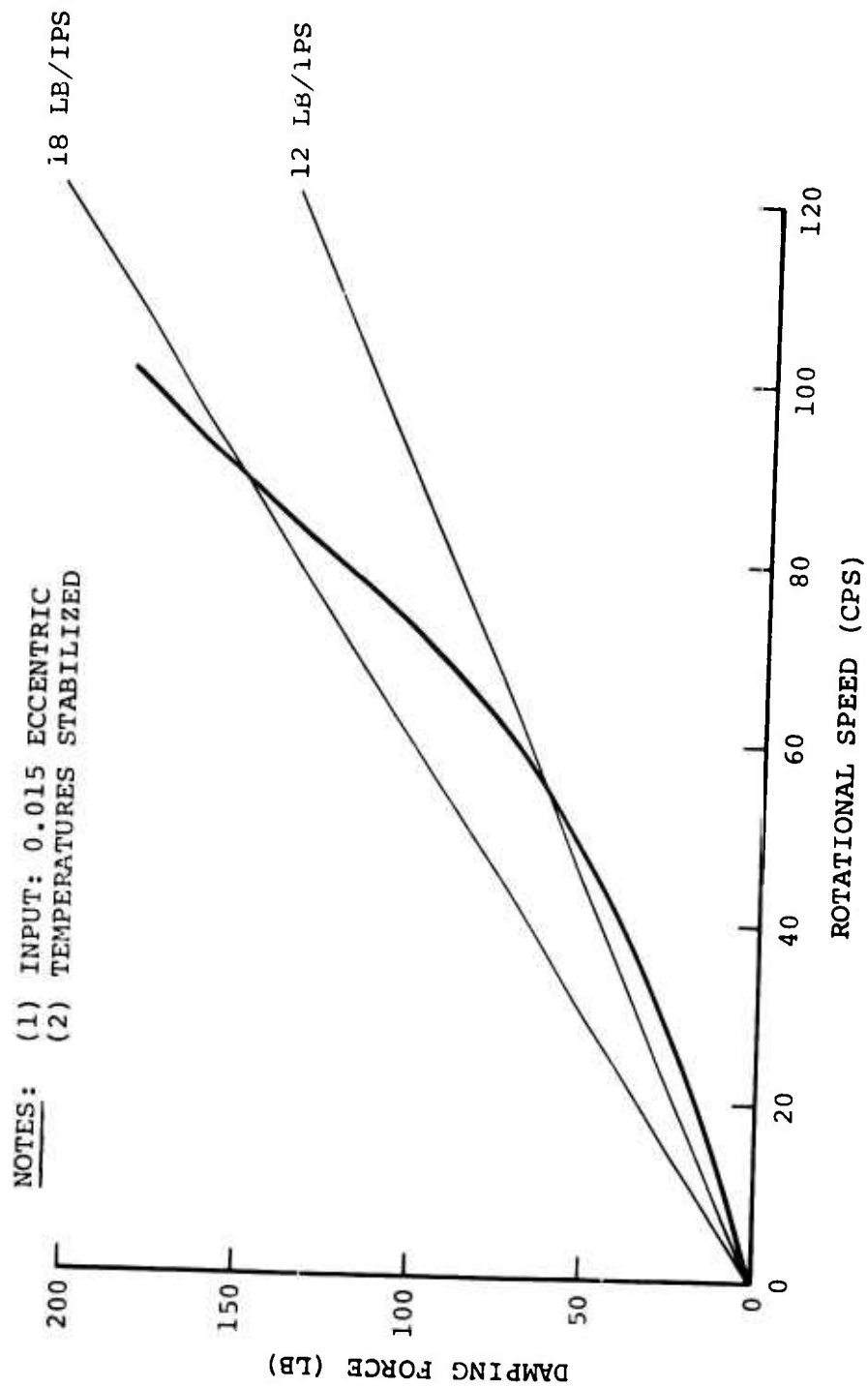


Figure 33. Force Versus Speed to 100 CPS at 160°F.

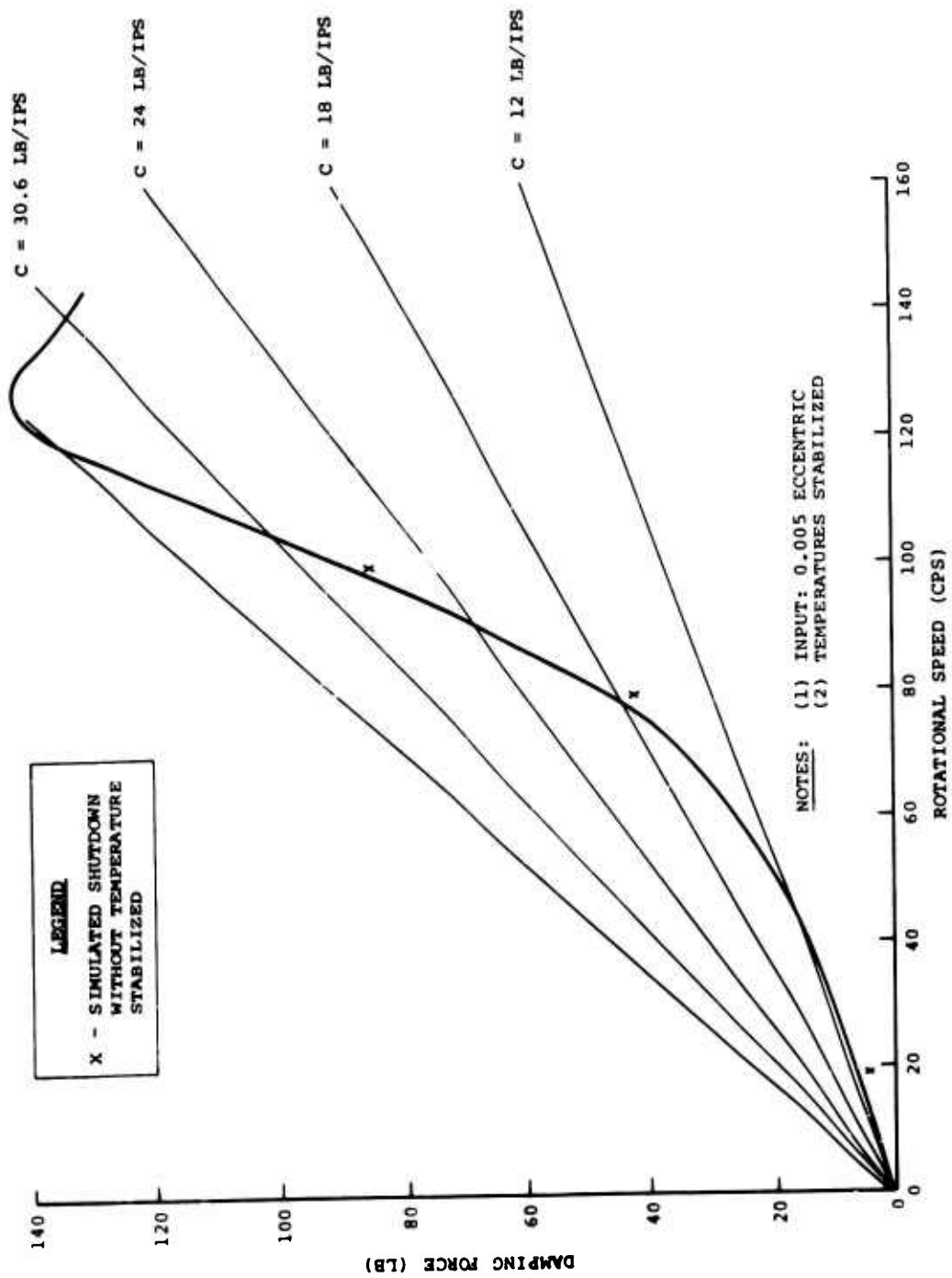


Figure 34. Force Versus Speed to 140 CPS at 160°F.

A nonlinearity in the damping curve was observed at frequencies over 80 Hertz (see Figure 34). The fact that the damping force peaks and then drops off with higher frequencies indicates a resonant condition either in the damper support structure or within the damper body. Observation with a strobe light of the damper under test revealed that expansion of the rubber occurs 90 degrees ahead of the eccentric deflection of the test machine. This out-of-phase expansion of the rubber indicates that the resonance is within the damper itself rather than in the structure. The expanding rubber causes a resultant load in the opposite direction (90 degrees behind the eccentric). This load is in the same direction as the normal damping force, so the two forces must be added to represent the total damping force. The drop in total damping force as the frequency is increased is attributed to a probable breakdown of the internal damping caused by the pumping action of the fluid. The total damping force is then supplied by the expanding rubber, or pressure bulge, 90 degrees ahead of the normal damper eccentric. This occurs only at high speed.

The temperature effect on this resonant condition verifies the assumption, because increased internal temperatures should decrease the spring rate of the elastomer and lower the natural frequency. The curve in Figure 29 with a 0.005-inch eccentric at +32°F has no peak. No bulge in the elastomer was noticed with the strobe. The effect of temperature could be minimized by stiffening the rubber section against the bulging action, which should linearize the damping curve to higher frequencies.

Figures 35, 36, and 37 show the stabilized temperatures measured at the inner and outer damper members throughout the test program. Each data point on these curves also represents the point at which the damper force data were recorded.

The damping force and temperature versus the frequency with only one chamber filled with fluid are shown in Figures 38 and 39. This test represents what would happen if the fluid were lost from one chamber due to malfunction. Even with the lower damping force that exists, the temperatures recorded on the metal parts of the damper are essentially the same as those recorded with both chambers filled.

Figure 40 shows the damping force at 140 Hertz and the temperatures of the inner and outer damper members during the 24.5-hour endurance test. Several times during this test there was a sudden, rapid temperature rise so severe that the test had to be interrupted. At the high temperatures encountered during the test, the grease in the bearing became thin and ran out around the threaded bearing retainer. Data indicated that the bearing itself was the primary source of heat. After 7 hours of testing, the bearing was removed, cleaned of all grease, and lubricated with a light oil. This stabilized the temperature and damping-force measurements for approximately ten more hours, when the temperature again rose suddenly. At this point (17.5 hours of testing), the procedure was stopped and a new bearing was installed. With the new bearing, the damping force and temperature were substantially reduced. After the data were plotted at the end of 22.5 hours, it was noted that the damping force recorded for the period from 17.5 to 22.5 hours was considerably lower than normal. The low data led to the belief that there was an error in the instrumentation readout. The damper was therefore placed back in the test setup and run for another two hours. The damping force measured for this final period was much closer to the normal levels. On this basis, the damping force readout for the 17.5- to 22.5-hour period was assumed to be incorrect. The cause of the error is not known.

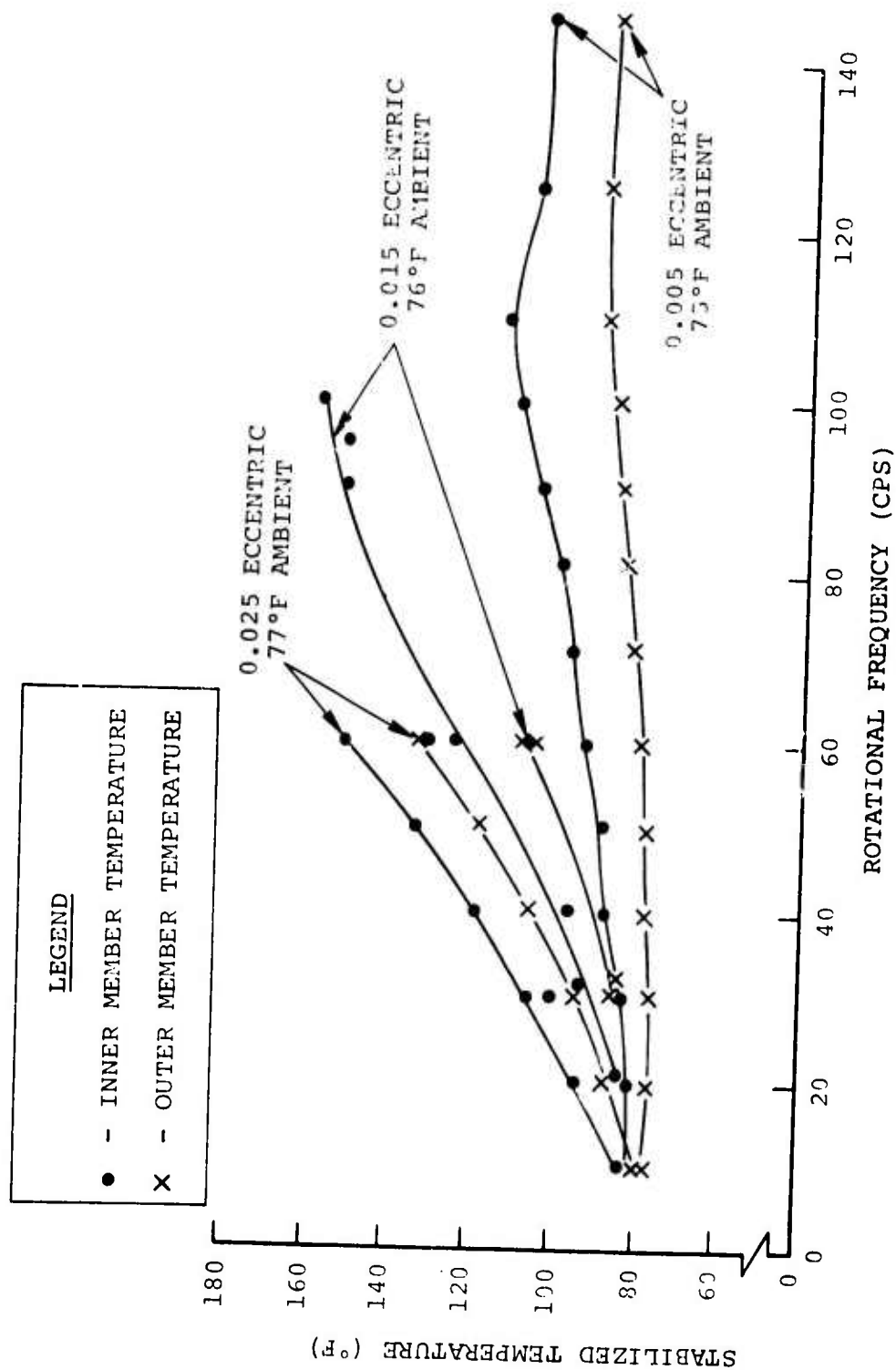


Figure 35. Stabilized Temperature Versus Speed at 70°F.

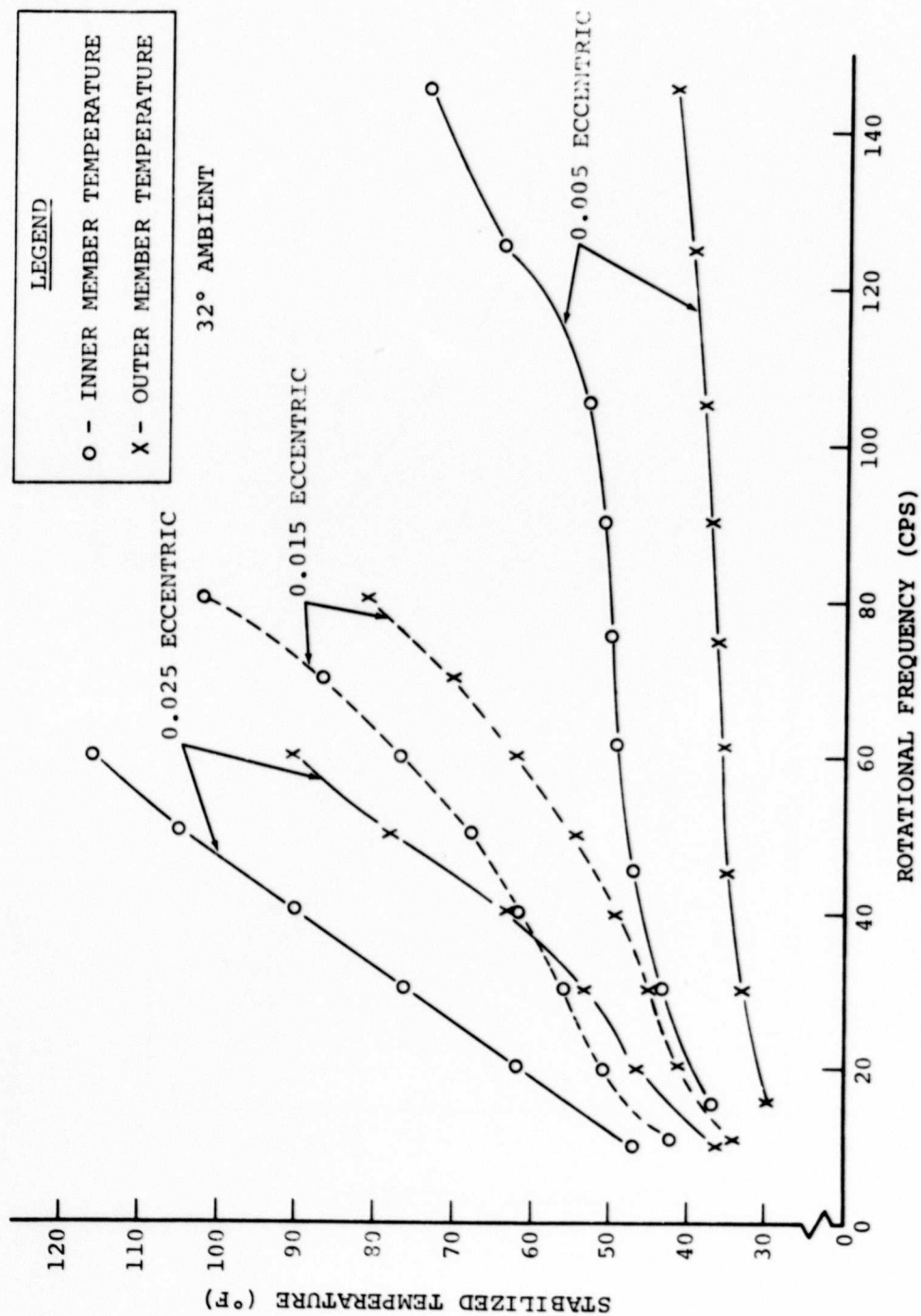


Figure 36. Stabilized Temperature Versus Speed at 32°F.

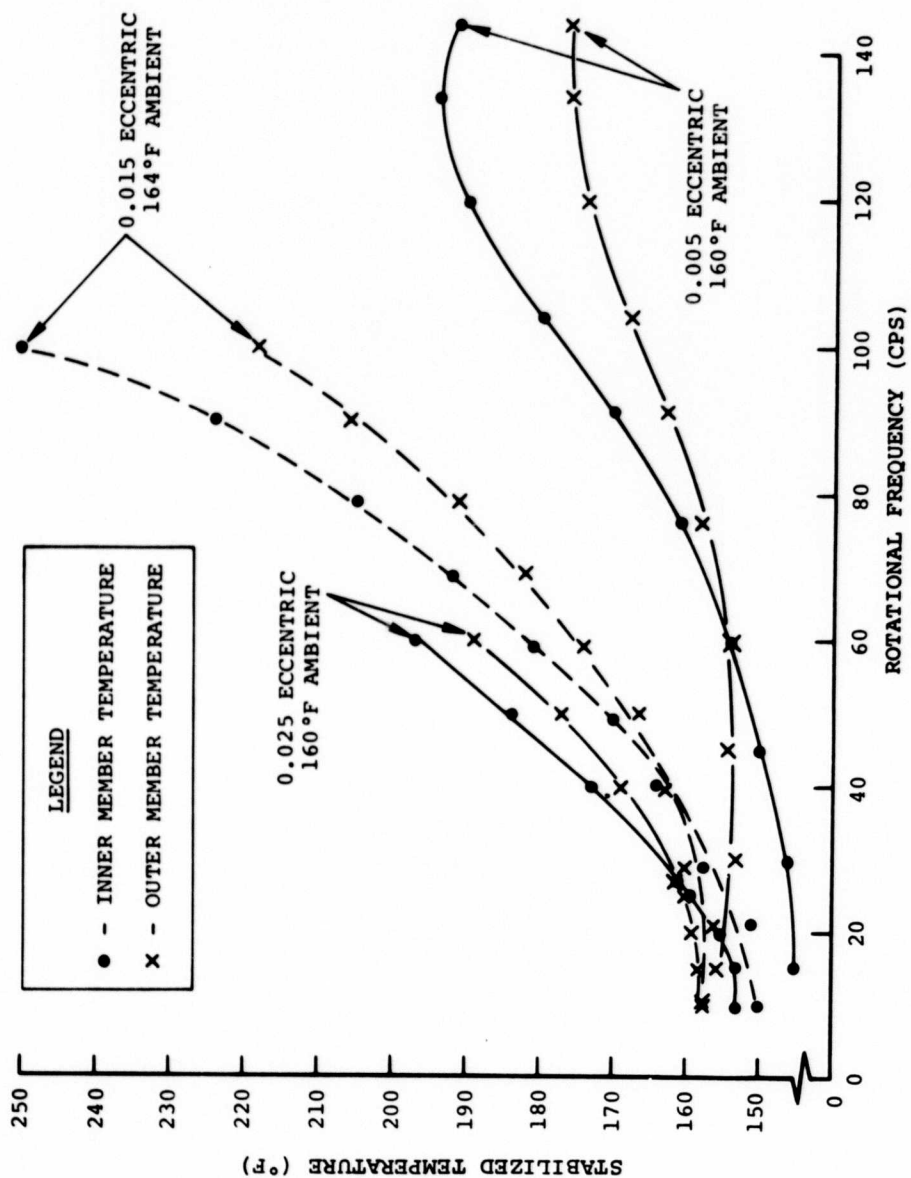


Figure 37. Stabilized Temperature Versus Speed at 160°F.

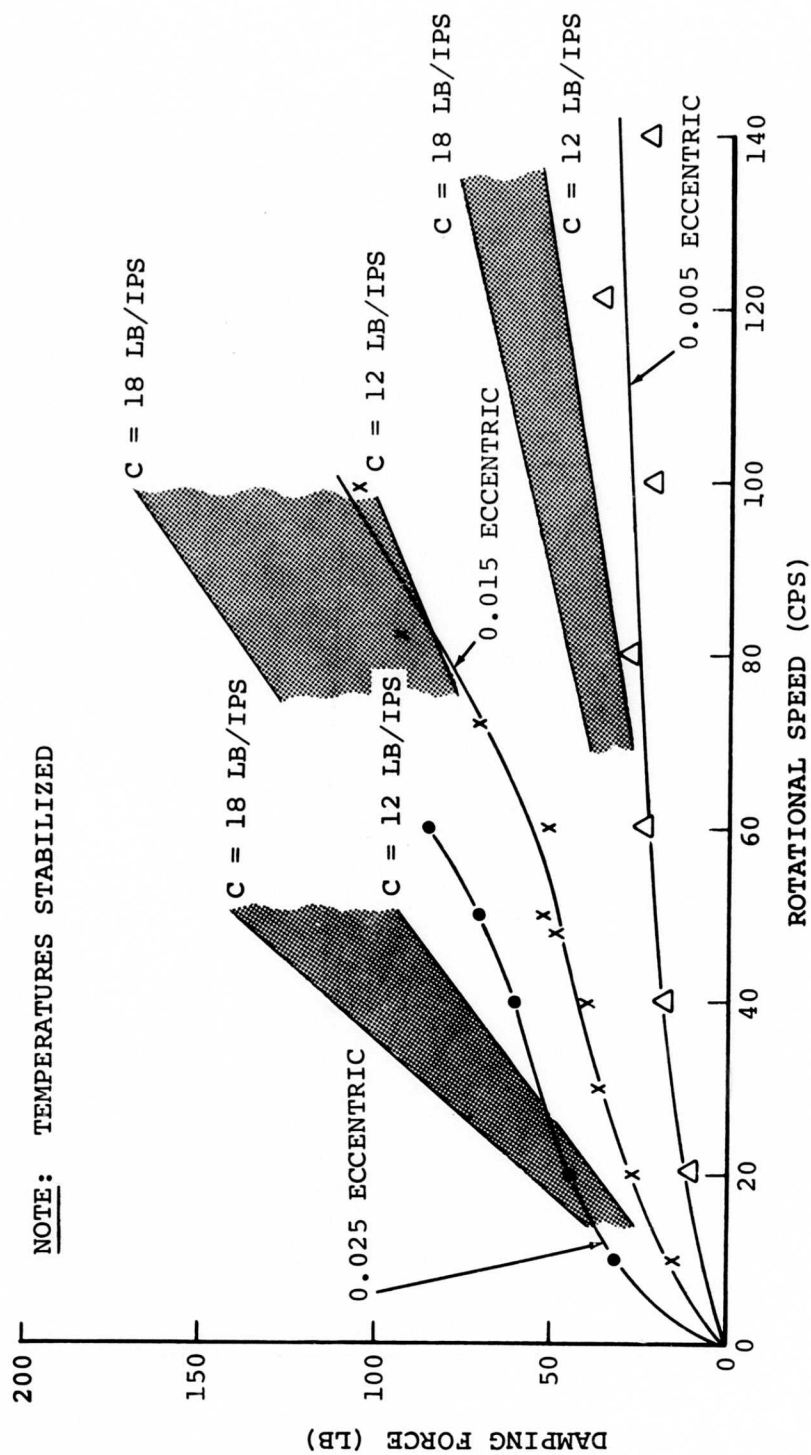


Figure 38. One Chamber Damping Force Versus Speed at 70°F.

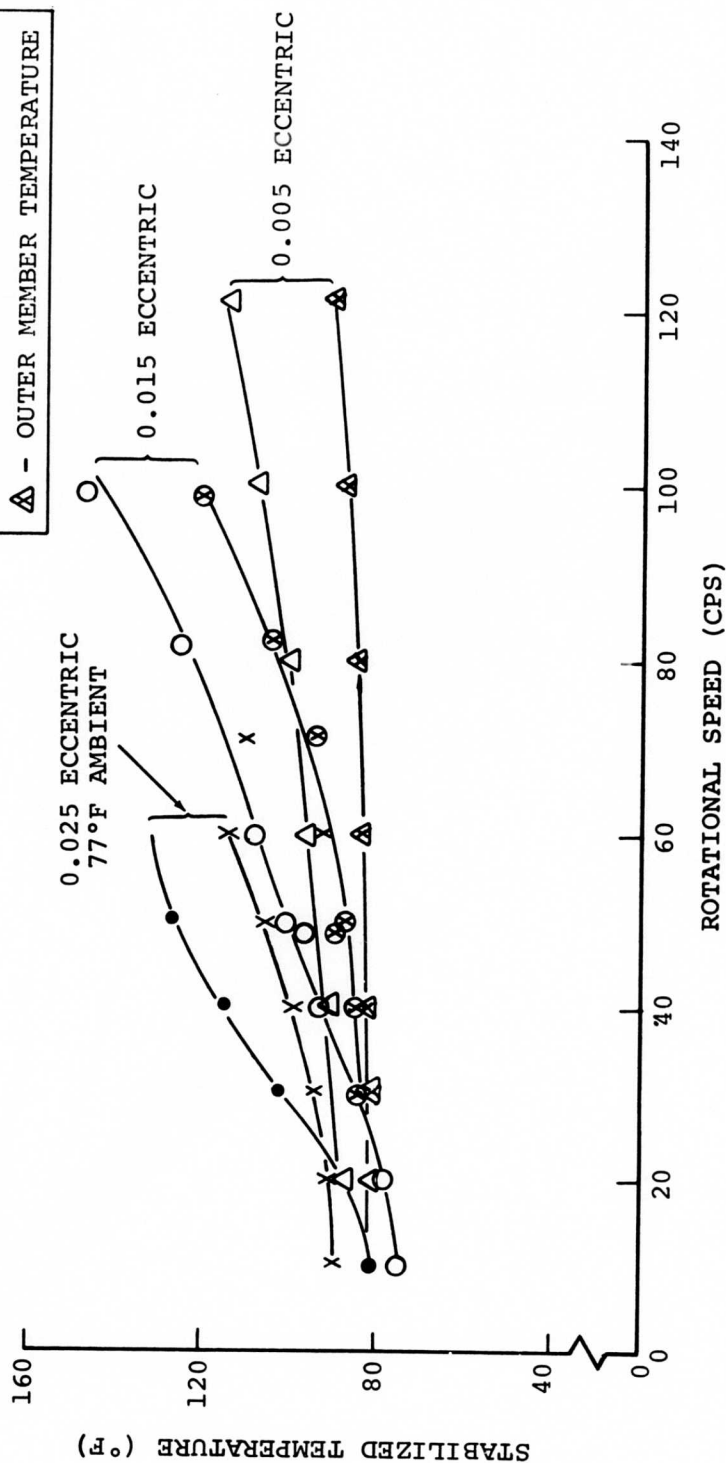
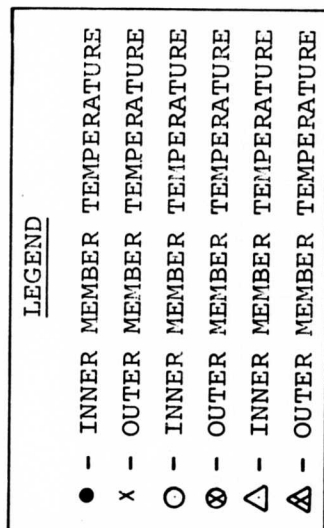


Figure 39. One Chamber Stabilized Temperature Versus Speed at 70°F.

NOTES:

- (1) INPUT: 0.005 ECCENTRIC
- (2) TEMPERATURE: +160°F
- (3) FREQUENCY: 140 HERTZ

LEGEND

- △ - INNER MEMBER TEMPERATURE
 ○ - OUTER MEMBER TEMPERATURE
 X - DAMPER FORCE

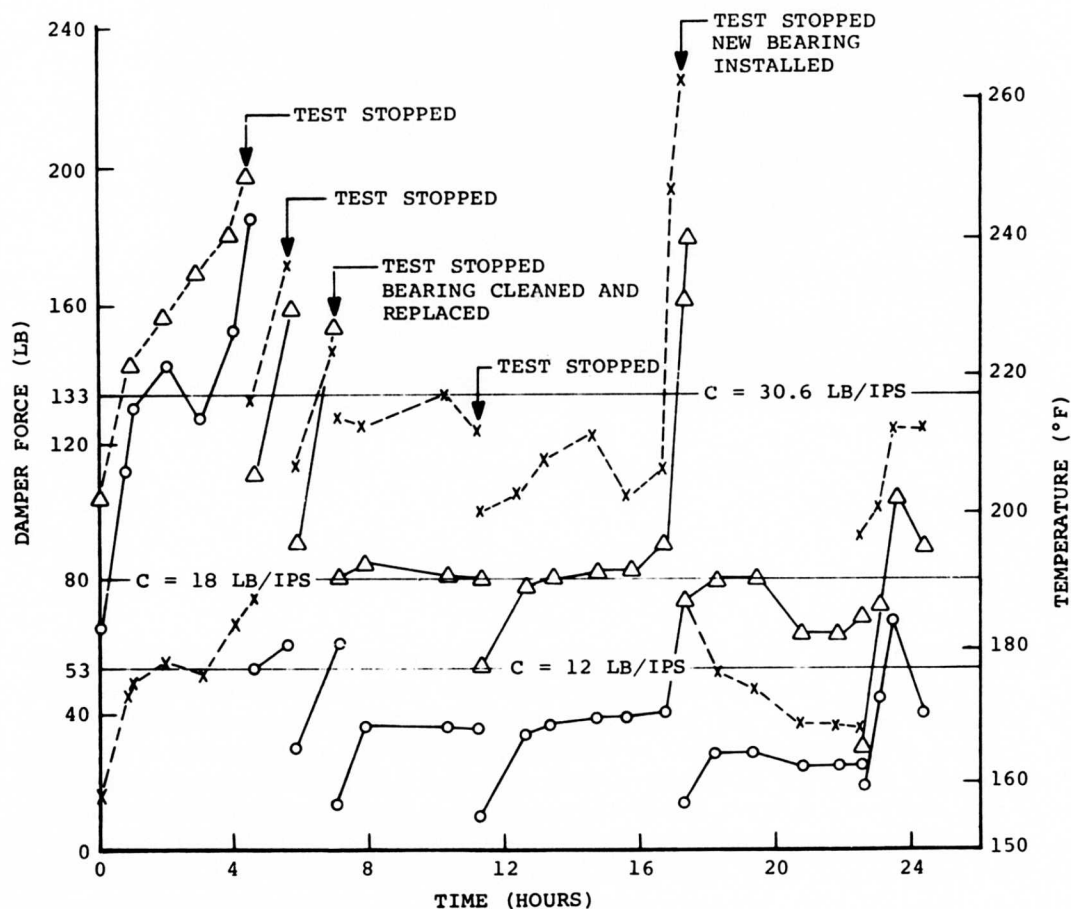


Figure 40. Temperature and Force Versus Time - Endurance Test at 160°F.

After the test, the damper was completely disassembled and was examined visually for signs of deterioration in the elastomeric parts. No deterioration was apparent (see Figure 41). When the bearing was operating properly and adequate lubrication was maintained, the temperature rise of the damper components recorded during the test program was well within the limits of the elastomer employed.

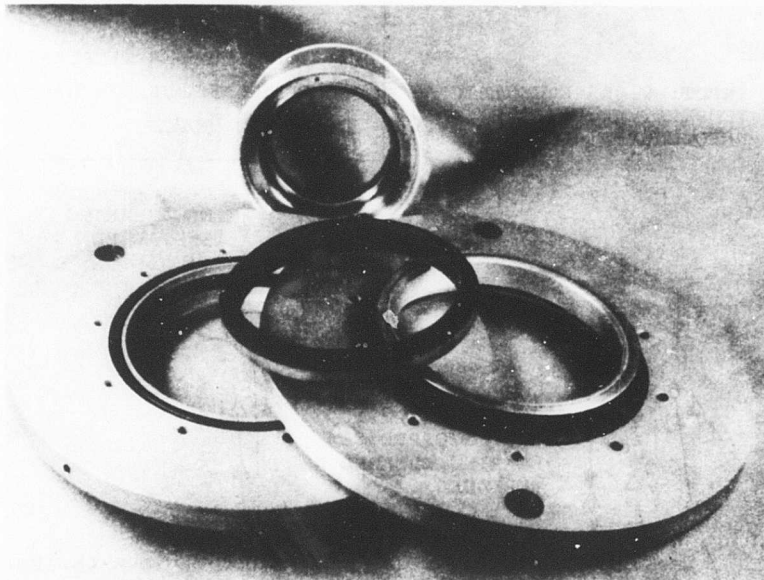


Figure 41. Disassembled Damper .

SUMMARY

The tests indicated that the damper characteristics fall within the general limits established for the specification. The damping coefficient is higher than intended under some conditions but not sufficiently high to warrant changing at this time. The damper has demonstrated a fatigue life in excess of ten million cycles at elevated temperatures and at motions far in excess of those normally expected in service. The damper was tested at an ambient temperature of 160° F and five times the expected excursion. The bearing could not withstand these conditions and had to be relubricated and replaced to complete the test run. Satisfactory damper performance has been demonstrated under these severe conditions, and satisfactory performance for the bearing is projected when normal operating limits specified for the aircraft installation are not exceeded.

The diaphragm separating the dual chambers of the damper was found to have failed sometime during the testing prior to testing the damper with one chamber empty. The failure occurred adjacent to a mark left by a sprue, or vent, in the elastomeric mold. Under deflection, the member received high stresses in this area; the additional stress concentration caused by the

mark resulted in the failure. New parts were made with this sprue relocated in a less critical area. All tests were repeated. The diaphragm then performed in a satisfactory manner.

The nonlinear damping characteristics noted at the higher frequencies have been explained (under Test Results) as a pressure wave preceding the deflection by 90 degrees and causing an expansion of the elastomer at this spot. The reaction to the expansion acts through the damper in the same direction as the damping force from the viscous action of the fluid, and addition of these two forces gives the total damping of the unit. The nonlinear characteristics could be eliminated by making the elastomer more resistant to expansion in this direction.

Damper failures from the bench testing have been attributed to working of the elastomer resulting from the initial bend in the shaft acting as a crank and the shock wave expansion caused by excessive fluid shear. Neither cause is related to the dynamic deflection of the flexible system. Removing the crank effect by straightening the shaft and machining the field splice adapter flanges reduced the flexing of the elastomeric sections and allowed the dampers to function in a satisfactory manner.

CONCLUSIONS

The damper as developed for this program successfully controlled the deflections of the supercritical-speed shaft as balanced during the tests. It operated satisfactorily in the environment of the aircraft within the temperature limits tested.

The failures that occurred during this test program were a result of excessive shaft motions. Excessive motions at the damper regardless of the source (crank effect or deflections from unbalance in the shaft) caused unacceptable loads on the damper, bearing, and structure. When these motions and loads were reduced to acceptable levels, the damper performed in a satisfactory manner.

The nonlinear damping characteristics did not present additional problems in balancing the shaft. The independent effect of this variable was not considered in the actual test program. Increased stiffness of the elastomer in the damper may be a desirable improvement.

The damper (J-12331-5) is capable of a minimum of 21 hours of service in the aircraft at the conditions used for this endurance test, if temperatures are closely monitored and maintained below approximately 200° F at the bearing retainer.

The motions at the damper must be kept within the design limits to prevent excessive heat buildup and deterioration with eventual failure of the elastomeric section. The damping characteristics of the unit establish the load transmitted through the bearing to the structure, and excessive motions will produce excessive loads for the bearing. Excessive motions can be caused by the initial bend in the shaft (producing a crank effect) or from dynamic deflections as a result of excessive unbalance in the flexible shaft. Both motions must be controlled within acceptable limits if satisfactory performance is to be obtained.

TORSION TEST

The torsion test specimen consists of a short section of drive shafting assembled with standard flexible-coupling adapters at each end and with the special adapter sections designed for the damper installed near the center. A drawing of the torsion fatigue specimen is included in Appendix II. The adapters at the center were assembled to simulate an actual aircraft installation. The damper bearing and retainer sleeve or spacer was used so the retaining nuts could be torqued to the same value specified on the installation drawing and thereby provide the same stress loading on the section as expected in service. The rivets used for the adapters were the same as specified on the full-size shaft, including the 3/8 rivet with the small hole for the strain gage lead wires. Standard assembly procedure was used throughout with normal quality control and inspection for parts.

TEST MACHINE AND INSTRUMENTATION

The torsion test was run in an IV-20 fatigue machine operating at 20 cps. The measurements obtained during the test included steady and alternating load, frequency of vibration, and total number of cycles. The load was applied by the test machine and measured by torsion strain gages applied to the test specimen. The signal was amplified by a bridge amplifier, and the signal was presented or observed on a single-beam oscilloscope. The number of cycles was totaled by a counter on the test machine and recorded in the test log as the test progressed.

The measurements obtained during the torsion test included steady and alternating load, frequency of vibration, and total number of cycles. The load was applied by the test machine and measured by torsion strain gages applied to the test specimen. The signal was amplified by a bridge amplifier, and the signal was presented or observed on a single-beam oscilloscope. The number of cycles was totaled by a counter on the test machine and recorded in the test log by the supervising technician as the test progressed.

TEST PROCEDURE

This test was intended to demonstrate the life and safety of the new shaft adapter design beyond the conditions expected in the ground and flight test programs.

One end of the test specimen (see drawing ST10220 in Appendix II) was mounted to a fixture rigidly attached to the working surface of the test machine. The other end was secured to a shaft mounted on bearings to allow radial motion. A 14-inch torque arm was attached to the shaft and platen of the IV-20 fatigue test machine. A steady load was applied to the test specimen through the platen by adjusting a jack screw against a spring (see Figure 42). The alternating force was applied by a rotating eccentric mass which turned at 1,200 rpm (20 cps). The magnitude of the alternating force could be changed by adjusting the amount of eccentricity. Load in the specimen was measured by a four-arm torsion bridge mounted on the specimen and precalibrated.

The test was run with the following schedule:

- Design Torque Load with 15 Percent Alternating Torque Load

Temperature	—	Ambient $70^{\circ}\text{ F} \pm 5^{\circ}\text{ F}$
Loading	—	26,700 inch-pounds
Alternating	—	4,000 inch-pounds
Duration	—	10,000,000 cycles

- Design Torque Load with 25 Percent Alternating Torque Load

Temperature	—	Ambient $70^{\circ}\text{ F} \pm 5^{\circ}\text{ F}$
Loading	—	26,700 inch-pounds
Alternating	—	6,674 inch-pounds
Duration	—	Test to failure

This test was conducted by first applying the steady load, then starting the machine and adjusting the rotating mass to the desired alternating load. The test was continued for the required number of cycles.

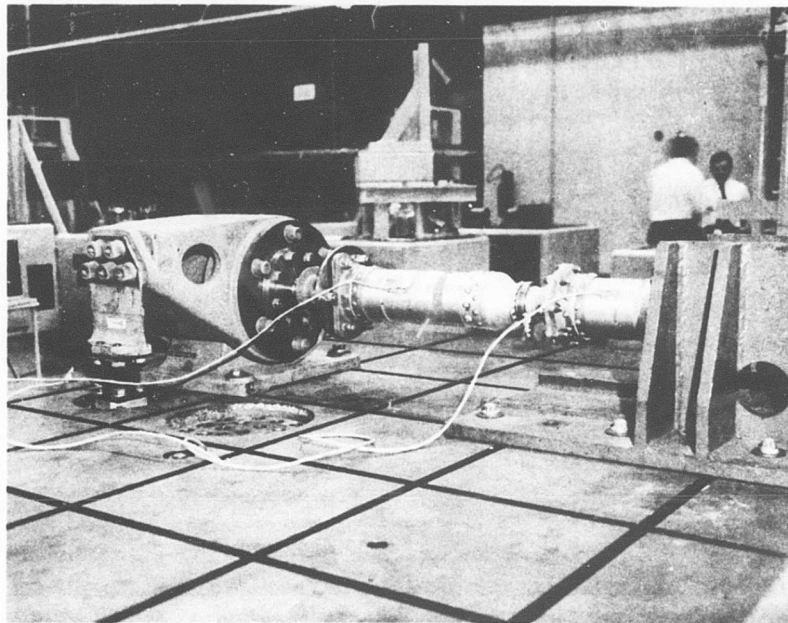


Figure 42. Torsion Test Torque Arm.

TEST RESULTS

The test was run with the following schedule:

Test Run	Load Level (inch-pounds)	Cycles x 10 ⁶	Remarks
1	26,700 ± 4,000	10.037	Runout
2	26,700 ± 6,674	15.006	Runout
3	26,700 ± 12,000	1.583	Failure

The specimen completed the desired 10 million cycles in good condition. The alternating load was increased according to schedule with the supposition that failure would occur within the next 5 million cycles. When 15 million more cycles were completed without failure, the alternating load was again increased. The test continued for 1.6 million additional cycles at this loading before the specimen failed. The total number of cycles on the specimen at failure was 26.6 million.

When the adapter (SK16763) was removed from the tube (SK16760), the following observations were made (see Figure 43):

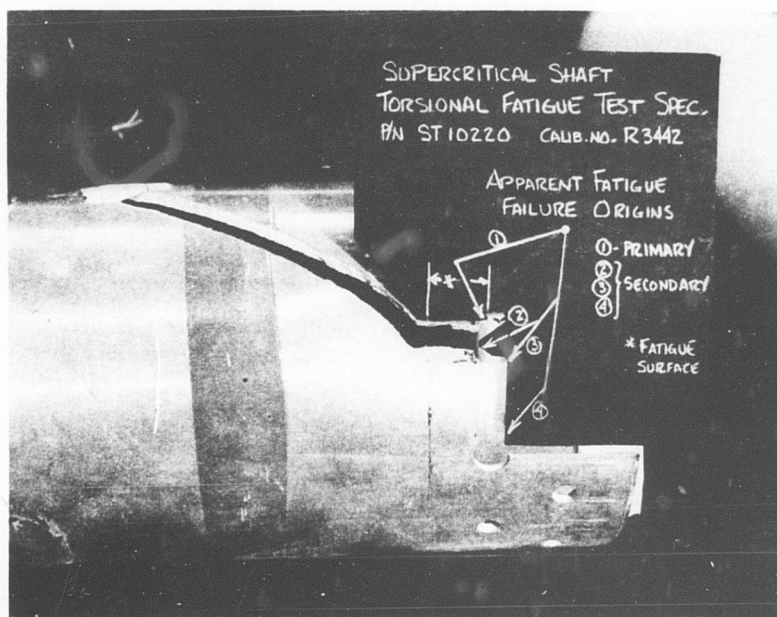


Figure 43. Torsion Test Failure Analysis.

- Fatigue cracks appear to have originated at the MS20470D8 rivet.
- Primary fatigue origin was along the longitudinal axis of the specimen with a fatigue crack along that axis.
- Secondary origins are noted 30° and 90° counterclockwise from the primary origin in the MS20470D8 rivet hole.
- A fatigue origin is noted perpendicular to the longitudinal axis in the MS20470D12 rivet.

SUMMARY

A smaller diameter spline and the requirement of increased bending rigidity through the joint, together with change in rivet size, necessitated a cross-sectional area change in the material of the adapters. The torsion fatigue test successfully demonstrated the soundness of the revised adapter joint. The test specimen successfully completed ten million cycles under design torque loading conditions with 15 percent alternating load. Then, the alternating load was increased to 25 percent, and the test continued for another fifteen million cycles. At this point, the alternating load was increased to 45 percent, and the test continued to an intentional failure, which occurred after 1.58 million cycles at this loading. Failure occurred after a total of 26.6 million cycles.

The torsion fatigue test specimen was disassembled after the intentional failure for inspection and analysis. The initial failure occurred at a standard rivet, traveled along the shaft fatigue surface to the tube surface at the edge of the adapter, and then proceeded in a normal 45° torsional (shear) failure around the shaft. Secondary failures occurred from the initial rivet hole to the special 3/8-inch-diameter rivet and in the opposite direction toward the adjacent 1/4-inch-diameter rivet. This was a normal torsion fatigue failure.

The coned surfaces which provide alignment of the adapter joint were completely free of damage. The fretting problem which was present in the previous design at the contacting surfaces had been corrected.

The new design has demonstrated an adequate safety margin to proceed with confidence to a flight test program as originally outlined.

CONCLUSIONS

The coned surfaces used for alignment of the shaft adapters performed their intended function. Match marks, while accomplishing the alignment of the parts, could be troublesome, and a more positive arrangement should be considered for future designs. Joints that will assemble only in one position are preferable.

The high torque used to assemble the cone surfaces across the spline accomplished the desired result of aligning the parts and of preventing fretting of these parts. Standard wrenches were incapable of applying the torque, and special wrenches had to be developed. Difficulty was encountered in removing the nut for disassembly even with the special wrenches.

The splined adapter joint was adequate for the severe bending and loads imposed by a crooked and unbalanced shaft. This joint may not require the amount of torque used to assemble it and still remain free of the fretting problem. Tests to determine the appropriate value for assembly torque may be required. Installation torques could in all probability be reduced if shaft design loads were not exceeded.

The adapter joint at the damper must carry the steady torque of the drive system together with the alternating torque component. It must carry the bending loads of the supercritical speed shaft and is also subjected to loads from the damper and bearing. The combination of loading at this fitting produces fretting of the joining surfaces, a most severe and troublesome design condition. The adapter joint must be made so it can be disassembled and reassembled without disturbing the balance of the shaft. Therefore, it must be reassembled with exactly the same static runout characteristics it had before disassembly. The splines must engage the same teeth relative to its mating part, the split-cone washer must have precisely the same alignment, the field splice must be assembled with match marks aligned, and assembly torque should be consistent.

Criteria for successful operation of the adapter are:

- Adequate Bending Strength
- Adequate Torsional Strength
- Freedom from Fretting
- Precise Alignment (to preserve balance)

FULL-SIZE SUPERCRITICAL-SPEED SHAFT TEST

SHAFT SPECIMEN

The full-size shaft specimen (see drawing in Appendix II) was designed as a replacement for the standard interconnect shaft used between the combining transmission and the forward transmission on the CH-47B. It carries the same torque and turns at the same speeds. The shaft has a diameter of 4.50 inches and a wall thickness of 0.120 inch with a 2024 T3 extruded aluminum alloy tube. The distance between the centers of the couplings at each end of the shaft is 338.5 inches (see Figure 44). The flexible metal coupling plates are attached to the shaft with three bolts into standard adapters which are riveted to the shaft with 24 quarter-inch aluminum rivets (see Figure 45). The dampers are attached as shown in Figures 46, 47, and 48. The shaft is necked down at these areas to allow a smaller diameter bearing to be used. The D/N value (diameter/speed) of the bearing is near the upper limit for grease-lubricated applications. Torque is carried through the adapters by fine-tooth splines which are made of steel. Added strength is required for retaining nut threads in this area as well. The coned adapters are sized for adequate strength with special attention being directed to maintaining the stiffness of the section equal to or greater than the tube itself. In other words, the adapter section at the dampers was designed to carry bending loads through the joint with no change in stiffness. Two complete shaft assemblies were fabricated.

After completion of the prior contract, the test specimen was inspected, and severe fretting was discovered on the highly loaded surfaces which carry the bending loads through the joint. To alleviate or remove this trouble, the joint was constructed so that it would be supported between coned surfaces (similar to the tapered bearings in the front wheel of an automobile). These surfaces provide precise alignment in an axial, lateral, and angular direction at the same time (see Figure 46). The joint must be absolutely free of flexing or relative motion to eliminate fretting. Also, the joints must be reassembled in exactly the same position if proper balance of the shaft is to be maintained. The cone surface on one side of the spline is matched by the cone surface of the adapter and split cone washer on the other side to provide this alignment. The very high torque used will assure that tension will always be maintained through the joint regardless of the bending present under normal operating conditions.

The supercritical-speed shaft test specimen was assembled using extruded tubes as they came from the mill. The initial bend of 0.005 inch per foot of length was about one-half the allowable bend according to the specification. No attempt was made to straighten the bend at this time. Special tools were used to buck the rivets inside the long tubes; otherwise, standard assembly procedure was used throughout. After the first damper failure, the tubes were straightened by physically bending them beyond the yield point. The total correction was made by bending at three stations where each station made part of the correction. Slight final corrections were made at the point of deflection only. Maximum runout after straightening was less than 0.020 total indicator reading (TIR) at any point on the shaft. The straightened shaft was run for a series of tests until the second damper failed. This failure was attributed to excessive motion caused by the crank action remaining after the tubes were straightened. Crank action is possible in straight shafts if the flanges joining the sections are not square. The flanges were out of square from 0.013 to 0.017 TIR. They were ground square with the shaft supported between centers; runout then was less than 0.0005 inch at any point. After the tubes were straightened and the flanges ground, the shaft ran to top speed without exceeding

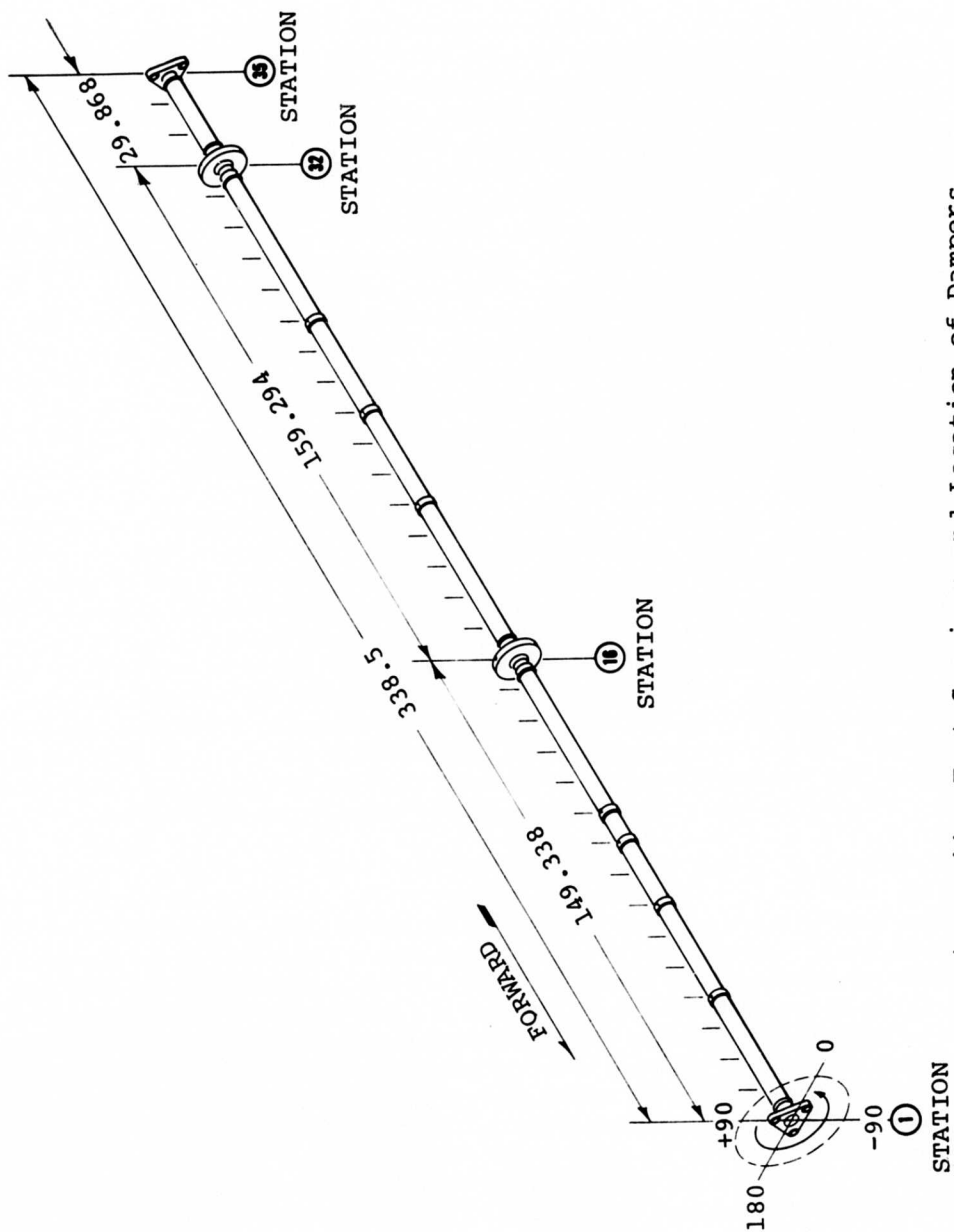


Figure 44. Test Specimen and Location of Dampers.

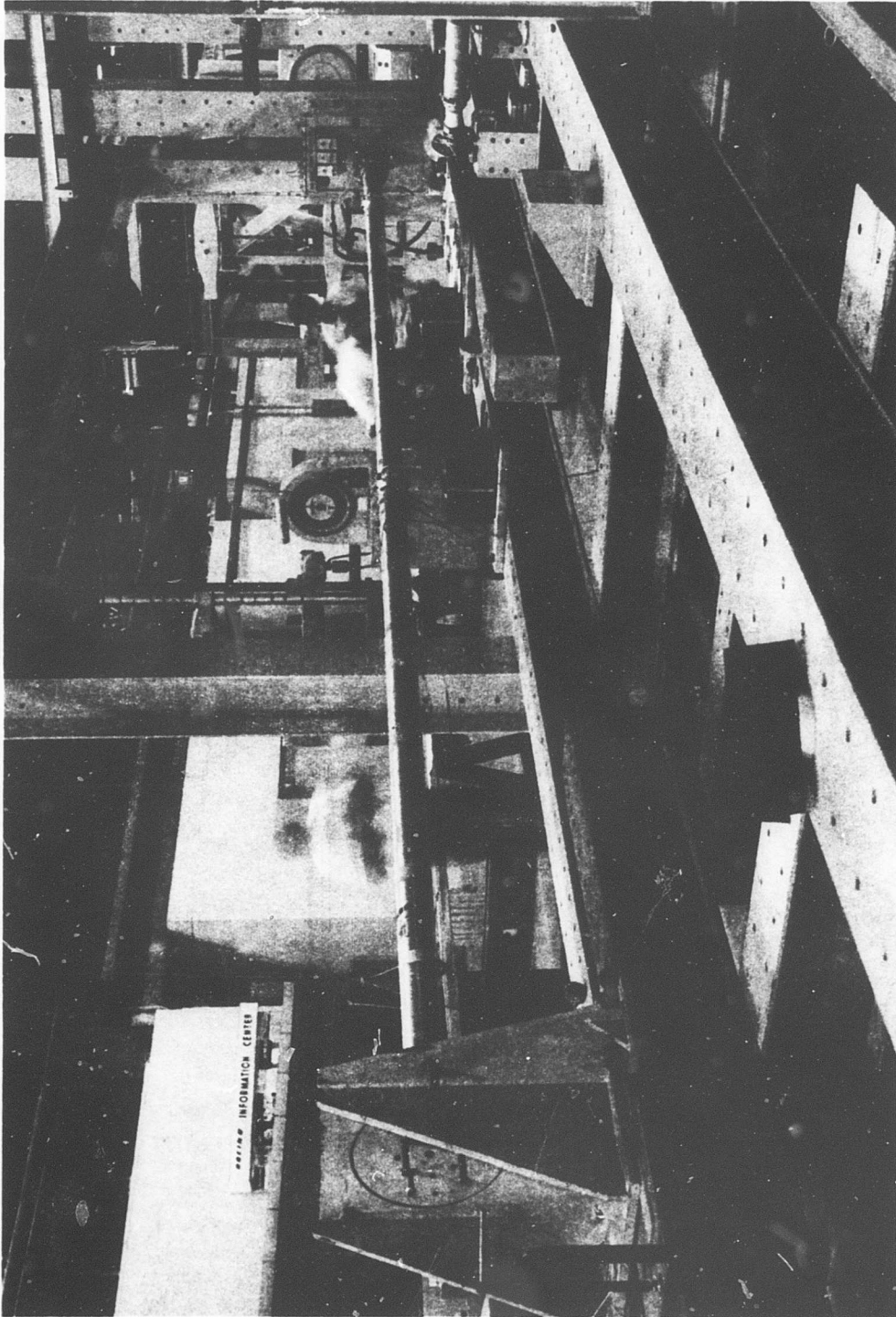


Figure 45. Calibration Test Shaft.

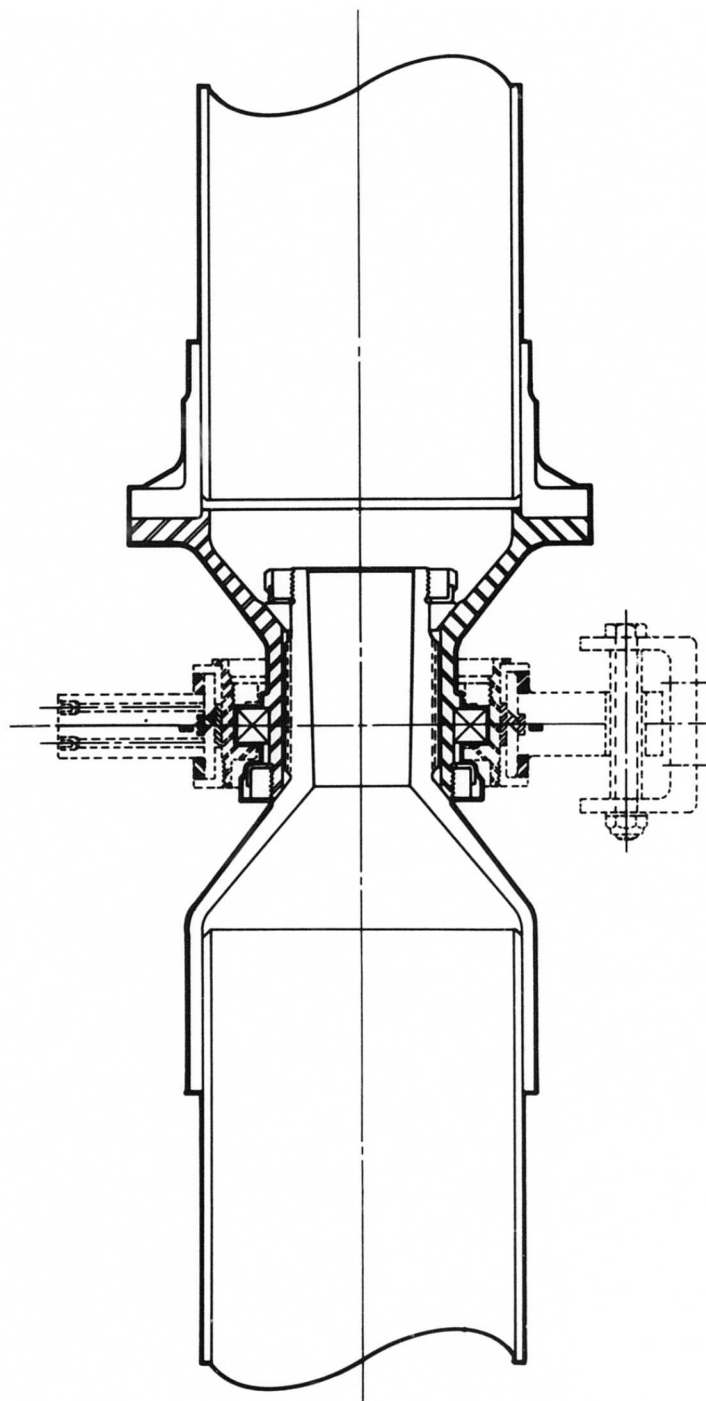


Figure 46. Shaft Adapter - Sectional View.

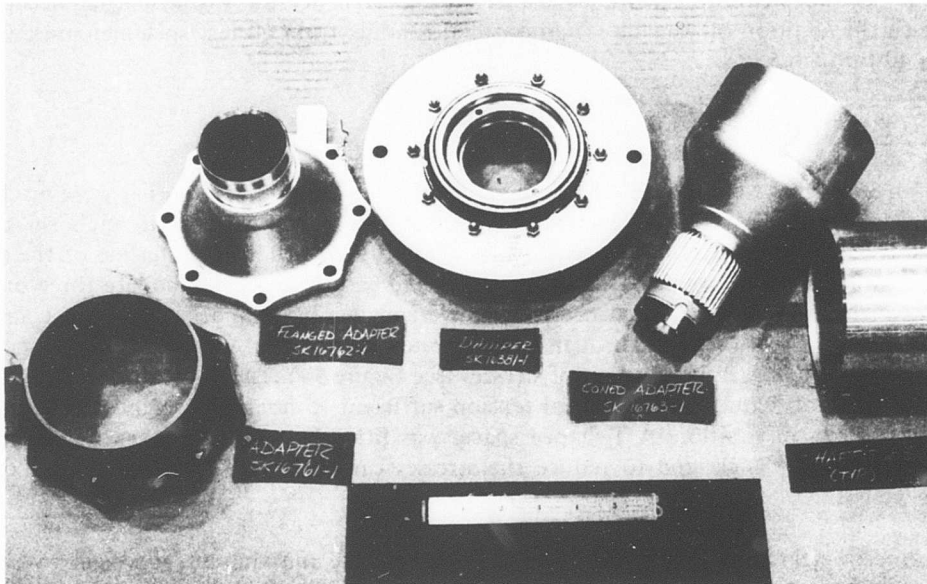


Figure 47. Splined Adapter Details.

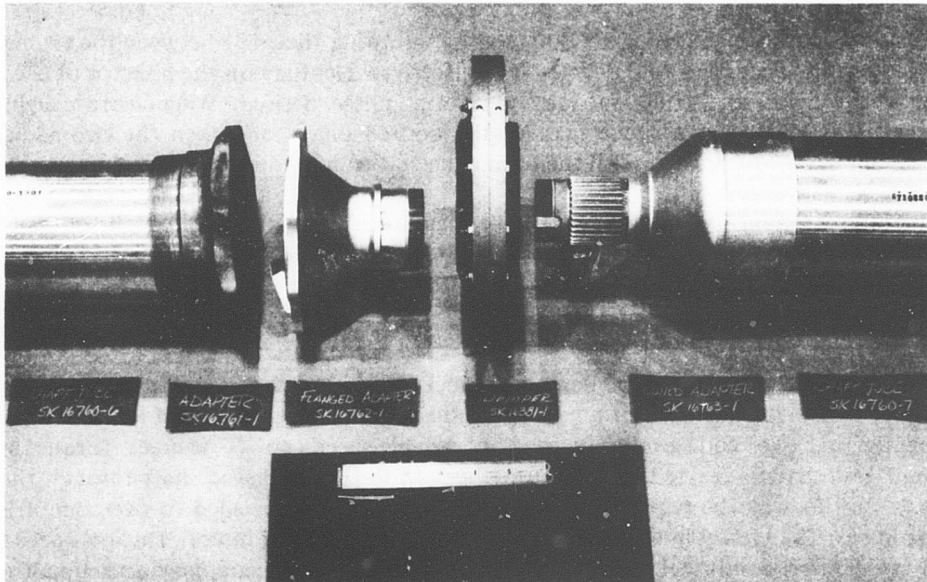


Figure 48. Splined Adapter Assembly Procedure.

the limit bending stress even without balance weights. Balance was brought to an acceptable level with the addition of weights. The measured runouts from all test specimen are given in Figures 49 through 53.

BALANCE WEIGHTS

The balance weights were located on raised pads of glass-reinforced plastic that were machined concentric with the outside diameter of the shaft. Each pad was 0.050 inch thick and completely covered the strain gage wire packs along the longitudinal centerline of the shaft. Each pad was 4.600 inches in diameter and was wide enough to accommodate three or four balance-weight assemblies. The balance weights were made of steel blocks and were secured to the shaft by NAS tension bolts through a heat-treated steel strap. A flat square-radius washer was used to assure equal distribution of stresses (see Figure 54). The steel strap was formed so tightening the bolt would provide initial tension sufficient to hold the weight in place under centrifugal forces of rotation. A T-shaped spacer was fitted between the tangs of a steel strap to assure a positive angle and to reduce the stresses caused by the centrifugal loads of the balance weight.

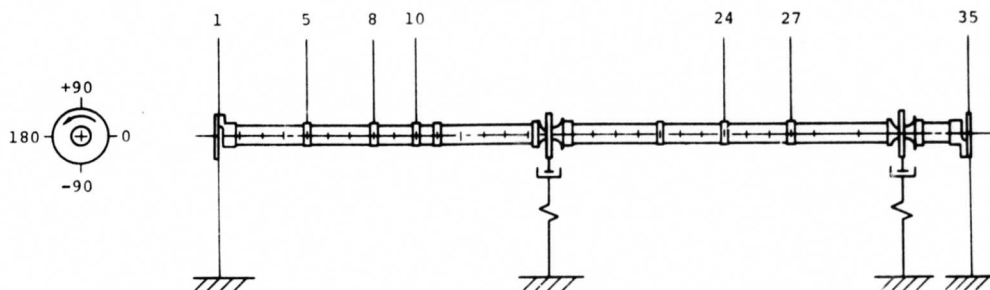
The balance weights could be adjusted for any phase angle and amount of weight by simply slacking off the retaining bolt and repositioning the weight assembly. If two weight assemblies were installed 180 degrees apart, the center of gravity of the shaft section would not be changed. If they were aligned at the same angle, the unbalance would be equivalent to the sum of the two weights (100 grams). The balance-weight mass was located 2.65 inches from the shaft centerline.

Any desired balance weight could be obtained by adjusting the angle between the two weight assemblies from 180 degrees to 0 degrees. The effective weight lay on the bisector of the angle between the weights and could be located at any phase desired. When more weight was required, it was located as a single mass at the desired phase, and then the two additional weight assemblies were adjusted until the total equaled the desired balance weight.

The table and diagram in Figure 55 show the magnitude of the balance weight obtained for various angles.

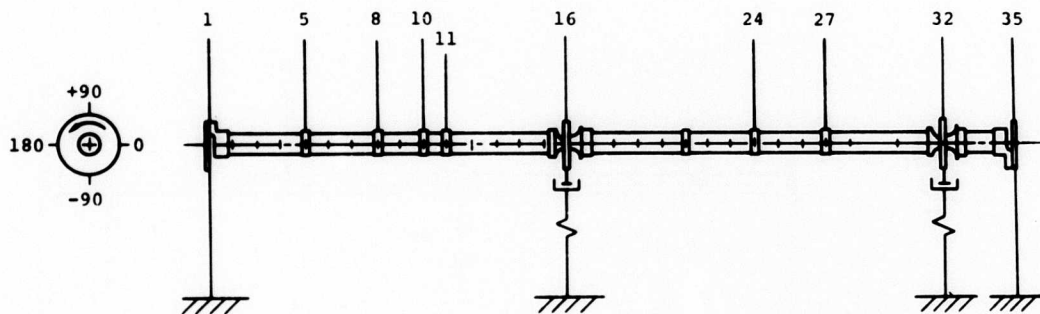
THE BENCH TEST MACHINE

The bench test machine FT 3590 (Boeing Number X95137) (see Figure 56) is a four-square regenerative test unit composed of a high-speed shaft (the test specimen), a low-speed shaft, a torquing device, two end gearboxes, and a variable-speed power source. Torque in the high-speed test shaft is reacted by the torque locked in the low-speed shaft through the end gearboxes. In this way the required power is only that which is needed to overcome friction and gear losses. The locked-in torque is not supplied by the driving motor. The low-speed shaft is made up of short solid-steel segments connected with gear-type couplings and supported on standard pillow blocks. It contains a Houdaille rotary hydraulic actuator with a capacity of 71,000 inch-pounds torque joining two of the segments. This torque is equivalent to 30,600 inch-pounds in the high-speed shaft. Torque can be added to the system by changing the relative angular position of the shaft segments by applying hydraulic pressure to the unit through a rotary union while the shaft is turning. The torque in the test specimen is monitored



SHAFT STATION	DEFLECTION AT PHASE ANGLE								RUN OUT TIR	DEFLECTION PLOT
	0	-45	-90	-135	180	+135	+90	+45		
1	500	501	500	502	500	502	497	497	0.005	
5	500	511	521	524	514	503	492	492	0.032	
8	300	320	333	340	331	316	300	293	0.047	
10	238	251	258	260	257	245	235	232	0.028	
24	243	229	172	104	058	068	125	199	0.185	
27	358	340	286	229	200	2717	274	330	0.158	
35	500	494	498	489	486	490	496	494	0.014	

Figure 49. Initial Bend as Manufactured - Serial 2.



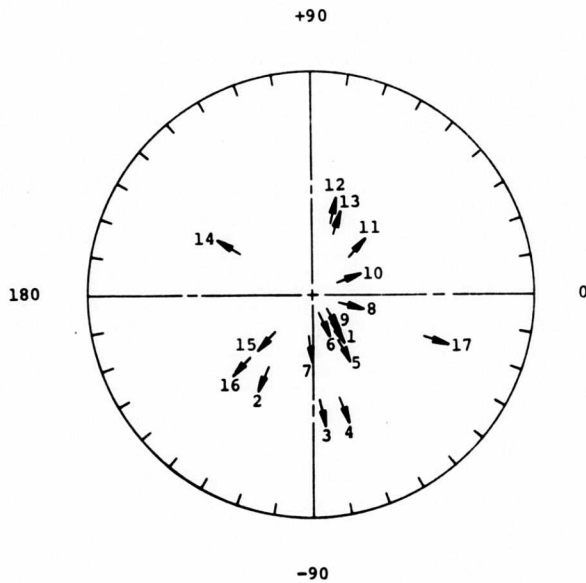
SHAFT STATION	DEFLECTION AT PHASE ANGLE								RUN OUT TIR	DEFLECTION PLOT
	0	-45	-90	-135	+180	+135	+90	+45		
1	550	549	548	542	545	547	548	546	0.008	
5	550	545	538	532	529	533	540	545	0.021	
8	300	298	291	283	280	283	290	295	0.020	
10	550	545	530	518	521	527	537	545	0.032	
11	624	615	605	598	601	608	620	629	0.031	
16	465	469	474	475	471	463	459	460	0.016	
24	200	198	185	166	159	154	166	187	0.046	
27	500	497	489	477	464	455	468	488	0.045	
32	400	388	385	390	401	410	413	409	0.028	
35	500	498	-	501	497	498	-	503	0.006	

Figure 50. Initial Bend After Straightening - Serial 2A.

SHAFT STATION	DEFLECTION AT PHASE ANGLE								RUN OUT TIR	DEFLECTION PLOT 0 180 0 -90 +90
	-22-1/2	-67-1/2	-112-1/2	-157-1/2	+157-1/2	+122-1/2	+67-1/2	+22-1/2		
1	797	797	793	796	795	792	793	794	0.005	
2	578	577	583	576	584	572	571	574	0.013	
3	525	527	527	523	520	517	516	521	0.011	
4	518	520	519	514	512	510	508	513	0.012	
5	516	517	515	512	512	511	510	512	0.007	
6	514	515	515	512	511	512	511	513	0.004	
7	508	509	502	508	506	504	504	507	0.007	
8	506	506	507	505	503	504	505	508	0.005	
9	482	483	482	479	478	478	477	482	0.006	
10	465	464	464	464	464	463	467	468	0.005	
11	468	462	464	466	467	469	472	472	0.010	
12	472	466	463	468	472	473	475	475	0.012	
13	460	457	458	461	463	462	465	464	0.008	
14	538	539	543	548	547	545	545	544	0.010	
15	545	548	551	554	548	546	546	547	0.009	
16	552	555	557	557	554	549	548	548	0.009	
17	611	607	605	604	600	598	604	610	0.013	
18	437	433	427	423	416	413	422	433	0.024	
19	433	428	419	415	410	409	423	432	0.024	
20	422	415	407	401	397	398	413	423	0.026	
21	510	503	497	495	489	485	495	509	0.025	
22	504	507	509	499	495	494	504	506	0.015	
23	516	511	511	510	508	503	510	519	0.016	
24	514	512	508	504	507	505	512	516	0.012	
25	527	526	517	510	511	513	520	525	0.017	
26	532	528	528	528	522	515	520	530	0.017	
27	527	523	525	526	519	514	525	532	0.018	
28	539	538	535	532	532	533	538	537	0.007	
29	537	538	538	541	541	537	539	539	0.004	
30	628	627	626	634	634	627	630	633	0.008	
31	551	548	550	555	555	554	556	556	0.008	
32	535	532	534	538	541	542	542	539	0.010	
33	430	426	423	426	432	432	429	428	0.009	
34	411	411	411	412	415	417	417	415	0.005	
35	626	625	624	623	622	623	627	623	0.005	

Figure 51. Initial Bend After Straightening and Machining - Serial 2B.

SCALE
0.005 INCH



AVERAGED DATA;
SEE TABLE I

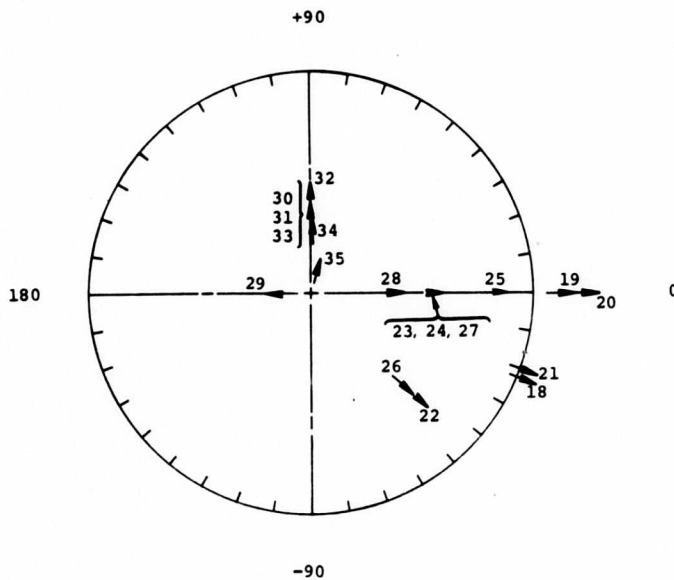


Figure 52. Polar Deflection Initial Bend - Serial 2B.

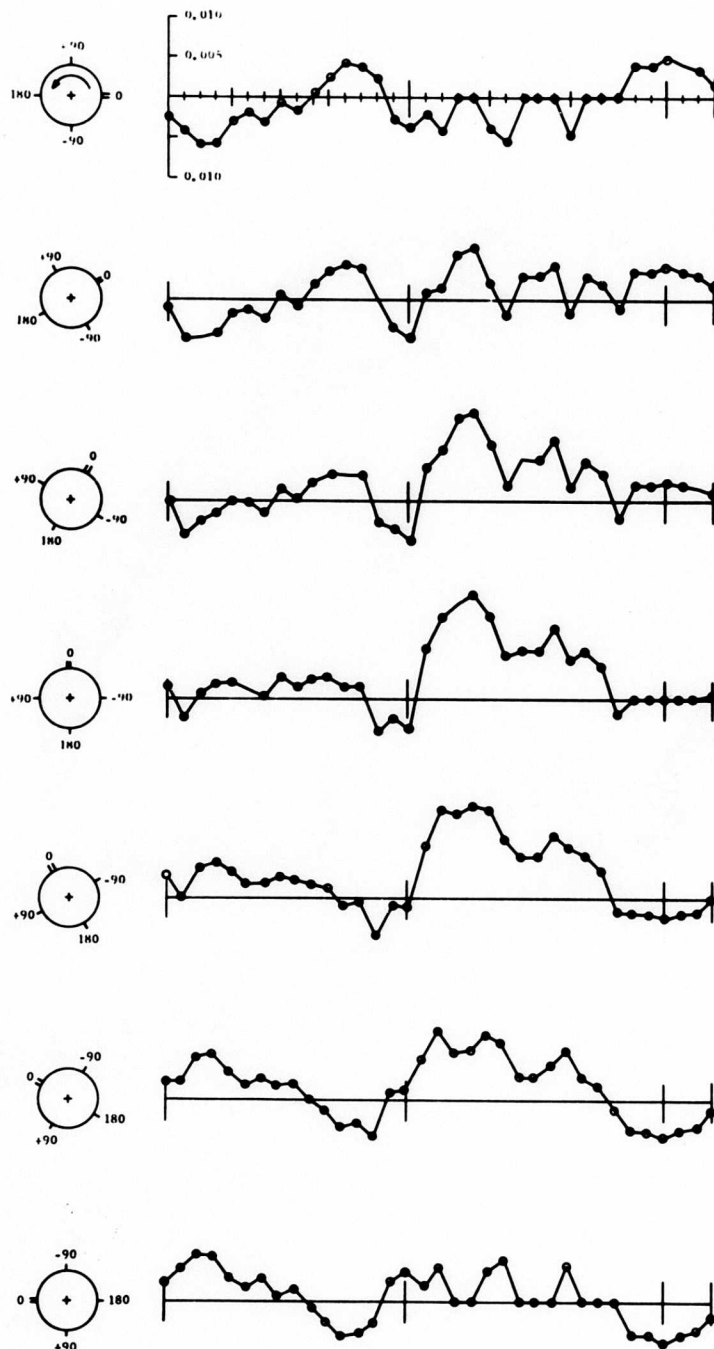


Figure 53. Time History of Initial Deflection for 180 Degrees of Shaft Rotation.

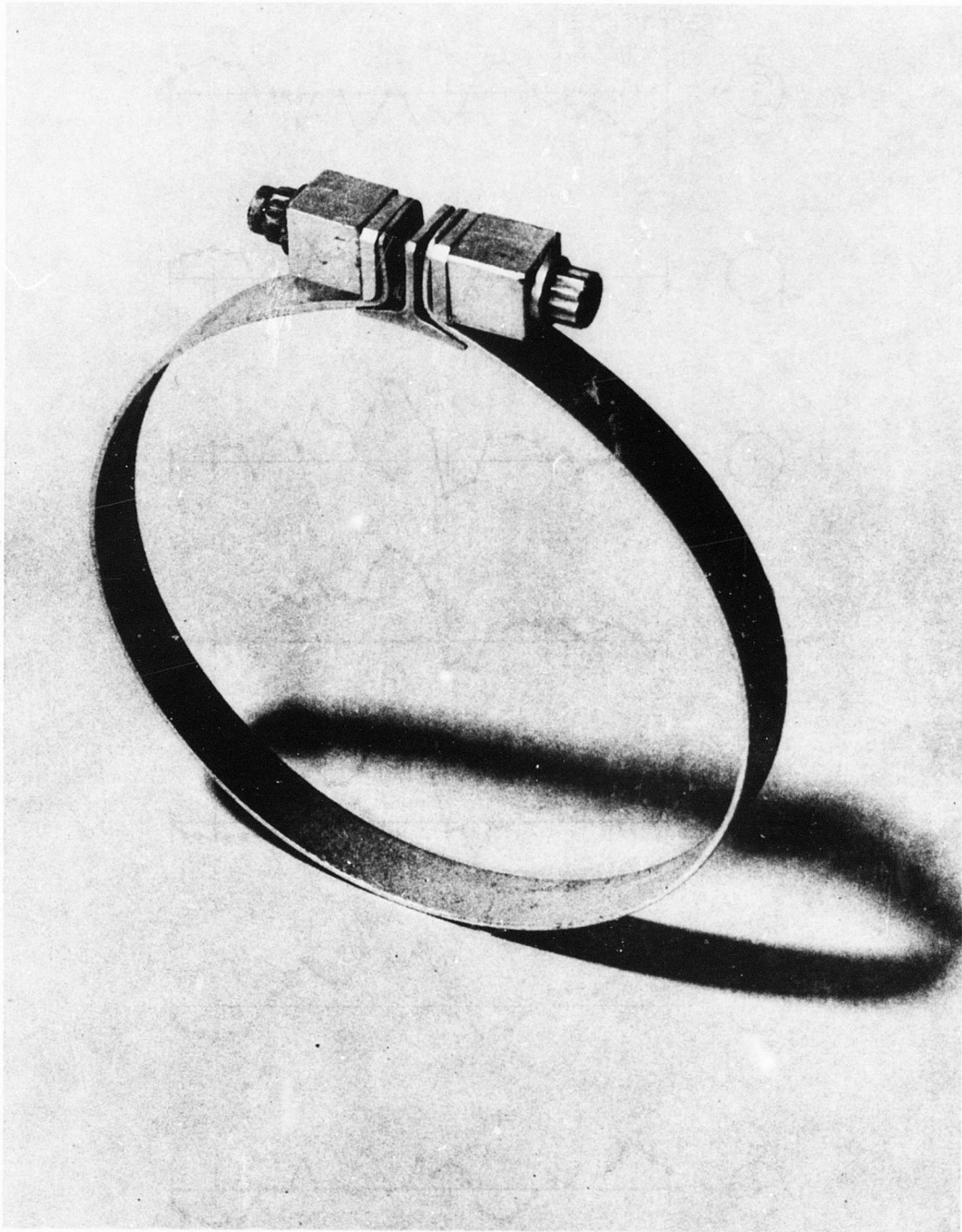
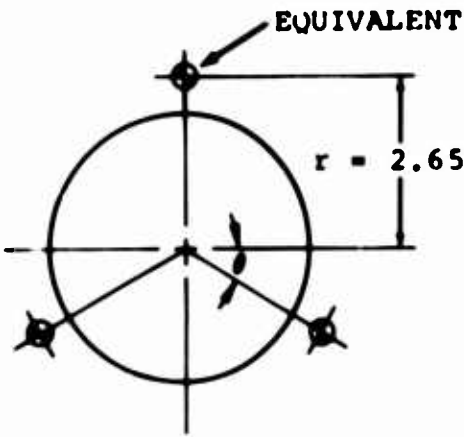


Figure 54. Balance Weight Assembly.

WEIGHT ADDED AT INDEX - GRAMS	SINE θ	ANGLE θ - DEGREES	WEIGHT ADDED AT INDEX - GRAMS	SINE θ	ANGLE θ - DEGREES
2	0.02	1.2	52	0.52	31.4
4	0.04	2.5	54	0.54	32.7
6	0.06	3.5	56	0.56	34.1
8	0.08	4.6	58	0.58	35.4
10	0.10	5.8	60	0.60	36.8
12	0.12	6.9	62	0.62	38.3
14	0.14	8.1	64	0.64	39.8
16	0.16	9.2	66	0.66	41.3
18	0.18	10.4	68	0.68	42.3
20	0.20	11.5	70	0.70	44.4
22	0.22	12.7	72	0.72	46.1
24	0.24	13.9	74	0.74	47.7
26	0.26	15.1	76	0.76	49.5
28	0.28	16.3	78	0.78	51.3
30	0.30	17.5	80	0.80	53.2
32	0.32	18.7	82	0.82	55.1
34	0.34	19.9	84	0.84	57.1
36	0.36	21.1	86	0.86	59.4
38	0.38	22.3	88	0.88	61.7
40	0.40	23.6	90	0.90	64.1
42	0.42	24.8	92	0.92	67.0
44	0.44	26.1	94	0.94	70.0
46	0.46	27.4	96	0.96	73.3
48	0.48	28.7	98	0.98	78.5
50	0.50	30.0	100	1.00	90.0



DERIVATION

$gm\ r = 2\ W\ (\sin\ \theta)\ r$
 $gm\ (2.65) = (2)\ (50)\ (\sin\ \theta)\ (2.65)$
 $gm = 100\ \sin\ \theta$

LEGEND

θ - ANGLE OF BALANCE WEIGHTS

Figure 55. Balance Weight Chart.

with precalibrated strain gages. Under full torque, the breakaway friction of the test machine was so great that the machine could not be started; therefore, the load was applied after the test machine was in motion. The power available is adequate to run the machine under the design torque after the lubricating film is established.

The gearboxes on each end have a 2.3194 stepup ratio through the gears. Each box has an external oil system for lubrication and cooling. The oil system has a reservoir of 50 gallons and operates under 10- to 15-psi pressure. It circulates 30 gallons per minute with up to 100,000 BTU-per-hour cooling capacity ($\Delta T = 20^{\circ} F$). The high-speed shaft is connected to the gearboxes with multiple plate couplings at the end adapters similar to the couplings used to install the shaft in the aircraft. The position of the end adapters can be shifted to simulate axial motions resulting from fuselage deflections in flight and landing conditions.

Power to turn the machine is supplied by a variable-frequency power supply with an output of up to 180 kilowatts, 0.9 pf, at 400 to 600 cycles per second. A manual means of controlling frequency from 5 to 60 cycles per second is provided. Automatic control is provided for the frequency range between 60 and 600 cycles per second. Adjustment steps of 0.5 cycle are possible. Voltage-to-frequency ratio is held constant within a range of plus or minus 0.5 percent. Power output is constant from 400 to 600 cycles per second. The equipment is capable of an output of 150 percent of the rated load for a period of 5 minutes.

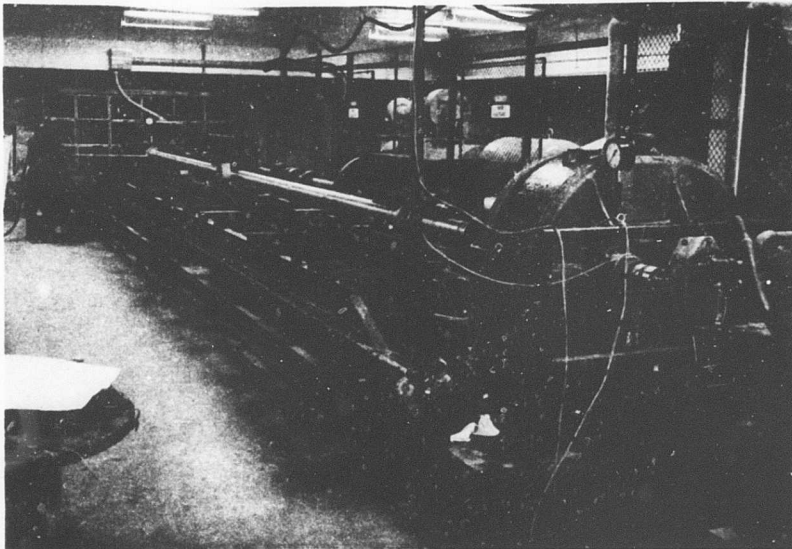


Figure 56. Bench Test Machine.

The supply contains all components, controls, and accessories necessary for operation from a single power input of 2,400 volts (plus or minus 5 percent), 3 phase, and 60 cycle. The power supply consists of two motor generator sets, an ac motor controller, frequency regulation system, voltage regulation system, and miscellaneous control accessories. A 250-horsepower

600-cycle three-phase induction motor that will turn up to 3,950 rpm will drive the test machine directly through the low-speed shaft. The power and speed of this output motor are supplied by the variable-frequency system described above. The high speed test shaft will operate up to 8,300 rpm with 15,000 inch-pounds maximum continuous torque. The adapters are capable of applying up to 0.150 inch compressive deflection at each end.

DAMPER SUPPORTS

Simulated aircraft structure is used to support the dampers in the test machine. Horizontal loads in the aircraft are transferred directly to the crown skin in shear, and this load path is quite rigid. Vertical loads in the aircraft are taken by two stainless-steel beams and thereby transferred to the aircraft frames. This load path is less rigid. To simulate the aircraft structure, the same stainless steel beams are used to support the dampers in the test machine. The ends of the beams are rigidly attached to the structure of the test fixture. The rigidity in the aircraft horizontal plane is simulated by restraining the damper support motion with a flexure at this point. (A flexure will take load in one direction but will allow motion in the other.) The rigidity in the aircraft vertical plane is simulated by allowing the steel beams to carry the load in the same manner as in the aircraft. The flexibility of the aircraft frames has not been simulated.

Figure 57 shows the center damper support with the shaft in place. The vertical direction on the test machine is horizontal on the aircraft.

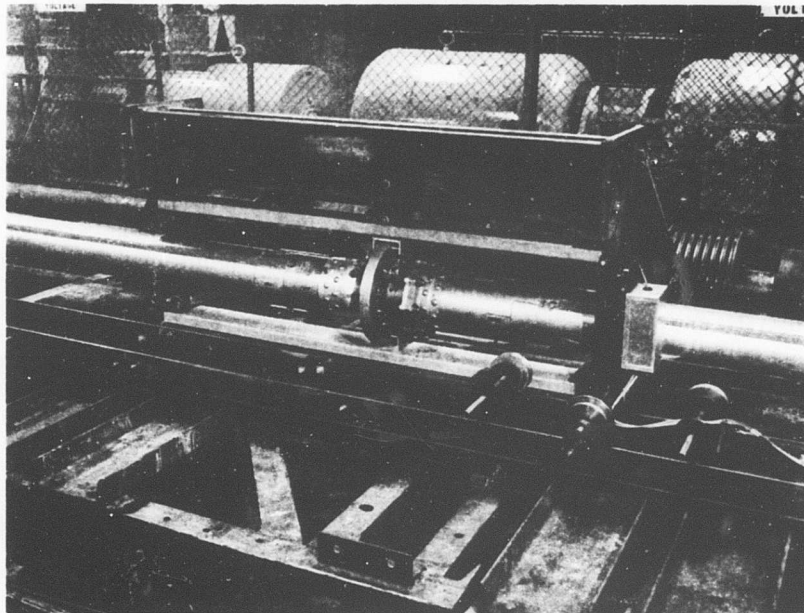


Figure 57. Bench Test Damper Structure.

INSTRUMENTATION

The bench test instrumentation package was constructed to obtain data from the balance and endurance test as well as from the flight test portion of the program. Part of the instrumentation is common to both the bench and flight tests. The recording system was designed to make maximum use of the flight test digital data system.

Data obtained from the bench test program include

- Shaft index or one-per-revolution indication as a sharp blip
- Shaft index or one-per-revolution as a sine wave signal
- Number of revolutions per minute from an electronic counter
- Shaft deflection amplitude from optical pickup locations along the shaft
- Shaft deflection amplitude from a proximity pickup
- Vertical and horizontal center damper motion
- Vertical and horizontal end damper motion
- Inside member and outside member center damper temperature
- Inside member and outside member end damper temperature
- Shaft strain in the 0/180 degree and +90/-90 degree planes at stations
4, 15, 17, 31, and 32
- Shaft torque at station 34
- Strain gage data for orbiting end load magnitude and phase

The recording system for the bench test was a fourteen-track tape recorder, the same system can be used for the aircraft test. A narrow-band direct-recording technique was used. Twelve data channels were multiplexed to each magnetic tape direct-record track. Solid-state voltage-controlled oscillators and wide-band record amplifiers were used in the multiplex. Millivolt-controlled oscillators were used in place of voltage-controlled oscillators where transducer output levels were compatible. A wide-band frequency modulation recording technique recorded parameters that controlled coordination of data between narrow-band channels. The output of Wheatstone Bridge type transducers (strain gages) was conditioned through balance modules and amplifiers. The amplifiers were eliminated where output levels were sufficient to drive millivolt-controlled oscillators. An automatic standardization system was incorporated into the instrumentation system. This system was required to coordinate bench, aircraft, and ground station sensitivities and to correct for system drift during testing. Time code correlation was prerecorded on the tape. An oscillograph record was used for detail interpretation and analysis during part of the bench test program. An X-Y plotter was used to display and record amplitude versus rpm during the balance tests. An oscilloscope was used for monitoring purposes.

List of Instruments

Accelerometers	Piezo Electric - Endevco 2272
Accelerometers	Unbonded wire - Statham A5-2-350
Amplifiers dc	NEFF model I-200 or equivalent
Amplifier rack	NEFF model I-005 (6 channel or equivalent)
Strain gage power supply	NEFF model 2-302

Voltage controlled oscillator	Sonex model TEX3095HC
Summing amplifiers	Sonex model TEX 3295H
Mounting chasis for VCO's	Sonex model TEX 4095HS
Reference oscillator	Sonex model TEX 3495H
Magnetic tape transport	Ampex with electronics
Balance panel conditioner	24 channel B & F
Charge amplifier	Endevco model 2640
Low pass filter	UTC - LPM 200
Record coder	Record identification
Pulse shaping network	Data correlation
Standardization system	Vertol Division
Transducer	Electro 721856
Optical pickup	Vertol (shaft deflection)
Optical pickup	Vertol (shaft index - sine wave)
Magnetic pickup	(Shaft index - sharp blip)
Proximity pickup	Wayne-Kerr DM 100
Electromagnetic shaker	Calidyne Manufacturing Co. model 44
Phase meter	ACTON Lab Inc. model 320 AB
Oscillograph	Consolidated Electrodynamics Corp. model 5-124
X-Y plotter	F. L. Mosley Co. model 2 DR
Temperature recorder	Barber-Colman Co. series 8000
Oscilloscope	Tektronix Dual Beam type 502

Optical Pickup

A number of methods were available to determine the performance of the shaft. Deflection was the most apparent method, and a system was developed to monitor the amplitude of the deflected loops on the shaft without touching or disturbing the surface. An optical system was used wherein a shadow of the shaft fell on a light-sensitive element of a solar cell. The solar cell was substituted for the photocell used in the previous program, because the solar cell permitted the use of solid-state elements in the circuit. The position of the shaft determined the amount of light striking the cell and changed the voltage in the system. The change in voltage was calibrated by using a micrometer to move an obstruction across the light beam and throw a shadow on the solar cell element. The shadow simulates shaft displacement. Figure 58 shows a chart of calibration response and a schematic of the electronic circuit used. The optical pickup unit (see Figure 59) was mounted on a track located parallel to the test shaft so that it could traverse the full length of the shaft and define the mode shapes by measuring the deflection amplitudes as it progressed. The phase of the deflection can be obtained by comparing the phase of the deflection signal with the phase of the index signal from the end of the shaft.

TEST PROCEDURE

The test program covers two general areas: a forced response shape and frequency check, and the balancing of the shaft.

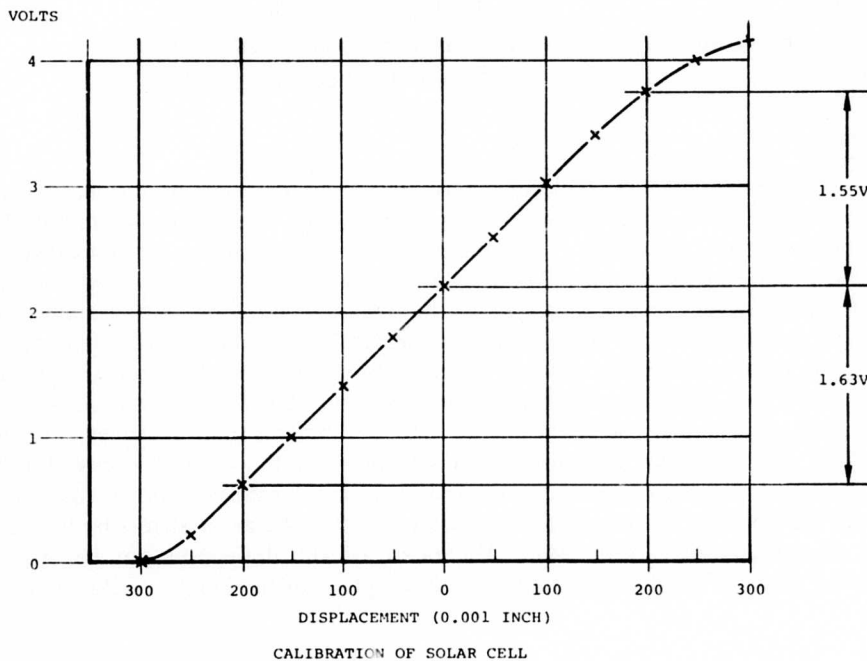
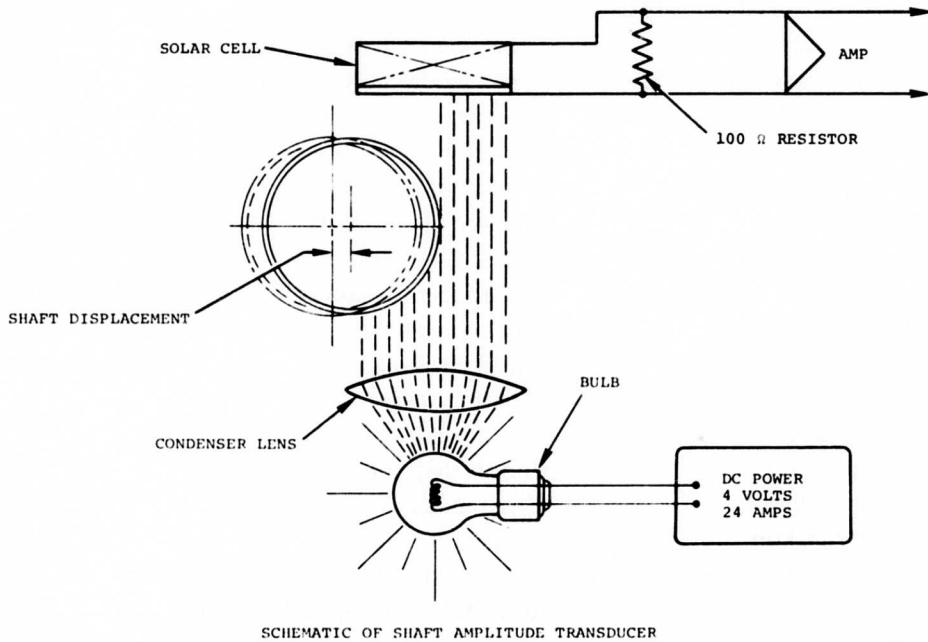


Figure 58. Schematic and Calibration of Solar Cell Transducer.

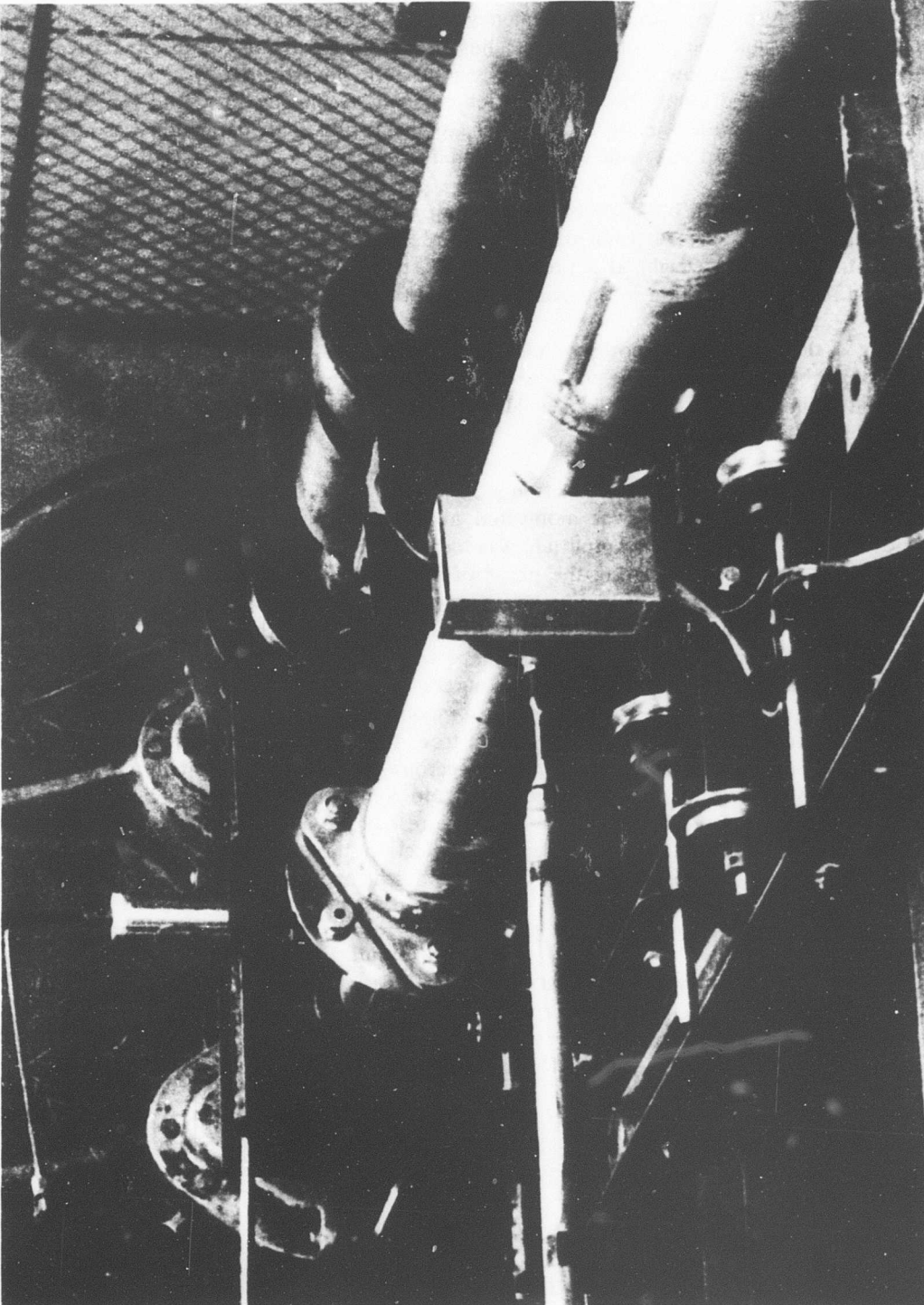


Figure 59. Optical Pickup Trolley.

For the forced response shape and frequency check, the test specimen was excited in a horizontal plane and the frequency was adjusted until a resonant condition existed. All resonant frequencies below 150 cycles per second were investigated. The optical pickup instrument was moved along the track at each resonant frequency to record the deflected shape. Phase between the forcing function (shaker load) and shaft deflection was noted by phase meter as the record was made of the deflected shape.

Before any rigid shaft can be balanced, the amount of unbalance present and the position of the unbalance must be determined. A standard shaft can be balanced by adding a compensating (balance) weight at a predetermined station and adjusting the amount of the weight and its angular position so the mass center and the geometric center coincide.

Balancing a flexible shaft is more complex than balancing a rigid one, but the same basic factors must be considered. The purpose of these tests was to reduce the reaction to the structure to a minimum by applying balance weights so that the mass center and the geometric center coincide.

The phase and amplitude of shaft deflection were measured and this information related to the unbalance. Shaft performance was monitored in different ways; the instrumentation used depended on the way selected. Amplitude was measured by the optical or proximity pickup. Phase was measured by comparing the phase of the signal in question with the phase of an index signal. End load was measured by strain gages on the restraining links at the end bearing support. Shaft bending was obtained directly from strain gages on the shaft or by calculations using shaft deflection measurements. Mode shape was obtained by measuring magnitude and phase of deflection at various shaft stations along the length. Damper motion was read directly from accelerometers mounted to the damper components in two planes and from optical or proximity pickup instruments. The information from these signals was compared and used to generate other data useful to the program. Dangerous operation is associated with excessive deflection, loads, stresses, motions, temperatures, etc. Safety limits were established for these areas, and the limits were not exceeded during the test. Since deflection is the most apparent indication of shaft performance, the acceptable deflection limit, as related to bending stress in the shaft, was calculated for various speeds and modes of operation.

Estimated Critical	Approximate cps	Approximate rpm	Limit Deflections Measured at Station 4 (inches)	Orbit End Load (pounds)
2nd	22.5	1,350	0.159	118
3rd	36.0	2,160	0.110	118
4th	48.0	2,880	0.094	153
5th	93.0	5,580	0.059	203
6th	125.0	7,500	0.044	236

Figure 60 is a standard format for presenting deflection data versus rotational speed. a limit deflection line is included as a guide and safety factor. This figure also shows the end load limit line versus rotational speed. The limit line for deflection and load was calculated using 2,500 psi shaft bending as the criterion. The derivation of limits is explained in the stress section.

The specimen was installed in the machine for the test, and the appropriate instrumentation was activated. The speed of rotation was controlled and the performance monitored. If the shaft performed within limits, the speed was carefully increased. The test was discontinued when any of the monitored signals reached a preestablished limit. Test data and balance theory indicated the position and magnitude of the balance weights. The test was continued to gather more data and improve performance until satisfactory operation was demonstrated.

Mode shape data is a necessary part of the program, and the test procedure was modified slightly to obtain it. When mode shapes were desired at specific speeds, the shaft speed was held constant, and the deflection was recorded by moving the optical pickup from one end of the shaft to the other. The nodes and antinodes were apparent on the plot of amplitude versus shaft station. Phase was obtained by comparing the phase of the deflection signal with the phase of the index signal. the same technique was used for determining phase as was used for the amplitude versus rpm investigation.

TEST RESULTS

This section deals with the vibrated response of the dynamic system. The shaft was installed in the test machine with the flexible plate couplings at each end and with the dampers acting. A dynamic shaker applied force at shaft station 4 in a horizontal plane, and the response of the shaft was then measured. Figure 61, a plot of a frequency sweep with the response at the shaker input position, indicates the calculated natural frequencies and the operational speeds of the system.

A phase meter was used for the signals of shaker motion and force. A resonant frequency is indicated when these two signals are separated by 90 degrees. A 90-degree phase difference did not occur at each critical as expected, which made determining resonant frequencies difficult. The frequencies used for mode shapes were selected when the phase most nearly approached the 90-degree position.

Figure 62 shows the forced response along the length of the shaft. The envelope for these diagrams was obtained by measuring the alternating signal from the optical pickup instrument as it moved the length of the shaft. The frequency and phase of the force-motion signals appear opposite each diagram. The solid line shows a probable mode shape.

Shaft serial number 2, manufactured with the bend shown in Figure 49, was placed in the test machine. The instruments and controls were checked out, and the amplitude was monitored by watching the signal width displayed and recorded on the oscillograph tape. Figure 63 shows the results of the first attempt to run the shaft through a critical speed. The test was discontinued when the amplitude exceeded the established limit or 2,500 psi bending stress. Balance weights would have to be added. The phase on this diagram at 1,200 rpm is 90 degrees. This speed is below the calculated critical, and it is assumed the phase will shift rapidly as the critical is approached. The phase angle is assumed to be +55 degrees when the

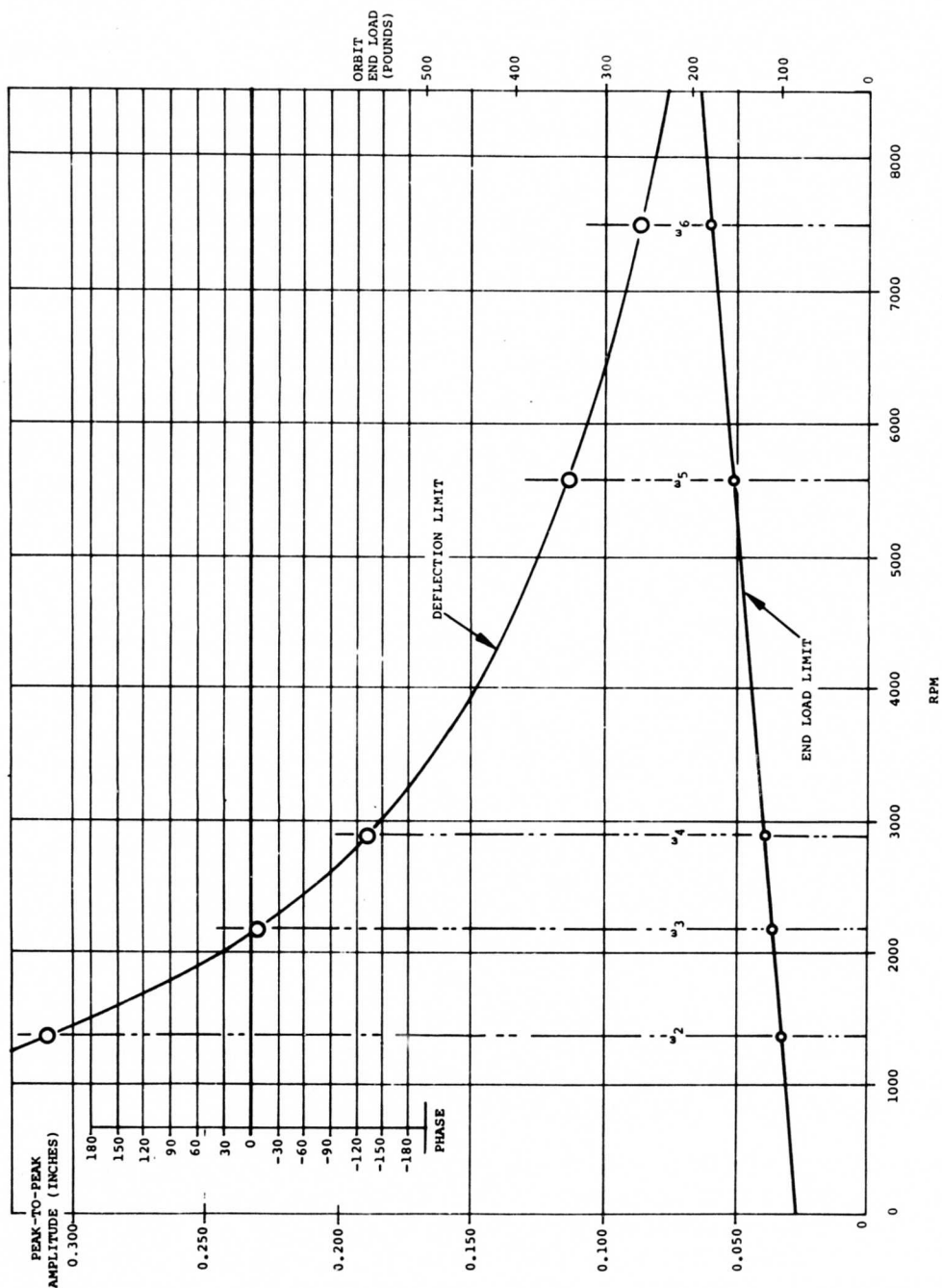


Figure 60. Standard Format for Presenting Deflection Data Versus Rotational Speed.

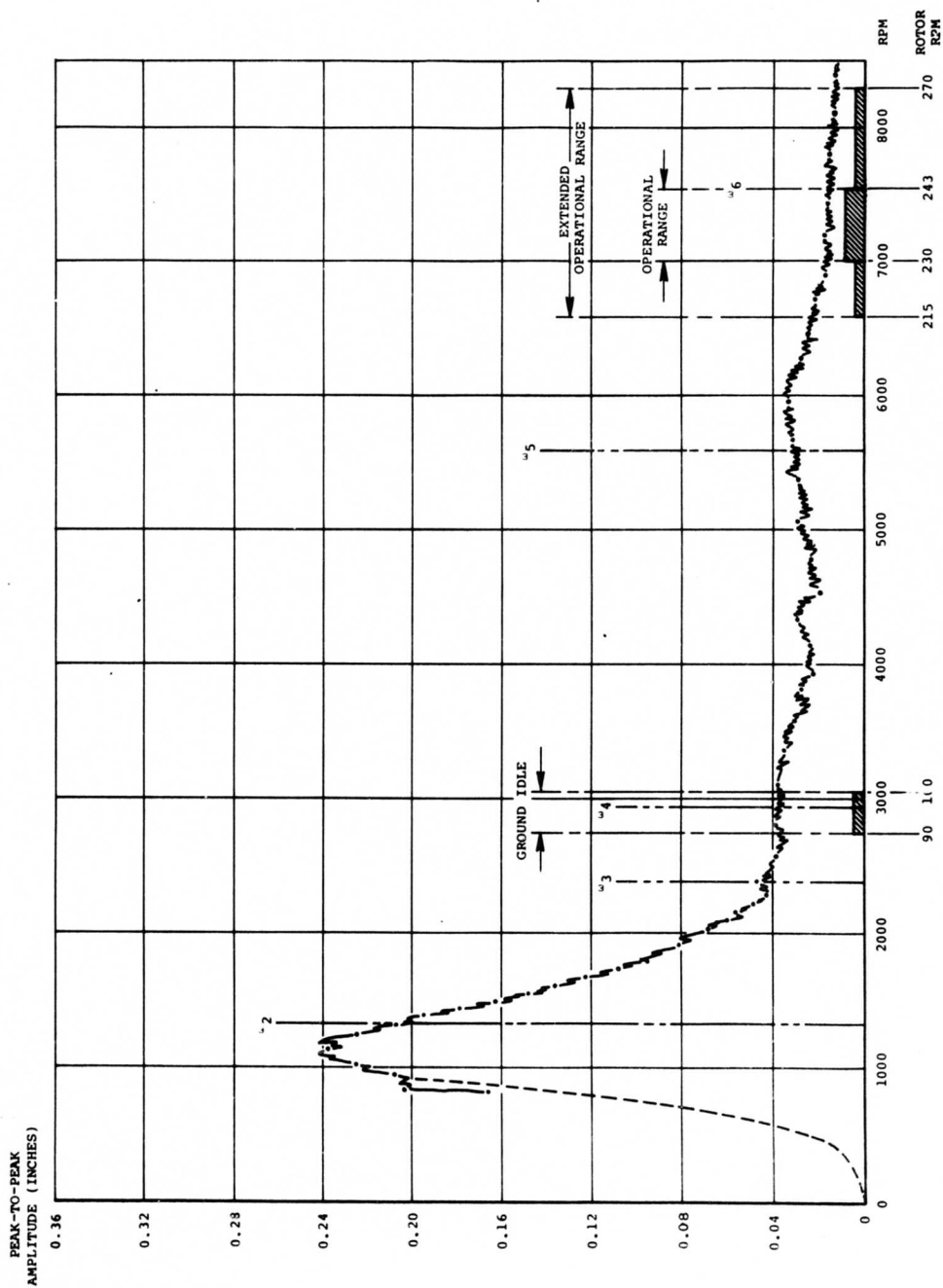


Figure 61. Displacement Versus Frequency (Vibrated).

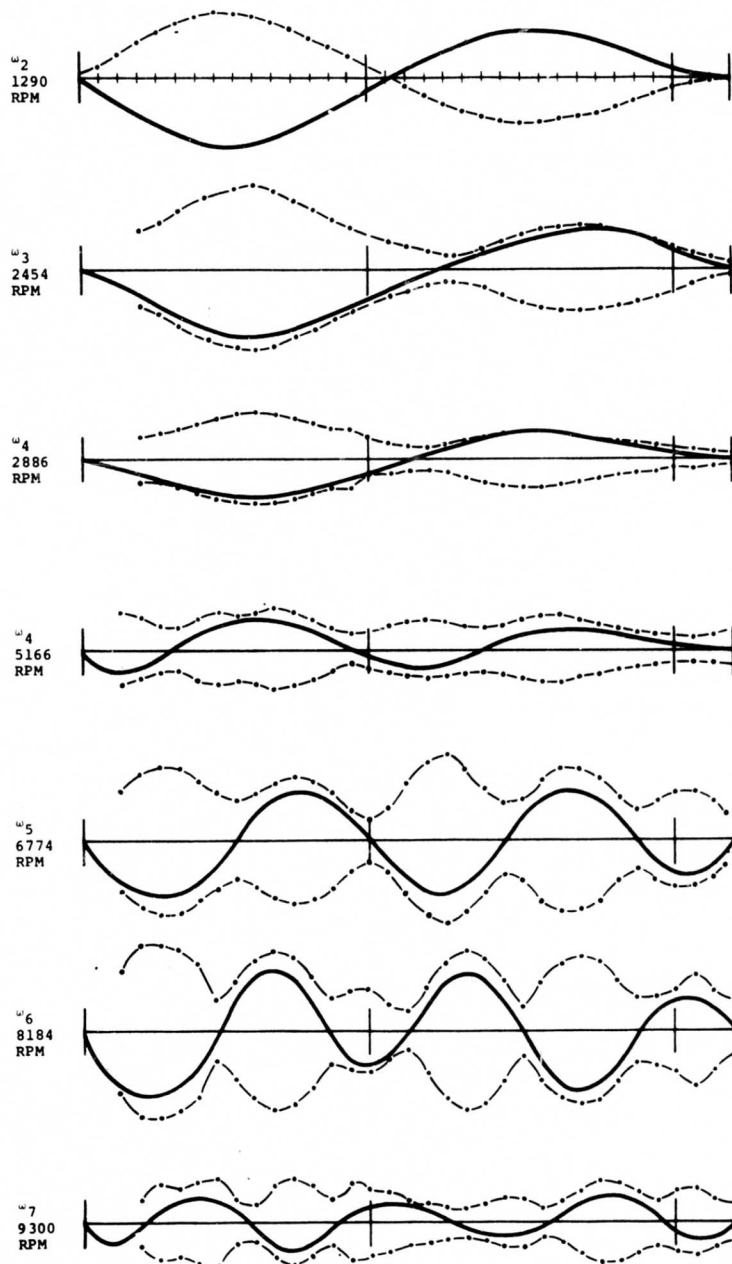
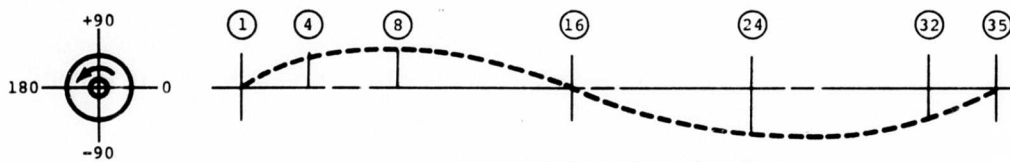


Figure 62. Vibrated Mode Shapes.



DEFLECTION AT SHAFT STATION 4

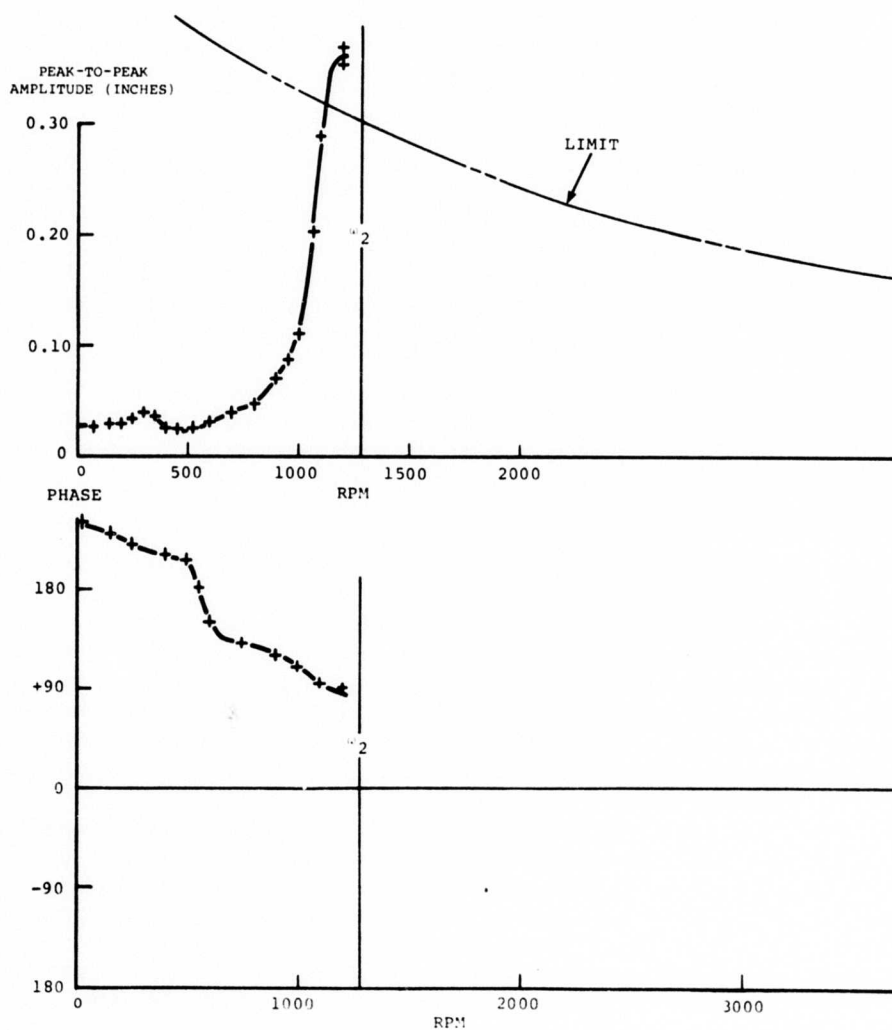


Figure 63. Test 5 - No Balance Weights - Serial 2.

speed of rotation reaches the calculated or resonant frequency at 1,290 rpm. Experimental balance weights were therefore placed 90 degrees behind this phase. Balance weights of 10 grams were installed at station 8 and station 24 to observe the effect on shaft performance. The small improvement noted indicated that much larger balance weights would be required. They were arbitrarily increased to 100 grams each.

Figure 64 shows the first run to pass the second resonant frequency at 1,290 rpm. Data from other instrumentation gathered during the test run are plotted along with the deflection to show the general relationship of data from various sources. The damper motion can be determined from the lateral acceleration of the damper body and the structure. It is possible to calculate the damper load by applying the known damping coefficient to this motion along with the frequency. A damping coefficient of 18 pounds per inch per second was used in plotting the points.

Weights were installed according to the analytical balance approach developed under the previous test program using the vibrated mode shapes (see Figure 62). The shaft was not balanced well enough to pass the second critical speed with this approach (see Figure 65). A comparison of the balance weights, as suggested by the computer program, with those found to be successful by use of the experimental approach indicates that the weight at station 8 is at an incorrect angle to correct the deflection. The input data were reviewed, and a further attempt at balancing the shaft using the analytical approach was made later.

A series of runs was made with the two 100-gram weights located at various phase angles. The weights at station 8 were placed 180 degrees opposite the weights at station 24 for each test. Figure 66 is a plot of amplitude versus frequency for a number of test runs where the angle of balance weight has been changed. It is apparent which angle produces the best performance—minimum deflection.

Figure 66 contains an overlay of a series of tests which contained weights from 150 to 300 grams distributed equally at the antinodes of the second critical mode and positioned at the best angle found in the previous test series. Selecting the best angle for a balance weight through a series of runs where the angle has been the variable and then optimizing the amount by a series where the weight is the variable is typical of the approach used for improving the performance of the supercritical-speed shaft. The rationale used for this approach to balancing is that the deflection in the shaft occurs 90 degrees behind the unbalance (forcing function) at the critical speed and that the mode shape is the same as predicted by the calculations.

A series of tests was run to investigate the most effective distribution of weights between the balance planes. First, the weights were proportioned and placed opposite the initial bends. Next, the weights were proportioned according to the initial bends but placed at the optimum angle as determined by tests. Then the weights were equally divided between the stations and placed at the optimum phase angle as determined by dynamic deflection under test conditions. Weights placed by this system produced the best results across the speed range tested. Further tests were conducted on analytically determined balance weights. The weights calculated by the analytical approach failed to balance the shaft.

Figure 67 shows deflection at -170 degrees at station 4 when the speed reached 5,200 rpm.

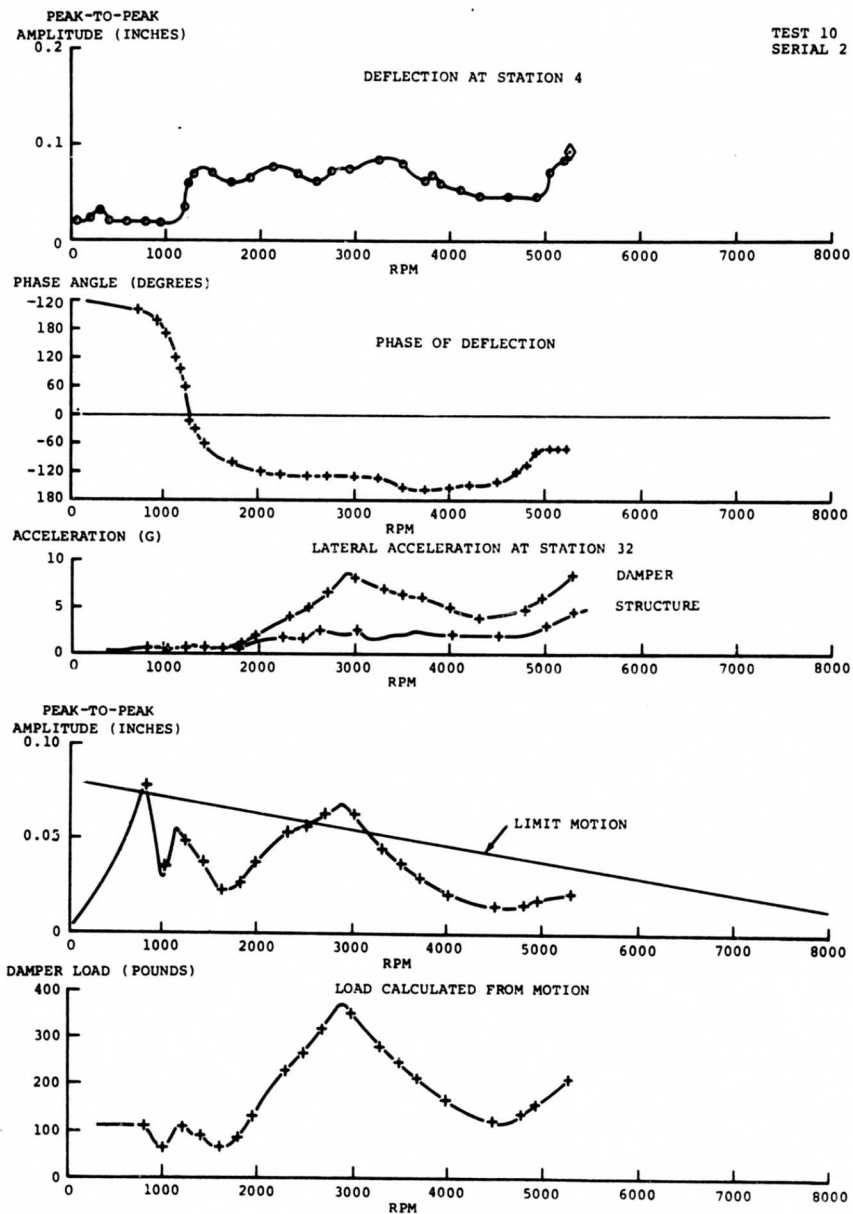


Figure 64. Summary Data From Test 10 With Balance Weights - Serial 2.

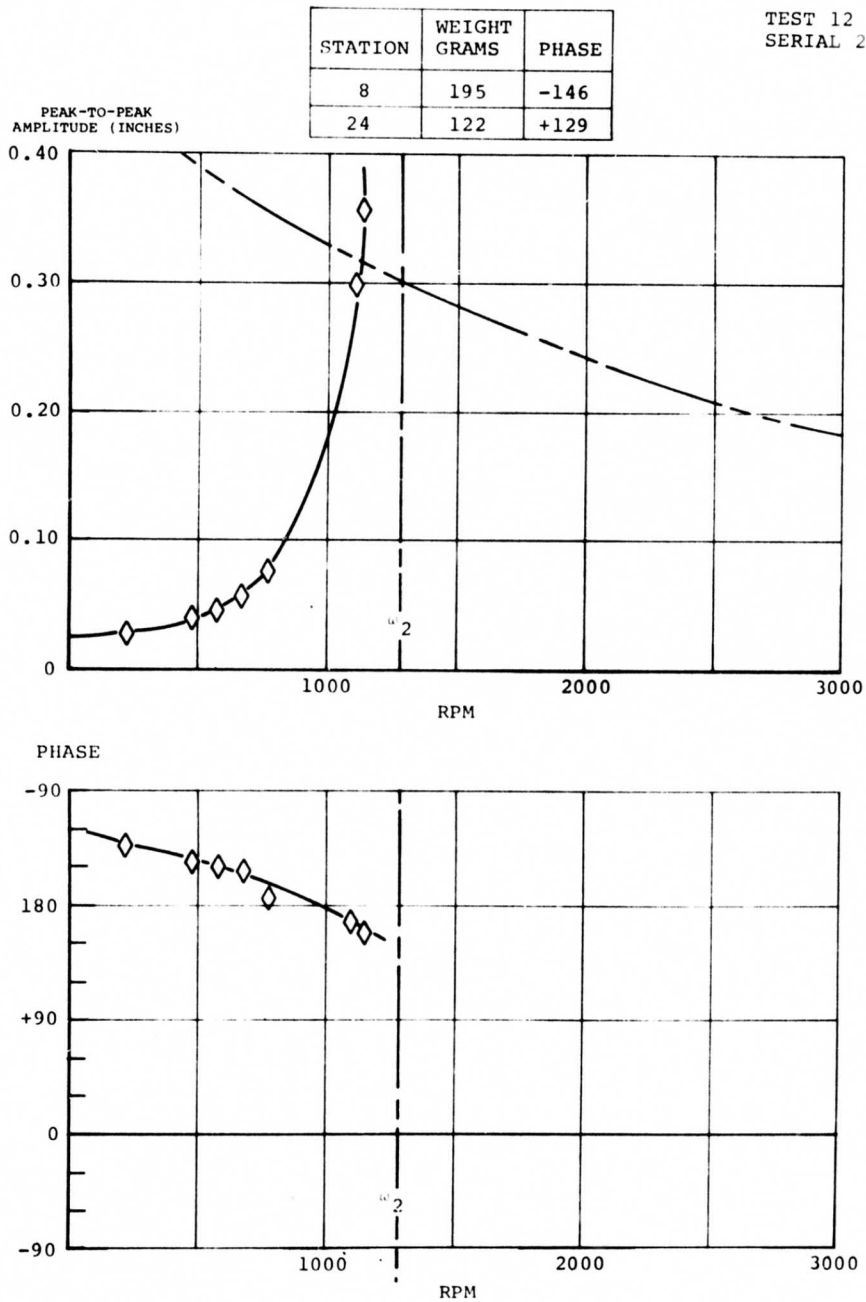
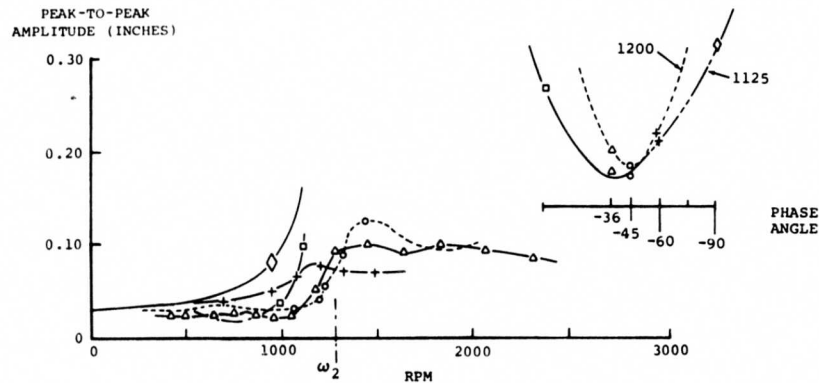


Figure 65. Test 12 - Calculated Weights - Serial 2.

VARIABLE PHASE CONSTANT WEIGHT

SYMBOL	TEST RUN	STATION 8		STATION 24	
		WEIGHT	PHASE	WEIGHT	PHASE
Δ	10	100	-36	100	144
\square	17	100	0	100	180
\circ	18	100	-40	100	135
+	19	100	-60	100	120
\diamond	20	100	-90	100	90



VARIABLE WEIGHT CONSTANT PHASE

SYMBOL	TEST RUN	STATION 8		STATION 24	
		WEIGHT	PHASE	WEIGHT	PHASE
+	19	100	-60	100	120
\square	23	150	-60	150	120
\diamond	24	125	-60	125	120
\circ	24	75	-60	75	120

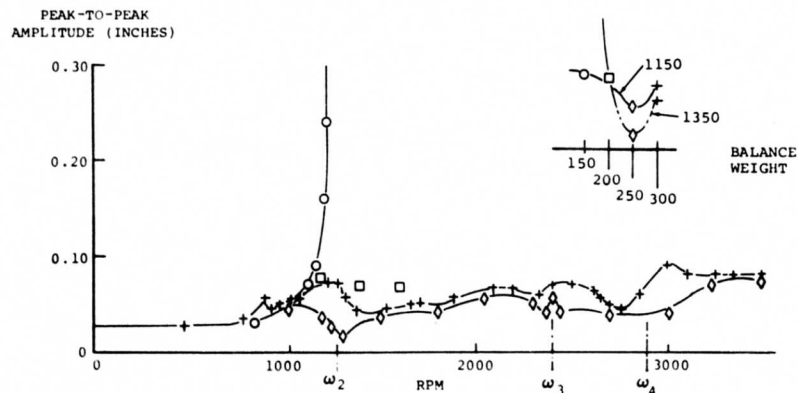
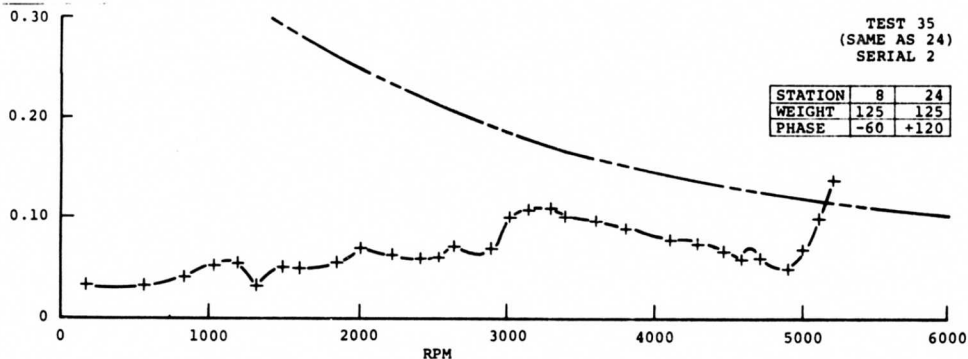
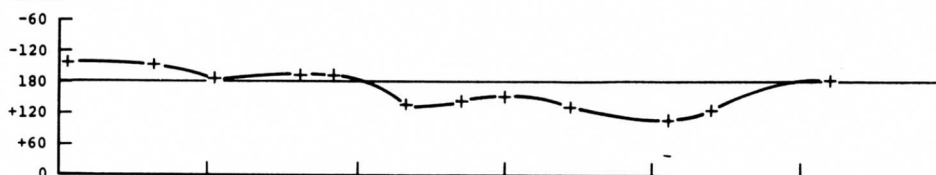


Figure 66. Optimum Phase and Weight.

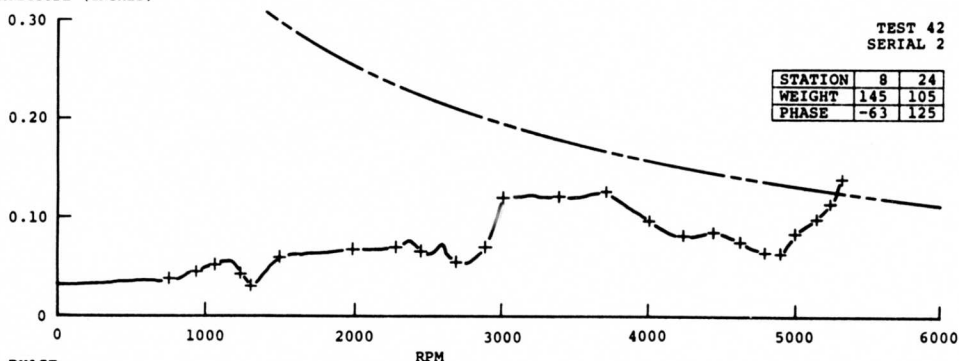
PEAK-TO-PEAK
AMPLITUDE (INCHES)



PHASE



PEAK-TO-PEAK
AMPLITUDE (INCHES)



PHASE

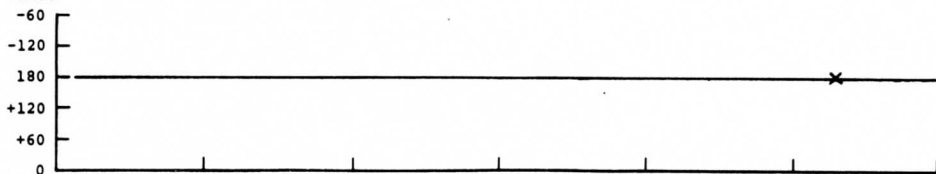


Figure 67. Test 35 and 42 - Serial 2.

With the mode shape in Figure 68, fourth-secondary 5,166-rpm deflections at stations 8 and 24 would be +10 degrees. Balance weights should therefore be placed 90 degrees behind the deflection, or at -80 degrees on both stations. Adding 20 grams at stations 8 and 24 and then adding vectorially to obtain the new angles and new weights for the test in Figure 67 gives 145 grams at -63 degrees and 105 grams at +125 degrees.

Results show the same angle and about the same amplitude at 5,200 rpm as before adding the weights. This is improbable with this much weight (40 grams). If the mode shape is correct, 40 grams would have a tremendous balancing effect. However, if the mode shape is reversed on the aft portion of the shaft as shown in Figure 69, the weight at station 8 will counteract the weight at station 24, and the result will be no change in shaft performance at this speed. Therefore, the mode must be different from that shown in the first figure.

In subsequent tests, with balance weights located according to the revised mode shapes, the shaft responded by changing phase and amplitude as expected. This information points to the need for more accurate mode shapes.

A summary plot, Figure 70, was made of test 35 in Figure 67 for comparison with the summary from test 10 in Figure 64. The summary plot shows the damper load to be excessive at several places.

The damper at shaft station 32 failed at 5,200 rpm during the test as shown in Figure 71. Shutdown was accomplished with the center damper providing control of the shaft. No damage was visible on the exterior surfaces of the damper. The only indications of failure were the performance of the shaft and an oily residue left by the damper fluid. Shaft amplitude at the second critical went beyond the allowable value on shutdown. After the failure, the shaft was again accelerated carefully, and when the amplitude approached the limit near the second critical, the test was discontinued (see Figure 71). The conclusion was that the damper characteristics had changed, and the damper was removed for careful inspection by the manufacturer. The unit demonstrated no measurable damping when placed on the damper test machine. The elastomer had failed, allowing damper fluid to escape to the atmosphere (see Figure 72). Upon disassembly, a failure of the diaphragm making up the dual chamber was also noted (see Figure 73). A small screw was placed in the break in the diaphragm to separate the parts for the photograph.

Investigation was directed to find a reason for the failure. The running time for each test was not over a few minutes, and the total time on this particular part was only a few hours at most. The endurance run on the damper (a separate test of the damper alone) had just been completed; the damper was tested at top speed for over 24 continuous hours. Therefore, our test conditions must have been more severe. Motion in excess of that designed for the dynamic system was present at the damper (see Figure 64). The initial bend (crank effect) of the shaft as manufactured caused a working of the damper elastomeric sections, and to eliminate this undesirable condition, the shaft had to be straightened. Figure 49 gives runout measurements made of the original shaft assembly as manufactured (serial number 2). However, no measurements were made of the motion at the damper stations. Figure 50 gives runout measurements made of the same shaft after straightening (serial number 2A). It should be noted the runout was still present at the damper positions (0.016 and 0.028 respectively), but it was decided to test this configuration since the balance procedure should normally tend to reduce the runout.

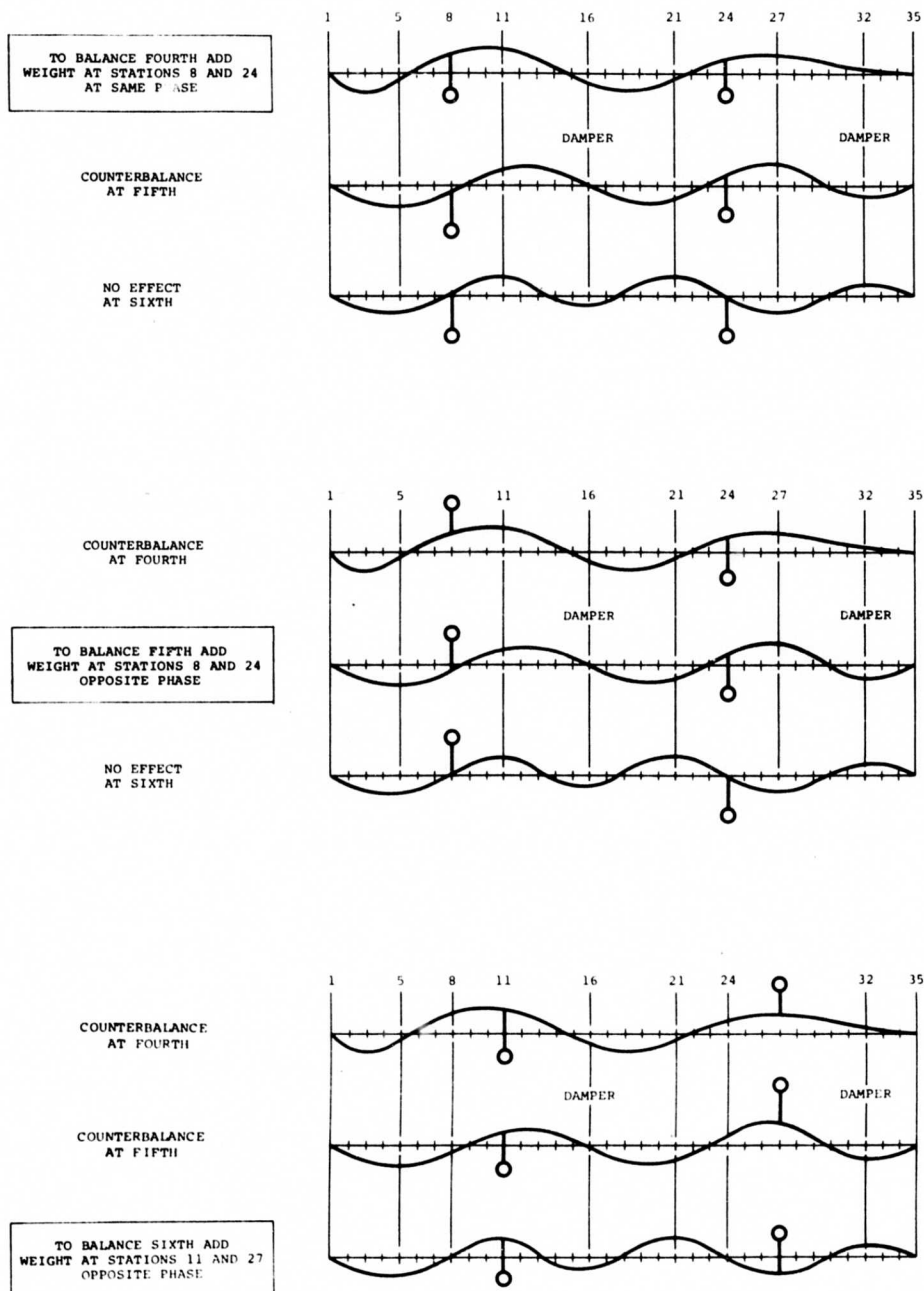


Figure 68. Initial Mode Shapes for Balance Purposes.

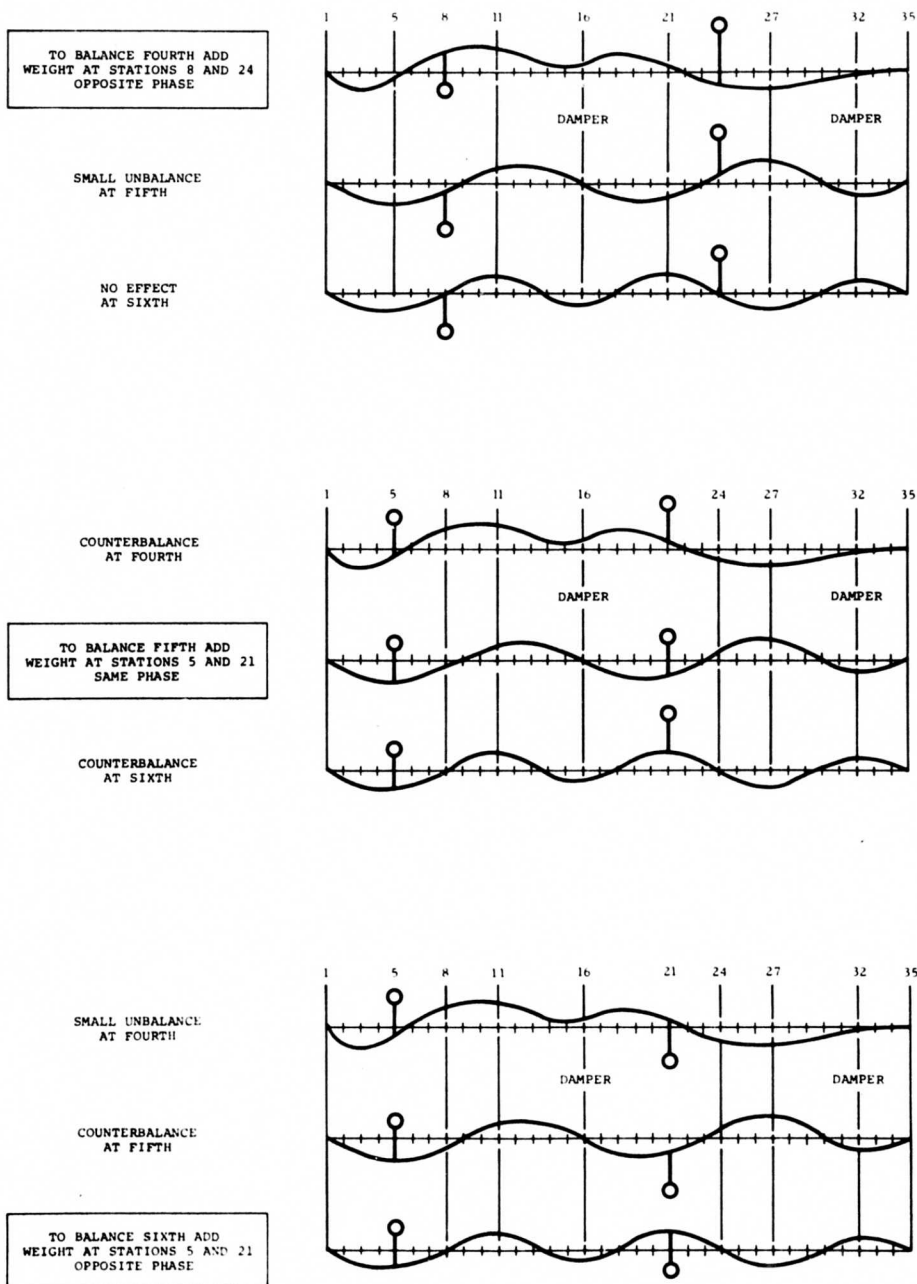


Figure 69. Revised Mode Shapes for Balance Purposes.

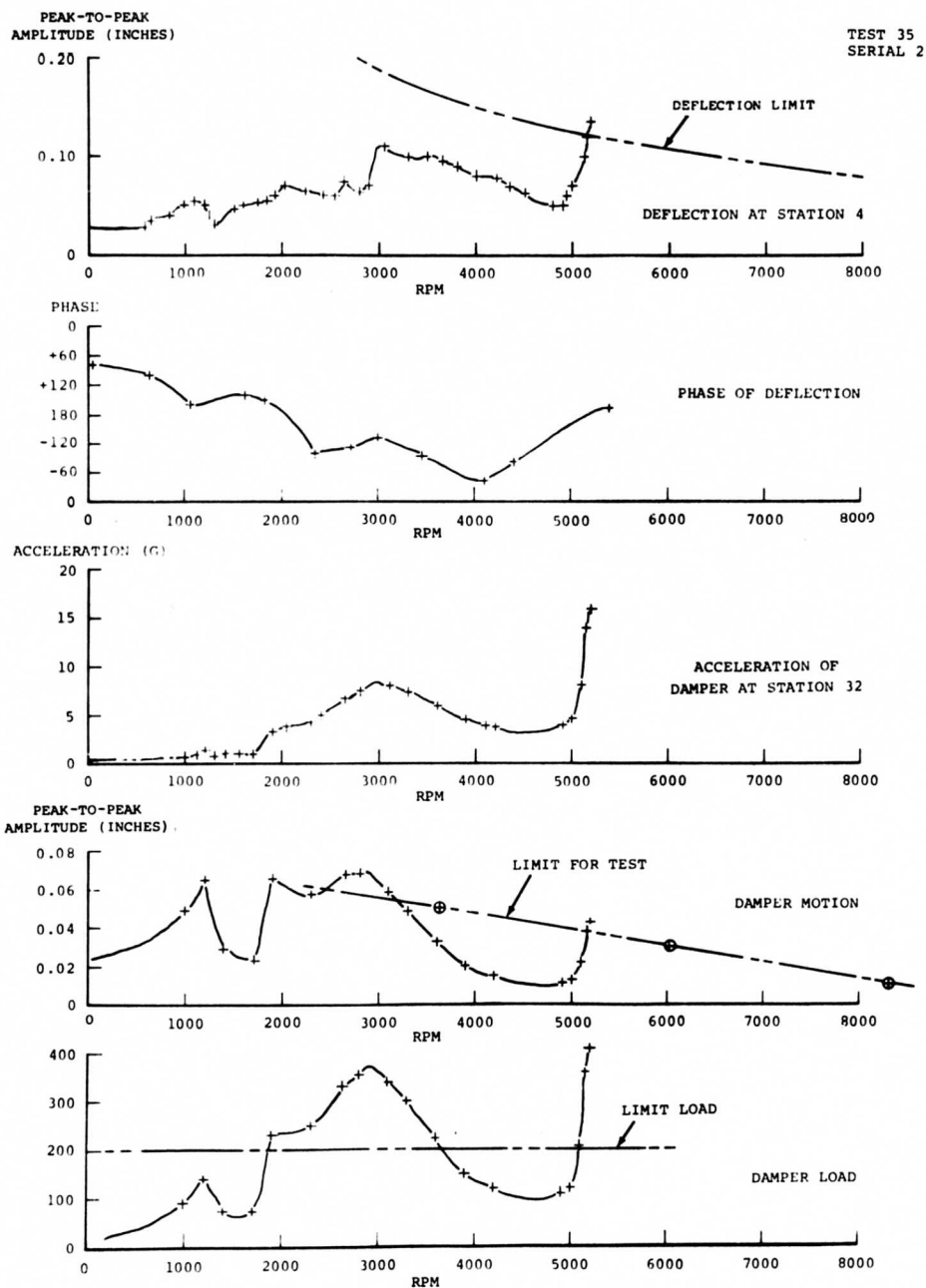


Figure 70. Summary Data From Test 35 - Serial 2.

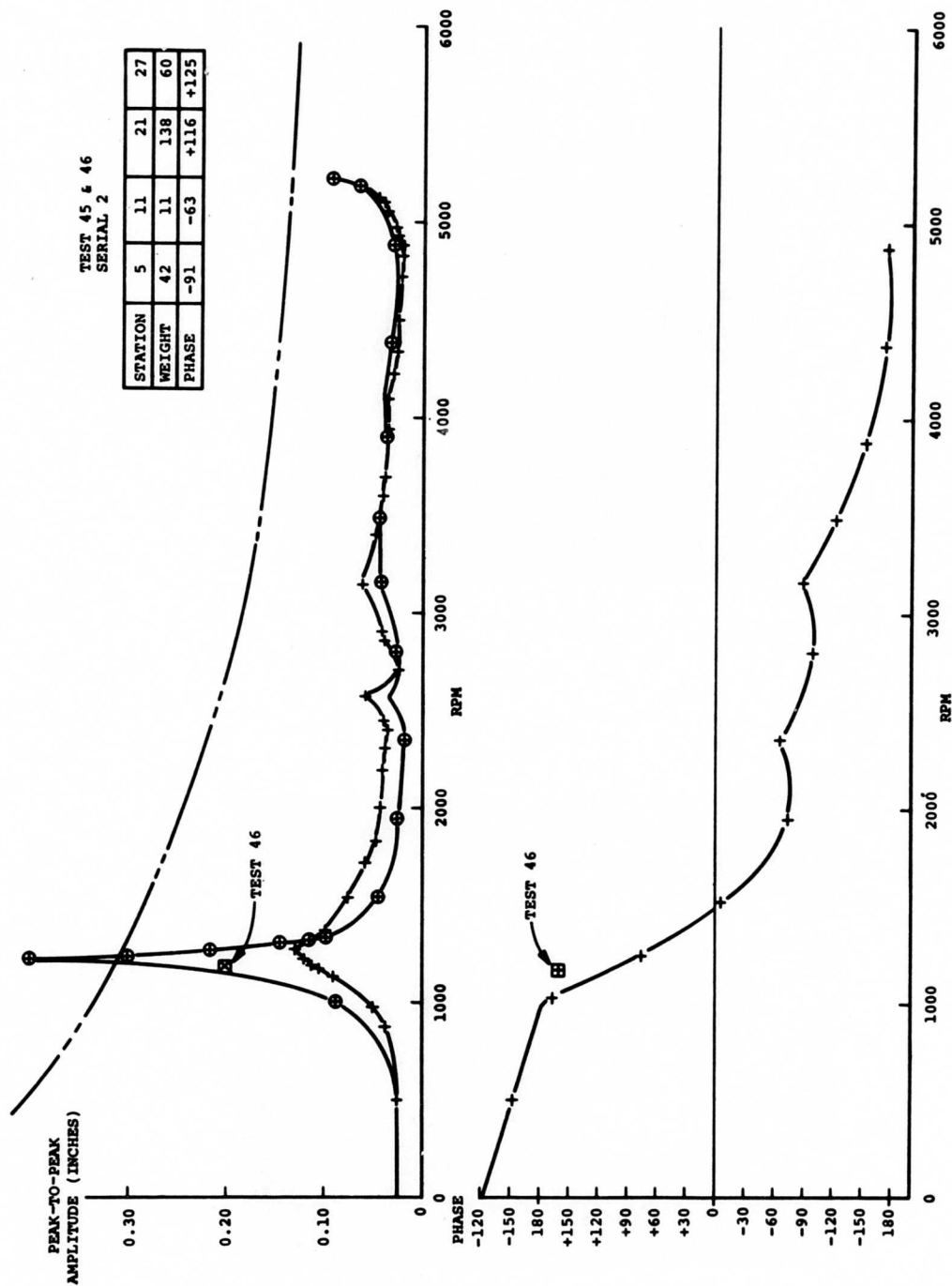


Figure 71. Tests 45 and 46 - Serial 2 (Damper Failure).

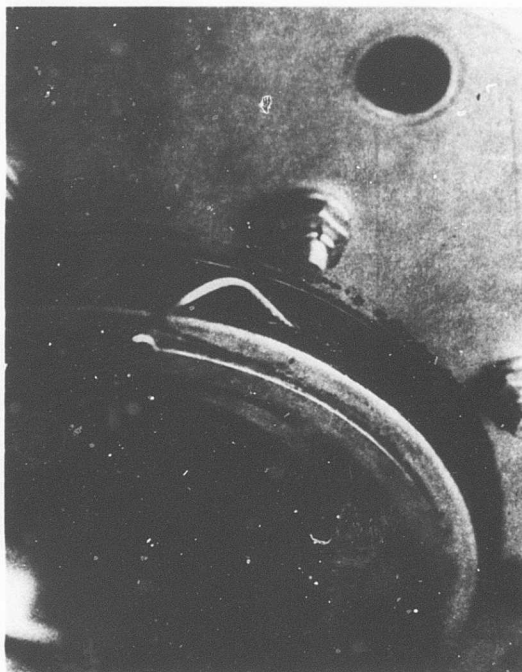


Figure 72. Damper Failure - External.

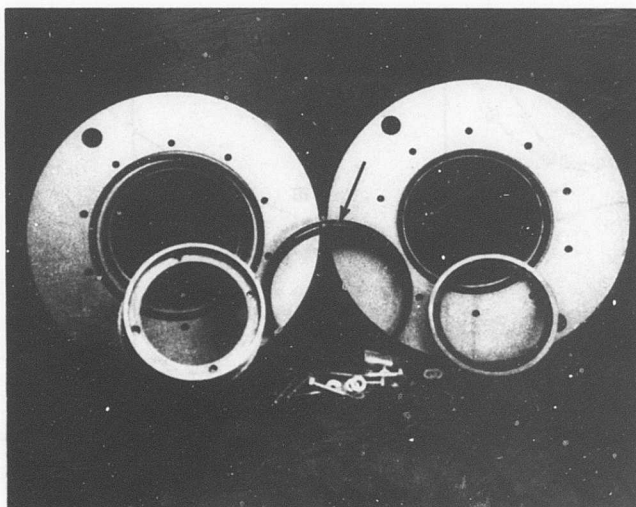


Figure 73. Damper Failure - Internal.

A spare damper was installed, the shaft was assembled, and the tests continued. The series of tests to check the instrumentation with the straightened shaft (serial number 2A) and to balance the second critical speed of this new configuration followed. The series of tests in Figures 74 and 75 covered an attempt to balance the shaft to run through 5,300 rpm, which proved to be a very troublesome fifth critical speed.

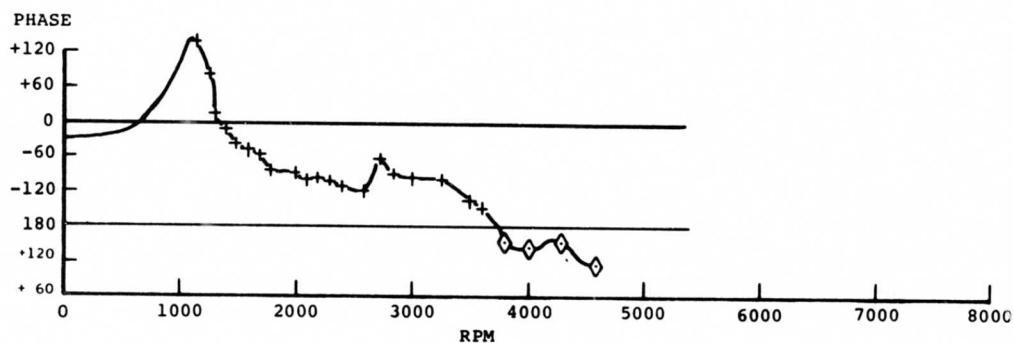
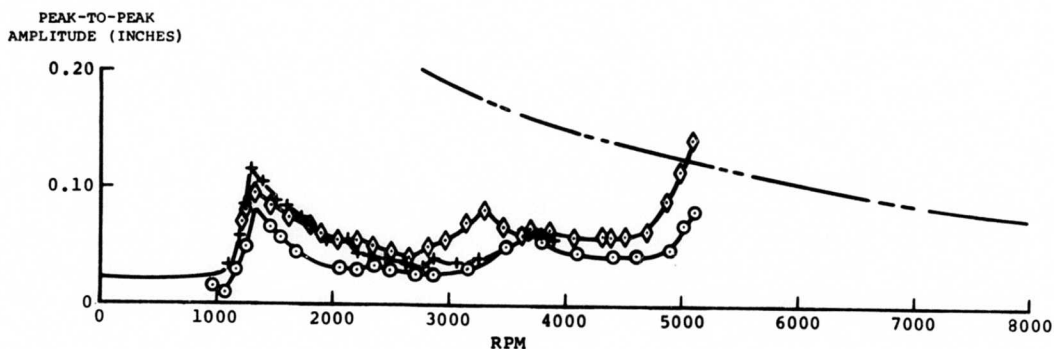
In the course of the investigation to balance the shaft, a vibration study on the test machine indicated a damper structural resonance close to the troublesome frequency. It was decided to remove the flexibility of the simulated aircraft structure and see if the performance would improve. Figure 76 shows shaft performance before and after stiffening the structure. The plot of amplitude shows increased deflection at the second critical speed (1,290 rpm) and a new peak at a speed of 2,900 rpm. There is a gradual phase change at 5,000 rpm. The conclusion from the first run with increased stiffness at the damper structure is that the effect is significant and that balance at the second critical should be optimized before attempting the more difficult problems associated with the fifth critical.

Tests were conducted to optimize the balance at the second critical speed by using balance weights at four stations.

Experimental adjustment of the balance weight (see Figures 77 and 78) allowed the shaft to pass through the fifth critical at 5,300 rpm. However, difficulty was encountered with excessive deflections at 6,000 rpm, an area that was free of critical speeds according to the calculations. A study of rotated mode shapes indicated multiple-plane bending at the higher speeds. Figures 79 and 80 show a number of mode shapes constructed by drawing lines through the maximum deflection. The phase of the bend in the shaft is shown by a small bar drawn from the center of the section view included at the stations where the measurement was taken. The plane was not constant along the shaft as originally supposed. Consistent results were obtained on repeat tests. Those results indicated that more detailed and exact measurements of mode shapes should be made.

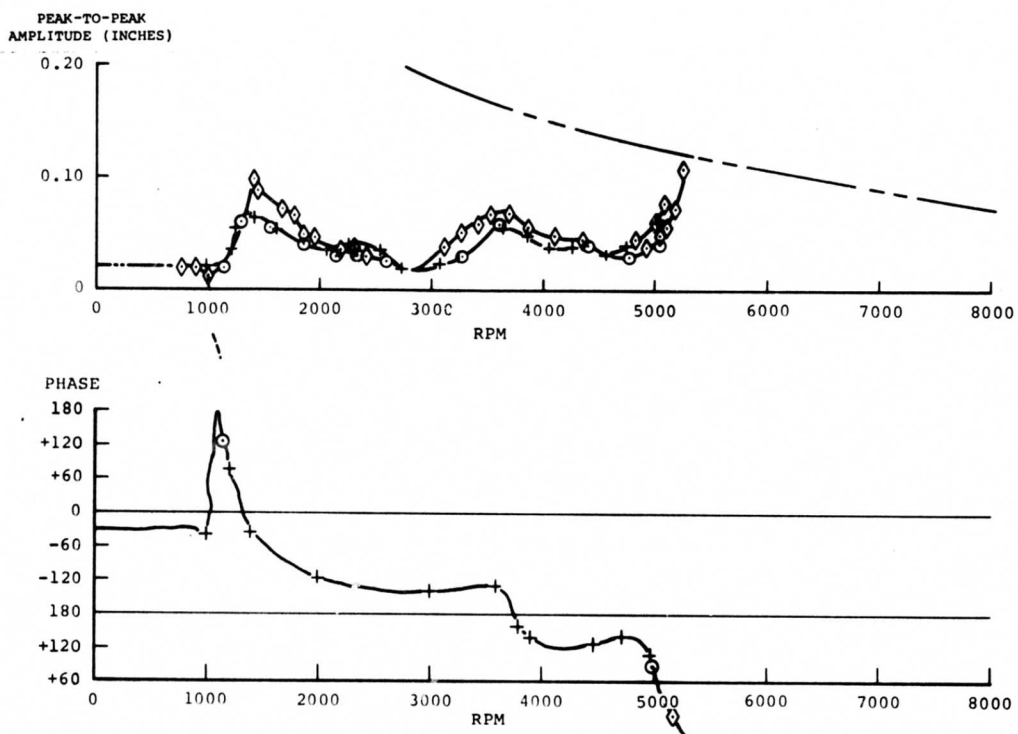
The damper at station 32 failed while running at 5,840 rpm to obtain the mode shape near 6,000 rpm. The mode shape was being investigated to find the reason that balance weights were not correcting the deflection. The damper failure was observed as a fan-shaped spray of fluid which was gone in a fraction of a second. The shaft performance did not seem to be adversely affected at this speed by the failure, and the mode-shape test run was completed. On shutdown, the shaft amplitude reached excessive proportions at a number of critical speeds, and the shaft deflected sufficiently to hit the guards installed near the damper support structure. Contact with the guards marked the strain gage wire pack on the outside of the shaft but did not affect their operation. The shaft was removed and disassembled to check the damper. Again, no damage was apparent by normal visual inspection.

This second damper failure should not have been caused by the crank action of the shaft, and the investigation into the cause of the failure was directed elsewhere. The runout at the damper (0.028 peak to peak, see Figure 50) was within the allowable tolerance as established by the bearing load limit of 200 pounds if a damping coefficient of 18 pounds/ips is used. However, the damping coefficient is not 18 at this amplitude and frequency. Figure 28 indicates that the damping is nonlinear. The actual coefficient from this chart is about 24 at 5,200 rpm. The higher coefficient (as explained in the damper test section) is due to excessive shear rate on the damper fluid or to shock wave causing a pressure expansion of the elastomer



TEST	SYMBOL		BALANCE WEIGHT						COMMENT
		STATION	5	8	10	21	24	27	
66	+	WEIGHT PHASE		65 -90			65 +90		2 WEIGHTS 130 GRAMS VIBRATED MODES
67	◇	WEIGHT PHASE	64 -90		17 -90	59 +90		25 +90	4 WEIGHTS 130 GRAMS VIBRATED MODES
68	○	WEIGHT PHASE	35 -90		53 -90	51 +90		39 +90	4 WEIGHTS 150 GRAMS ROTATED MODES

Figure 74. Tests 66, 67, and 68 - Serial 2A.



TEST	SYMBOL	STATION	BALANCE WEIGHT				COMMENT
			5	10	21	27	
69	+	WEIGHT	35	53	51	39	10 GRAMS STATION 5 10 GRAMS STATION 21
		PHASE	-76	-90	+102	+90	
70	○	WEIGHT	35	53	51	39	CHANGE PHASE OF WEIGHT AT STATION 21
		PHASE	-76	-90	+76	+90	
71	◇	WEIGHT	35	53	56	39	CHANGE PHASE OF WEIGHT AT STATIONS 5 AND 21
		PHASE	-64	-90	+66	+90	

Figure 75. Tests 69, 70, and 71 - Serial 2A.

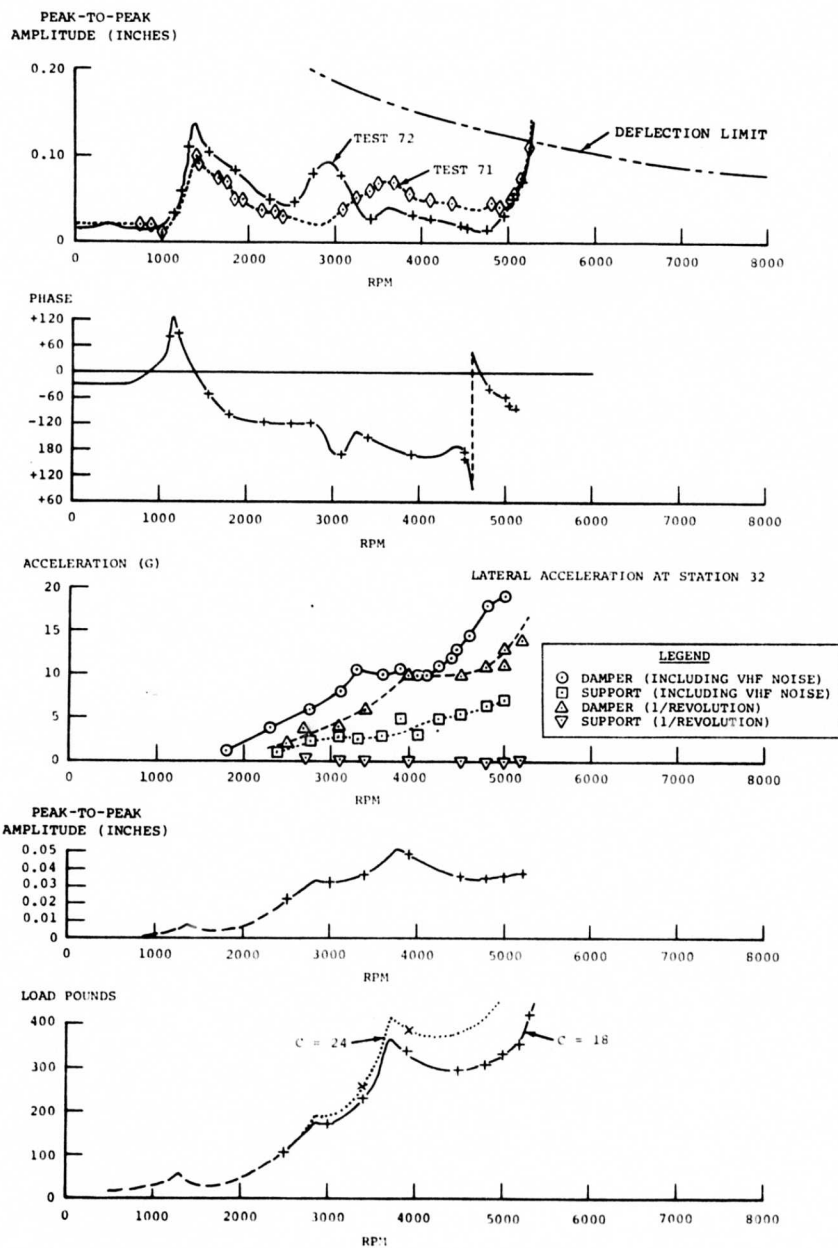
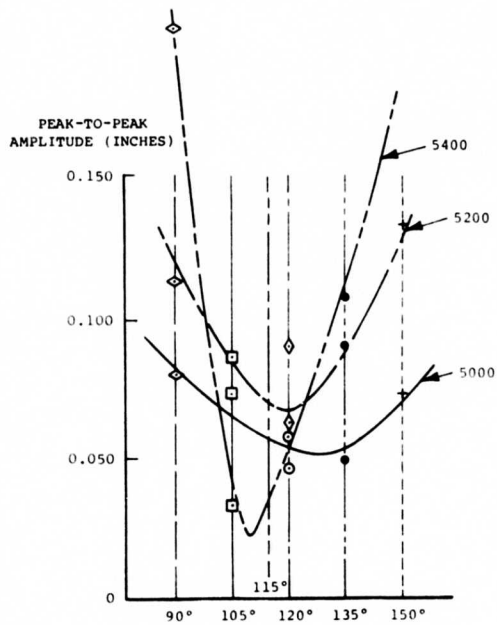
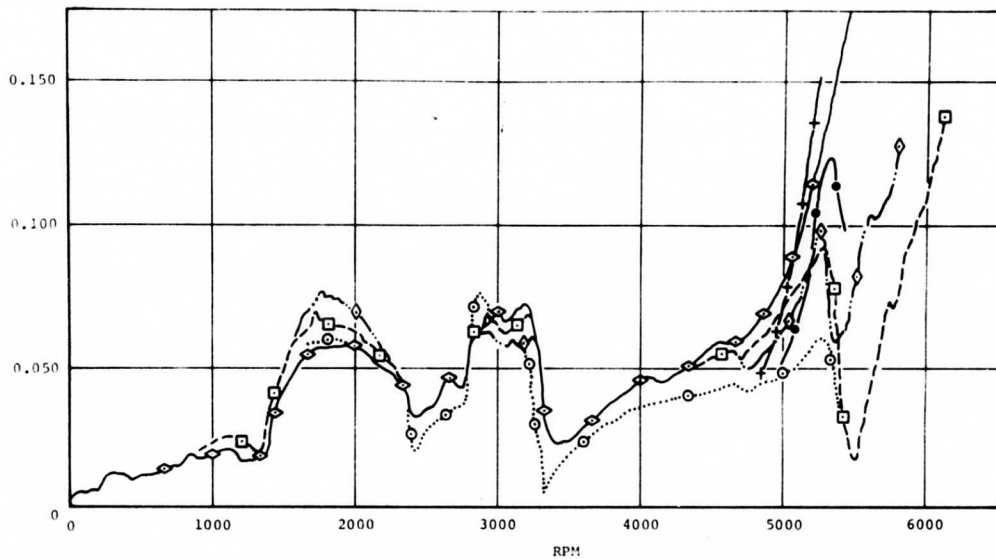


Figure 76. Summary Data From Tests 71 and 72 - Serial 2A.

PEAK-TO-PEAK
AMPLITUDE (INCHES)



SYMBOL	TEST	WEIGHT	PHASE
•	94	40	135
+	95	40	150
⊙	96	40	120
◊	97	40	120
◻	98	40	105
◈	99	40	90

Figure 77. Optimum Angle Tests 94 through 99 - Serial 2A.

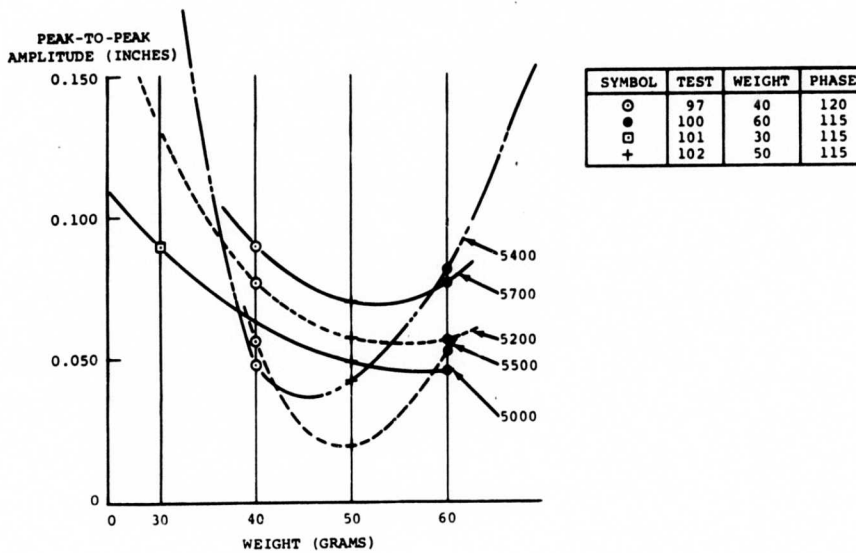
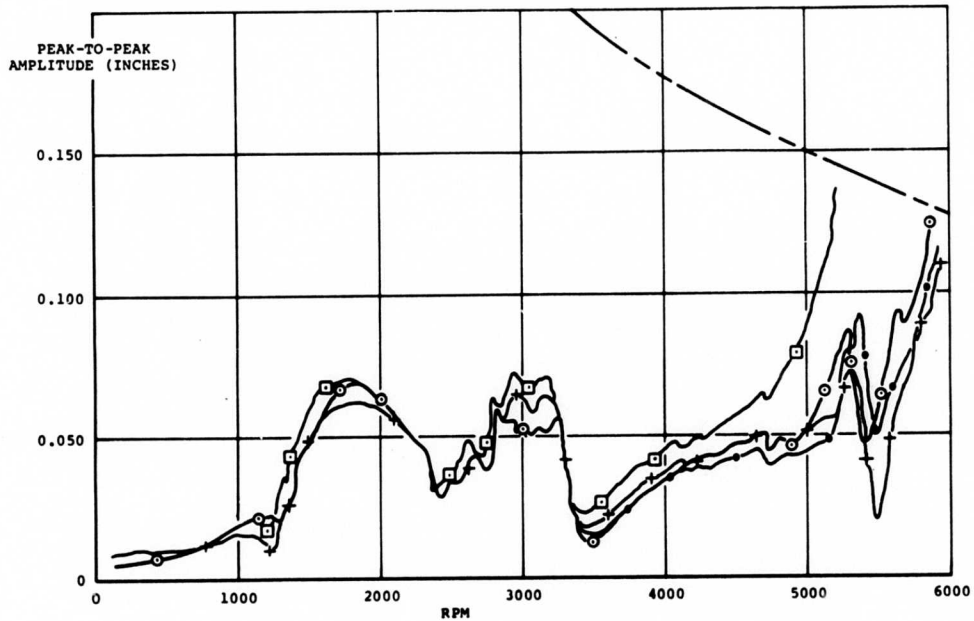


Figure 78. Optimum Weight Tests 97, 100, 101, and 102 - Serial 2A.

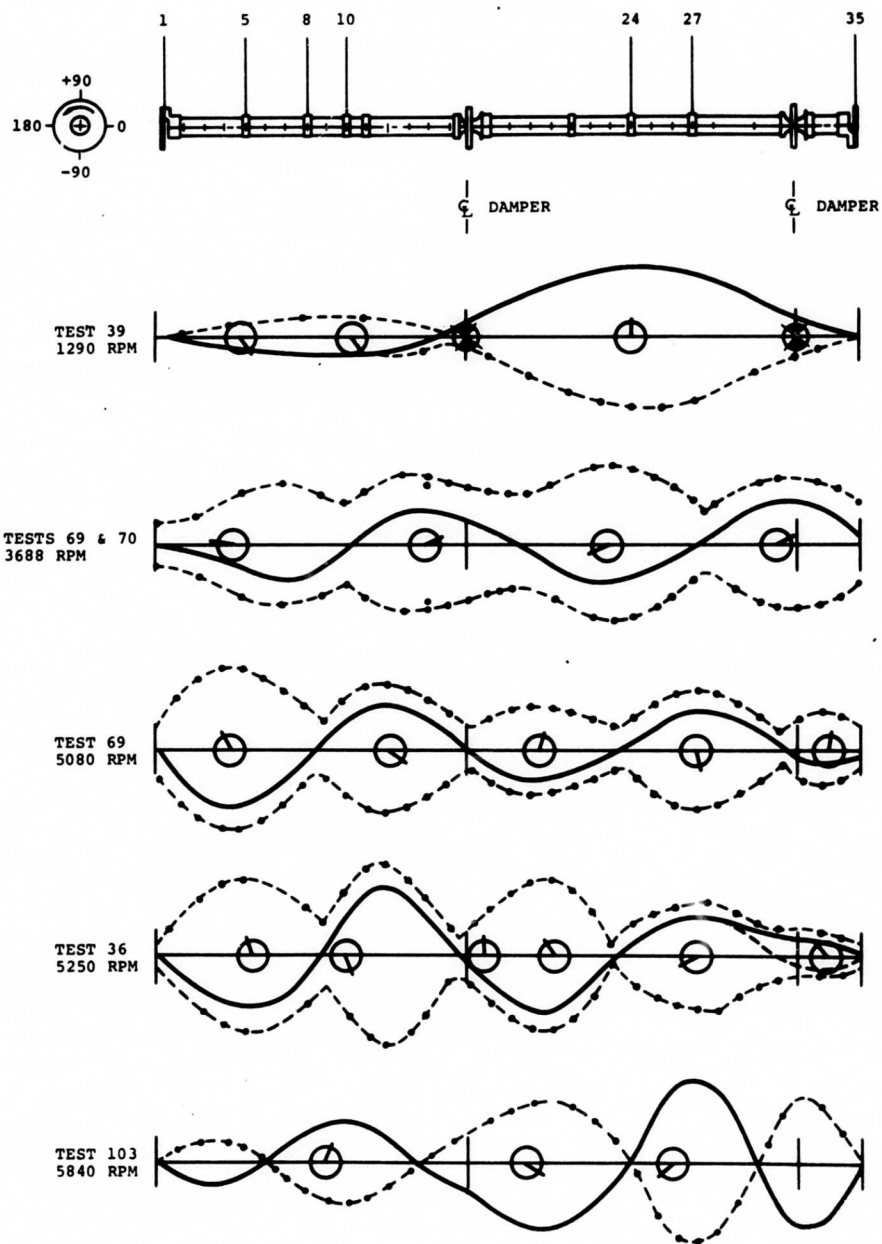
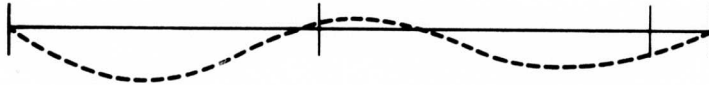


Figure 79. Rotated Mode Shapes - Serials 2 and 2A.

TEST 89 1181 RPM
1230-1350 RPM COMPUTED



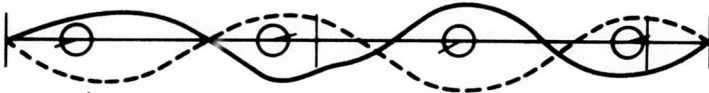
1800-1920 RPM COMPUTED



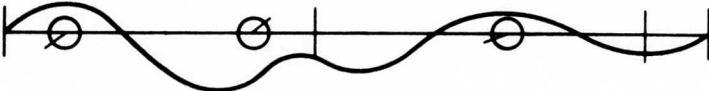
TEST 89 3021 RPM



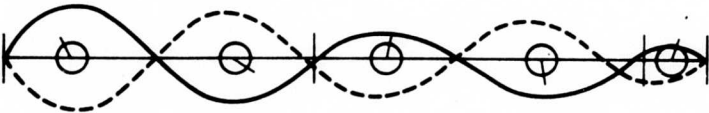
TESTS 69 & 70 3688 RPM
3240-3300 RPM COMPUTED



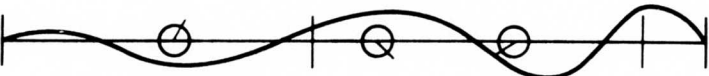
TEST 89 4478 RPM



TEST 69 5080 RPM
5580-5640 RPM COMPUTED



TEST 103 5840 RPM
WITH FAILED DAMPER



8184 RPM VIBRATED
7560-7800 RPM COMPUTED

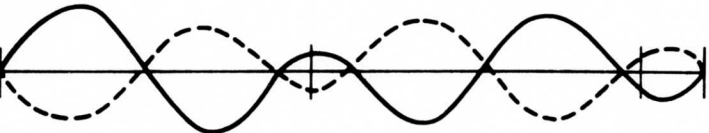


Figure 80. Rotated Mode Shapes - Serial 2A.

90 degrees ahead of the damper deflection. This expansion out of plane with damper motion caused excessive working of the elastomer, which resulted in failure of the damper.

The field splice flanges, not perfectly square after the shaft was straightened, were now machined. A true surface was obtained by supporting and turning the shaft segment on its centers. The mating flanges were ground square within 0.0005 inch total indicator reading (TIR) using this setup.

The shaft was reassembled using a new damper. The initial bend (static runout) was measured for this configuration after the shaft was reinstalled in the test machine (see Figure 51). A change in the initial bend in the shaft would change the center of mass and therefore would affect the balance of the system. All balance weights were removed before testing, since this change, for all practical purposes, was the same as starting with a new shaft. Tests were then run to progressively refine the balance using the experimental approach mentioned earlier and to investigate mode shapes in more detail. Mode shape information (Figures 81, 82, and 83), when plotted in the major and minor planes, disclosed a predominant second mode present in one plane at much higher speeds than the 1,290 rpm resonant frequency. This condition indicated a need for further investigation.

The test in Figure 84 was the first run to reach the target speed of 8,300 rpm. The shaft was then run to the target speed of 8,300 rpm without balance weights (see Figure 85). The amplitude at the second critical was near the limit, but the performance of the unbalanced shaft appeared to be better than the balanced shaft at higher speeds. There was an amplitude peak near 6,700 rpm which analysis revealed to be a combination of shaft deflection and a secondary signal equal to the frequency of the low-speed shaft of the test machine. These two signals were easily separated, and the maximum deflection was found to be caused by test machine motion rather than shaft motion. In fact, when the test machine motion was removed, the remaining shaft deflection was so small that it could no longer be measured by the optical pickup instruments.

Further tests were run using the more sensitive orbiting-end-load link instrumentation. The data from a test where the optical pickup and the orbiting end load instrumentation were used indicated that, while the deflection remained within the allowable envelope, the end load which should be related was beyond the acceptable limits. For this test, the pickup and load links were located in such a way that the phase of the two signals should have been the same throughout the frequencies tested. The phase was the same in some areas; however, it varied as much as 150 degrees in others (see Figure 86). The load on the end was severe (800 pounds) and had to be reduced. The noise level of the shaft and test machine appeared to be related to the high end load. The noise built up when this load increased and dropped off when the load decreased.

The strain gages at shaft station 4 were used to measure bending stress. A comparison of shaft deflection, orbiting end load, and bending stress in the shaft is presented in Figure 87. The phase of these signals is also shown. According to the original concept, the phase of these three signals should be the same and the magnitudes should be related. The only place this seemed to hold was at the second critical speed (1,290 rpm). Figure 88 shows the effect of 10 grams at shaft station 11 located at various phase angles. The deflection at station 4 was minimum at the fifth critical (5,300 rpm) when the weight was located at a phase of -15 degrees. The end load, however, was minimum when the weight was located at a phase of -75 degrees. The end

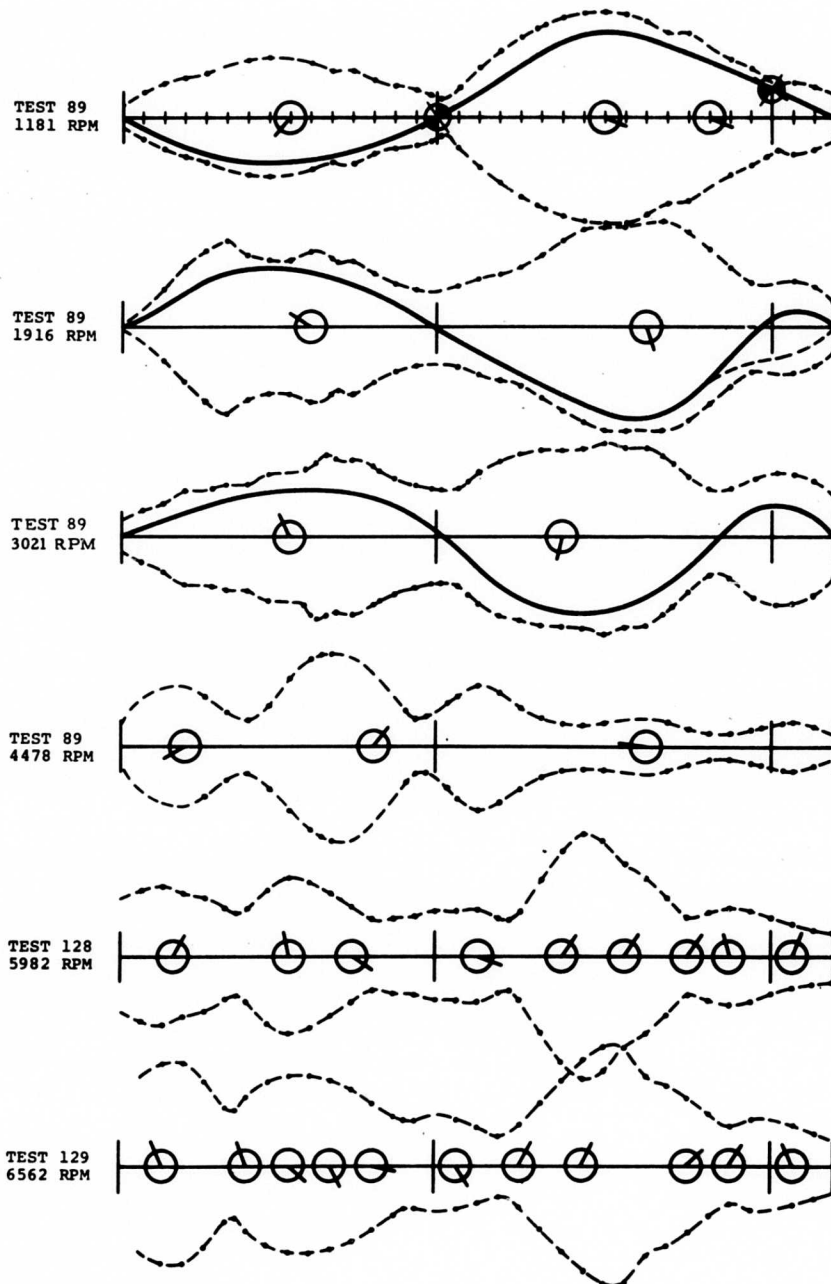


Figure 81. Rotated Mode Shapes - Serial 2A.

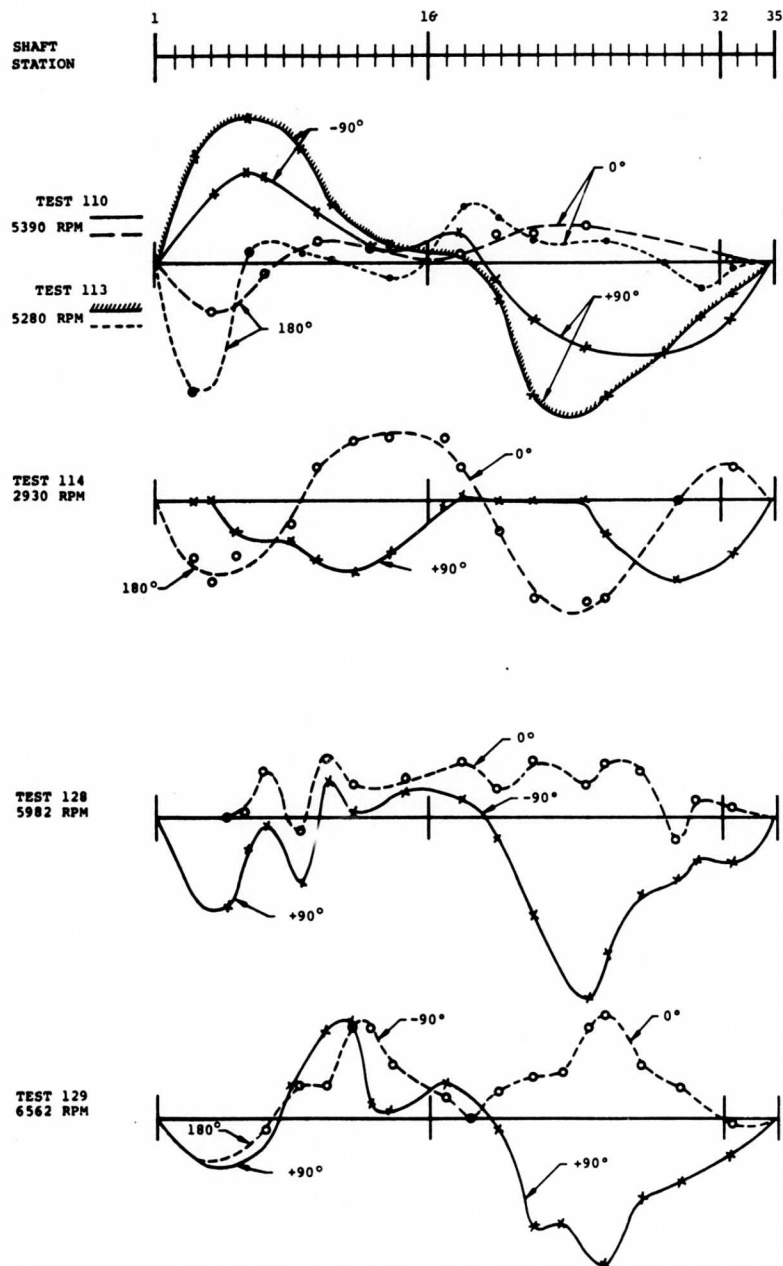


Figure 82. Deflection in Two Planes - Serial 2B.

SCALE
0.020 INCH

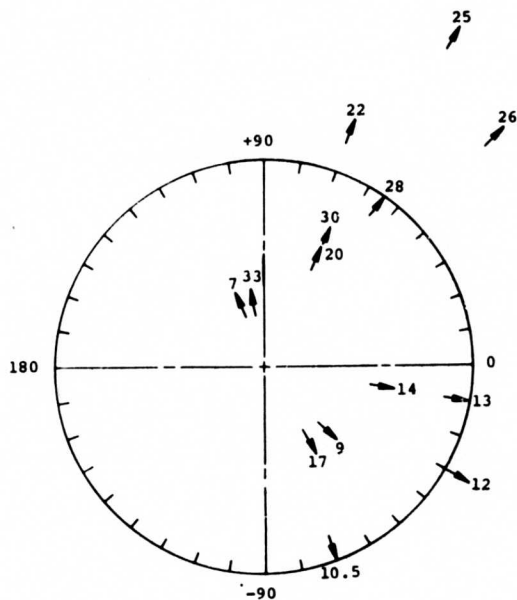
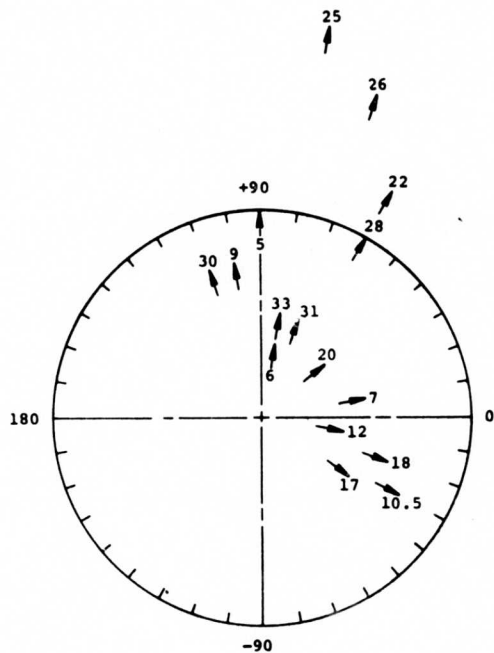


Figure 83. Polar Deflection at 5,982 and 6,565 RPM-Serial 2B.

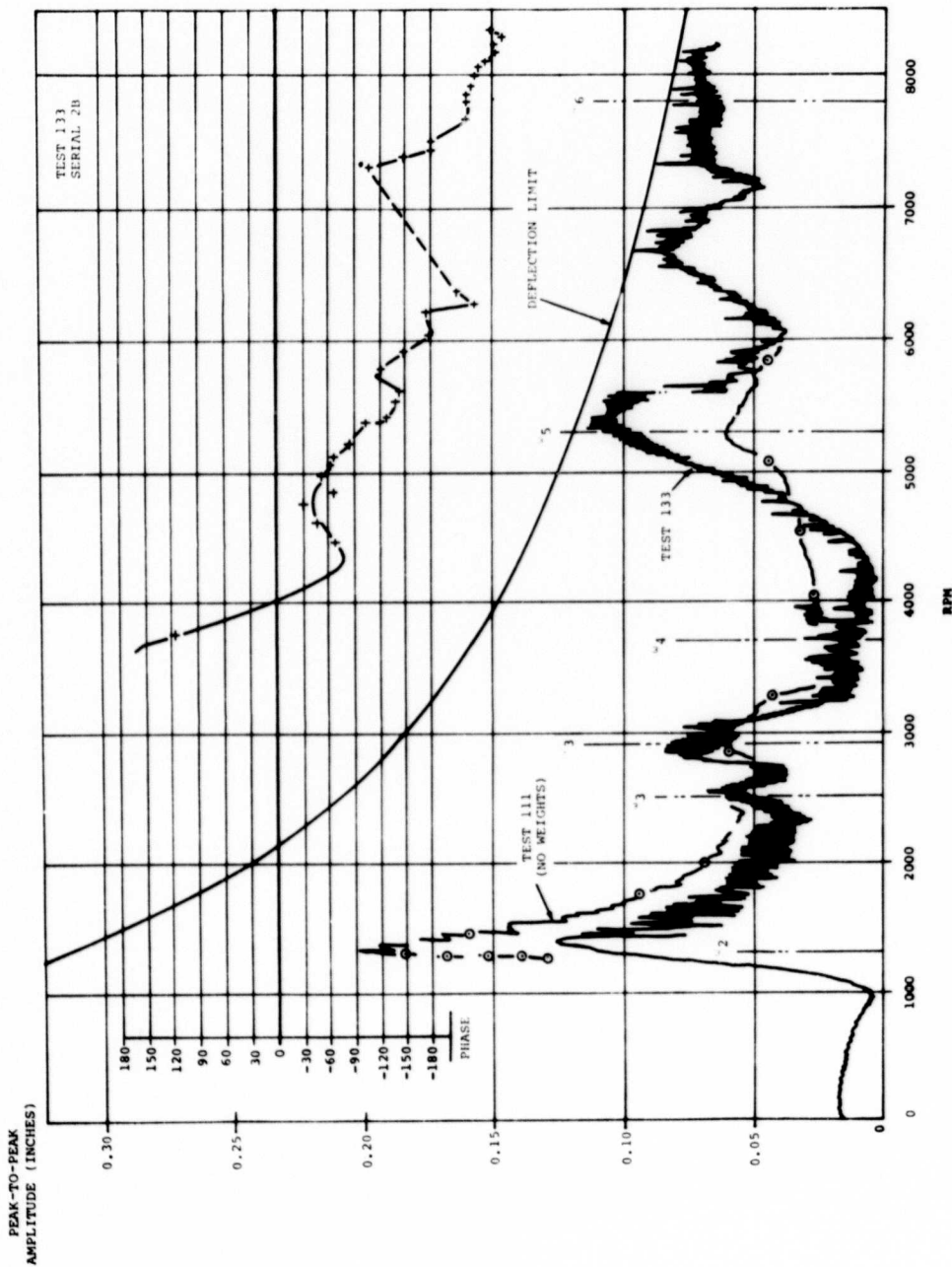


Figure 84. Deflection Versus Speed to 8,300 RPM - With Weights.

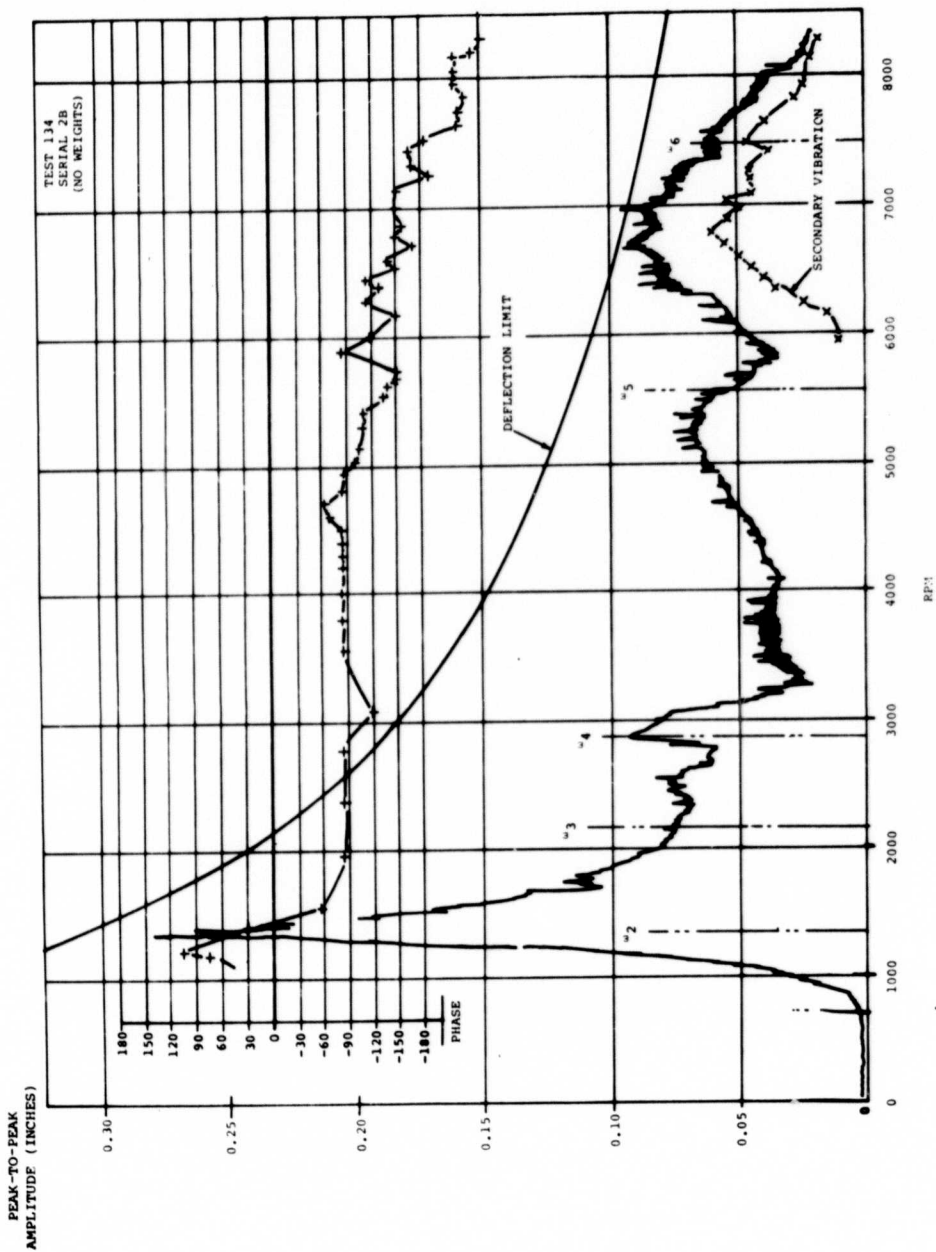


Figure 85. Deflection Versus Speed to 8,300 RPM - Without Weights.

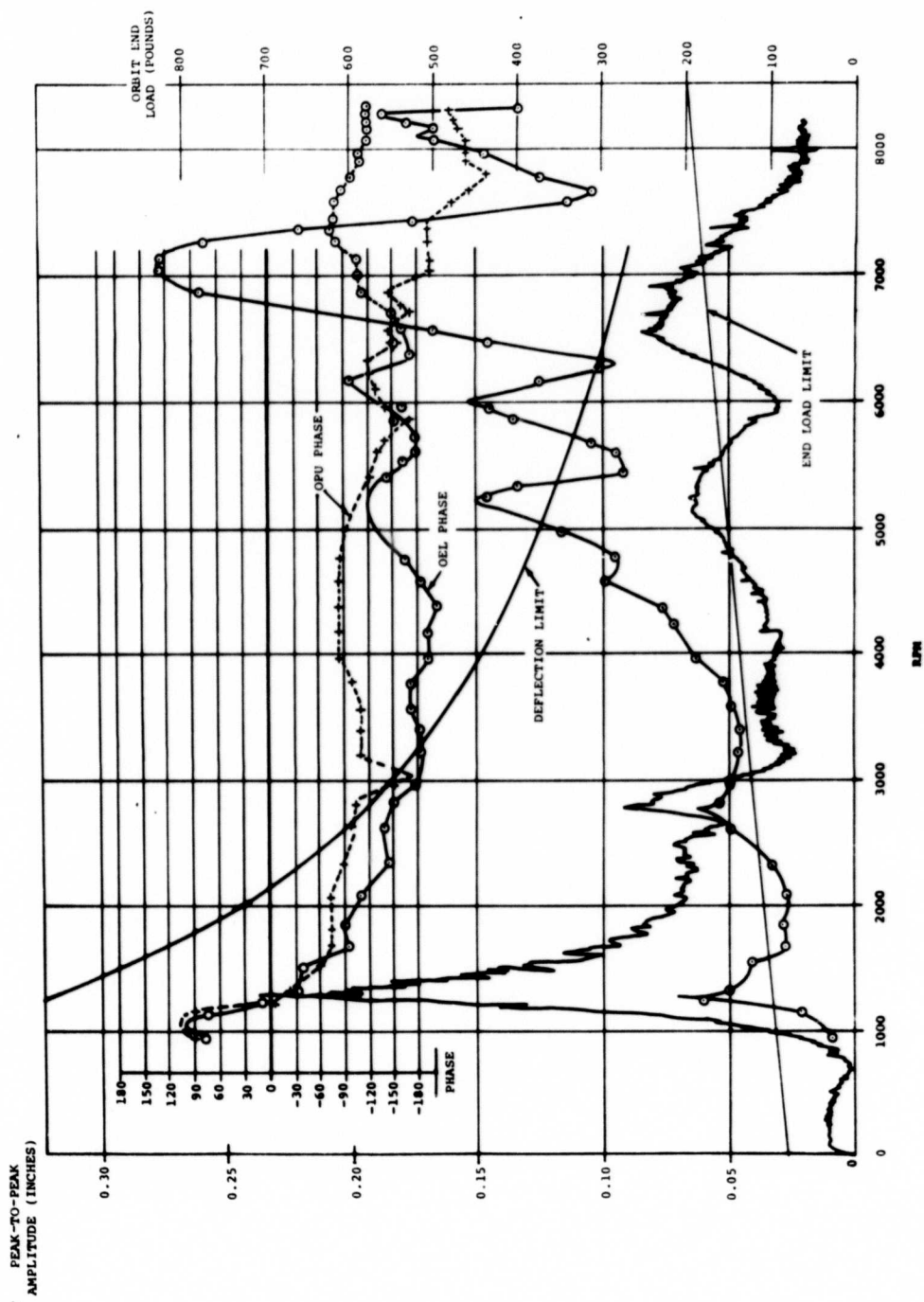


Figure 86. Deflection and End Load Versus Speed.

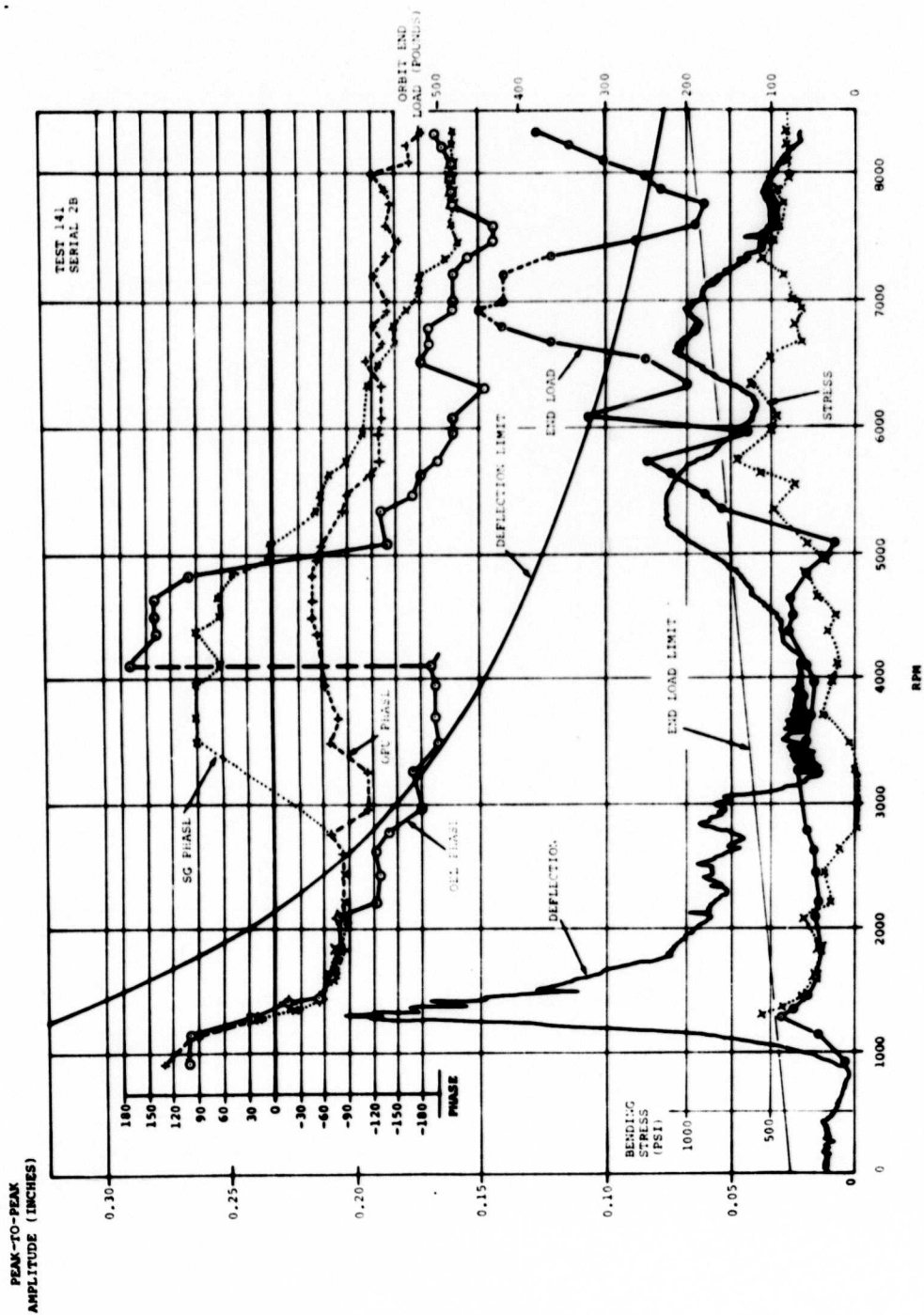
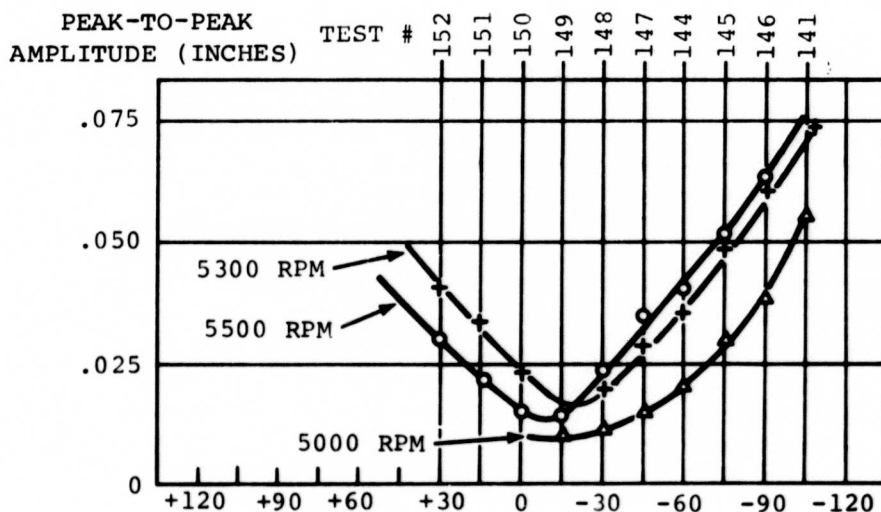


Figure 87. Deflection, End Load, and Strain versus Speed.

DEFLECTION VERSUS BALANCE WEIGHT ANGLE, STATION 11



END LOAD VERSUS BALANCE WEIGHT ANGLE, STATION 11

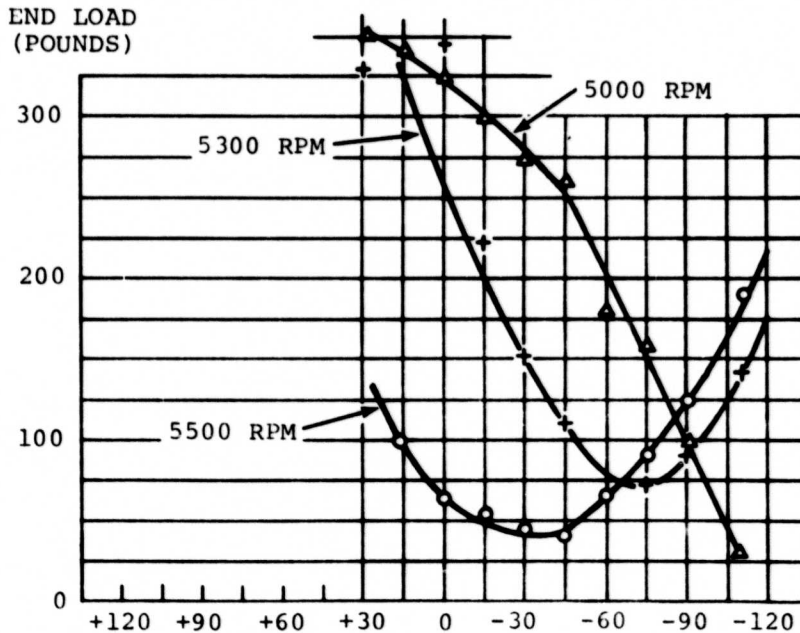


Figure 88. Effect of Balance Weight Phase on Deflection and End Load.

load was measured in two strain-gage links restraining the pillow block which supported the end of the high-speed shaft. When a circular orbiting load was present, the signals had equal displacement and there was a phase difference between them of 78 degrees. However, the phase relationship changed, and Figure 89 presents this change as a delta phase. A 0-degree phase would occur if the load were vibrating up and down with no circular component, and a 180-degree phase would occur if the load were vibrating in a horizontal plane with no circular component. A constant 78-degree phase would occur if the pattern for the orbiting load were a true circle. If the load were describing an elliptical pattern which was not oriented in the vertical or horizontal plane, the signals would be unequal in magnitude, and the orientation of the elliptical pattern could be determined by measuring the changes in magnitude. Analysis of the data gathered from this test indicated that the orbit end load was elliptical at times. This was substantiated by optical pickup data gathered by placing the instrument in a vertical and a horizontal plane (see Figure 90).

The shaft was run with torque and without torque, and the deflection was plotted (see Figure 91). There was no appreciable difference in the shaft performance. Figure 92 shows shaft performance when measured by the optical pickup located in a number of planes. Plots of the orbital path of the shaft at a number of speeds are shown by sections on the same figure. Plots of the shaft motion at the dampers (Figures 93 and 94) show similar orbital paths. The major axis of the elliptical planes is 90 degrees out of phase between the dampers. The optical pickup was moved the length of the shaft to obtain the deflected shape. Figure 95, obtained at 7,300 rpm, is a typical example of the test results. Mode shapes were obtained at 5,400, 6,000, and 7,300 rpm as shown by the polar plots of deflection at various shaft stations at these speeds. Two tests were run at each of these speeds for repeatability (see Figures 96, 97, and 98).

The major and minor deflection planes as determined by inspection of the polar plots were used to construct the information given in Figure 99. The plots contain a predominant second-mode shape in one of the planes at all three speeds selected. Figure 100 shows the mode shapes when the second mode component is removed. It shows a fairly reasonable correspondence with the calculated mode at those speeds. Figure 101 shows deflection of the shaft at 7,300 rpm when viewed as a time-history plot. One-half a revolution is presented. The dotted line is constructed by fairing a line through the average deflection; it represents the contribution of the second mode. A model shaft (Figure 102) was constructed with this deflection present. When the shaft was turned in one position, only the second mode was present; when it was advanced 90 degrees, the sixth mode was visible superimposed on a second mode.

An acoustic run was made for spectral analysis to determine the frequency of the objectionable noise present at the higher speeds. Figure 103 shows the deflection plot of test run 193; sound pressure and decibels versus frequency is plotted on the same chart. The result was that the predominant audio frequency corresponded to the running speed. Secondary frequencies can be disregarded. Subsequent runs produced lower noise levels, but acoustic measurements were not repeated for these tests.

Analysis of test results of a general nature seems to point to an unbalance in the end of the shaft unrelated to the supercritical-speed shaft performance. The high-speed shaft was removed, and vibration was still present. The low-speed shaft was removed, as it was not used unless torque was being applied to the high-speed shaft. The orbiting-end-load shaft was balanced using the strain-gage link signals. This unbalance pointed out that the

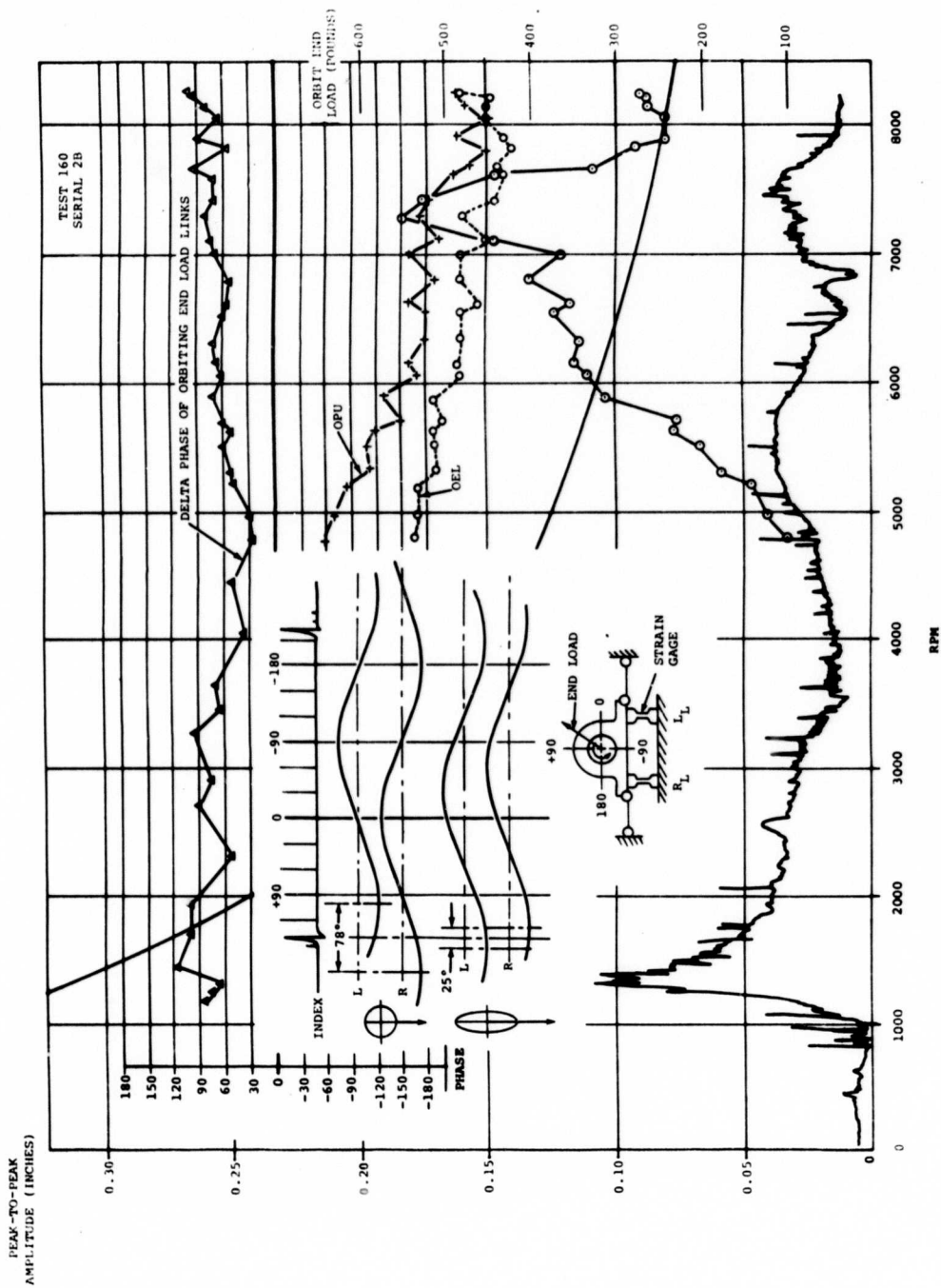


Figure 89. Delta Phase of End Load Links.

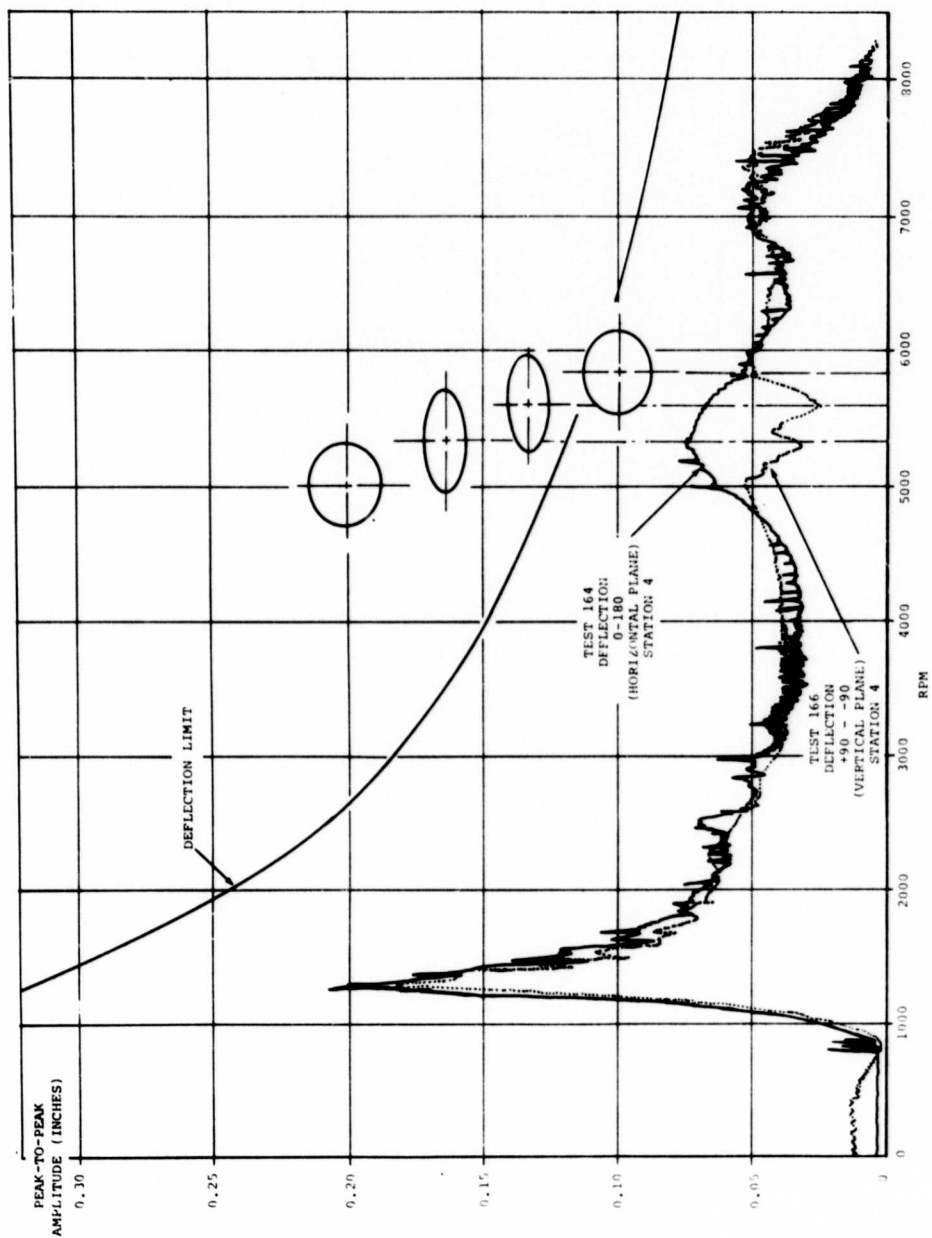


Figure 90. Horizontal and Vertical Deflection at Station 4.

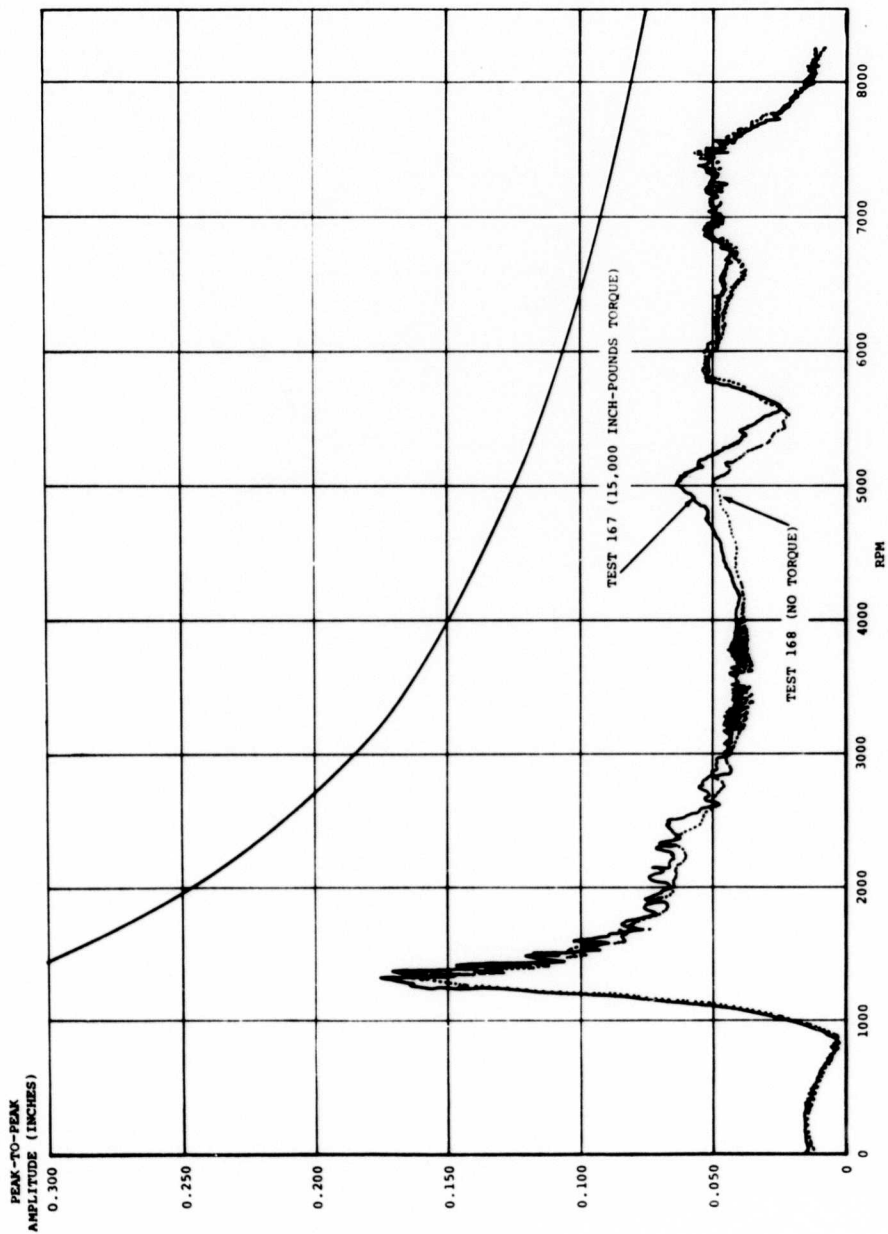


Figure 91. Effect of Torque.

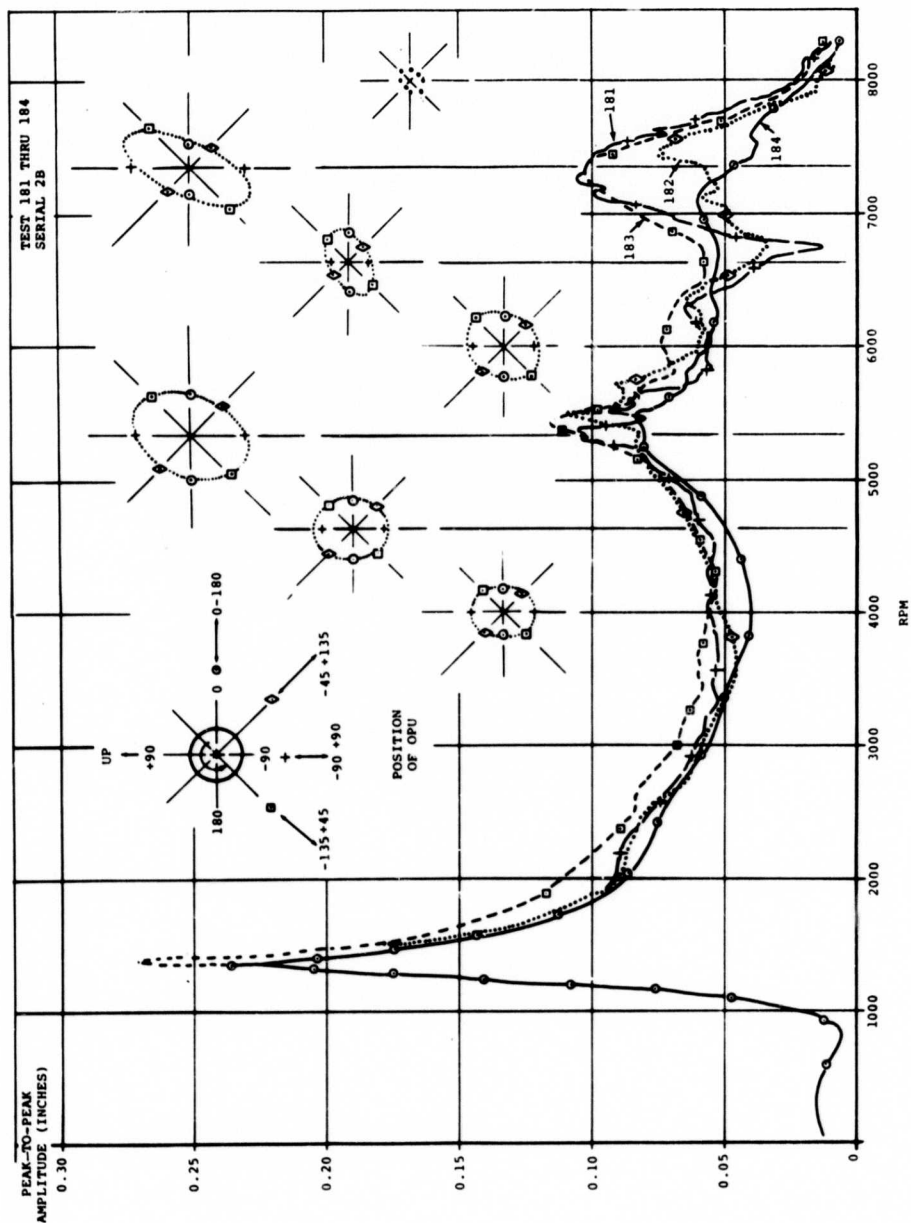


Figure 92. Deflection in Four Planes at Station 4.

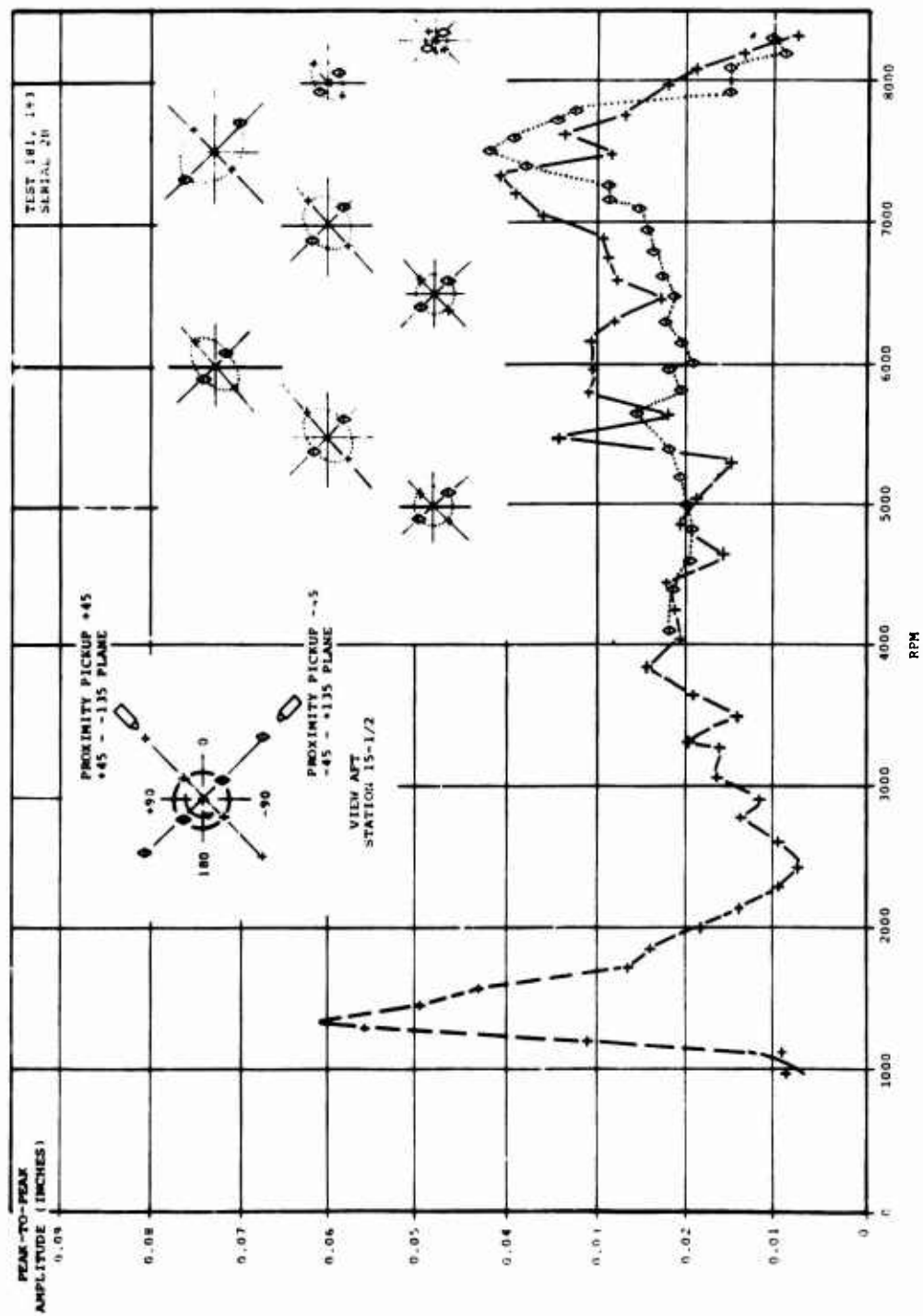


Figure 93. Damper Motion in Two Planes at Station 16.

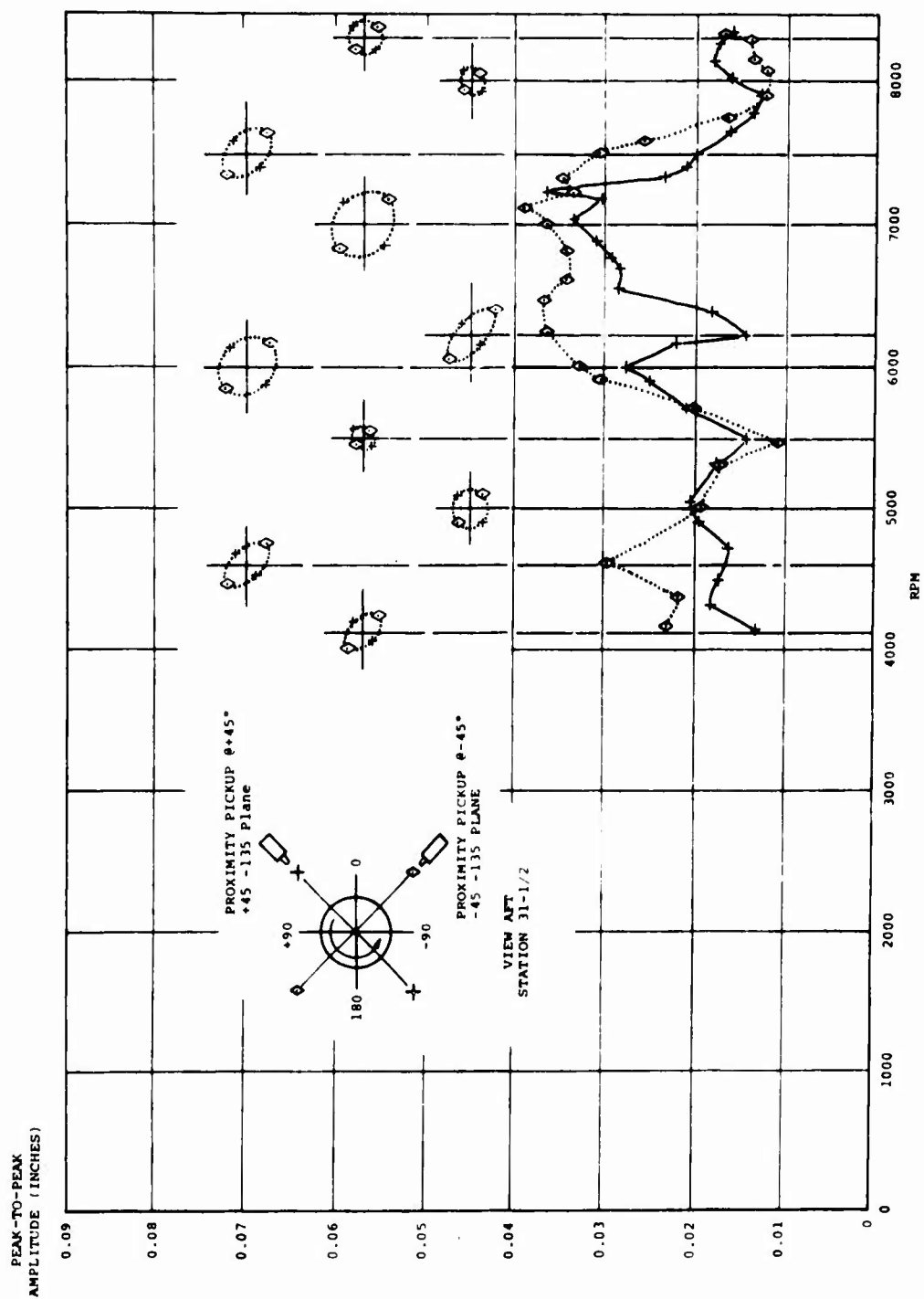


Figure 94. Damper Motion in Two Planes at Station 32.

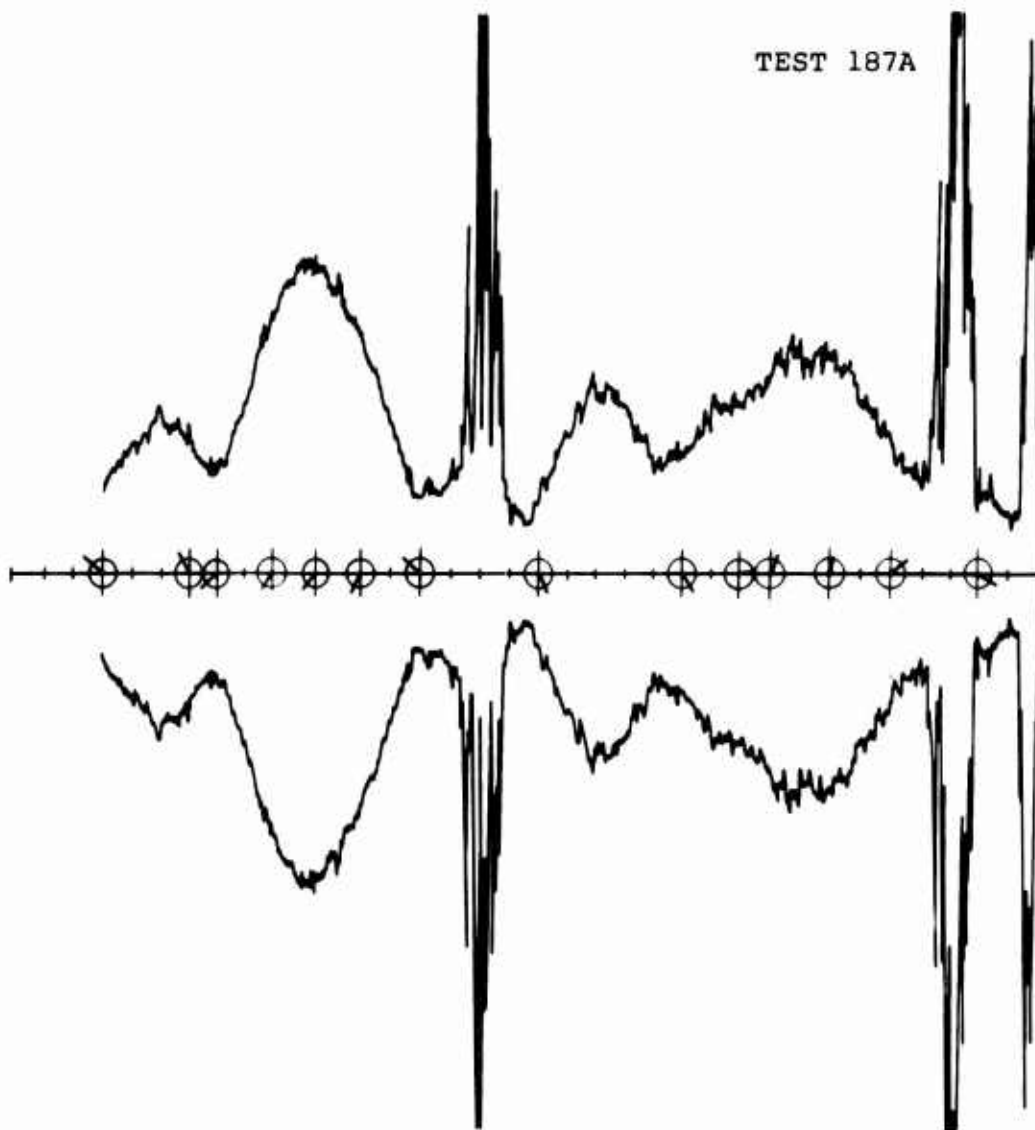


Figure 95. Mode Recorded by the Optical Pickup at 7,300 RPM.

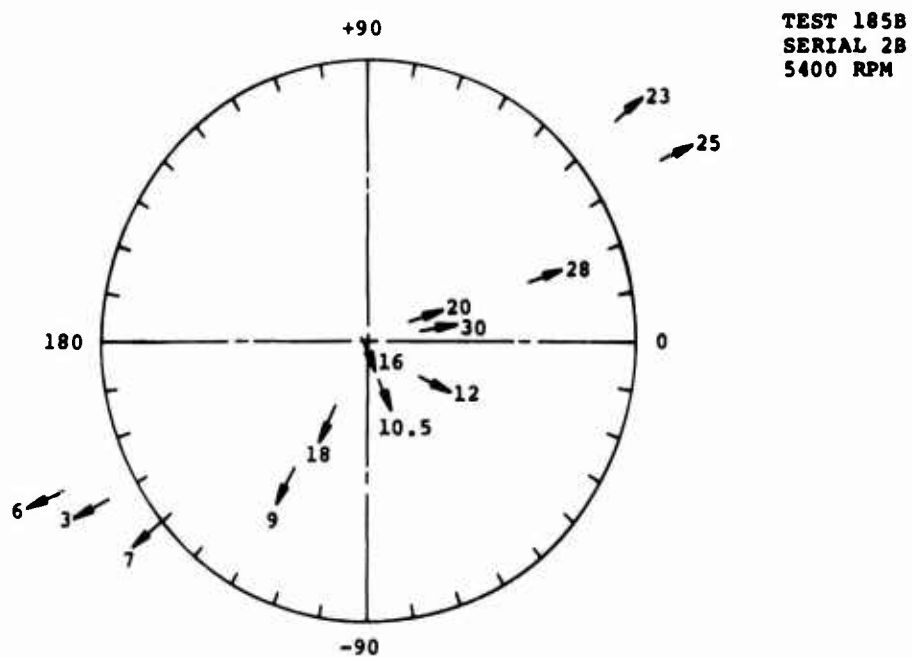
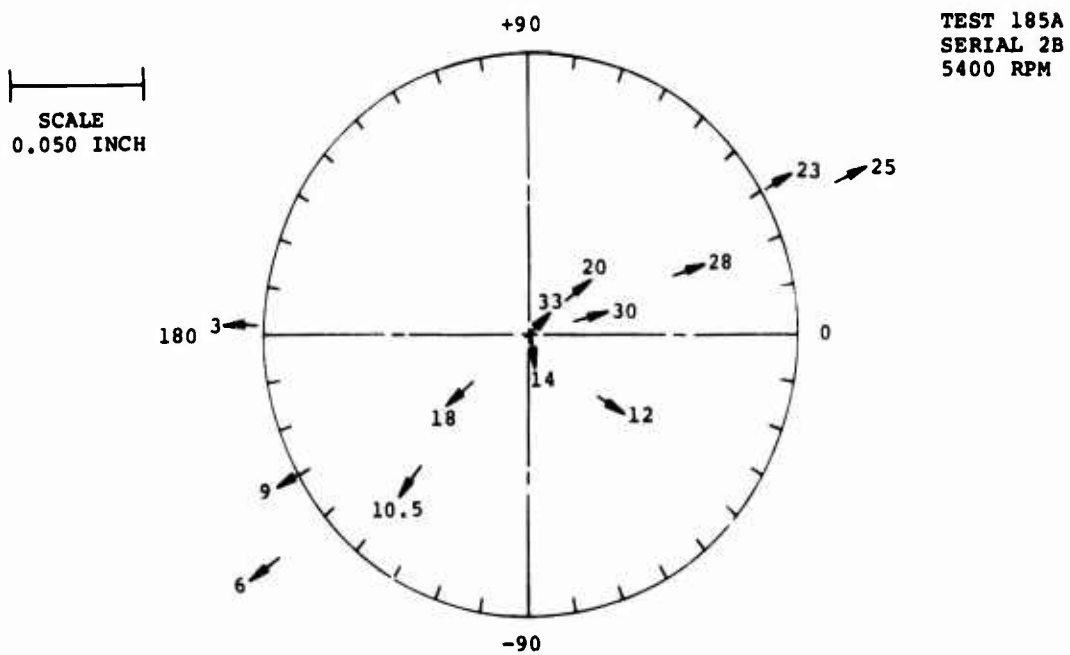


Figure 96. Polar Deflection at 5,400 RPM for Repeatability.

SCALE
0.050 INCH

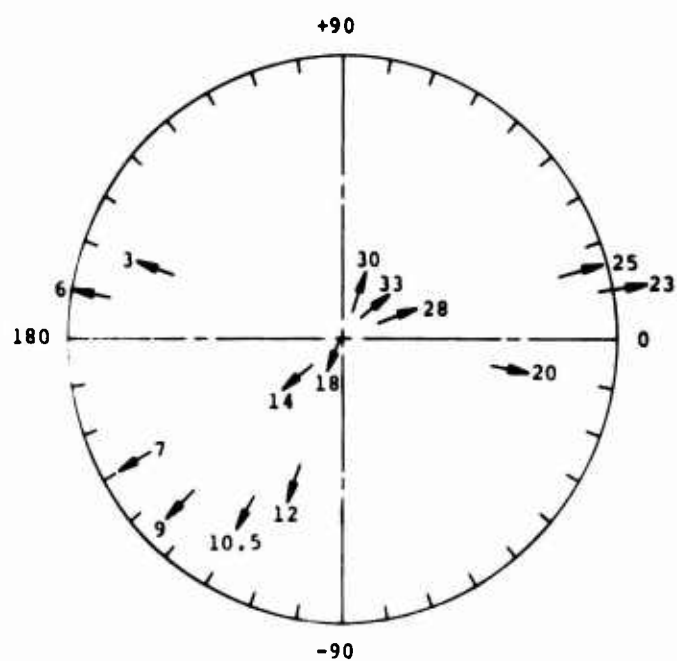
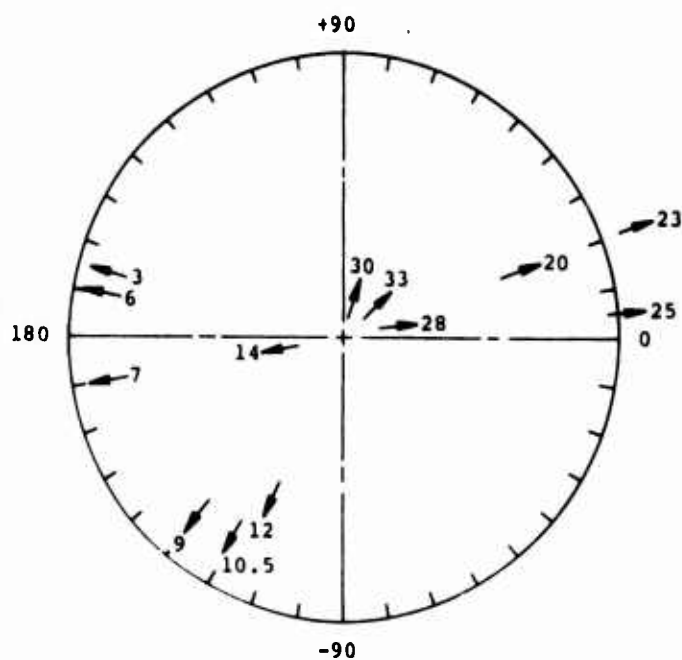


Figure 97. Polar Deflection at 6,000 RPM for Repeatability.

SCALE
0.050 INCH

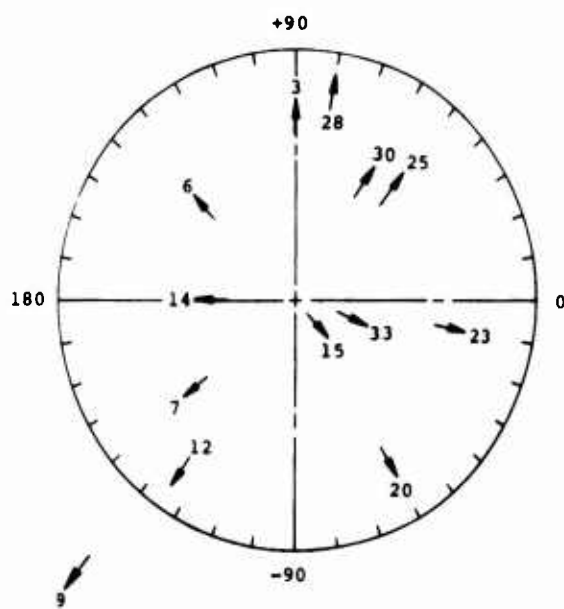
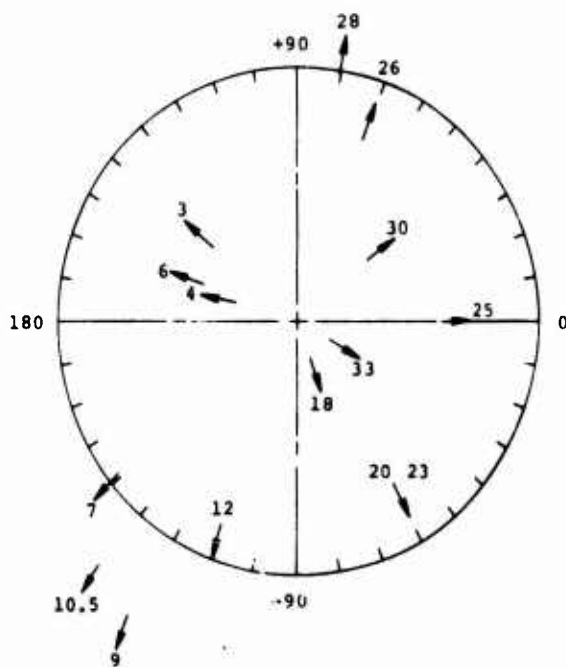


Figure 98. Polar Deflection at 7,300 RPM for Repeatability.

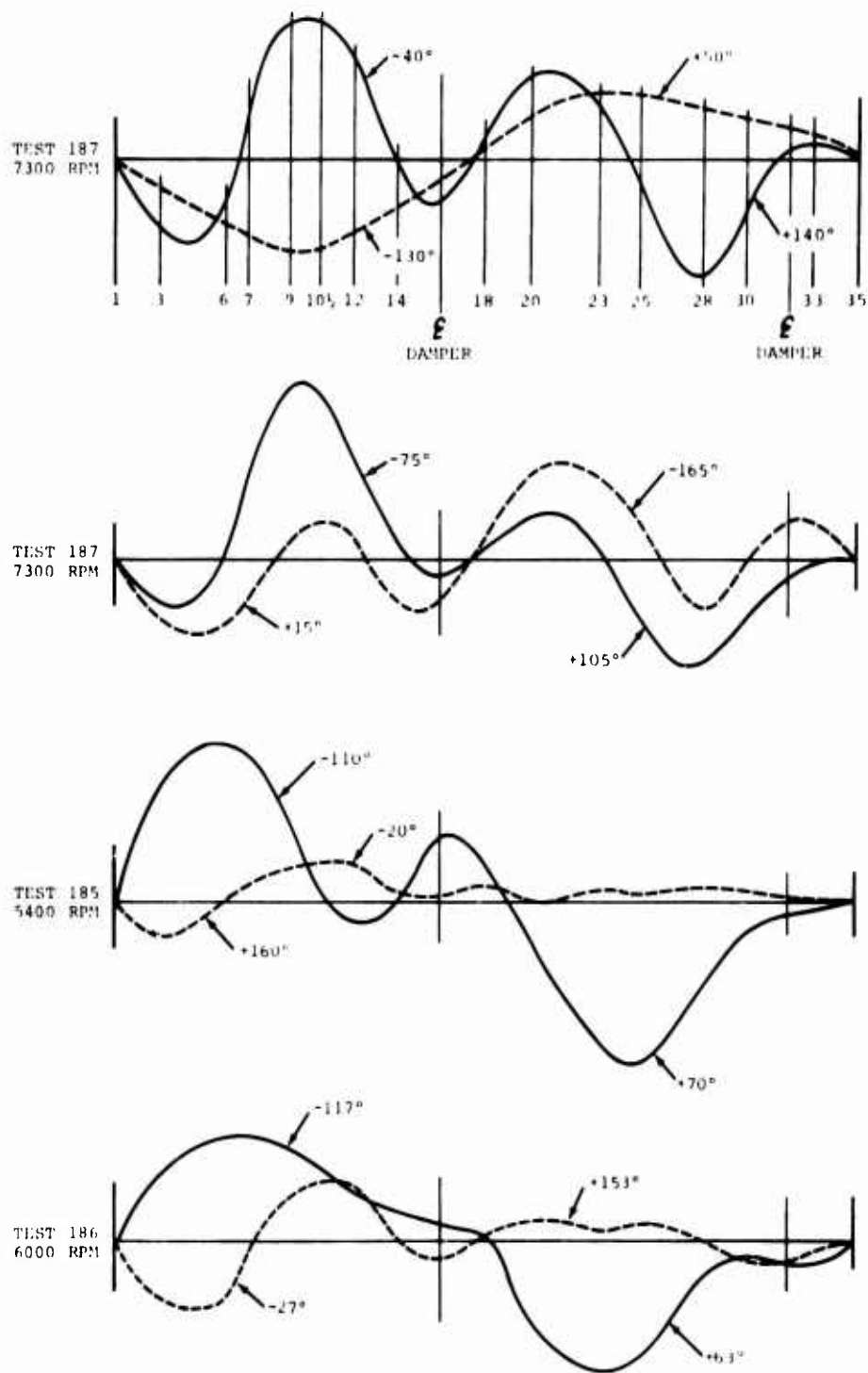


Figure 99. Deflection in Two Planes for Modes at 5,400, 6,000, and 7,300 RPM.

TESTS 185 & 187
SERIAL 2B

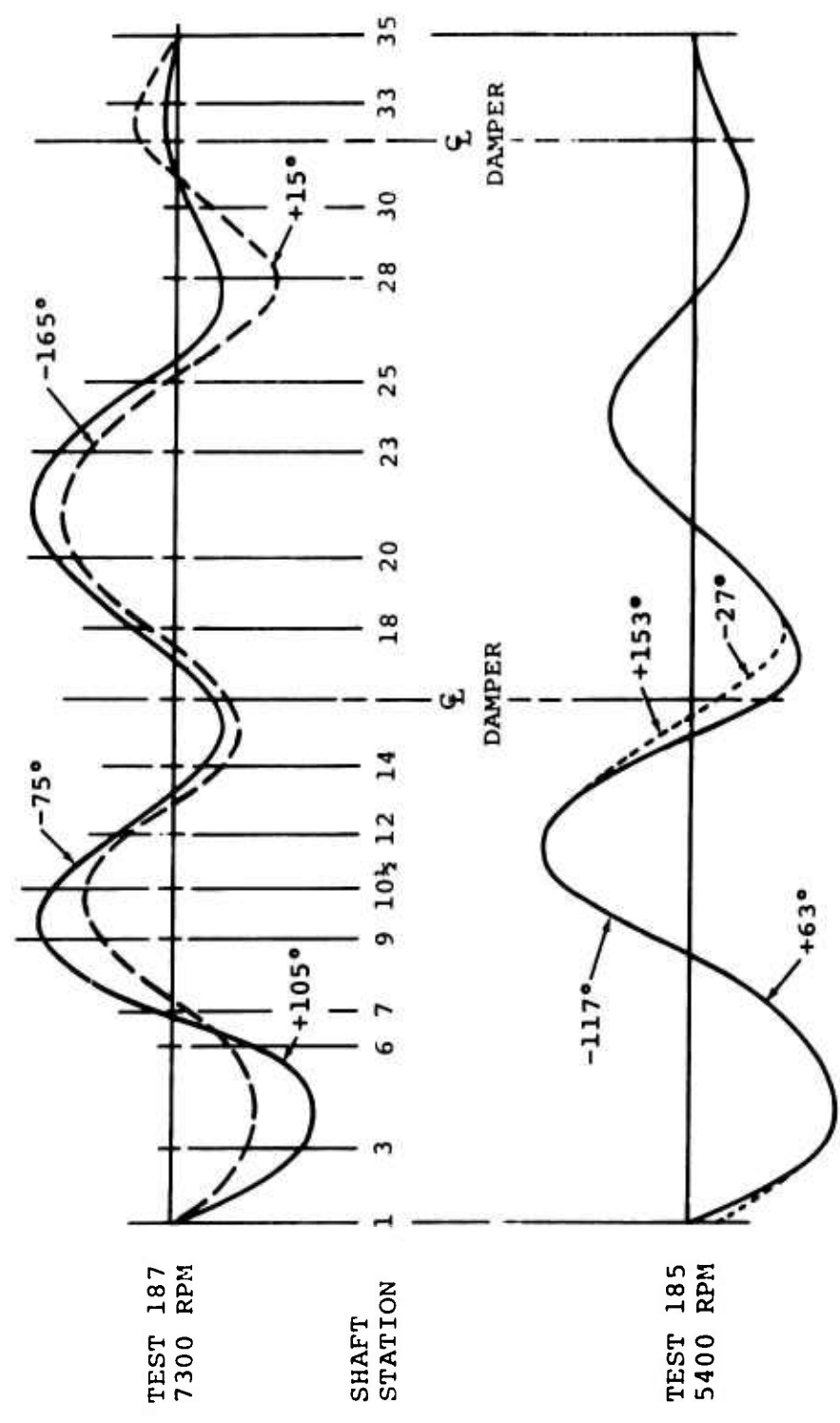


Figure 100. Mode Shapes with Second Component Removed.

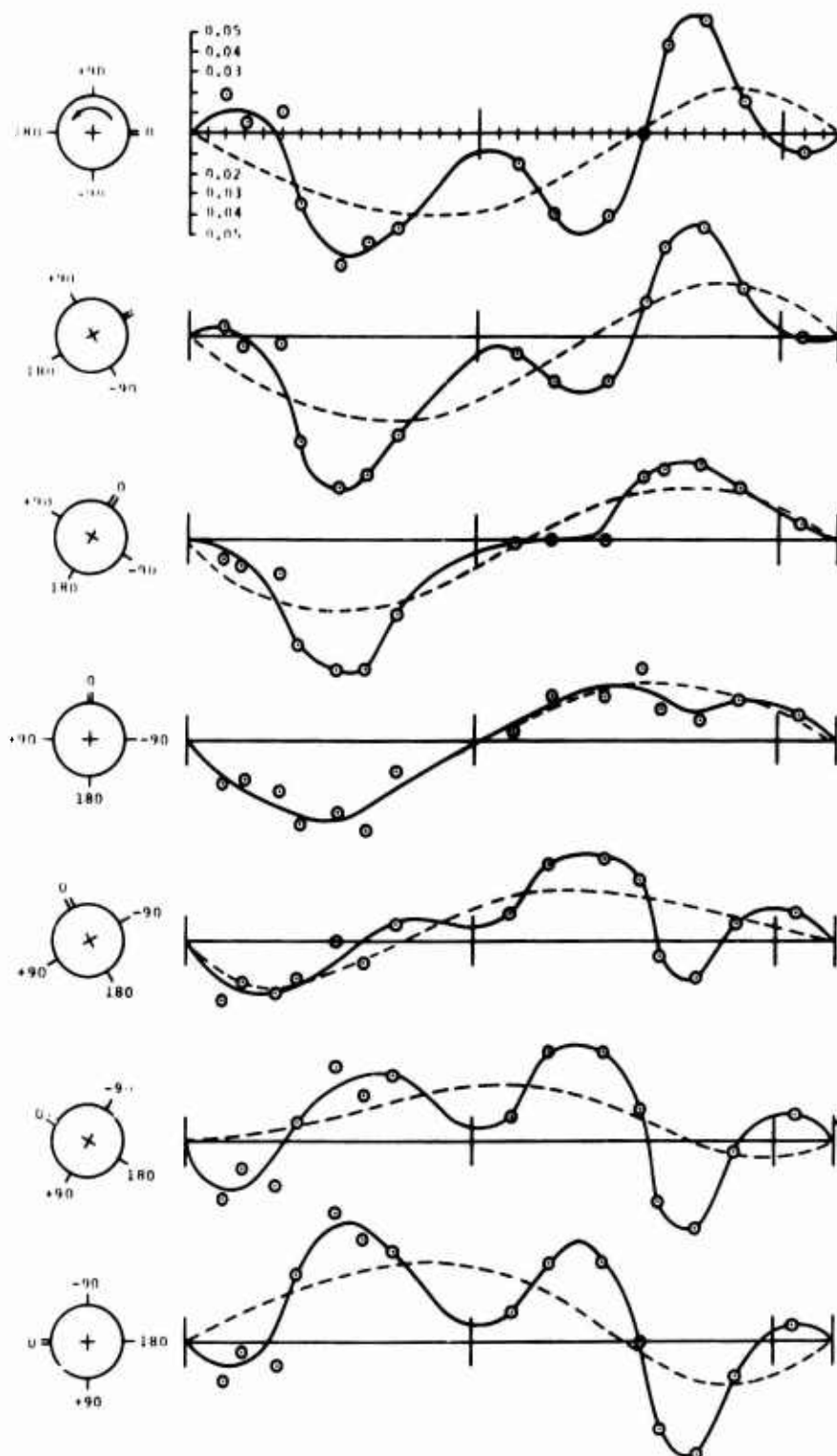
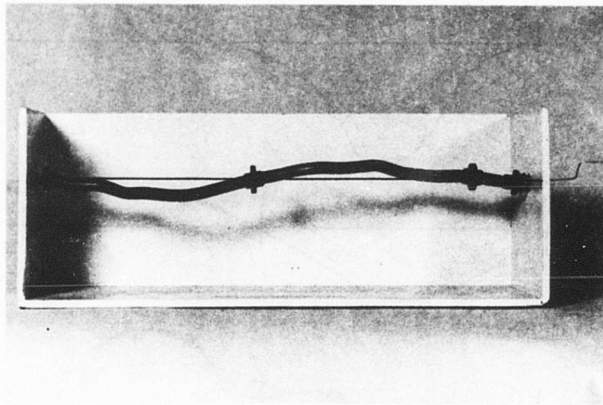
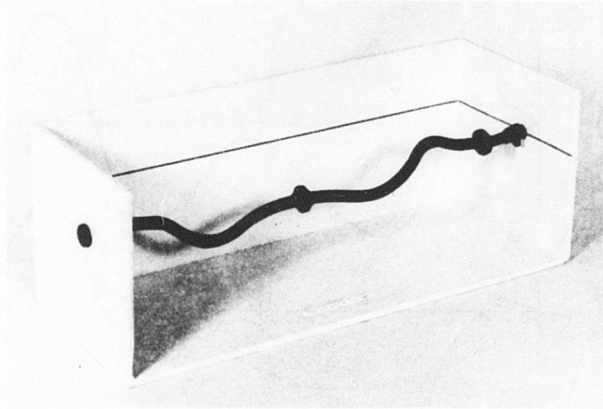
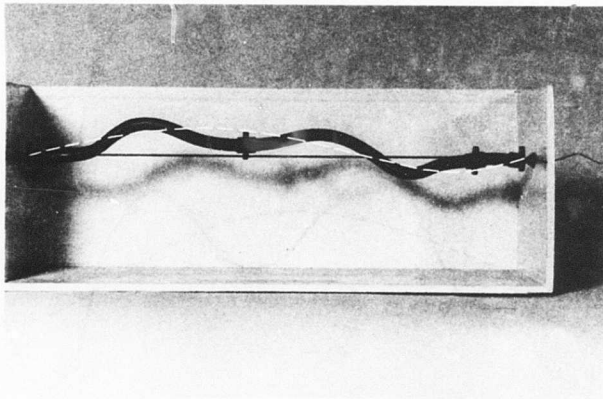


Figure 101. Time History of Response for 180 Degrees of Shaft Rotation at 7,300 RPM.



SHAFT PLANE $0^{\circ}/180^{\circ}$



SHAFT PLANE $-90^{\circ}/+90^{\circ}$

Figure 102. Model of Shaft Deflection at 7,300 RPM.

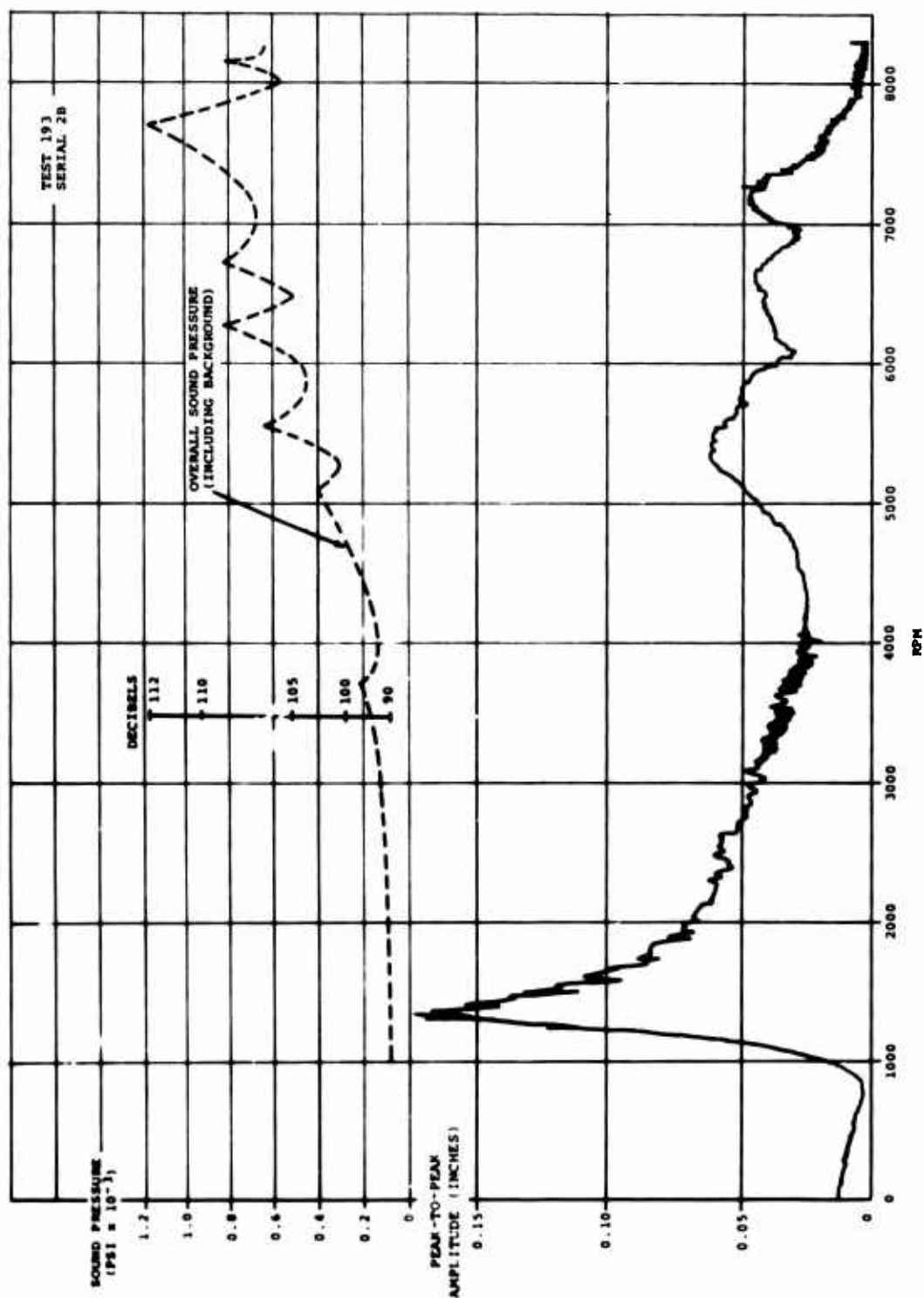


Figure 103. Acoustic Investigation - Serial 2B.

supercritical-speed test specimen might contain an unbalance on the end which could at times produce a greater reaction than the one from the deflected supercritical-speed shaft. These forces would combine and may be responsible for the phase difference between signals noted previously. To determine the unbalance in the end of the shaft, a speed (8,300 rpm) was selected where there was little deflection in the flexible shaft. A test series was conducted to investigate the effect of a small balance weight located at various angles on the end of the shaft. The end load of the series is shown in Figure 104 with plots of load versus angle of balance weight for 6,000, 7,300, and 8,300 rpm. From this plot the optimum angle and weight were determined. The phase change of the most effective angle between the speeds plotted, especially at the lower speeds, is attributed to the influence of the unbalance in the flexible system. The optimum balance weight for the end of the shaft is 12 grams at -20 degrees phase. This weight was installed and used in all the remaining tests. Figure 105 shows the relationship between orbit end load and deflection; this plot follows the expected pattern more closely.

Effectiveness of Balance Weights

Test evidence obtained while operating at a specific critical frequency indicated the influence of other modes on shaft performance at this speed. This fact became apparent when it was found that the measured deflections did not lie in a single plane. A further indication of noncoplanar mode shapes was suspected when balance weights, positioned according to the original concept for mode behavior and shape, did not improve the performance of the shaft. The angular positions of the weights were changed, sometimes as much as 180 degrees from the originally predicted position, to effect an improvement.

Because of the suspected presence of noncoplanar mode shapes and the fact that effective balance weight could not be predicted with the original approach, a series of tests was run to determine the most effective angle for the weight at each balance station. These tests were intended to determine the effectiveness of the balance weight in controlling deflection (inches per gram) as well as to determine the most effective plane for the balance weight.

Effectivity Data

Tests were conducted with a small balance weight located at various phase angles on all balance stations. Summary plots were constructed to show the effectiveness of a trial weight at various phase angles. Figure 106 shows the effectiveness of a weight at three phase angles located at balance station 5. The deflection and phase were measured at shaft station 4. The effectiveness of the weight was plotted for the second critical, the fifth critical, the sixth critical, and the top speed of the shaft. A polar plot of deflection and phase as measured at shaft station 4 is shown in Figure 107. Each balance station was investigated to determine the effectiveness of a similar weight at various angles and speeds. Shaft performance was always measured at station 4.

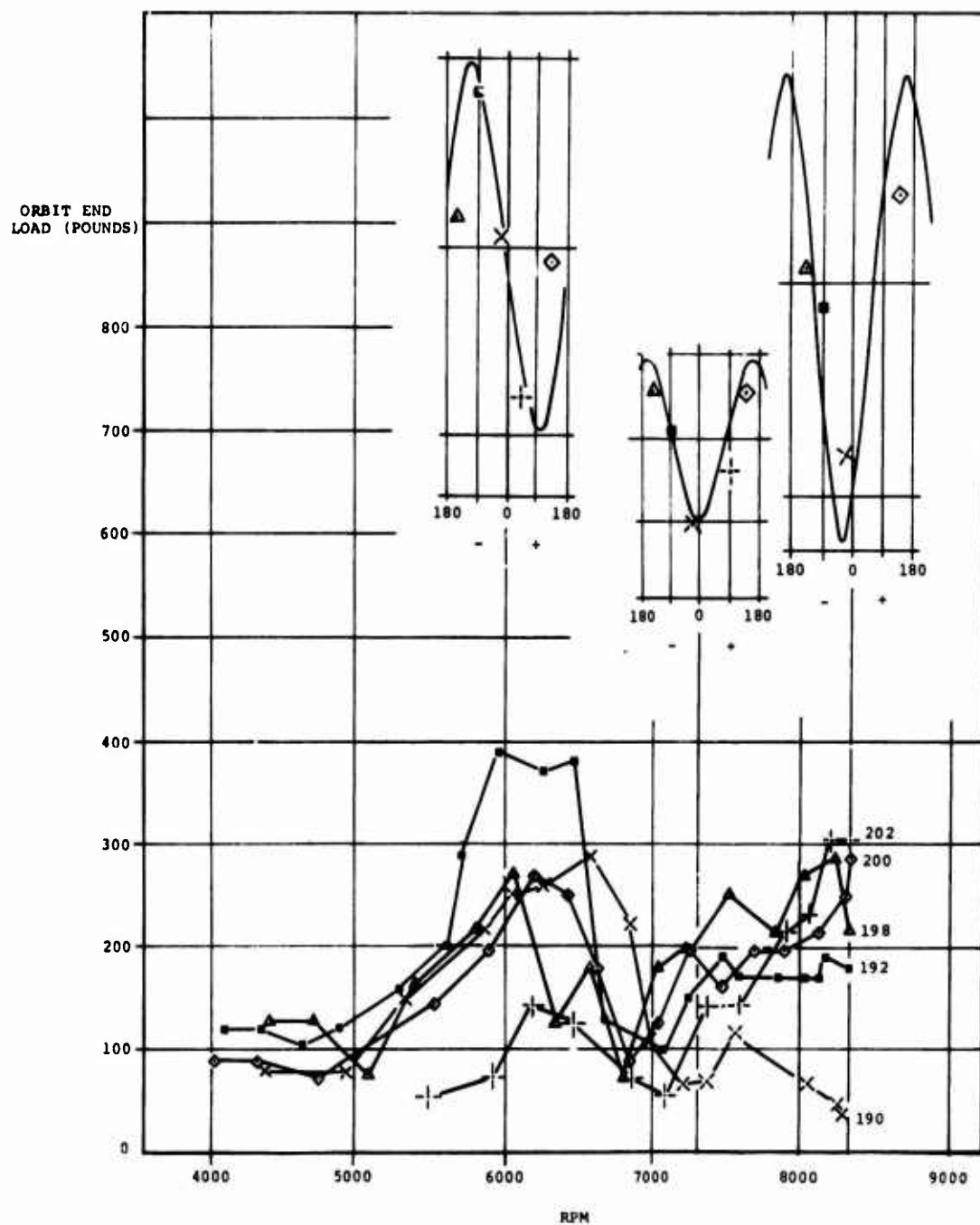


Figure 104. Balance End Load Test Series.

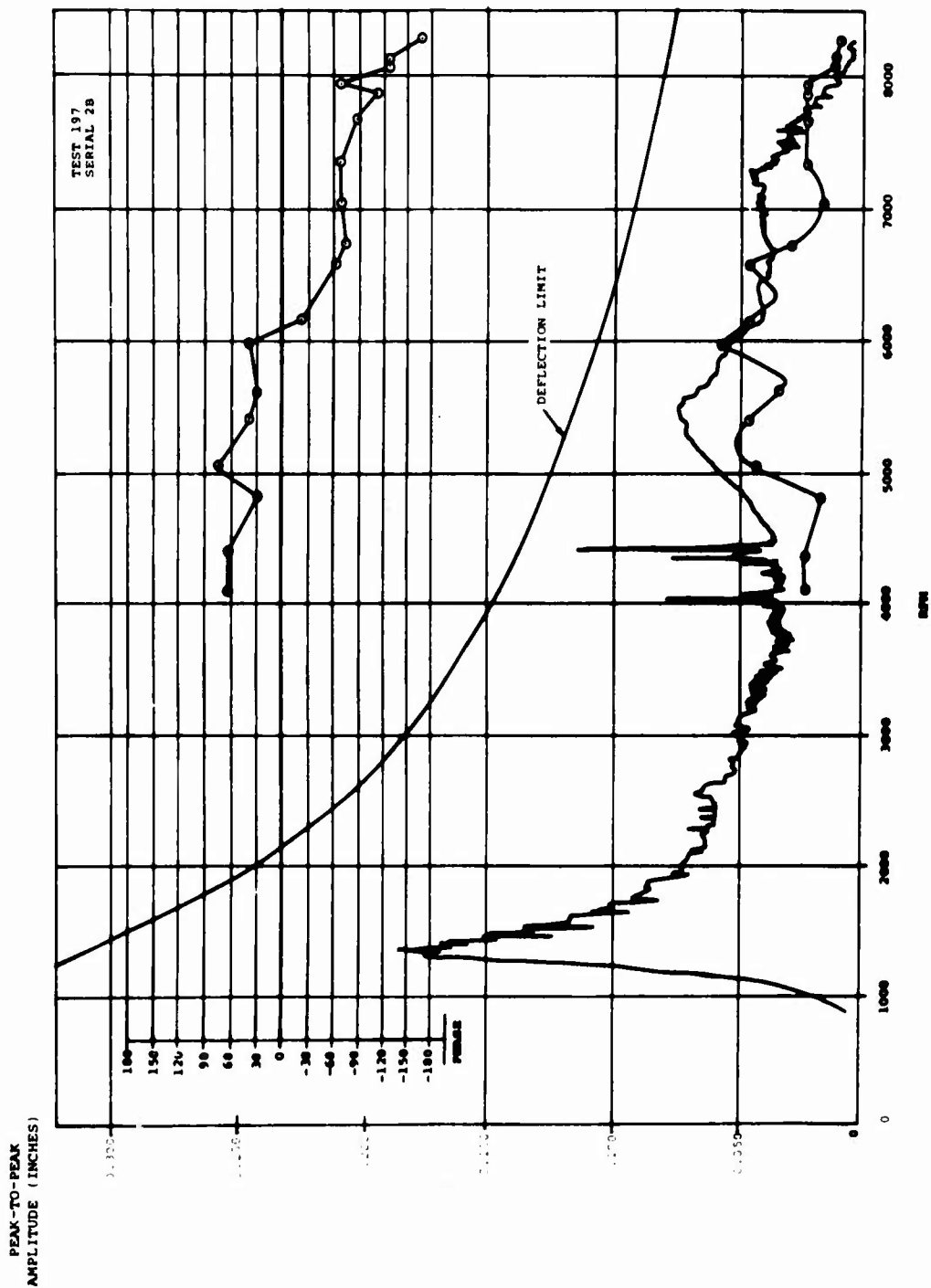
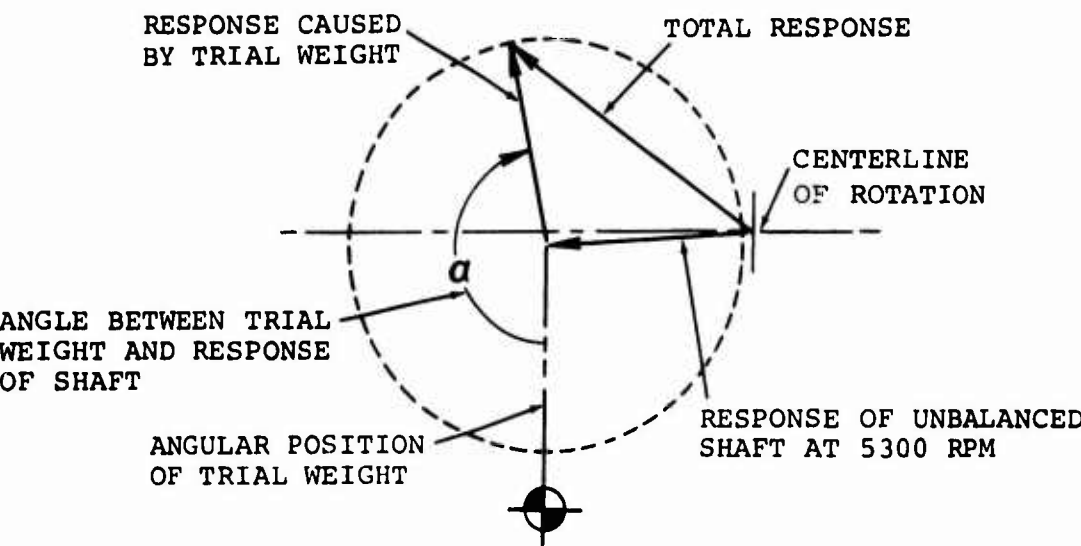


Figure 105. Deflection and Load Versus Speed After Balancing.

Shaft Balance Station		5	8	10	11	21	24	27
Figure Number	Deflection vs Speed	106	108	110	112	114	116	118
	Polar Plot	107	109	111	113	115	117	119

The effectiveness of a balance weight to change the deflection of the shaft at a given station was determined from the polar plots, where the deflection of the shaft at a given speed was shown without the trial weight and with the trial weight located at various phase angles. For a given rpm and trial weight location, the response to the trial weight held a constant or fixed relationship (see Figure 107). The amplitude of the response to the trial weight was constant since its radius vector traced a circular path as the angular position of the trial weight was varied.



The angle (α) between the trial weight and the resulting response was also a constant, as demonstrated when a shift in the angular position of the trial weight produced an identical shift in the angular position of the response vector (see Figure 107).

In essence, the effectivity testing is an experimental determination of the dynamic *influence coefficients* between the balance stations and the measurement station (shaft station 4). The effectivity of the trial weight in controlling shaft deflection is indicated by the diameter of the circle which encloses the response vectors caused by the trial weight. The most effective angle for the trial weight was obtained from the auxiliary curves constructed from the data given on the deflection versus frequency plots. The auxiliary curves resemble sine waves, and the best angle for the balance weight is that angle which corresponds to the minimum deflection. The most effective angle can also be obtained from the polar plots and the response vector circle if the angle of the trial weight is used to orient an azimuth scale (see Figure 107). The best angle for balance weight can be read directly from the azimuth scale. The optimum weight is the weight that reduces the total response vector to zero.

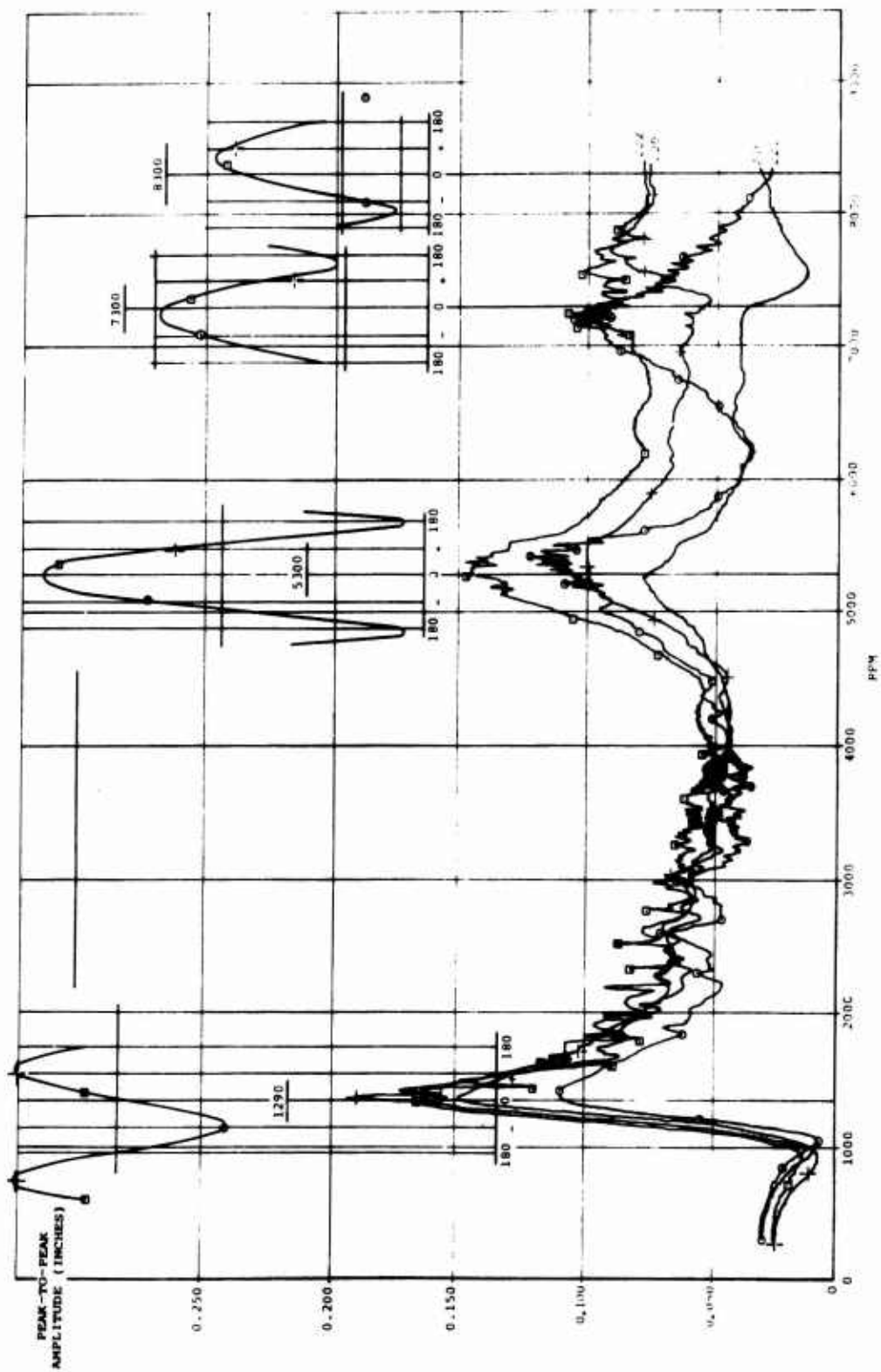


Figure 106. Deflection Versus Speed With Trial Weight at Station 5.

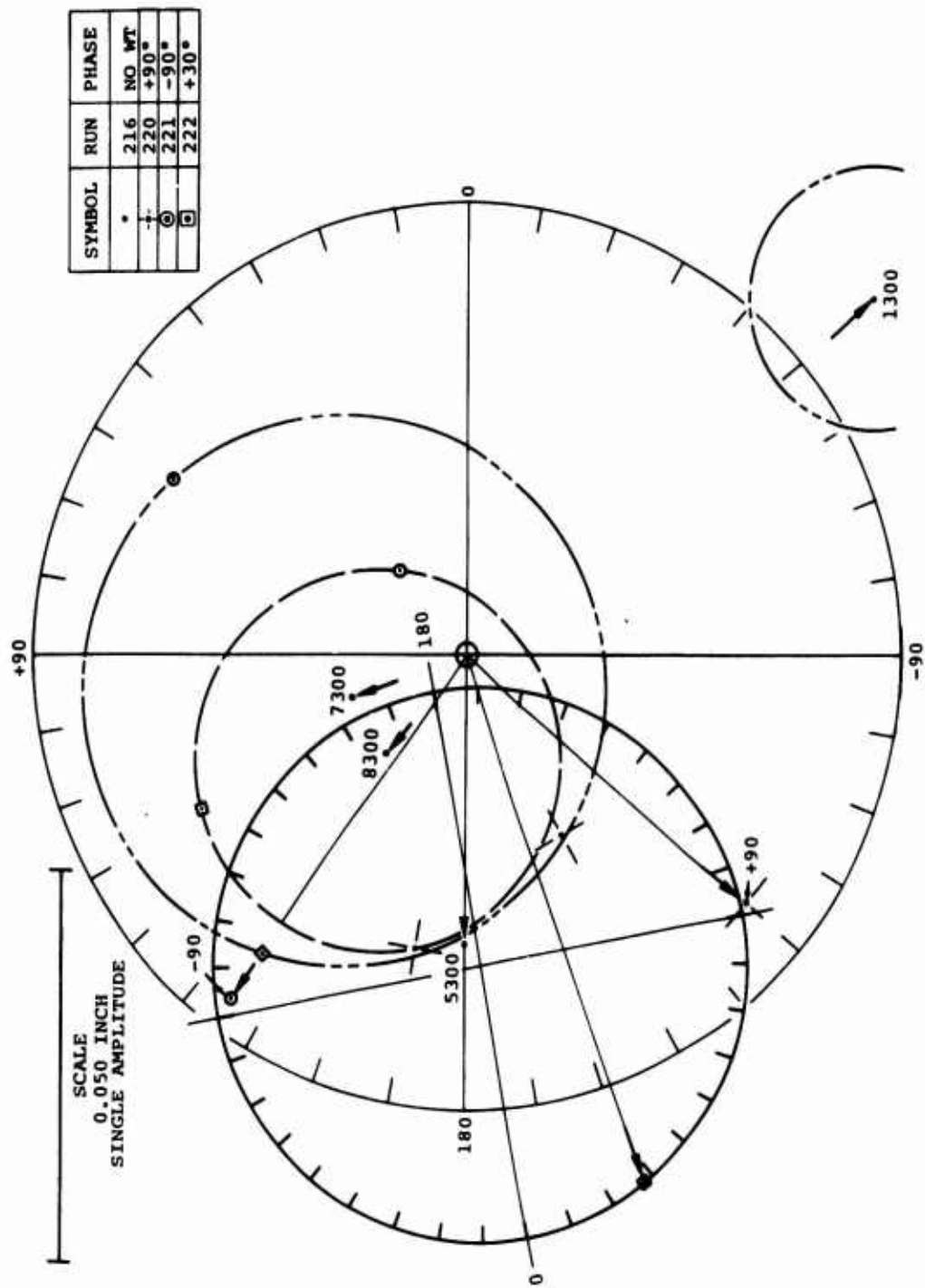


Figure 107. Polar Plot of Trial Weight at Station 5.

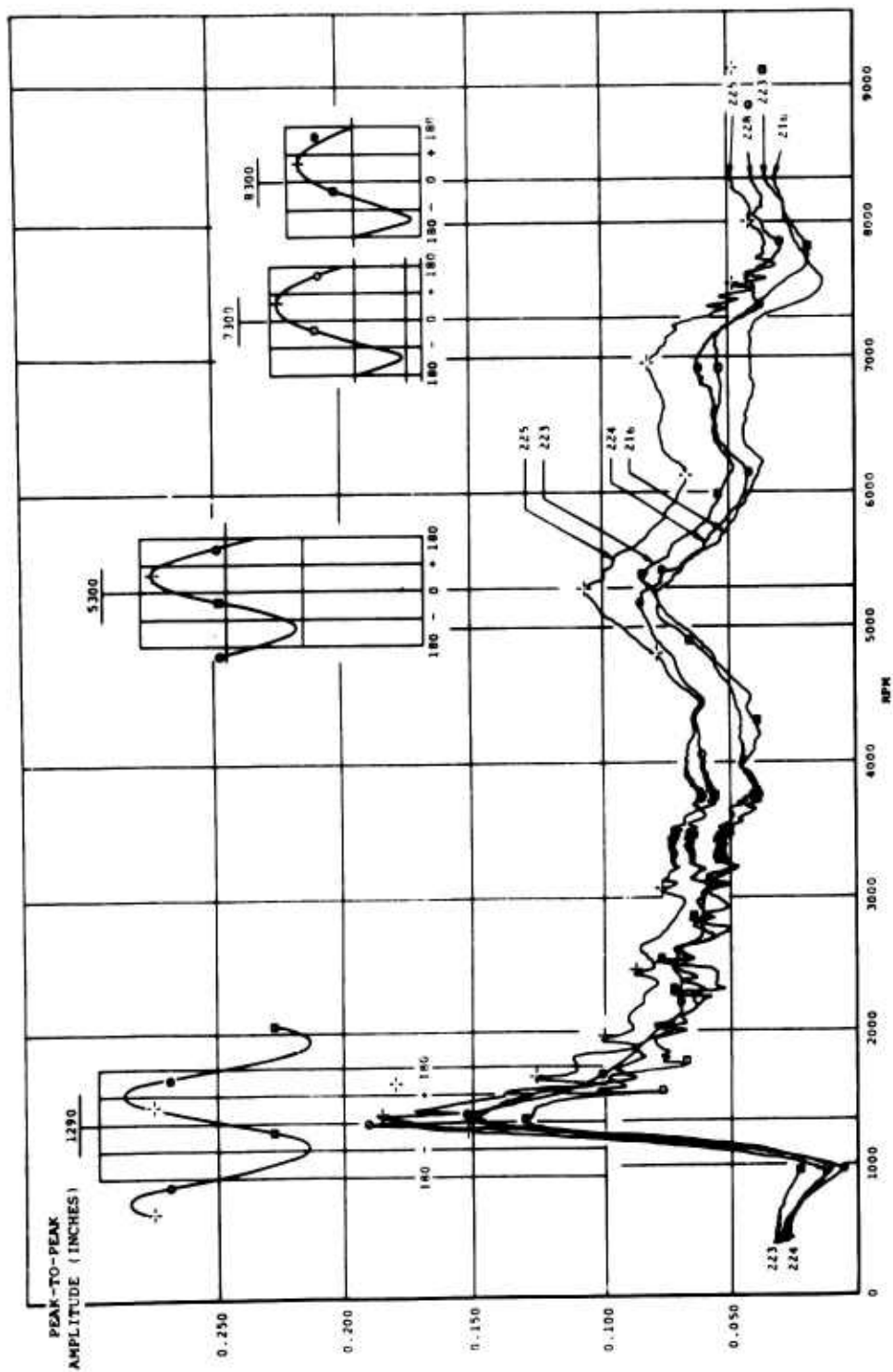
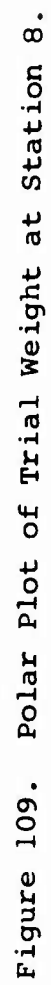


Figure 108. Deflection Versus Speed With Trial Weight at Station 8.



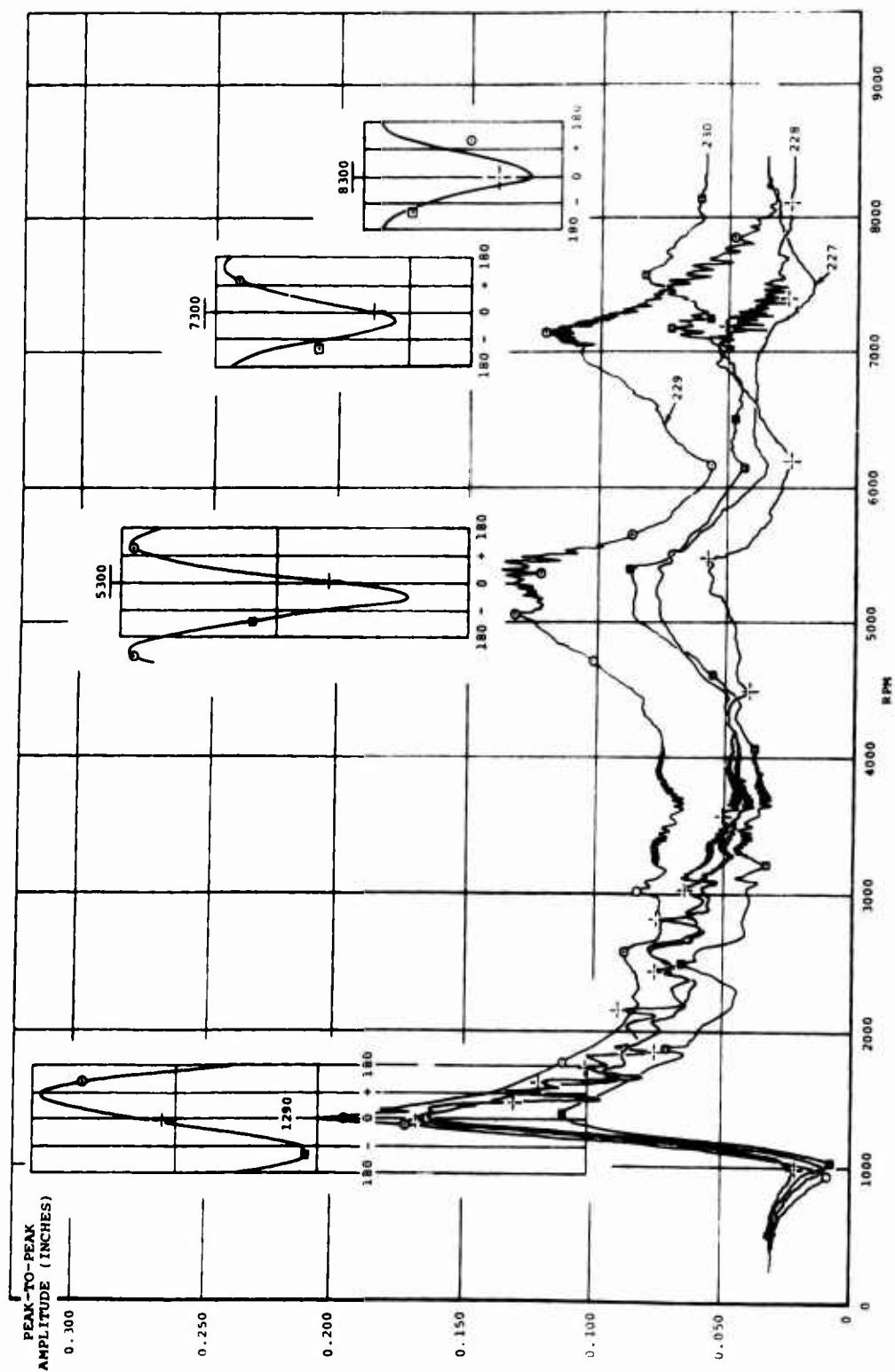


Figure 110. Deflection Versus Speed With Trial Weight at Station 10.

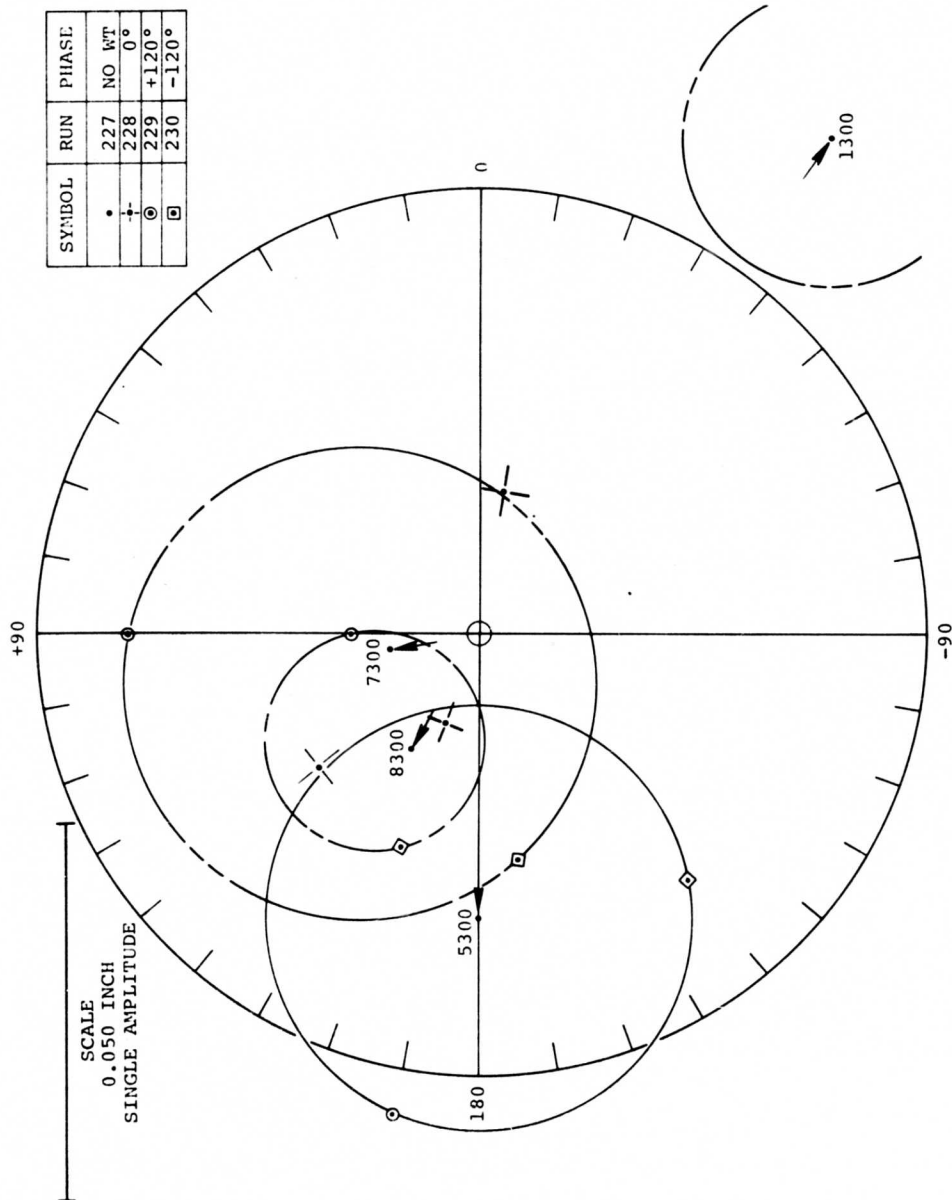


Figure 111. Polar Plot of Trial Weight at Station 10.

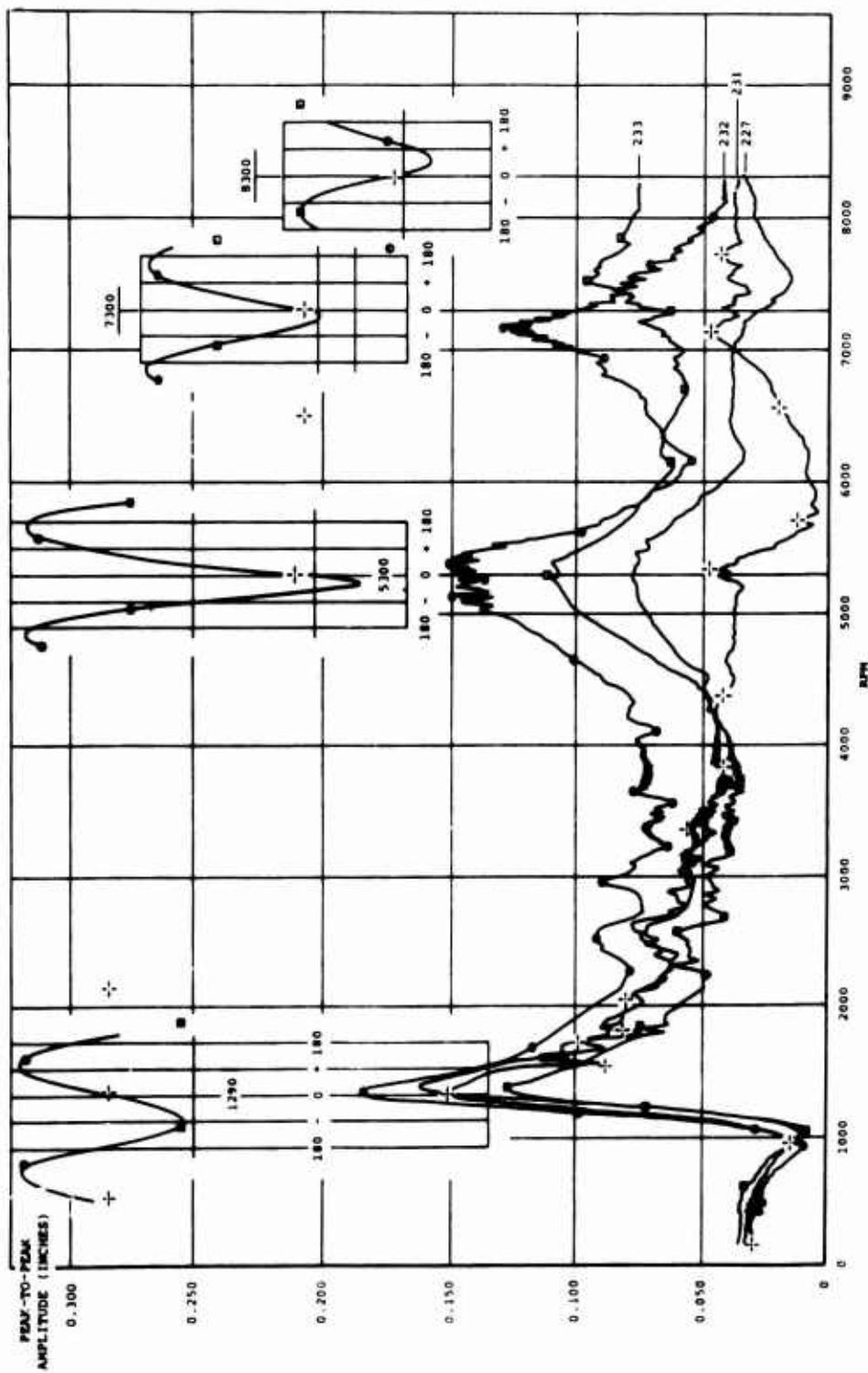


Figure 112. Deflection Versus Speed With Trial Weight at Station 11.

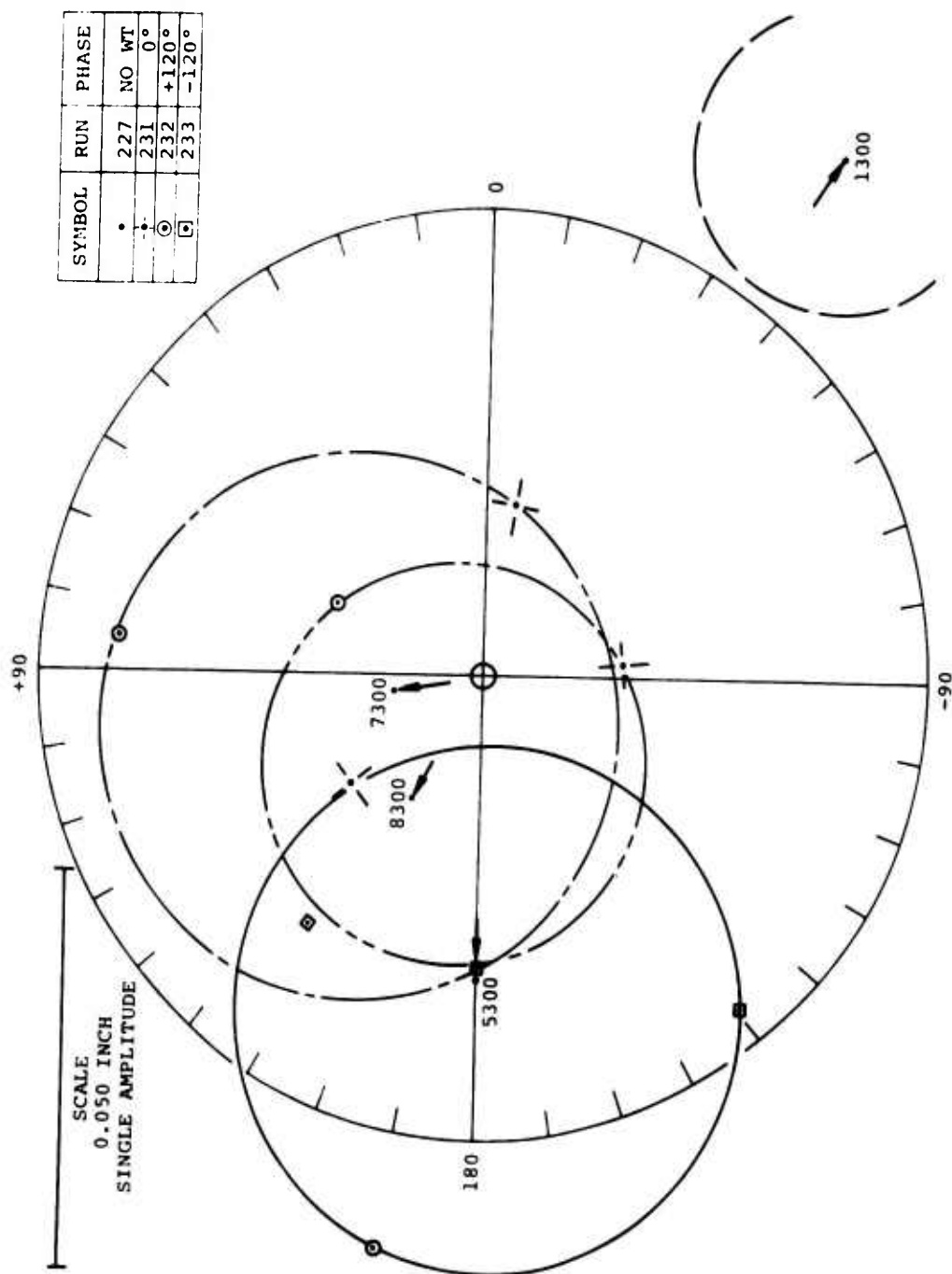


Figure 113. Polar Plot of Trial Weight at Station 11.

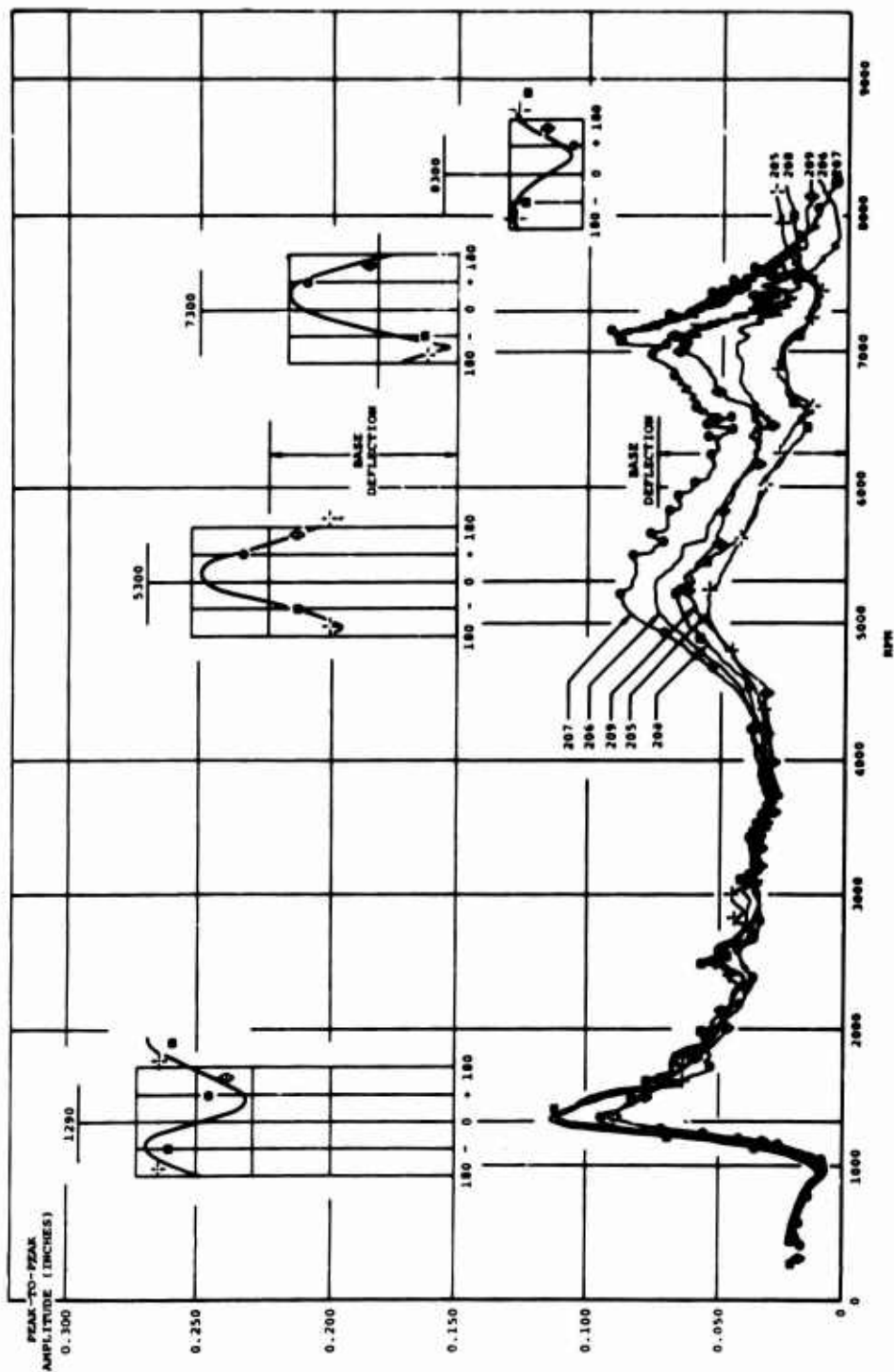


Figure 114. Deflection Versus Speed with Trial Weight at Station 21.

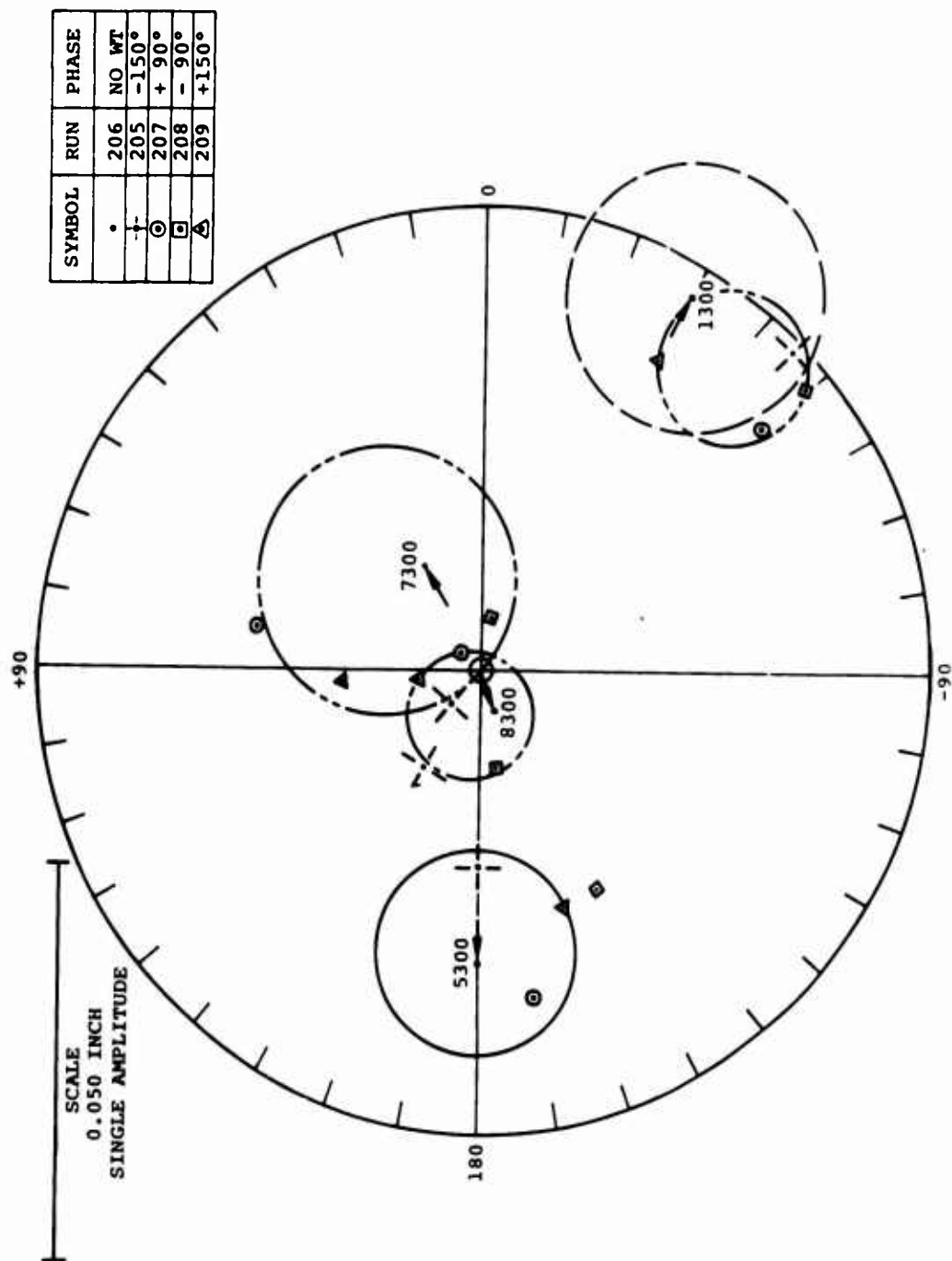


Figure 115. Polar Plot of Trial Weight at Station 21.

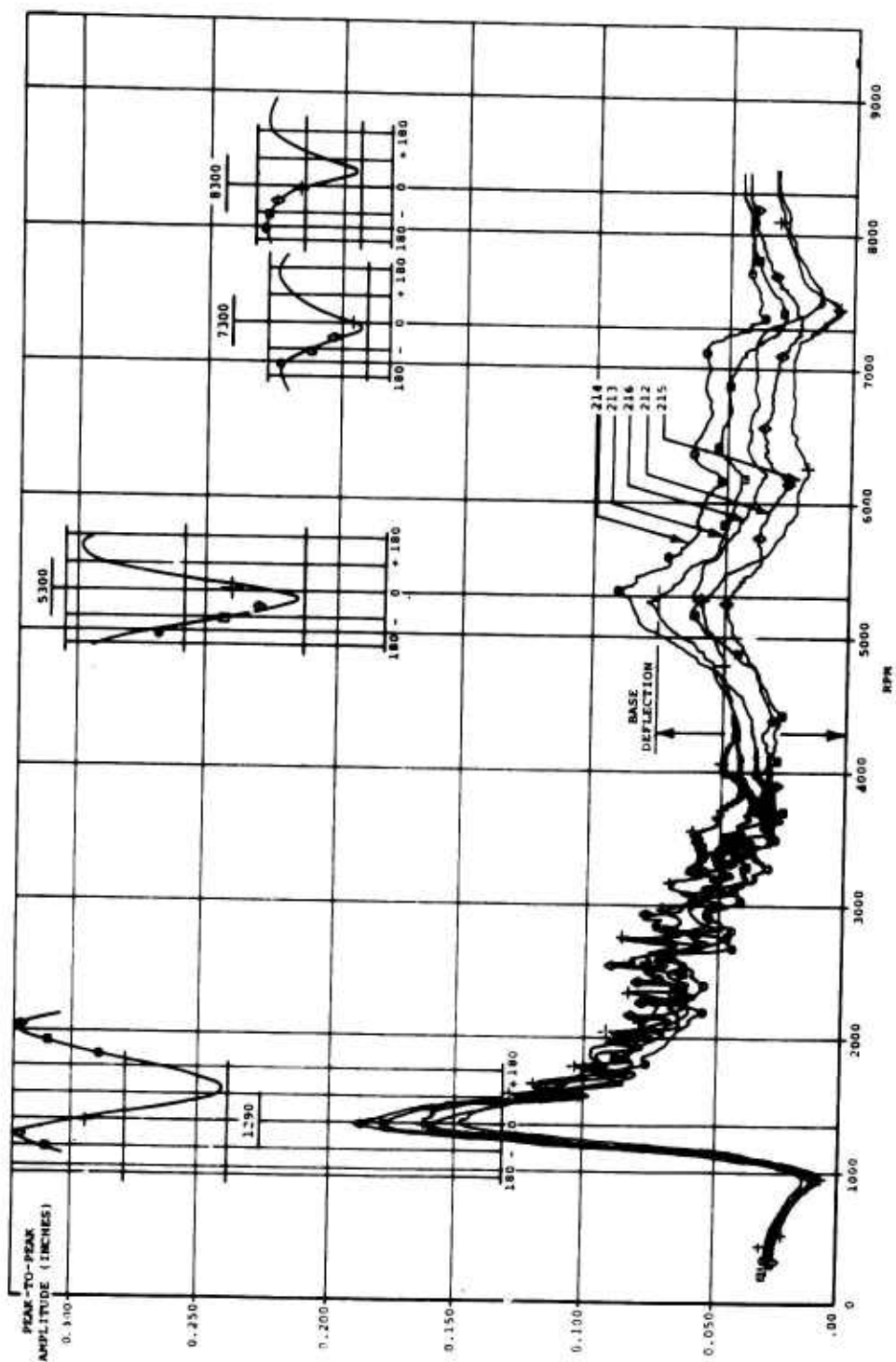


Figure 116. Deflection Versus Speed With Trial Weight at Station 24.

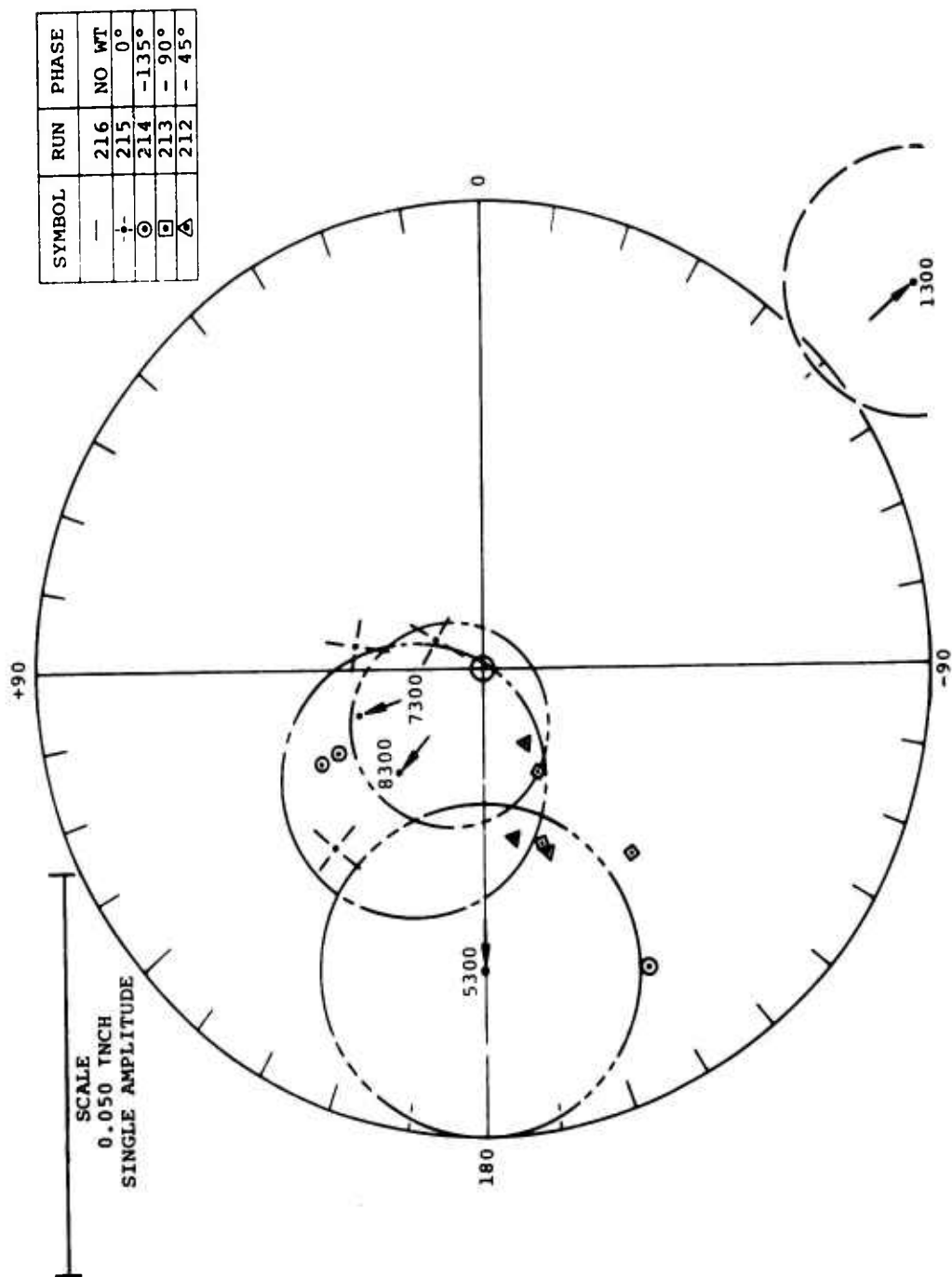


Figure 117. Polar Plot of Trial Weight at Station 24.

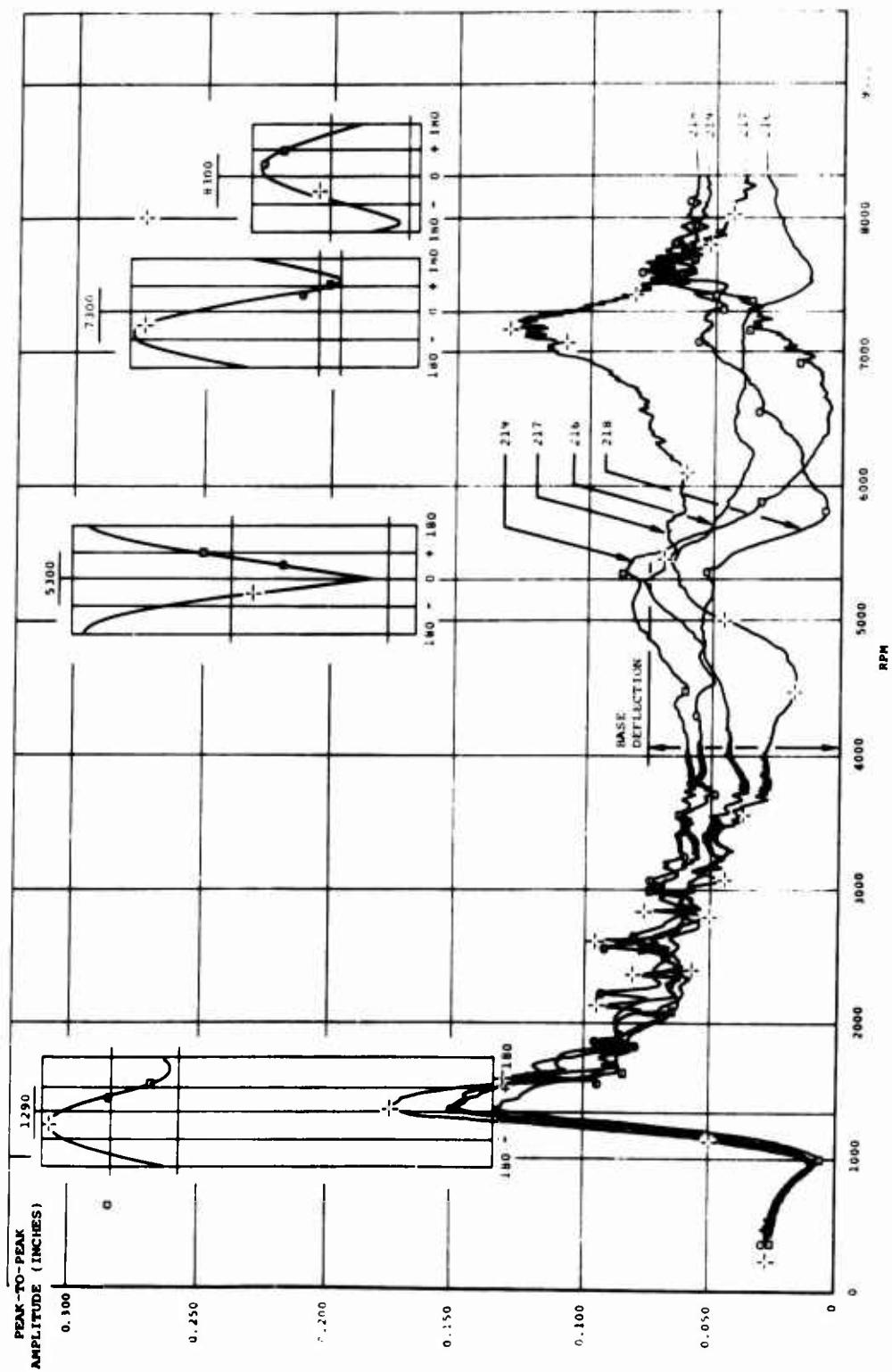


Figure 118. Deflection Versus Speed With Trial Weight at Station 27.

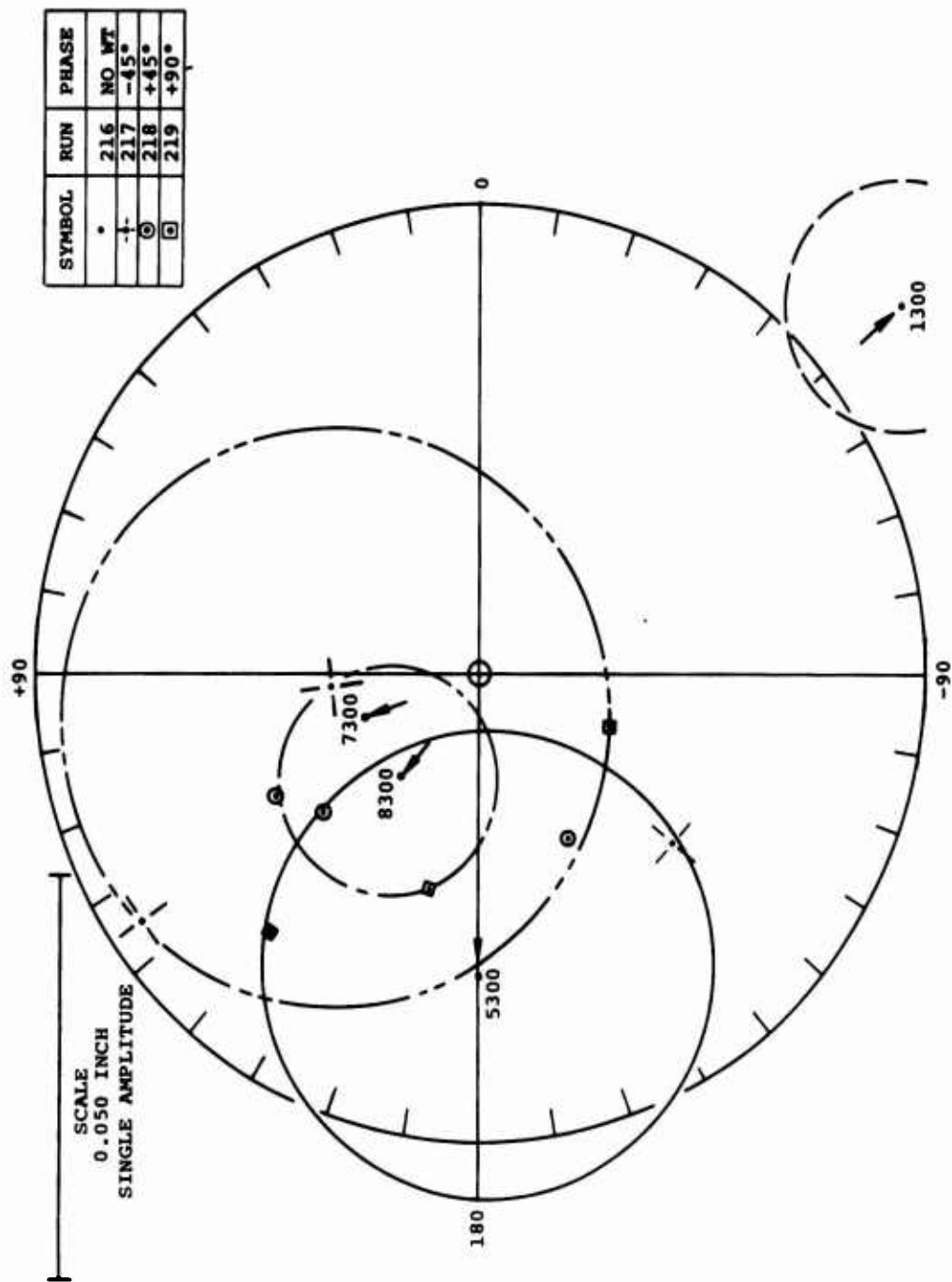


Figure 119. Polar Plot of Trial Weight at Station 27.

The results of this series of tests were further reduced by combining the response vectors from all balance stations at a given rpm by plotting both magnitude and phase. This polar plot of amplitude and phase is shown as the end view of a scale-model shaft (see Figure 120). An average effectivity plane was determined by inspection of the response vectors. A projection of the response vectors to the average effectivity plane was the basis for constructing the mode shapes in Figure 120. This figure presents effectivity mode shapes with the optimum angle for balance weight shown by a radial line on each of the circles in each figure. The best angle is shown for each speed of interest and at each balance station tested. As with the unbalanced shaft, the response to the trial weight was a combination of a number of modes. If the response were due to a single mode, the optimum angle for the balance weight would have been in a single plane. The fact that this optimum angle did not lie in a single plane, especially at the higher critical speeds, indicated that the response was a result of the superposition of modes as mentioned previously. An advantage of plotting modes in this manner is that the effect of static deflection is no longer present and the resulting mode more nearly represents the true mode shape. Provided there is no gross difference in physical properties, it is reasonable to expect that the *influence coefficients* (the diameters of the circles enclosing the response vectors) determined during this phase of testing will be valid for all shafts of the same configuration. The amplitude and phase of deflections from each shaft will be different, and if this information is known, it will be a relatively simple matter to graphically apply the known correction factor of the *influence coefficient* to remove the undesirable amplitude. Information from Figure 120 should facilitate placement of balance weights to improve unsatisfactory performance of any similar shaft over its entire speed range.

To illustrate how this diagram would be used to experimentally balance a shaft, a hypothetical case is presented for balancing a shaft at a second critical speed of 1,300 rpm. One balance weight reduces the deflection of a shaft an amount equal to the effectiveness of the weight at the station used. Weights placed at antinodes are the most effective. Weights at nodes will have no effect on the mode whatsoever. Similarly, the phase of a balance weight effects shaft performance. If properly placed, it will decrease shaft deflection. If it is placed 180 degrees out of phase, shaft deflection will increase. If it is 90 degrees out of phase, it will have a neutral effect on the shaft at that speed. These two factors are the major considerations in selecting the planes and angles for the balance weights to be used.

To balance the second critical speed, there are many choices for the location of the weights:

- A single balance weight could be used.
- The single weight could be placed on either loop of the deflected shaft.
- The single weight could be placed at any balance station by relating the magnitude of the weight to the effectiveness of the station selected.
- Two or more weights could be used.
- The multiple weight could be placed on one or both loops.

The requirement for balance is that the total amount of weight, after considering the effectiveness of the station and phase, must be equal to the unbalance in the system. If this requirement is met, the shaft will run true at this speed. Stations and weights are selected to

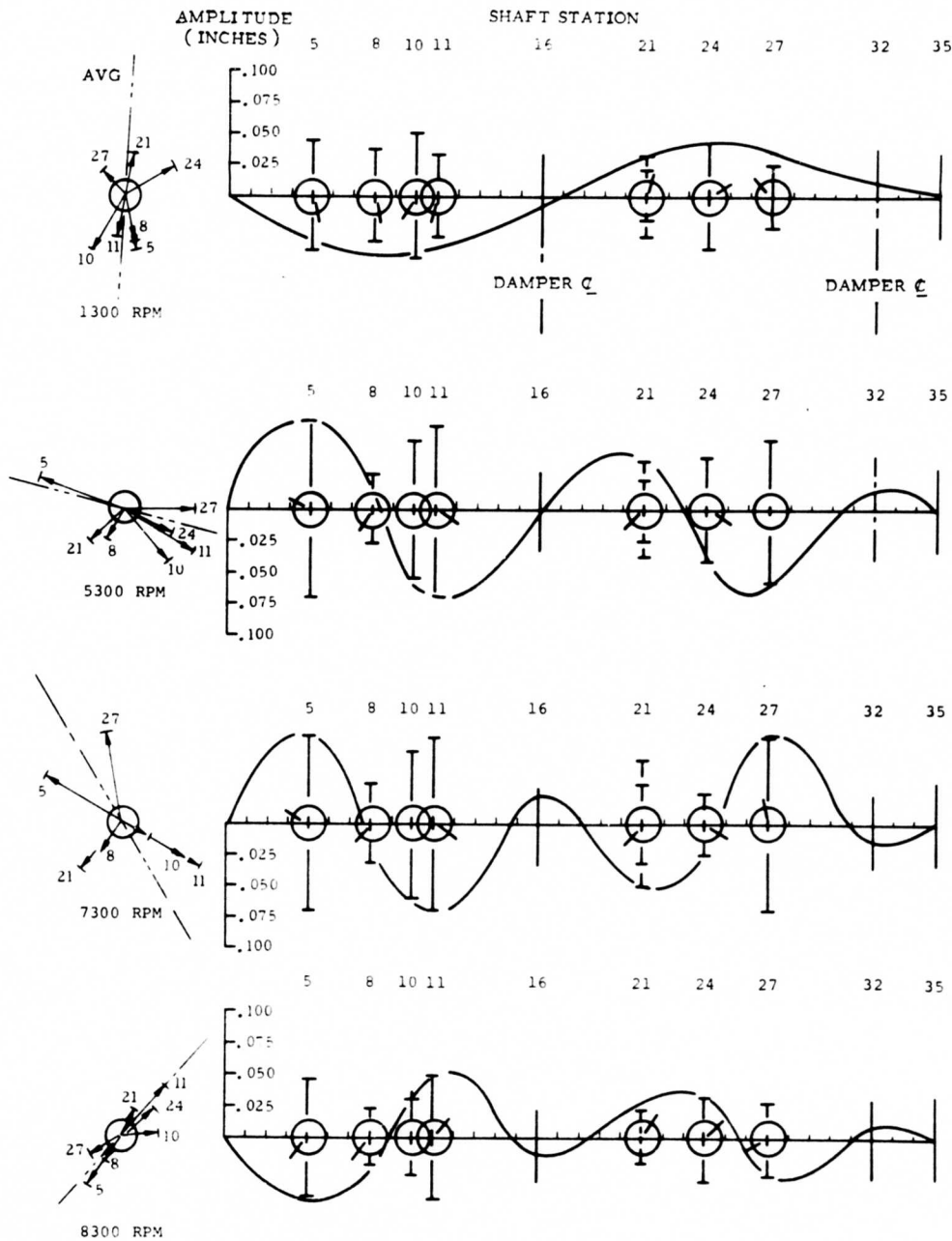


Figure 120. Developed Modes From Effectivity Tests.

work in unison to balance lower speeds and to work against each other at higher speeds. An example of this would be a balance weight placed at station 5 and one at station 11, both having the same phase. These weights work together to correct deflections in the second mode (1,300 rpm) but oppose each other at the fifth mode (5,300 rpm).

Stations 5 and 11 have about the same effectiveness in the fifth mode but with opposite signs. This conditions holds true for the sixth mode at 7,300 rpm and for the top speed of 8,300 rpm as well.

The products of weight and effectiveness are added algebraically as shown in the table below:

RPM	Station	Weight	Effectiveness	Product	Total
1,300	5	10	- 4.3	- 43	-93
	11	10	- 5.0	- 50	
5,300	5	10	- 8.5	- 85	- 5
	11	10	+8.0	+80	
7,300	5	10	- 8.5	- 85	0
	11	10	+8.5	+85	
8,300	5	10	+6	+60	0
	11	10	- 6	- 60	

Test Results With Effectivity Data

This approach was used to experimentally balance the second critical speed of the test shaft. The best combination of weights was used, and the shaft was run to the fifth critical speed. Figure 121 shows the best results obtained for this speed (5,300 rpm).

An analysis of phase information from this test indicated that further improvement of the fifth critical speed would cause the sixth to diverge. The fifth was therefore intentionally overbalanced slightly so that an additional balance weight could correct both the fifth and the sixth critical speeds at the same time.

The addition of weight in this manner produced the best shaft performance to date, and the result is shown in Figure 122. Mode shapes were obtained for this configuration and the secondary mode shape was still evident (see Figures 123 through 126).

The shaft was balanced with the simulated aircraft structure locked out. The damper structure was much stiffer than that expected in the aircraft, and it was desirable to compare the effect this change in stiffness had on the performance of the shaft. The locking mechanism was removed from the damper structure, returning the test rig to stiffness simulating the aircraft installation. Figure 127 is a comparison of a test run with flexible damper structure and a test run with the damper structure made rigid. The peak at 3,500 rpm was tentatively identified as resulting from a resonant condition of the damper-structure combination; the increased amplitude at 5,300 rpm occurred because the increased flexibility reduced the effective damping at this speed. The remainder of the test run shows very little effect.

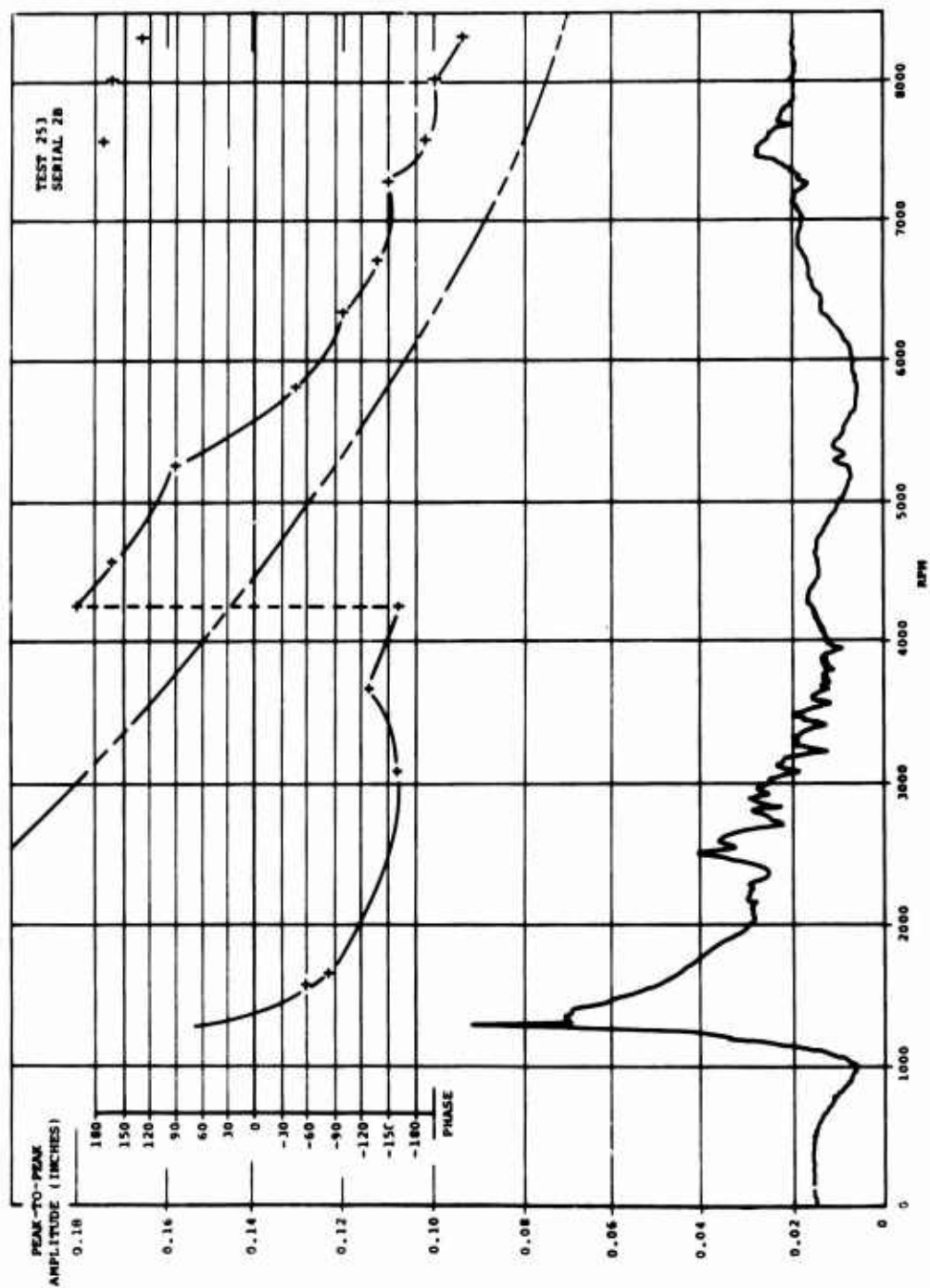


Figure 121. Effectivity Data Balance for 5,300 RPM.

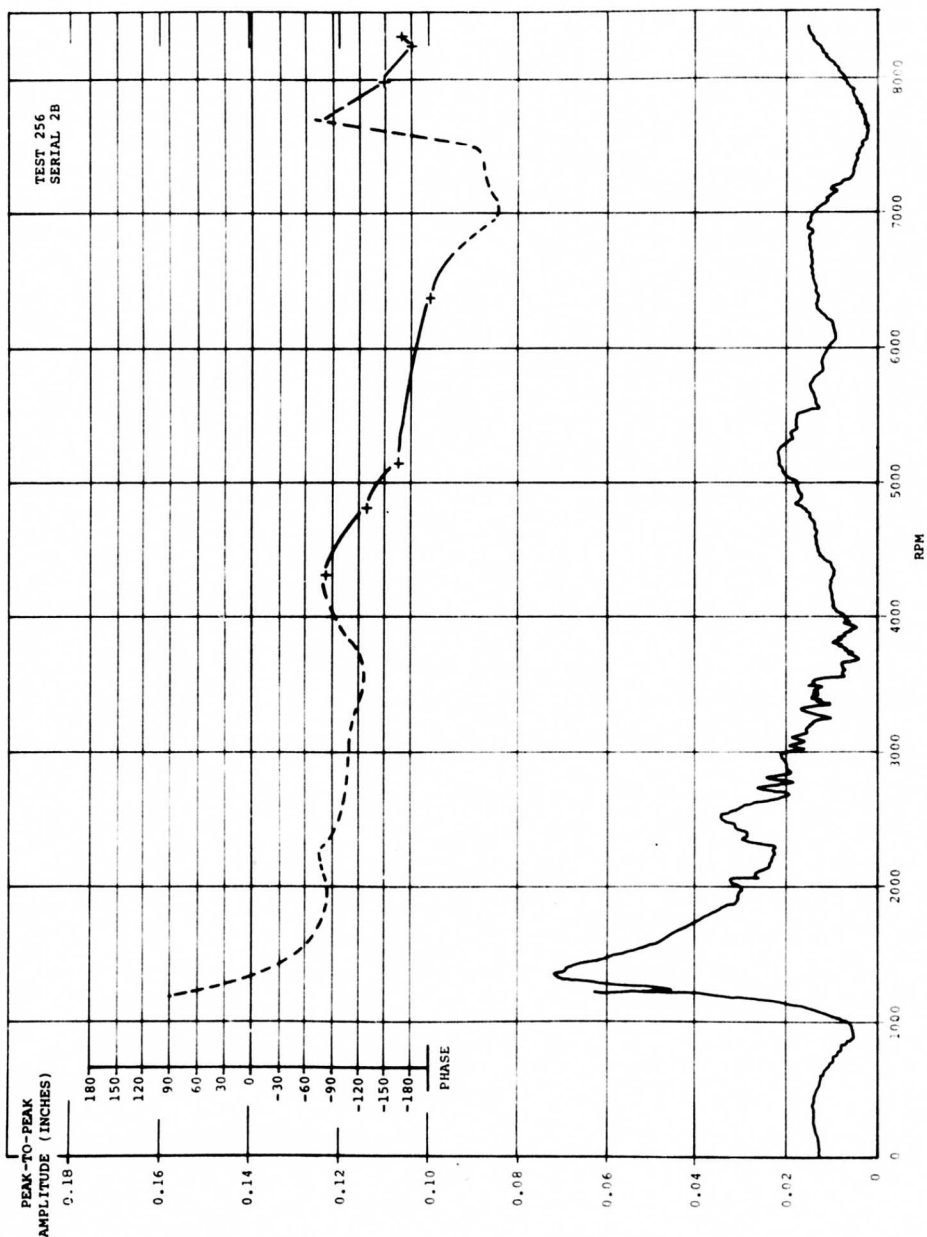


Figure 122. Effectivity Data Used for Balance at 7,300 and 8,300 RPM.

SCALE
0.050 INCH

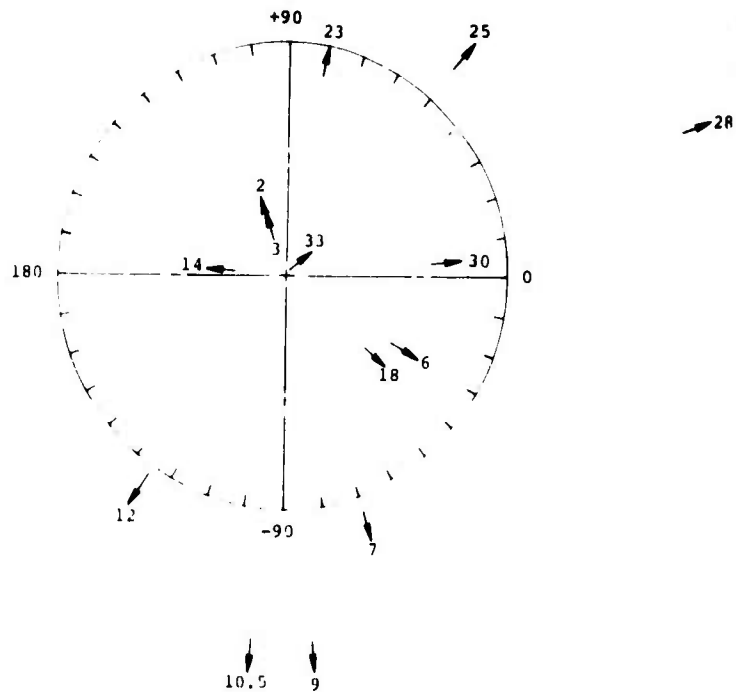
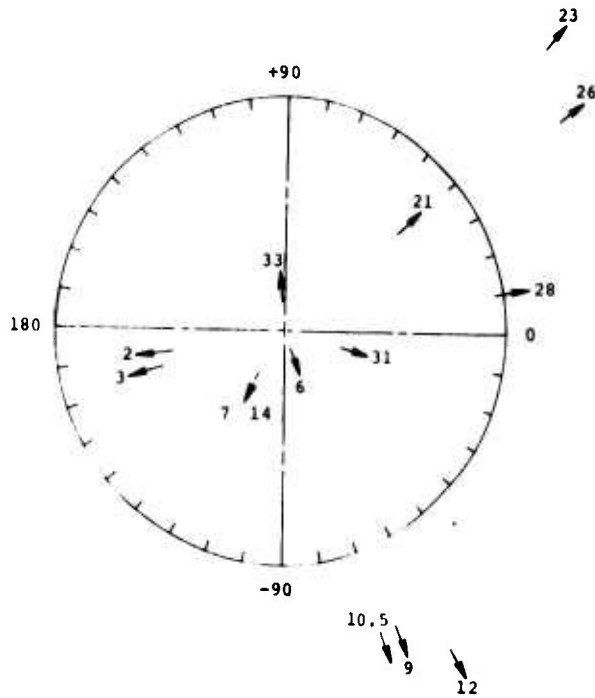
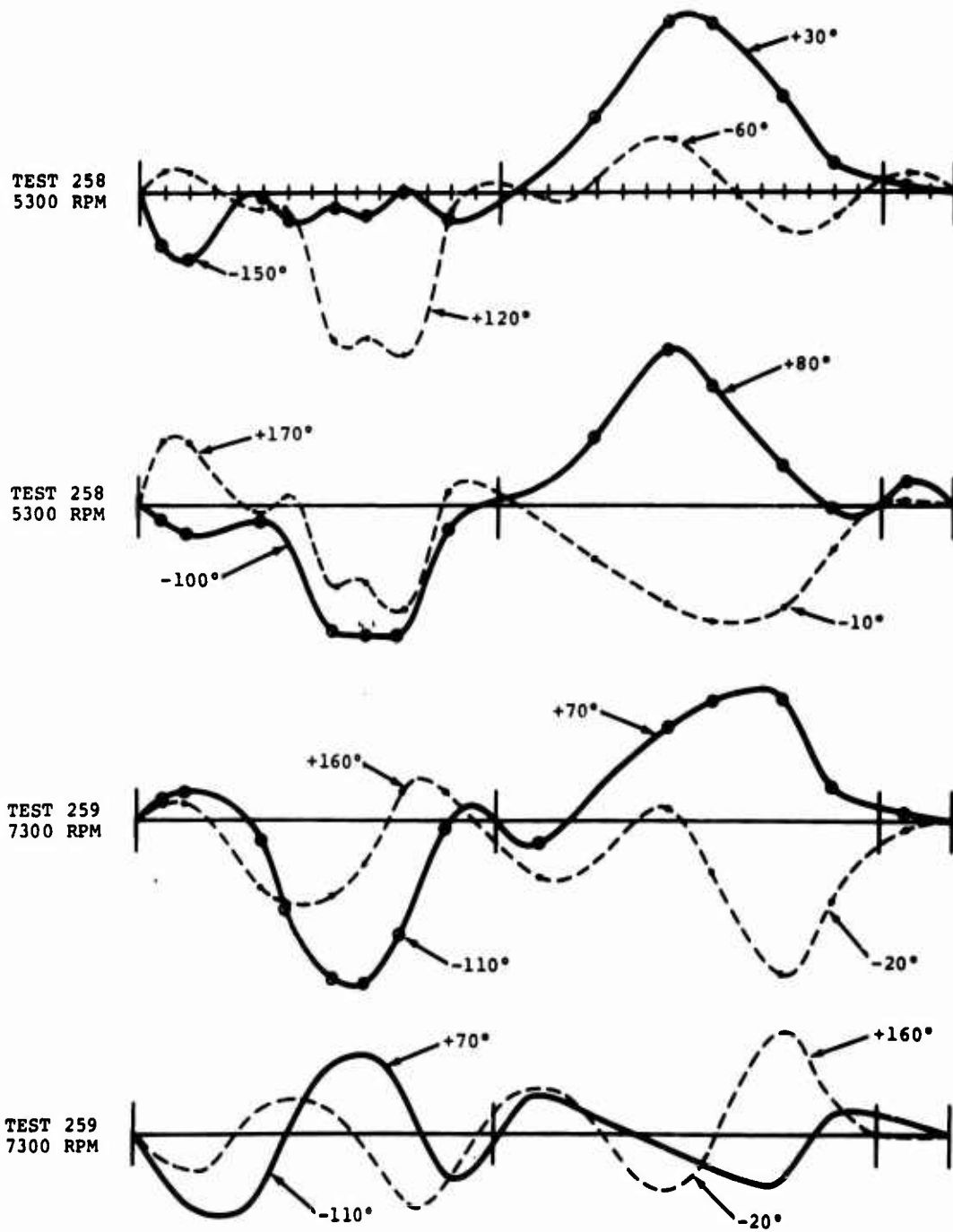


Figure 123. Polar Deflection at 5,300 and 7,300 RPM.



AFTER SUBTRACTING ω_2

Figure 124. Deflection Shapes in Two Planes.

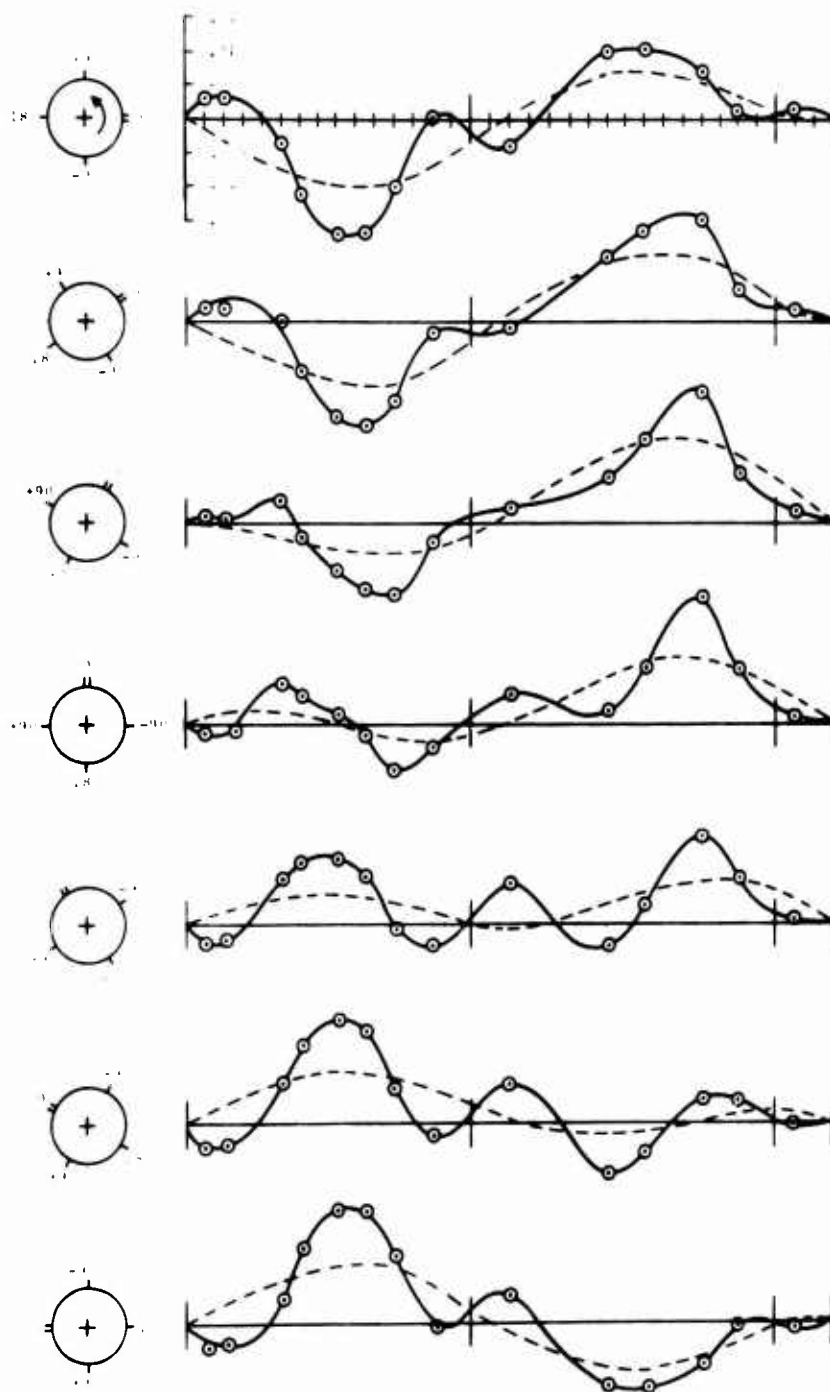


Figure 126. Time History of Shaft Deflection for 180 Degrees of Shaft Rotation at 7,300 RPM.

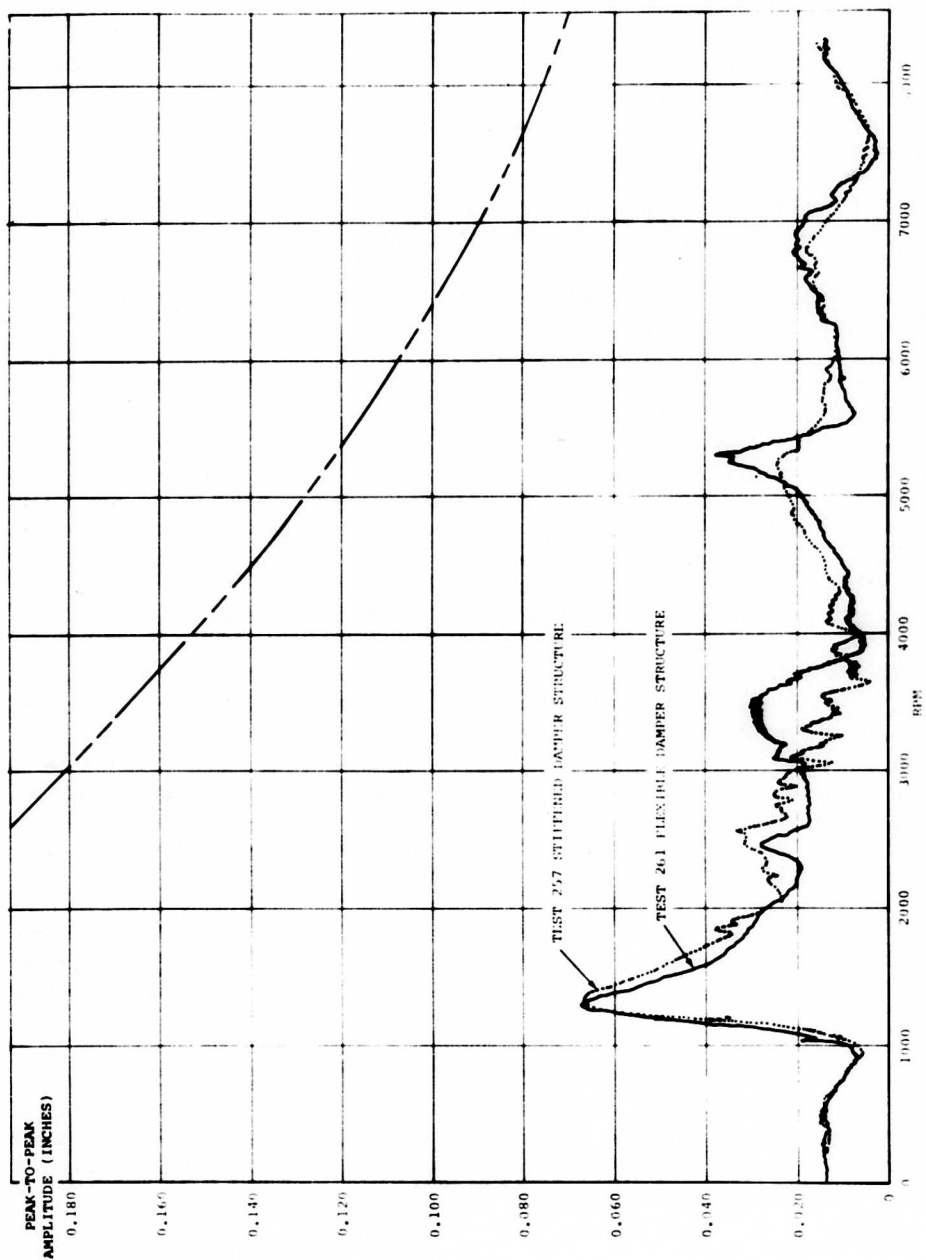


Figure 127. Stiffened Versus Flexible Damper Structure.

The shaft was intentionally unbalanced and run past the second critical speed to establish a baseline. A shaft guard was installed so that the effect of the shaft striking the guard could be observed during a test run. It was not known at the time if the guard would excite the motion and cause additional deflection. The flat spot on the top of the deflection peak in Figure 128 shows that the deflection was limited by the guard. Inspection of the specimen showed scrub marks on the protective covering over the strain gage wire pack on the outside of the shaft in this area. Only one wire pack was marked, indicating that the whirling was steady, and the shaft did not tend to rattle around inside the guard.

The shaft in Figure 122 was balanced as well as is possible with present technology and in the time available. It was not acceptable for a flight-test specimen for two reasons:

- The balance weights were an experimental type intended for rapid installation and adjustment.
- The balance weights on the end of the shaft were attached to part of the test machine, not the shaft itself.

Permanent balance weights were substituted for the temporary ones, and the balance weights for the end load were added to the test shaft. The first tests after installing permanent balance weights on the shaft were run to reduce the orbit end load to a minimum. Figure 129 shows the deflection of the shaft after the optimum weight of 18 grams was installed on the end of the shaft. The most effective angle was found to be -80 degrees. A sharp peak showed up at 5,300 rpm, and a series of tests was run to reduce the deflection at this speed.

An interesting characteristic was observed while testing for the optimum balance weight. In one test, 21.9 grams was added to shaft station 24 at -80 degrees. In another test, 29.2 grams was added. Both weights were intended to affect the performance at the fifth critical speed of 5,300 rpm only. The two test runs are presented in Figure 130. One test run shows higher deflections before the critical and lower deflections immediately after passing it. The other, with a slightly heavier balance weight, shows lower deflections before the critical and higher ones immediately beyond it. This indicates that there is a limit to the performance improvement that is possible with experimental balancing.

These two test results also show the selective response that is possible over a narrow speed range without affecting other speeds. Balance weights located at station 24 and at the proper angle will affect deflections of the shaft only in the immediate vicinity of the fifth critical speed of 5,300 rpm.

The 21.9-gram balance weight (Figure 130) produced the best performance measured to date. This performance is acceptable in terms of deflection, bending stress, damper motion, and temperature. The orbiting end load is higher than desired, but this factor is so sensitive to the application of small balance weights that it appears doubtful if practical overall improvement is possible with the existing instruments.

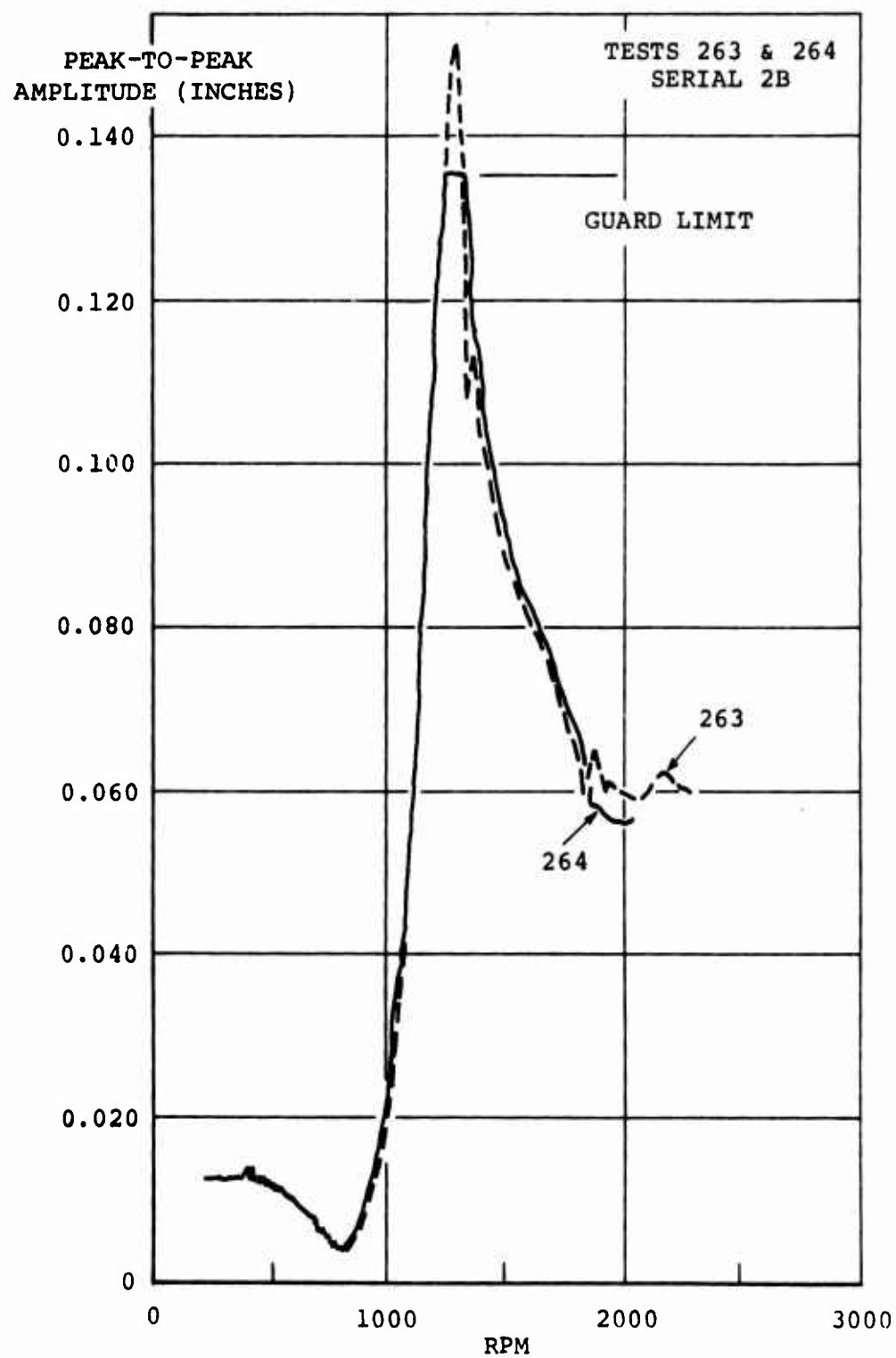


Figure 128. Intentionally Unbalanced To Hit the Guard.

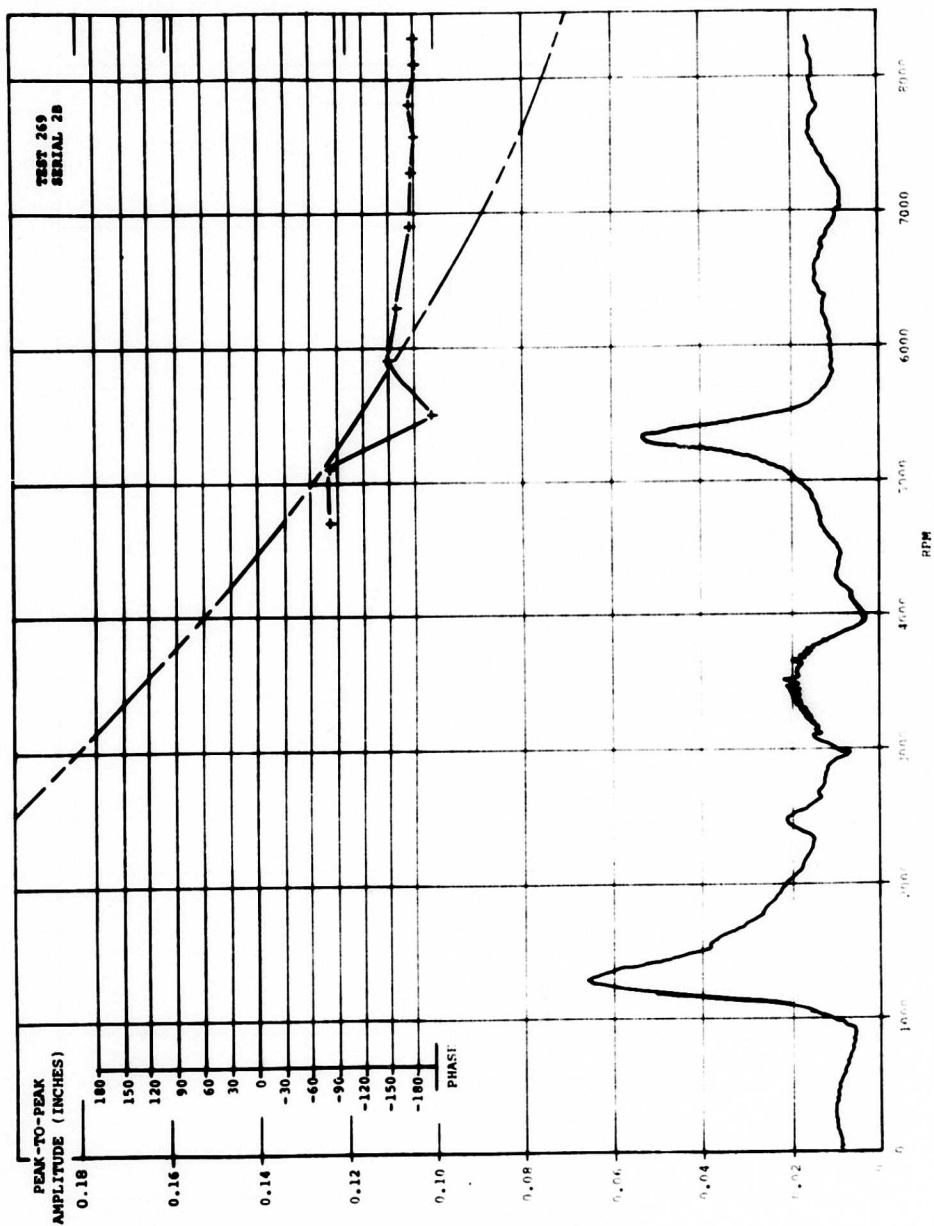


Figure 129. Substitution of Permanent Balance Weights.

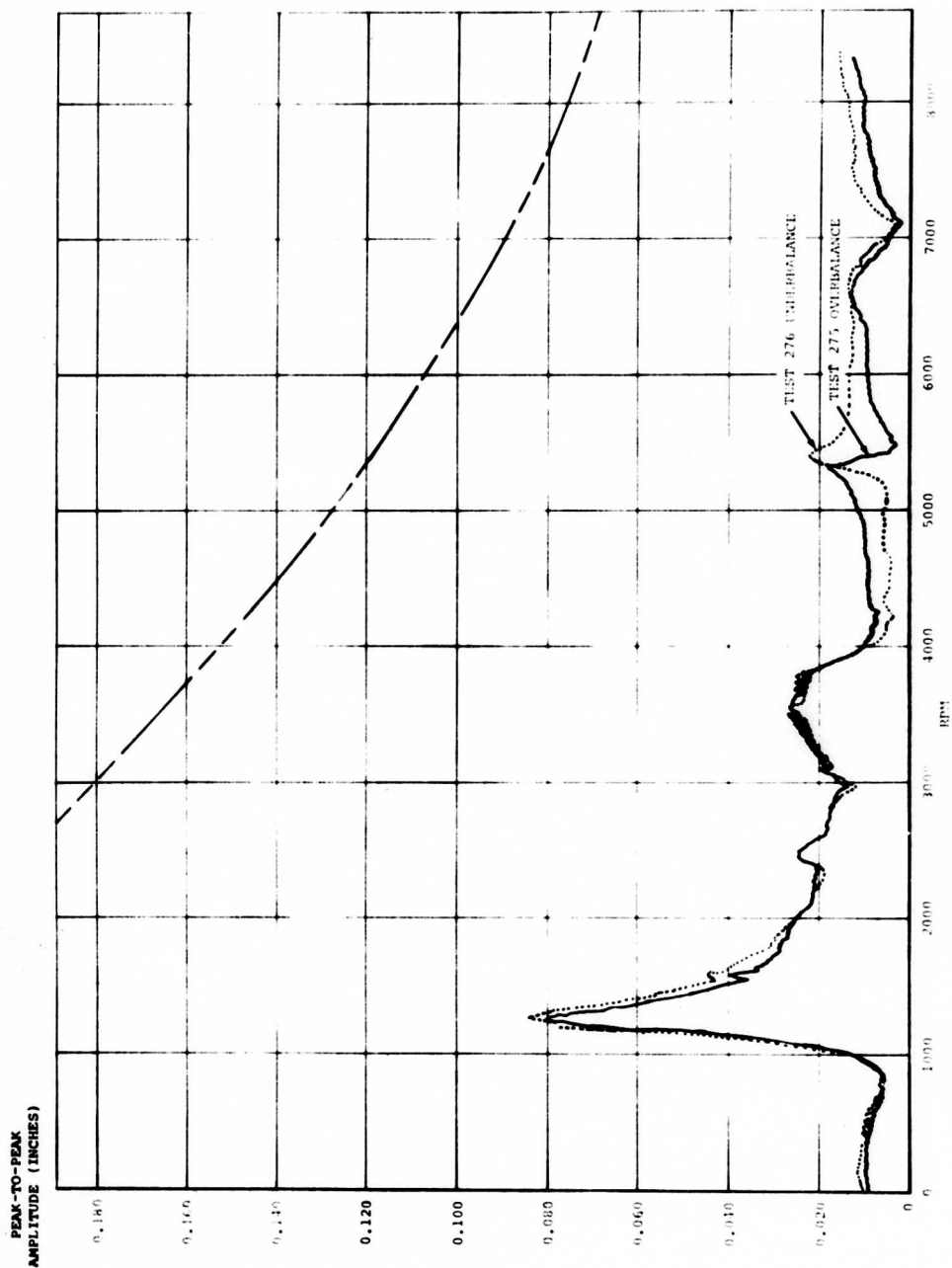


Figure 130. Effect of Under- and Overbalance on the fifth Critical.

TEST DATA FROM BALANCED SHAFT

Performance data taken from the tests of the shaft in final configuration are listed below and presented in the following illustrations.

	Figure
Shaft Deflection and Phase vs. Speed	
Station 3.5	131
Shaft Bending and Phase vs. Speed	
Station 4	132
End Load and Phase vs. Speed	
Station 1	133
Damper Deflection and Phase vs. Speed	
Station 15.5	134
Station 31.5	135
Shaft Deflection and Phase vs. Speed	
Station 24	136
Polar Plots of Deflection	
8300 rpm and 7300 rpm	137
5300 rpm and 3700 rpm	138
2300 rpm and 1300 rpm	139
Time History of Fixed System Displacement (Developed from Polar Plots of Deflection)	
8300 rpm	140
7300 rpm	141
5300 rpm	142
3700 rpm	143
2300 rpm	144
1300 rpm	145
Polar Plot of Balance Weights	146
Time History of Polar Plots	147

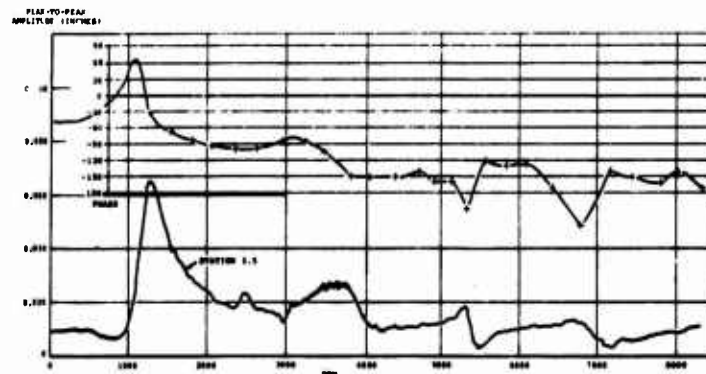


Figure 131. Deflection Versus Speed at Station 3.5.

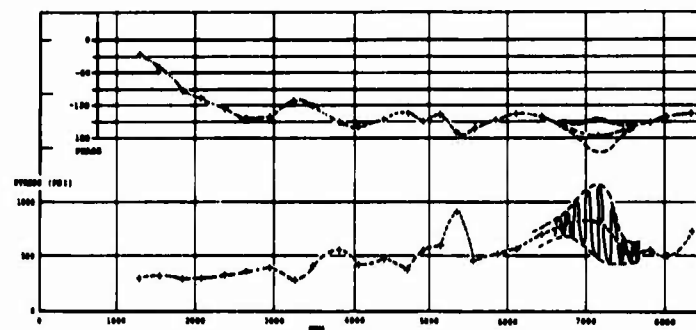


Figure 132. Bending Stress Versus Speed at Station 4.0.

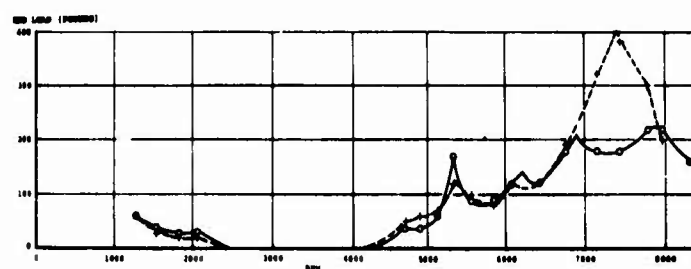


Figure 133. End Load Versus Speed at Station 1.0.

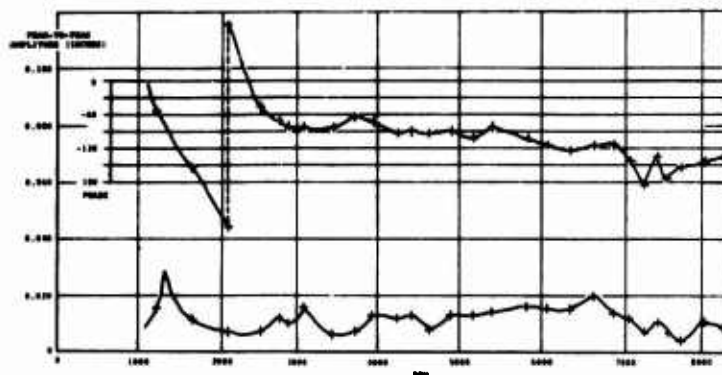


Figure 134. Damper Motion Versus Speed at Station 15.5.

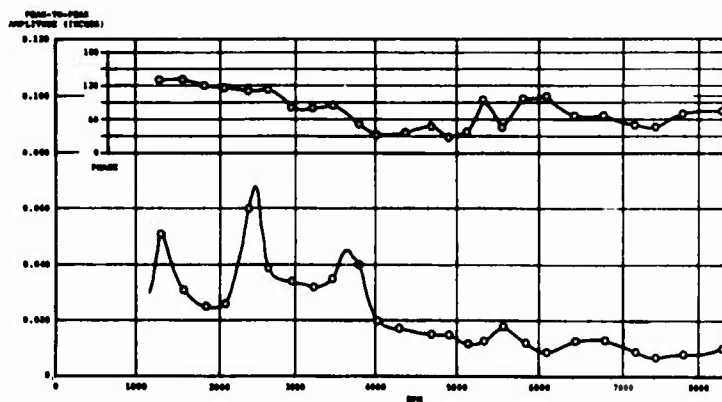


Figure 135. Damper Motion Versus Speed at Station 31.5.

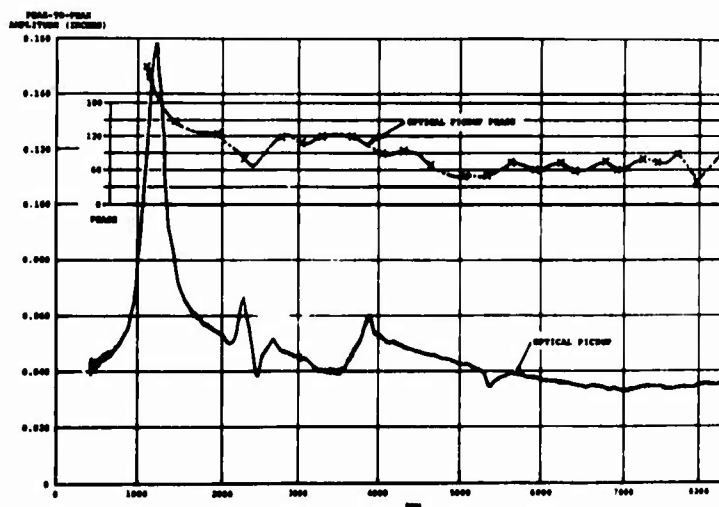


Figure 136. Deflection Versus Speed at Station 24.0.

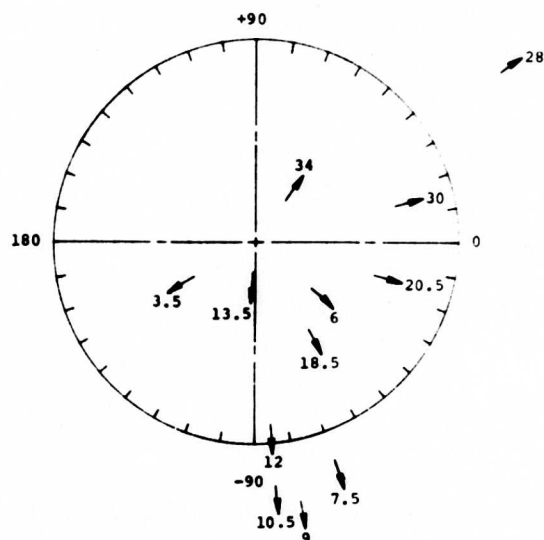
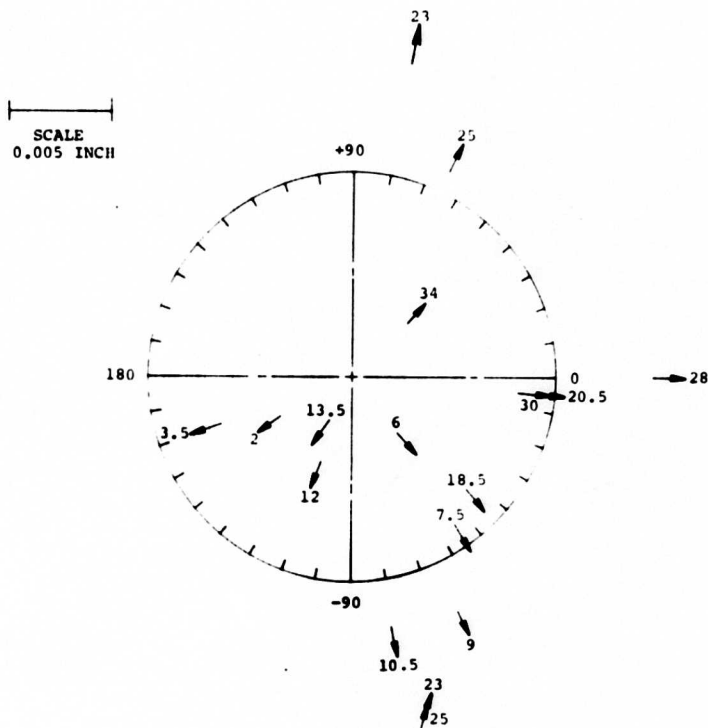


Figure 137. Polar Deflection at 8,300 and 7,300 RPM.

SCALE
0.010 INCH

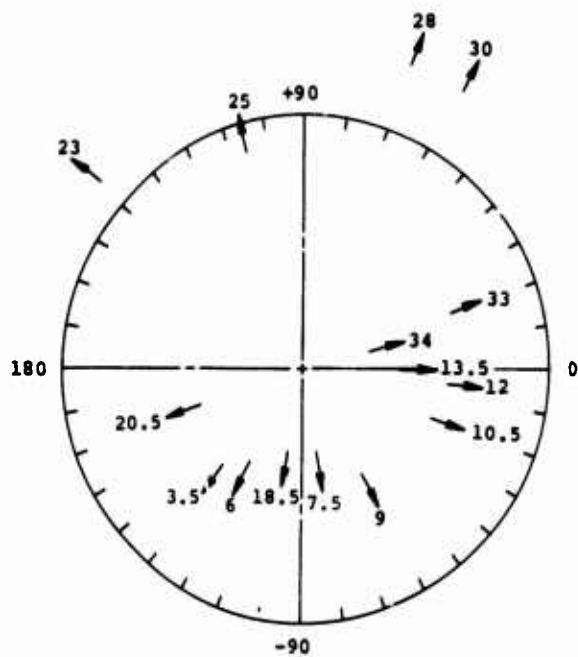
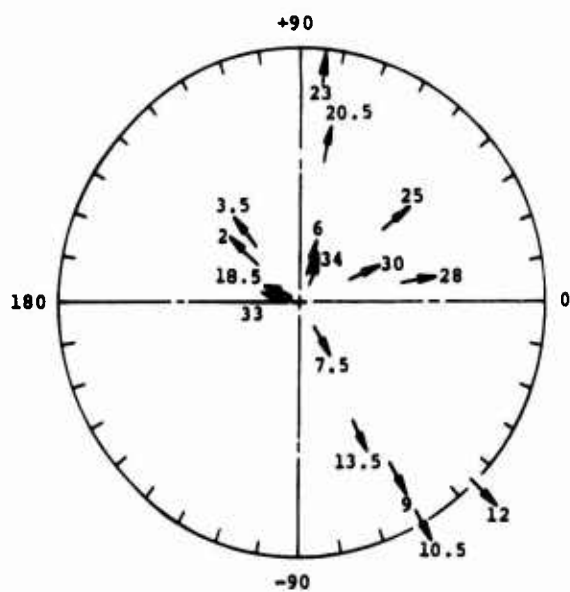
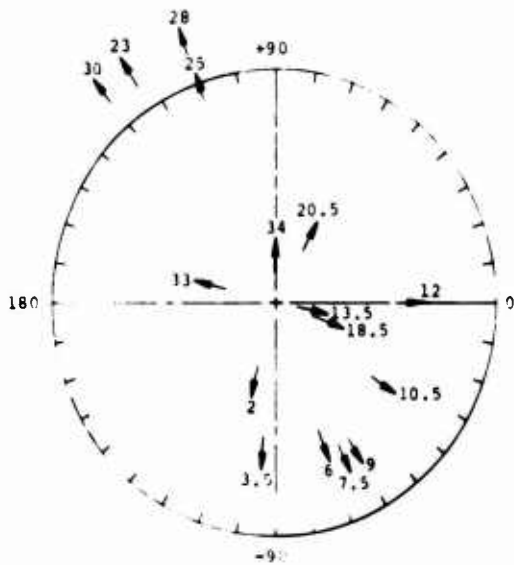


Figure 138. Polar Deflection at 5,250 and 3,570 RPM.

TEST 285
SERIAL 2B
2280 RPM

SCALE
0.010 INCH



TEST 286
SERIAL 2B
1150 RPM

SCALE
0.025 INCH

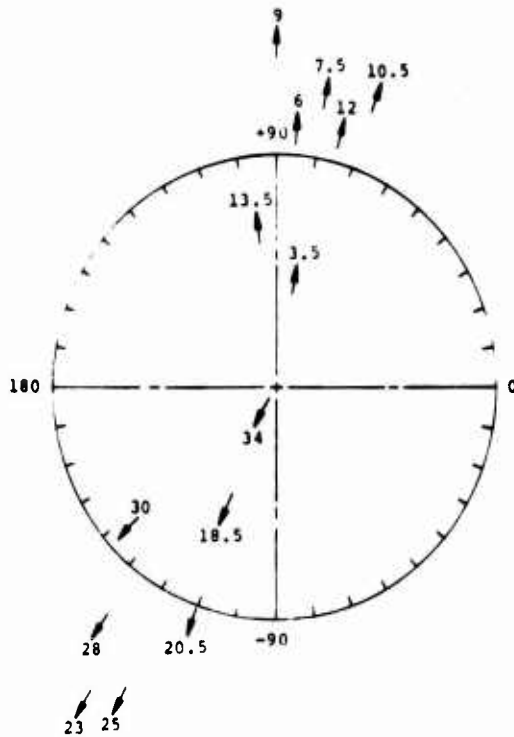


Figure 139. Polar Deflection at 2,280 and 1,150 RPM.

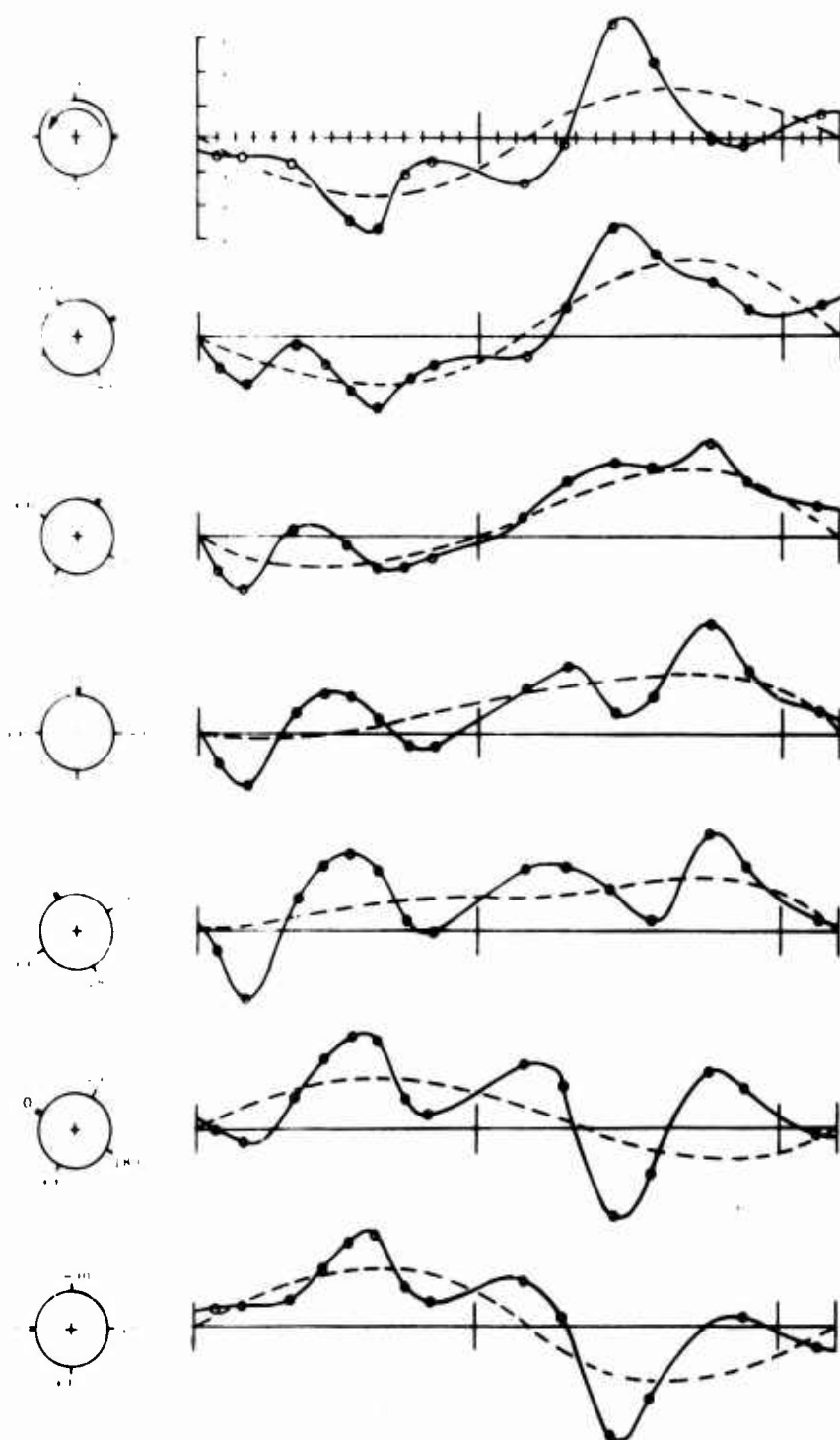


Figure 140. Time History of Shaft Deflection for 180 Degrees of Shaft Rotation at 8,300 R.P.M.

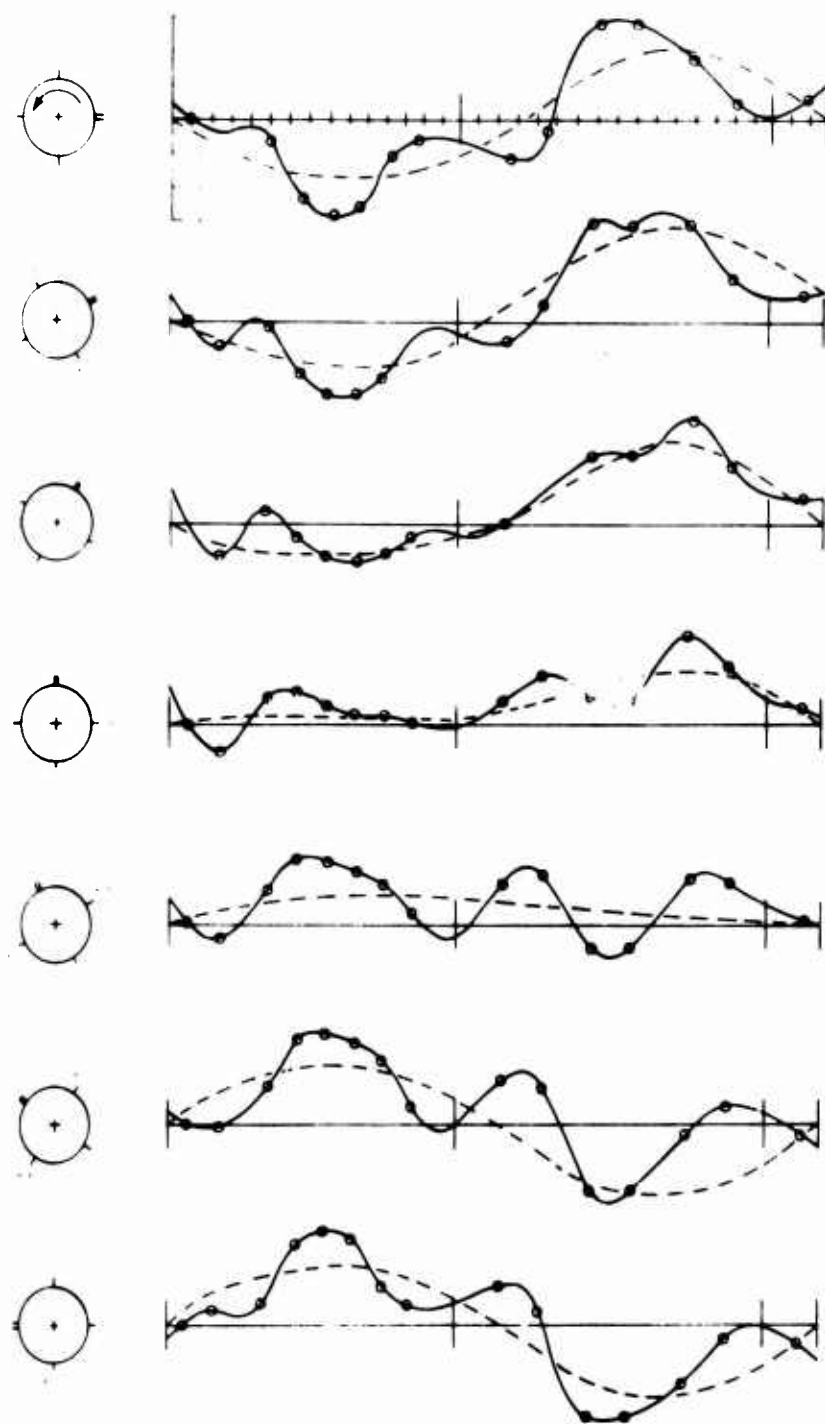


Figure 141. Time History of Shaft Deflection for 180 Degrees of Shaft Rotation at 7,300 RPM.

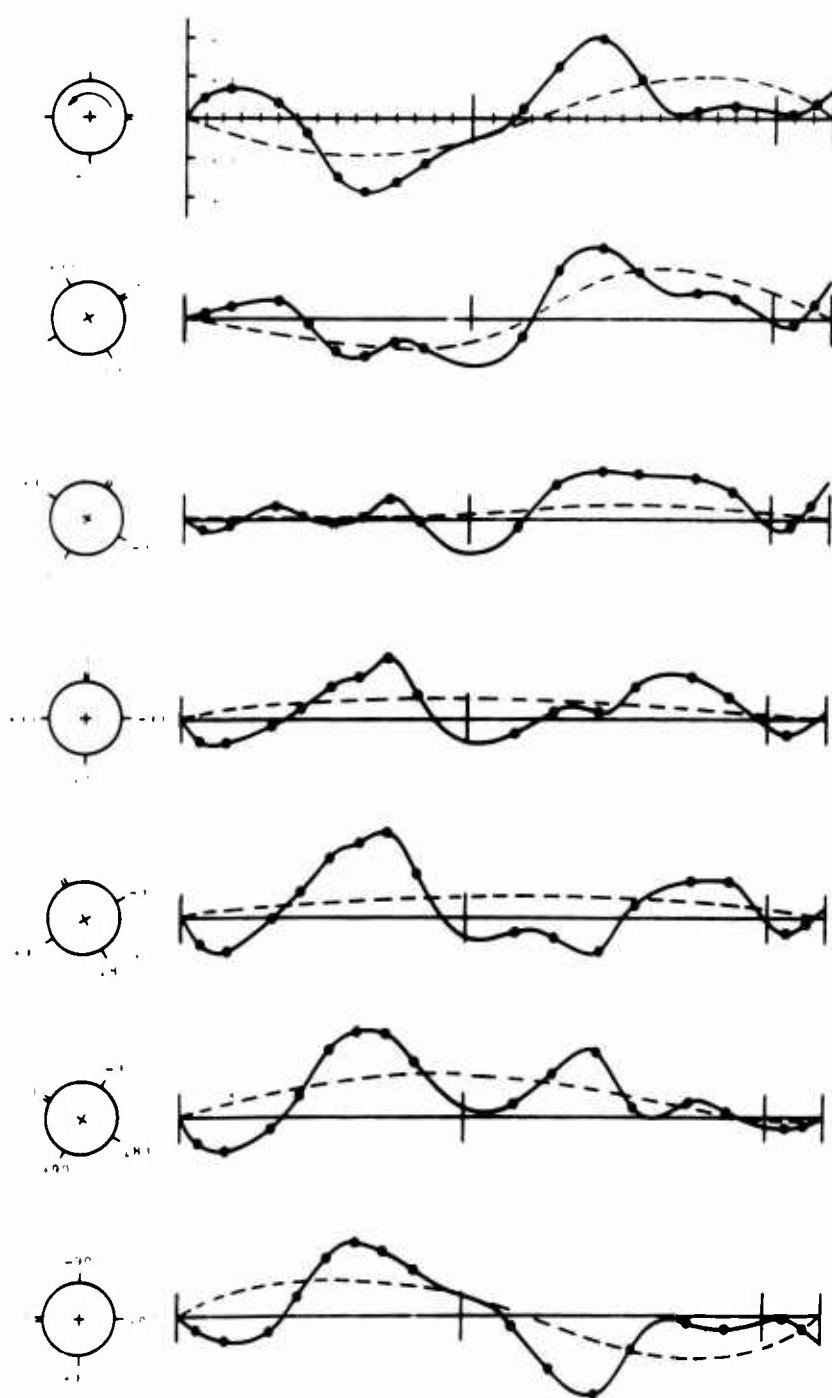


Figure 142. Time History of Shaft Deflection for 180 Degrees of Shaft Rotation at 5,250 RPM.

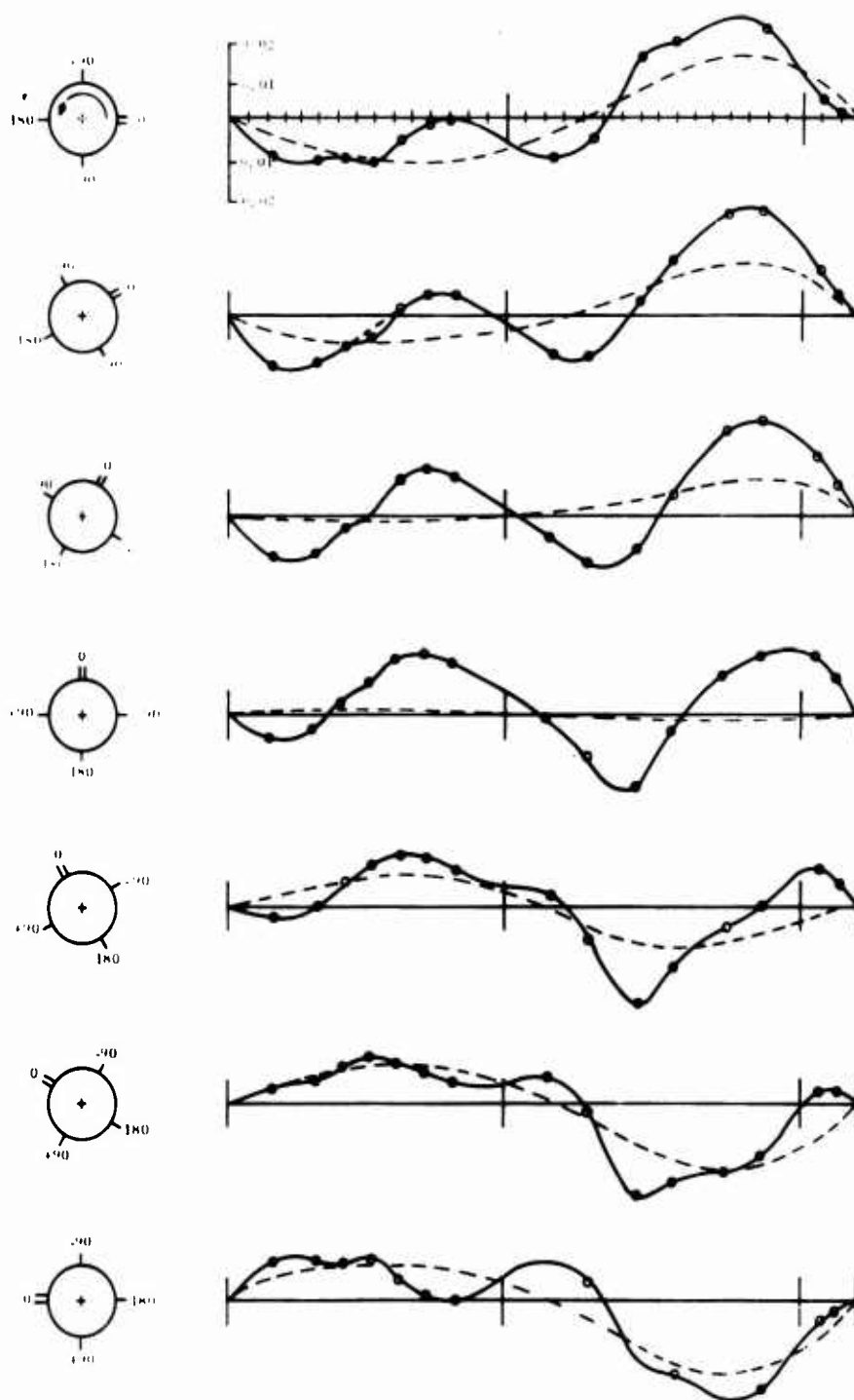


Figure 143. Time History of Shaft Deflection for 180 Degrees of Shaft Rotation at 3,570 RPM.

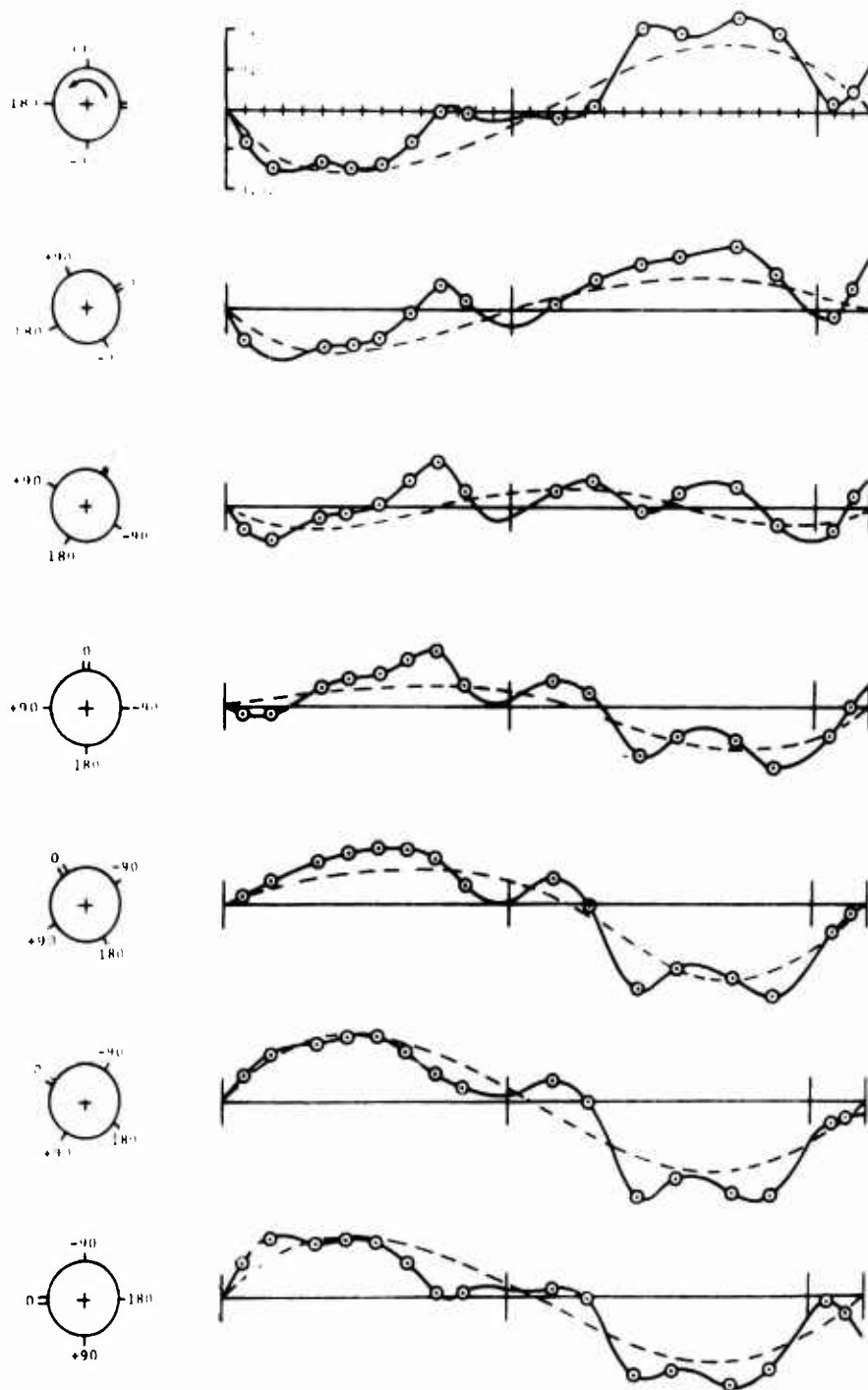


Figure 144. Time History of Shaft Deflection for 180 Degrees of Shaft Rotation at 2,280 RPM.

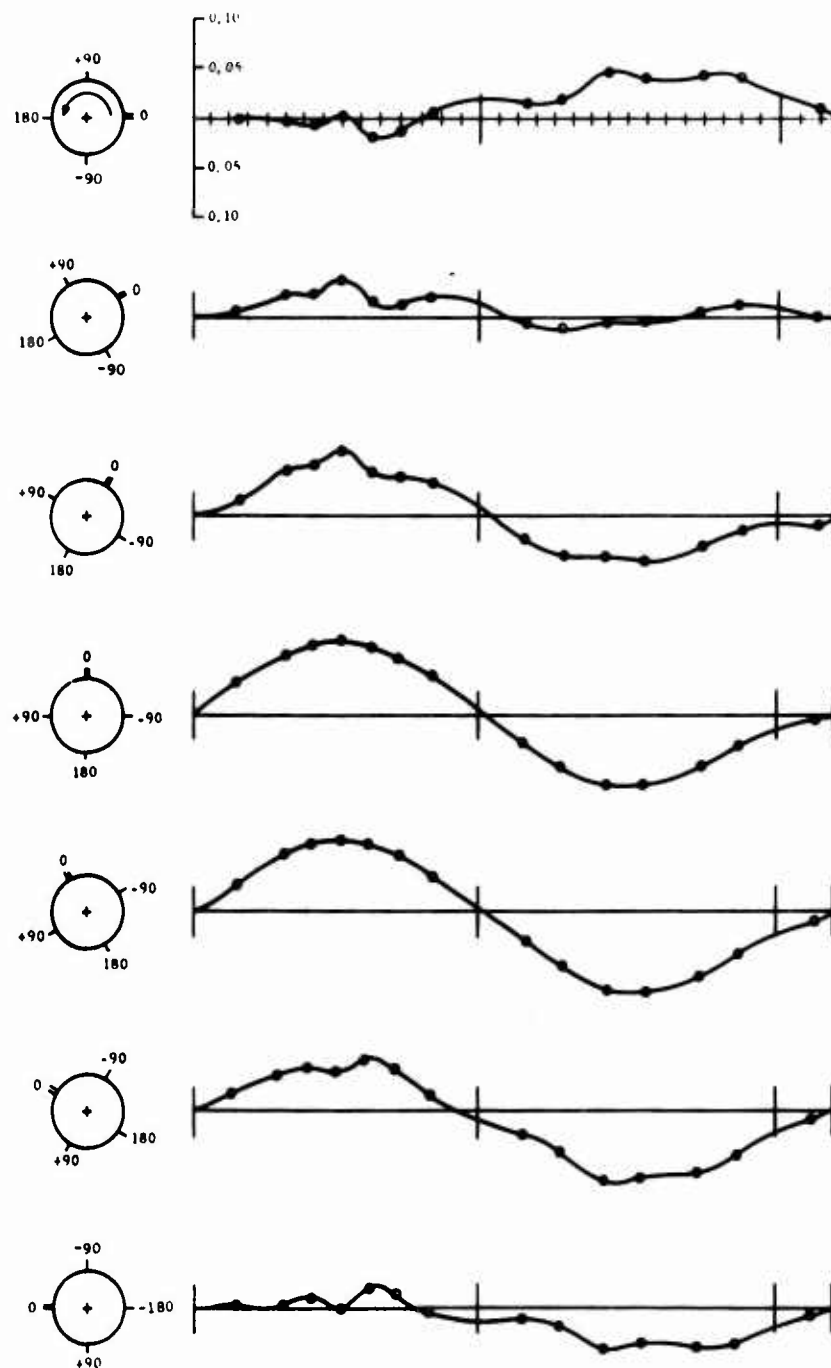
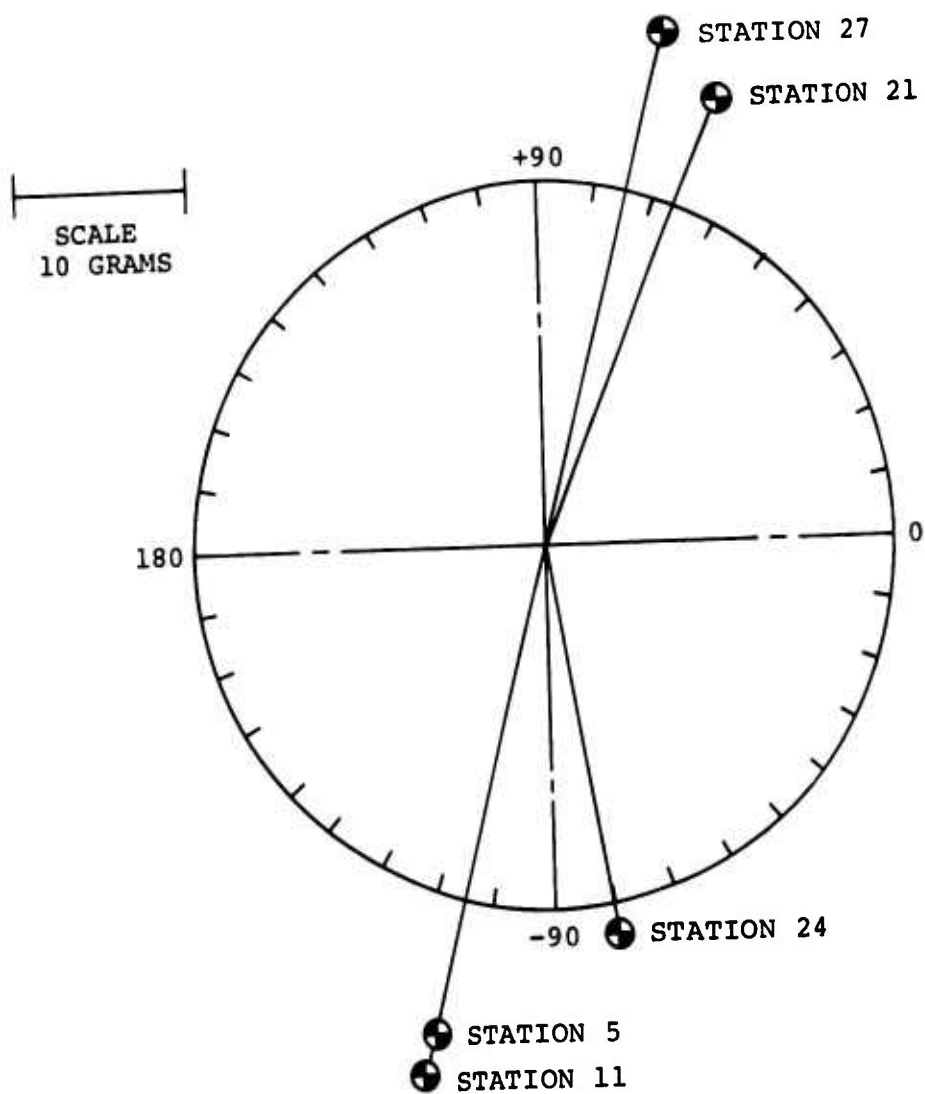


Figure 145. Time History of Shaft Deflection for 180 Degrees of Shaft Rotation at 1,300 RPM (Interpolated).



STATION	WEIGHT (GRAMS)	PHASE
5	27.6	-105
11	30.0	-105
21	19.6	+100
21	14.6	+ 20
24	21.9	- 80
27	28.8	+ 75

Figure 146. Polar Plot of Final Balance Weights.

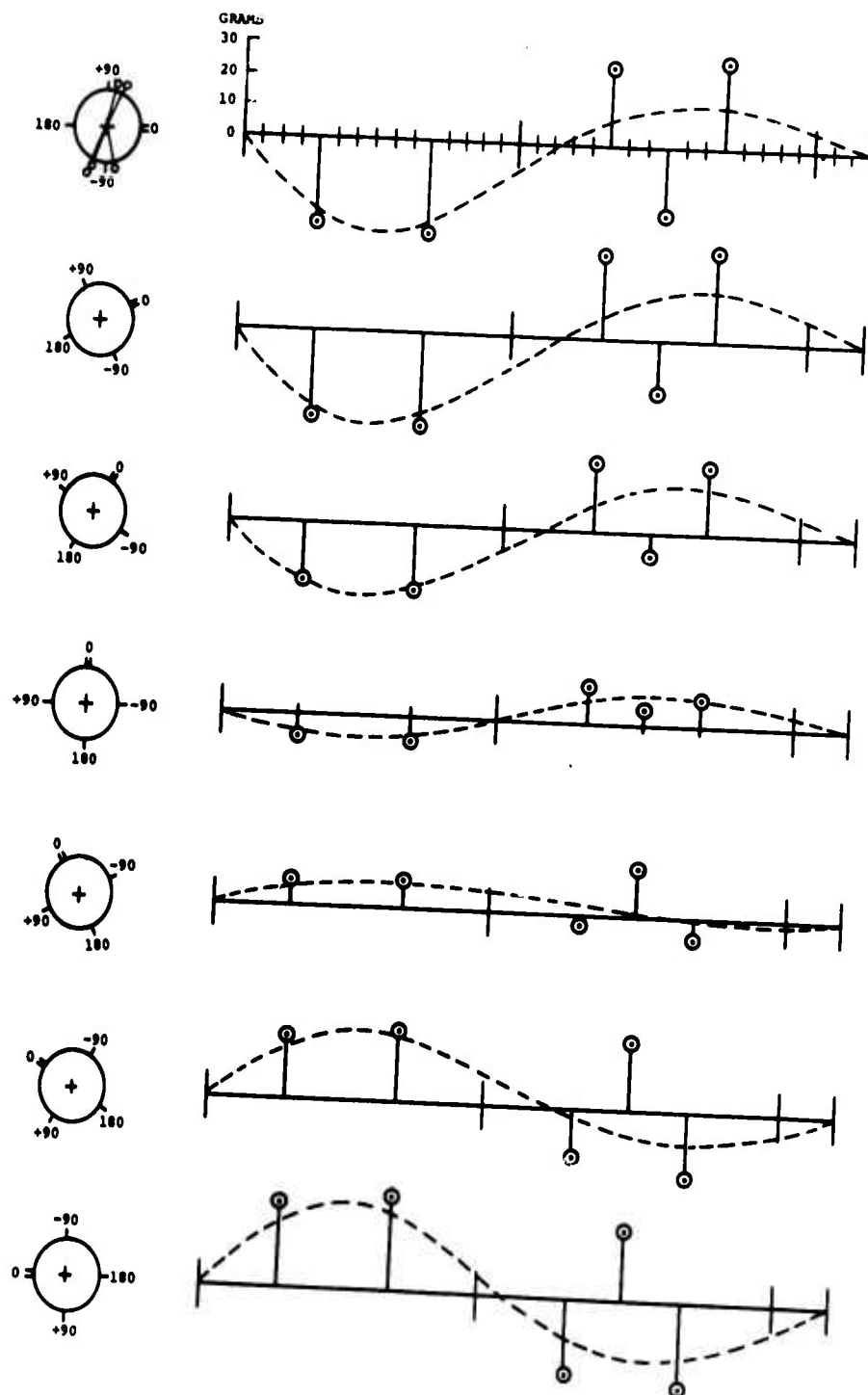


Figure 147. Time History of Final Balance Weight Effectiveness for 180 Degrees of Shaft Rotation..

SUMMARY

The shaft was assembled with tubes as received from the mill. The tubes were cut to length and the adapters riveted in place. Tests revealed that the crank effect from the initial bend produced undesirable damper motions, and the test specimen was subsequently straightened by bending in a press. The straightening operation did not completely remove the crank action at the damper because the flanges at the adapter field splices were not perfectly square with the straightened centerline of the tubes. The flanges were ground square by turning the tubes on centers. The reassembled shaft showed very little damper motion due to remaining crank effect.

Satisfactory performance of the supercritical-speed shaft was obtained by dynamically balancing the specimen. The previously developed experimental and analytical approach proved ineffectual in correcting shaft deflections because the mode shapes were not as predicted. A new method of experimentally balancing the shaft was developed. Test runs determined the effectiveness of balance weights at different balance stations, and from this information, effective mode shapes were established. The effective mode shapes are considerably different from calculated or measured mode shapes.

CONCLUSIONS

Available calculated and vibrated mode-shape data were not adequate for the solution of the balance problems encountered. The experimental and analytical balance techniques developed previously could not be used because the mode shapes were not correctly defined. Torque in the test specimen does not affect the performance. Secondary vibrations in the test machine became very troublesome when the major unbalance in the high-speed shaft was reduced. The unbalanced components of the test machine had to be balanced or removed because they affected the instruments. The mode shapes are complex combinations of the deflections of all modes. This factor must be considered when placing balance weights. The noise level of the system appears to be related to both damper loads and end loads. The noise seems to have a direct relationship to the deflections of the secondary modes present, specifically the deflection of the second mode when the shaft is turning at higher speeds. The problem of supercritical-speed-shaft balance includes a rigid body balance of the ends as well as balance of the flexible body of the shaft itself.

The test program has shown that the initial bend must be reduced so the crank action at the dampers does not produce motions and loads which exceed the design limits. This condition is independent of the motions and loads resulting from dynamic action of the shaft. In the future, it may be possible to correct shaft deflections of any magnitude and from any source, either static or dynamic, by this balancing technique, but this capability was not demonstrated in the test program.

Although present adapter design allowed disassembly and reassembly of the shaft without disturbing the balance of the system, it is too precise and requires too much care to be acceptable for a future design. Some improvement of this assembly joint is desirable.

Two design considerations must be a part of any supercritical-speed shaft if it is to operate satisfactorily. First, the shaft must be straight. That is, both the tube itself and the adapters joining it together must be free of characteristics which would cause the dampers to move regardless of the demands placed upon them by the deflection of the flexible system. The crank effect must be minimized. The final straightness of this shaft was held within 0.010 inch (0.020 peak to peak), and the flanges of the adapters were machined within 0.0005 inch TIR before assembly. The second consideration is that the shaft must be balanced. The flexible mode (supercritical) requires balancing, and the procedure becomes increasingly complex with each critical that must be passed. The balancing procedure is complex because the mode shapes are combinations of all modes simultaneously. The influence of each mode is a result of the unbalance in that mode. Since the unbalance is unknown and is different for each shaft, the amplitude is different for each shaft. The mode shape must be determined before the shaft can be balanced. The interaction of modes makes it impractical to measure modes directly, but they can be determined by considering the effectivity of balance weights.

The rigid-body mode (subcritical) also requires balancing which can only be accomplished by monitoring the end loads or deflections while rotating the shaft. This rigid-body balance cannot be accomplished if the flexible-mode deflections are excessive. The orbiting end loads will be a result of the static unbalance in the shaft and the end adapters, and of the remaining load caused by the unbalance still left in the flexible system. End load can be measured where minimum deflection was observed in the flexible mode. The measured end load at this point could be related to the centrifugal force caused by a given mass rotating at the corresponding speed. The best balance weight and the proper angle can be determined by experiment. Both ends of a supercritical-speed shaft have to be balanced. Balancing is complete when both the rigid body and the flexible modes of operation produce loads and stresses within acceptable limits to allow continuous operation for the design life of the system.

The shaft was not balanced to the degree originally intended. The balance that was achieved is smoother than the system it is intended to replace. Actual data from flight test has proven that the loads on the bearings and shaft hangers will be less on a supercritical-speed system than on similar components of the standard system.

Shaft performance responded to placement of balance weights, and further improvement is possible, though not considered necessary to achieve a satisfactory aircraft test installation.

INTERPRETATION AND ANALYSIS OF TEST RESULTS

During the test program, some aspects of the initial design analysis showed good correlation while others did not. In addition, a number of unanticipated results were encountered. Chief among these were noncircular whirling motions, measured deflections composed of superimposed mode shapes, and failure of the D-10 analytical balancing program to provide adequate balancing information. Test observations as they relate to these areas and the results of several investigations aimed at resolving the balancing problem are discussed in the following paragraphs.

GENERAL OBSERVATIONS

Comparison of Test and Initial Design Analysis

Calculated damped natural frequencies for the nonrotating system obtained during the initial design analysis are compared in Table II with the rotating test natural frequencies or critical speeds. Both the calculated and test results show shifts in the frequency of the peak response when the location of the exciting force (unbalance in the case of the test) is changed. This characteristic of a well-damped system makes it difficult to determine in a test program both the location and number of resonant frequencies. In general, there appears to be a test frequency corresponding reasonably well with each of the calculated frequencies; however, there are indications of other modes. Except for the appearance of a well-defined peak at 3,450 to 3,650 rpm, removal of the damper support stiffening produced no major change in the critical speeds.

A plot of the calculated nonrotating forced response at station 4 is compared in Figure 148 with typical test data for the unbalanced shaft. The comparison generally confirms the initial design analysis, which indicates that there are only three responsive modes within the operating range and that the remaining modes are heavily damped. Test response with and without damper support stiffening is shown in Figure 127. Since the balance configuration was identical in both cases, this comparison demonstrates the importance of the damper support stiffness on the fifth mode response.

Noncircular Whirling Motion

Deflection measurements with the optical pickup at various fixed system azimuth angles (Figure 92) indicate the presence of noncircular whirling motions at speeds above 5,000 rpm, but the deviation from a circular orbit does not appear significant except at 7,200 to 7,300 rpm. Examination of phase-angle data shows that these motions are forward whirling motions except in the area of 6,000 rpm, when there appears to be a reverse or backward whirling motion. Existence of noncircular motions in the range is confirmed by the presence of a 2-per-rev rotating system bending moment, which results from noncircular whirling motion.

The backward whirl motions were not present at 6,000 rpm on the final balanced configuration. (See strain gage test data from Figure 132.) The steady stress shows forward whirl with little or no 2-per-rev alternating stress except in the area of 7,300 rpm, where the alternating stress confirms an elliptical whirl pattern.

TABLE II. COMPARISON OF CALCULATED NONROTATING NATURAL FREQUENCIES AND ROTATING CRITICAL SPEEDS			
Calculated Mode	Calculated Damped Nonrotating Natural Frequency (rpm)	Test Critical Speed With Damper Support Stiffening (rpm)	Test Critical Speed Without Damper Support Stiffening (rpm)
1st	1140		
2nd	• 1230 – 1350	• 1300 – 1350	• 1300 – 1350
3rd	1800 – 1920	1800 – 1900 2500 – 2600	2450 – 2500
4th	3240 – 3300	2900 – 3100	3100 • 3450 3650
5th	• 5580 – 5640	• 5000 5450 5600 5700	• 5300 – 5400
6th	• 7560 – 7800	• 6300 – 6500 6800 6900 • 7100 – 7500	6300 • 6600 – 6800 7300 – 7500
• Major response speeds			

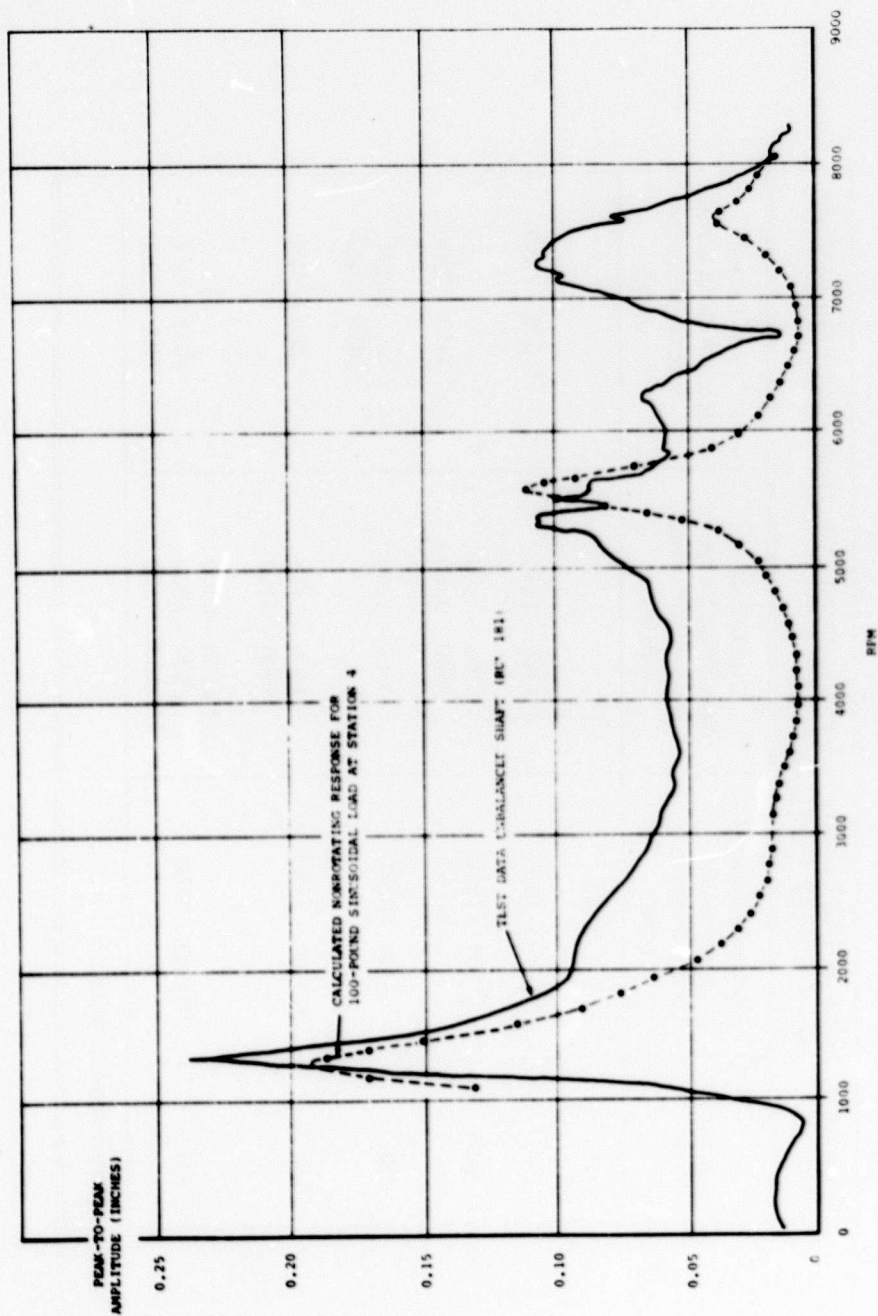


Figure 148. Comparison of Rotating Test and Calculated Nonrotating Response.

The presence of the noncircular motions is believed to be primarily due to unsymmetric (nonisotropic) stiffness of the shaft supports.

The possible orbiting motions of the shaft fall into one of the following four categories:

- Forward circular whirl
- Forward elliptic whirl
- Backward circular whirl
- Backward elliptic whirl

Figure 149 shows typical whirling motions of each type. For the simple elliptic cases, fixed system-displacement pickups oriented in the vertical and horizontal planes will measure different amplitudes. When backward whirling motions are present, a 180-degree phase difference in the location of the shaft bend is measured between the vertical and horizontal planes. Only the forward circular whirl does not result in a 2-per-rev rotating system-bending moment.

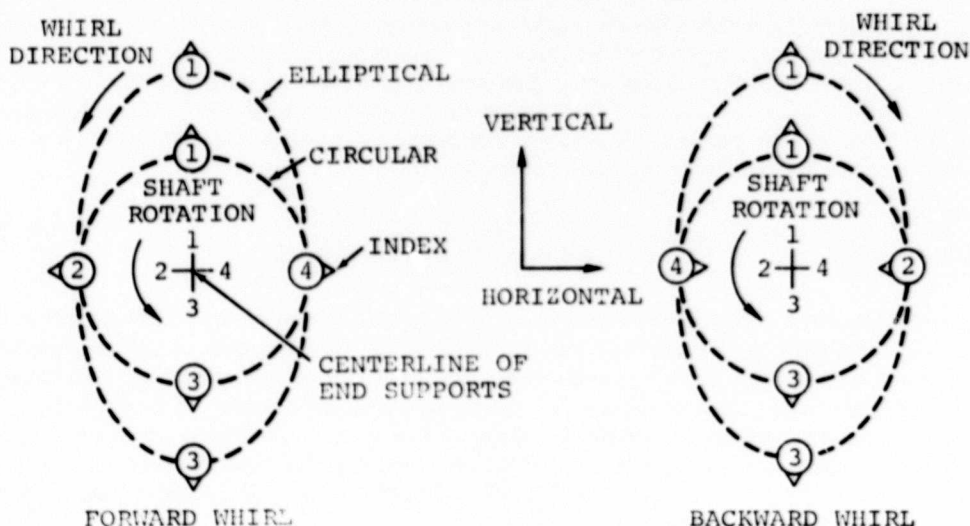


Figure 149. Whirl Pattern Types.

The bulk of the test data consists of measured deflections in the horizontal plane which can only be interpreted in terms of a circular motion. Up to approximately 5,000 rpm, the assumption of a circular whirl is well justified. Provided the area of backward (reverse) whirling near 6,000 rpm is of no concern, an assumption of circular whirling over the remainder of the speed range is not unreasonable.

Some error in phase would occur when the optical pickup instrument is used to measure elliptical whirling in a plane which is not parallel or at right angles to the light source. Clearly the largest errors could occur near 7,200 to 7,300 rpm, where the noncircular motion is most evident and, conceivably, could lie on some inclined plane.

Multiple-Mode Response

Test-response shapes also show a strong superposition of two or more modes at all the higher critical speeds. In particular, a significant second-mode deflection occurred even at the fifth and sixth critical speeds. Presumably, the observed results are due to the effects of initial shaft deformity, the relatively high damping, and the incomplete balancing of the second critical speed.

This situation is of concern primarily because it makes it difficult, if not impossible, to balance the shaft using the experimental modal balancing method. In essence, the modal balancing theory detailed in the previous report² involves balancing each critical speed in turn. The balance weights are distributed so that they do not affect a previously balanced critical and so that they minimally affect the subsequent balancing at higher modes. Successful application of the modal balancing method entails a reasonably accurate knowledge of the mode shapes and an experimental identification of the plane of the unbalance for the mode which is being balanced. When the shaft response at a critical speed is composed of contributions from several modes, difficulty is encountered in applying the modal balancing method. The distorting effect of the other modes prevents an accurate determination of both the mode shape and the location of the unbalance for the mode of interest.

ANALYSIS OF THE D-10 COMPUTER BALANCING PROGRAM

The D-10 program was written to provide a computerized version of the analytical balancing method developed in the previous report.² Basic input data required to use the program consist of the shaft geometric and mass properties, shaft fundamental modes and frequencies, and test data obtained at a number of speeds equal to the number of balance stations. Required balance weights are obtained utilizing the program and an initial set of test values. After the weights are added, a second set of test points is obtained; these data are used to further refine the balance-weight configuration. Repetition of this procedure should then result in a balanced shaft configuration.

The program did not perform as anticipated since balance weight predictions were consistently as much as 25 times higher than the actual weights used to balance the shaft. Typical results illustrating this discrepancy are presented in Table III. This large disparity between predicted and actual balance weights led to this present reevaluation of both the analytical approach² and the subsequent computer program.⁷

TABLE III. COMPARISON OF ACTUAL AND CALCULATED BALANCE WEIGHTS FROM D-10 ANALYSIS				
Shaft Station	Final Test Balance Weight		Calculated* Balance Weight	
	Grams	Angle	Grams	Angle
5	27.6	-105°	35.6	-112°
11	30.0	-105°	148.0	177°
21	26.0	68°	587.0	162°
24	21.9	- 80°	782.0	- 18°
27	28.8	75°	743.0	160°
* Based on a combination of test and analytical modes.				

The results of the analytical effort described in the previous report² can be summarized in Equations 3 through 6. Definitions of symbols used in this section are given in Table IV. Equations 3 and 4 describe the deflected shape along the shaft in two perpendicular axes. These deflections, $U(x)$ and $V(x)$, are expressed as functions of the initial deflected shape, shaft mode shapes and modal damping, forcing frequencies, resonant frequencies, and parameters describing the shape of the unbalance distribution.

$$U(x) = \sum_{n=1}^{\infty} \left\{ \frac{[\omega_n^2 - \omega^2] [\omega^2(a_n + e_n) + \omega \gamma_n b_n] + \omega^2 \gamma_n [\omega(b_n + g_n) - \gamma_n a_n]}{(\omega_n^2 - \omega^2)^2 + \omega^2 \gamma_n^2} \right\} X_n(x) \quad (3)$$

$$V(x) = \sum_{n=1}^{\infty} \left\{ \frac{[\omega_n^2 - \omega^2] [\omega^2(b_n + g_n) - \omega \gamma_n a_n] - \omega^2 \gamma_n [\omega(a_n + e_n) + \gamma_n b_n]}{(\omega_n^2 - \omega^2)^2 + \omega^2 \gamma_n^2} \right\} X_n(x) \quad (4)$$

$$\sum_{i=1}^h M_i \epsilon X_n(\xi_i) \cos \theta_i = -\rho A N_n r_n \quad (5)$$

$$\sum_{i=1}^h M_i \epsilon X_n(\xi_i) \sin \theta_i = -\rho A N_n S_n \quad (6)$$

$$\text{where } r_n = a_n + e_n, S_n = b_n + g_n$$

In their general form, the above equations consider the total deflections at all speeds to be a superposition of the response from all the modes, and the unbalance at all speeds is assumed to be composed of both the initial shaft deformation and a mass defect. The principal assumptions made in developing these equations are:

- The whirl pattern is circular—shaft and support stiffnesses are isotropic.
- The discrete dampers may be represented by an equivalent modal damping coefficient.
- The shaft has a uniform mass distribution.

TABLE IV. LIST OF SYMBOLS FOR D-10 ANALYSIS

A	shaft cross-sectional area
ρ	mass density of shaft material
L	shaft length
m	number of dampers
h	number of balance stations
n	mode number
ϵ	radius at which balance weight is added
ω	shaft speed
ω_n	critical speed of the nth mode
M_i	mass of the ith balance weight
θ_i	angular position of ith balance weight
ξ_i	spanwise location of ith balance weight
c_i	damper coefficient of ith damper
ξ_i	spanwise location of ith damper
x	spanwise coordinate along the line between supports
$\vec{\eta}_1, \vec{\eta}_2$	a set of perpendicular unit vectors fixed in the shaft
$U(x)$	total shaft deflection in the direction of the unit vector η_1
$V(x)$	total shaft deflection in the direction of the unit vector η_2
$\bar{X}_n(x)$	whirling mode shape of the nth critical speed
$U_0(x)$	$\sum_{n=1}^{\infty} a_n X_n(x)$, component of the initial shaft deformity in the direction of the unit vector $\vec{\eta}_1$
$V_0(x)$	$\sum_{n=1}^{\infty} b_n X_n(x)$, component of the initial shaft deformity in the direction of the unit vector $\vec{\eta}_2$

TABLE IV-Continued

$N_1(x)$	position of the mass center from the shaft geometric center in the direction of the unit vector $\vec{\eta}_1$
$N_2(x)$	position of the mass center from the shaft geometric center in the direction of the unit vector $\vec{\eta}_2$
a_n	$= \frac{\int_0^L U_0(x) X_n(x) dx}{\int_0^L X_n^2(x) dx}$
b_n	$= \frac{\int_0^L V_0(x) X_n(x) dx}{\int_0^L X_n^2(x) dx}$
c_n	$= \frac{\int_0^L N_1(x) X_n(x) dx}{\int_0^L X_n^2(x) dx}$
g_n	$= \frac{\int_0^L N_2(x) X_n(x) dx}{\int_0^L X_n^2(x) dx}$
C_n	$= \sum_{i=1}^m (C_i/L) X_n^2(\xi_i)$
γ_n	$= \frac{C_n}{\rho A}$, reduced damping ratio
N_n	$= \int_0^L X_n^2(x) dx$

In the case of the present shaft, test results indicate that the whirl pattern is slightly elliptical near the higher critical speeds; however, the importance of this noncircular motion is not obvious. Representation of the discrete damping as an effective modal damping is a generally accepted assumption for lightly damped systems. For the present system, this assumption is easily justified for the higher modes but somewhat questionable for the first through the fourth modes, where the damping ranges from 30 to 14 percent of critical. The assumption of a uniform mass distribution is quite clearly not justified since the local mass at the damper was shown in the design calculations to have a powerful effect on the dynamic behavior. This deficiency does not invalidate the method, but the equations must be modified to include the damper mass.

In general, the process of obtaining the required balance weight consists of gathering sufficient test data so that solutions may be obtained for a_n , b_n , and g_n from Equations 3 and 4. With these values, Equations 5 and 6 are used to compute the balance weight mass and angular position (M_i and θ_i). Two approaches to obtaining a solution are worthy of consideration. These approaches, referred to as Methods 1 and 2, may be summarized as follows.

Method 1—This approach obtains a solution to the equations in their most general form. Implementation requires the measurement of the shaft initial deformity and measured dynamic response for one location at a number of speeds equal to the desired number of balance stations. Measured response near each of the criticals is preferred. From the initial deflection data, the coefficients a_n and b_n may be computed directly, leaving $2n$ unknown coefficients (e_n and g_n) in Equations 1 and 2. If the dynamic responses $U(x)$ and $V(x)$ are measured at (n) different speeds, then there are $2n$ simultaneous equations from which the $2n$ coefficient values may be obtained. Using the values of a_n , b_n , e_n , and g_n , Equations 3 and 4 yield the balance weight mass and angular position for (n) different locations.

Method 2—This method, which is the method used in the D-10 program,⁷ is applicable to a system where the initial deformity contributes only to the unbalance in the first mode and constitutes the only unbalance in this mode. Unbalance in the higher modes is assumed to be due entirely to mass defects. This method was selected since it was felt that the assumption regarding the initial deformity was justified. In addition, it offered the advantage of eliminating the time-consuming measurement of the initial deformity.

If the above assumptions are made regarding the nature of the unbalance, then

$$e_n = g_n = 0 \text{ for } n = 1$$

$$\text{and } a_n = b_n = 0 \text{ for } n \geq 2$$

Thus, $2n$ coefficients are equal to zero and $2n$ unknown coefficients remain in Equations 1 and 2. As in the case of Method 1, if the dynamic responses $U(x)$ and $V(x)$ are then measured at (n) different speeds, the balance-weight mass and angular position for (n) different locations may be calculated.

As indicated previously in Table III, there is a large disparity between the D-10 calculated and test balance-weight configurations. Results shown in Table III were based on a combination of test and analytical modes and dynamic response data for the final reworked shaft configuration. The resultant rotating test mode at 1,275 rpm from test 110, which is very nearly coplanar, was used in conjunction with the analytical third through sixth modes. In addition to the balance weights, the D-10 program using Method 2 also calculates the initial deflection required to obtain the measured first-mode response. The derived initial coplanar deflection is compared with the measured initial shape in Table V. This derived initial shape agrees within approximately 20 degrees with the experimentally determined plane of unbalance at the first (1,350 rpm) response peak. However, there appears to be little if any correlation with the measured initial shape which is noncoplanar.

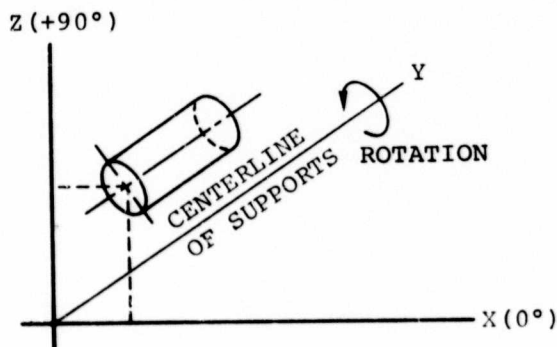
Clearly, the D-10 computer program is not adequate for the present shaft configuration. However, a valid analysis could possibly be obtained by including the damper mass terms and using the more general solution referred to as Method 1; but this approach was not evaluated because the influence coefficient method described in Reference 8 is apparently superior.

TABLE V. COMPARISON OF DERIVED AND MEASURED INITIAL DEFORMITY				
Shaft Station	Initial Deformity			
	Measured		Derived	
	Deflection (Inch)	Angle (Degrees)	Deflection (Inch)	Angle (Degrees)
1	0.002	- 55	0	0
3	0.006	- 84	0.010	+108.4
5	0.003	- 60	0.018	+108.4
7	0.003	- 90	0.023	+108.4
9	0.002	- 50	0.025	+108.4
11	0.004	+ 45	0.022	+108.4
13	0.004	+ 70	0.017	+108.4
15	0.004	- 135	0.009	+108.4
17	0.007	- 20	0	0
19	0.012	0	0.006	- 71.6
21	0.011	- 20	0.012	- 71.6
23	0.004	0	0.015	- 71.6
25	0.009	0	0.015	- 71.6
27	0.006	0	0.012	- 71.6
29	0.002	0	0.009	- 71.6
31	0.004	+ 90	0.005	- 71.6
33	0.004	+ 90	0.002	- 71.6
35	0.001	+ 72	0	0

GENERALIZED COORDINATE ANALYSIS OF TEST DATA AND BALANCING SYSTEM

A generalized coordinate analysis of test response shapes for the unbalanced shaft was conducted using analytical mode shapes. The purpose of the analysis was to separate the total response into its constituent modes and thus identify the plane of the unbalance and the response amplitude of each of the component modes. With this information it is then possible to determine the balancing requirements by analytical means. A similar analysis of the measured initial bend or static deflections was also performed to determine the correlation between the initial bend and the unbalance.

It is assumed that there exists a set of mode shapes—referred to as the generalized coordinates—defined by the function $H_n(y)$, which describes the deflected whirling shape of the shaft such that



$$X(y) = \sum_{n=1}^{\infty} A_n H_n(y)$$

$$Z(y) = \sum_{n=1}^{\infty} B_n H_n(y)$$

where: $Z(y)$ and $X(y)$ are the total deflections in the directions of the Z and X axes, which are fixed in the shaft, and A_n and B_n are coefficients defining the amplitude of the coordinates or mode shapes $H_n(y)$

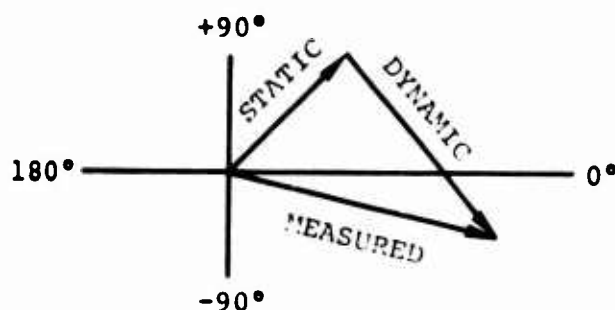
For the case of an undamped shaft, the mode shapes $H_n(y)$ correspond to the normal modes of the system, and it is the usual assumption that these modes are approximately correct for the case with damping. Analysis and test observations indicate that the shaft is operating below the seventh critical speed. For practical purposes, therefore, a summation of the first seven modes, $n=1$ to $n=7$ in the above equations, should yield a satisfactory approximation.

Assuming that the first seven mode shapes $H_n(y)$ are known and that the deflections $Z(y)$ and $X(y)$ are measured at a fixed shaft speed for a minimum of seven locations, two sets of seven simultaneous equations may be written from which the coefficients A_n and B_n can be calculated for the first seven modes. Thus, the contributions of the first seven modes to the total response are determined at the test speed. During the present investigation, Vertol's

computer program L-36 was used to obtain numerical solutions for the coefficients A_n and B_n . This program offers an advantage over the conventional procedure outlined above, in that measurements at more than seven locations may be utilized while still limiting the number of coordinates to seven. Since this results in more equations than there are unknowns, a polynomial curve-fitting procedure is used which results in a root-mean-square curve fit. This feature tends to minimize data error and results in a more accurate solution.

To gain some insight into the characteristic nature of the results in the absence of any possible test error, the forced response of a damped, nonrotating shaft computed from Vertol's D-97 program was analyzed. Results obtained using undamped modes (Figure 18) as coordinates are shown in Figures 150 and 151 as plots of modal amplitude at station 4 and the phase of the mode-versus-shaft speed. With a few minor exceptions, the amplitude plots display the general characteristics of uncoupled modes with each mode having significant response only in the area of its own natural frequency, which indicates a good selection of coordinates. Although the phase plots are somewhat confused, it is noted that at the natural frequencies each mode is approximately 90 degrees behind the exciting force. In addition, there is a tendency to be nearly in phase with the force below the natural frequency and nearly 180 degrees behind the force above the natural frequency.

The analysis of test results was conducted using test response shapes of the unbalanced shaft together with both the undamped modes and the damped modes (marked *D*) in Figure 18 as coordinates. Measured shaft deflection is the vector sum of the static and dynamic deflections. Since it is the dynamic deflection which was of interest, test data were first corrected to obtain the dynamic deflection.



Components of the test response shapes in two mutually perpendicular planes (0 and 90 degrees in the shaft coordinate system) were determined. Similarly, components of the static deflection, Figures 51 and 52, were determined, and the dynamic deflection was obtained by subtracting the static from the measured deflections. Using the dynamic deflections, the coefficients A_n and B_n were obtained from the L-36 program. The components defined by

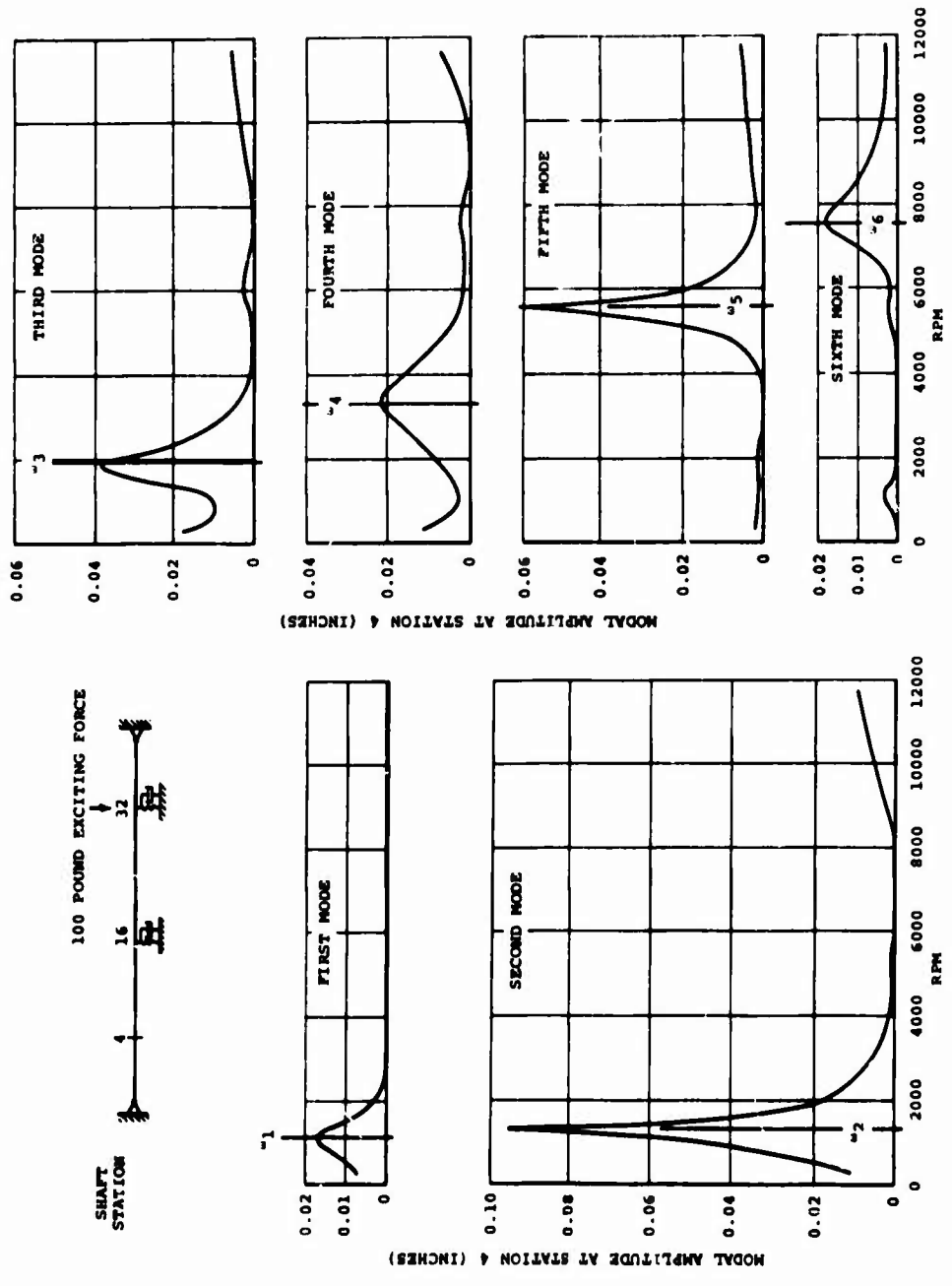


Figure 150. Generalized Coordinate Analysis of Theoretical Response - Modal Amplitude.

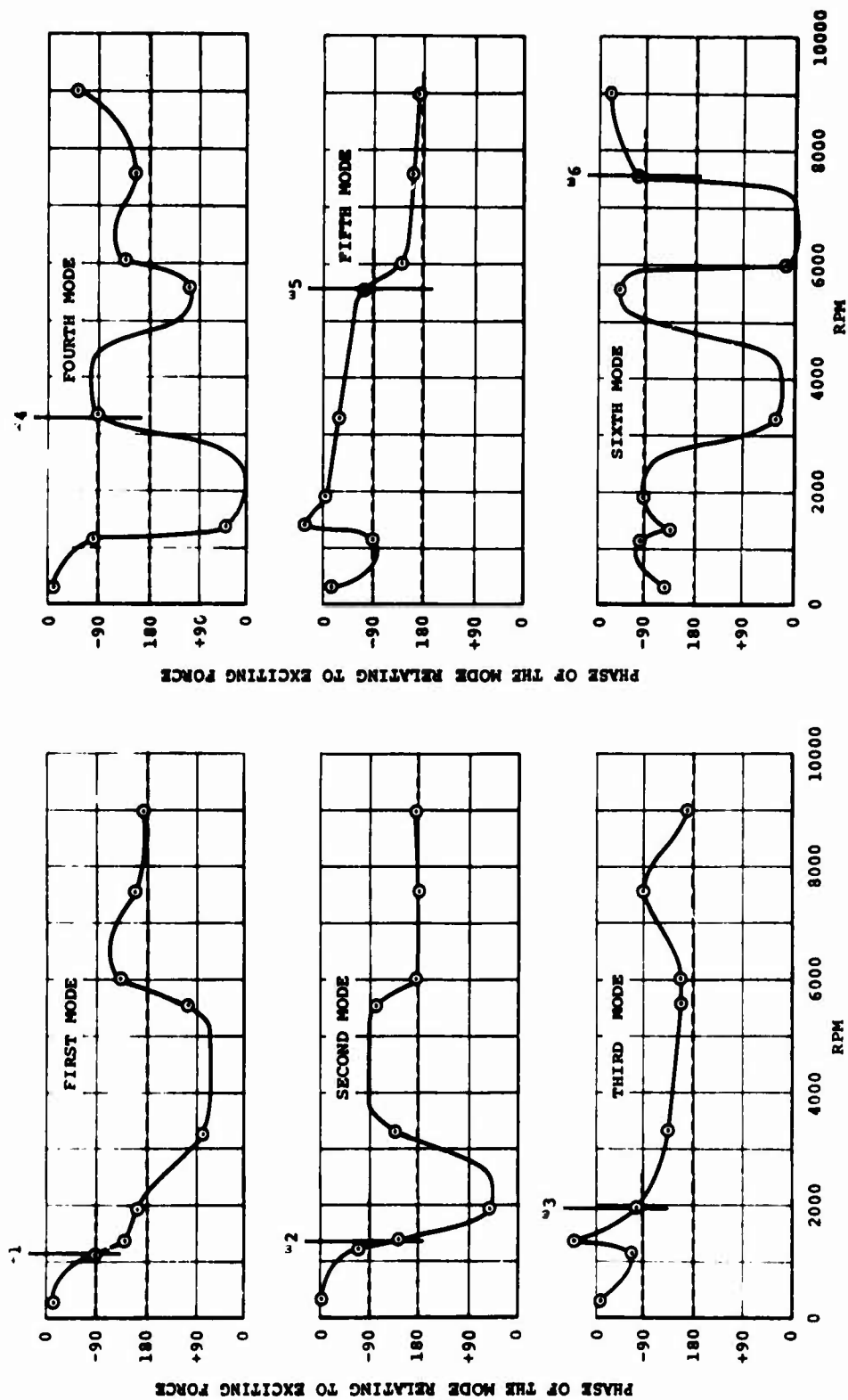
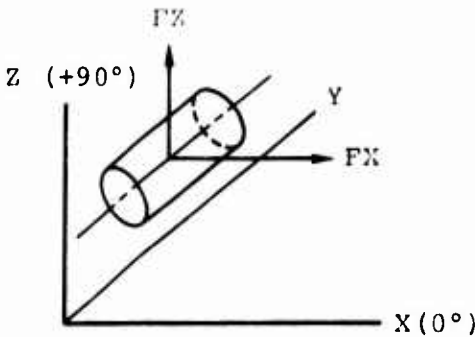


Figure 151. Generalized Coordinate Analysis of Theoretical Response - Modal Phase.

these coefficients were then recombined to find the resultant dynamic deflection and phase for each of the modes. A similar analysis was performed to determine the modal content of the initial bend. Detailed results for the analysis with the undamped and damped modes are compared in Figures 152 and 153 in the form of modal amplitude and phase at station 4 versus shaft speed. In general, the modal amplitude plots (see Figure 152) show a predominant peak for each mode in the area of its estimated natural frequency or critical speed. Notable exceptions are the second mode, which shows considerable response in the area of the fifth-mode frequency, and the third mode, which displays considerable response in the vicinity of the second mode and no tendency to peak at its own modal frequency. The estimated seventh-mode frequency is above the maximum operating speed; this appears to be confirmed by the absence of any significant peak for the seventh mode. Modal amplitudes with the damped coordinates exhibit the same general pattern as the undamped coordinates except that there is considerably more interaction. The first-mode amplitude is high over the middle speed range, and the second mode has a very large amplitude peak at the fifth-mode frequency. Levels for the third, fourth, and fifth modes are only slightly higher than the results with the undamped coordinates except in the vicinity of the second-mode frequency, where these modes contribute significantly to the overall response.

The plots of Figure 157 show the phase of the mode (at station 4) in the shaft coordinate system. Except for the first and third modes, the results with the damped and undamped coordinates compare favorably in the area of the estimated critical speeds. Using the results of the previous generalized coordinate analysis of a D-97 response as a guide, the phase of the unbalanced force can be identified. Since the precise location of the critical speeds is not known, an effort has been made to identify the 180-degree phase shift which occurs as the mode passes through resonance. These regions have been identified on the plots. In the case of the first and second modes, the phase tends to stabilize on a constant angle above the estimated critical speed, and it has been assumed that this angle is 180 degrees out of phase with the unbalanced force. As a general observation, the identification of the plane of the unbalance from the phase plots is subject to a good deal of judgment.

A summary of results is presented in Tables VI and VII for the undamped and damped coordinates respectively. In both cases, the generalized balance force and phase obtained from the analysis of test-response shapes are compared with values for the final test-balance configuration. For the undamped coordinates, the phase of the force required to balance the modal components of the initial bend is also shown. The generalized forces were obtained from the following expressions.



TESTS 110, 113, 185, 186, AND 187

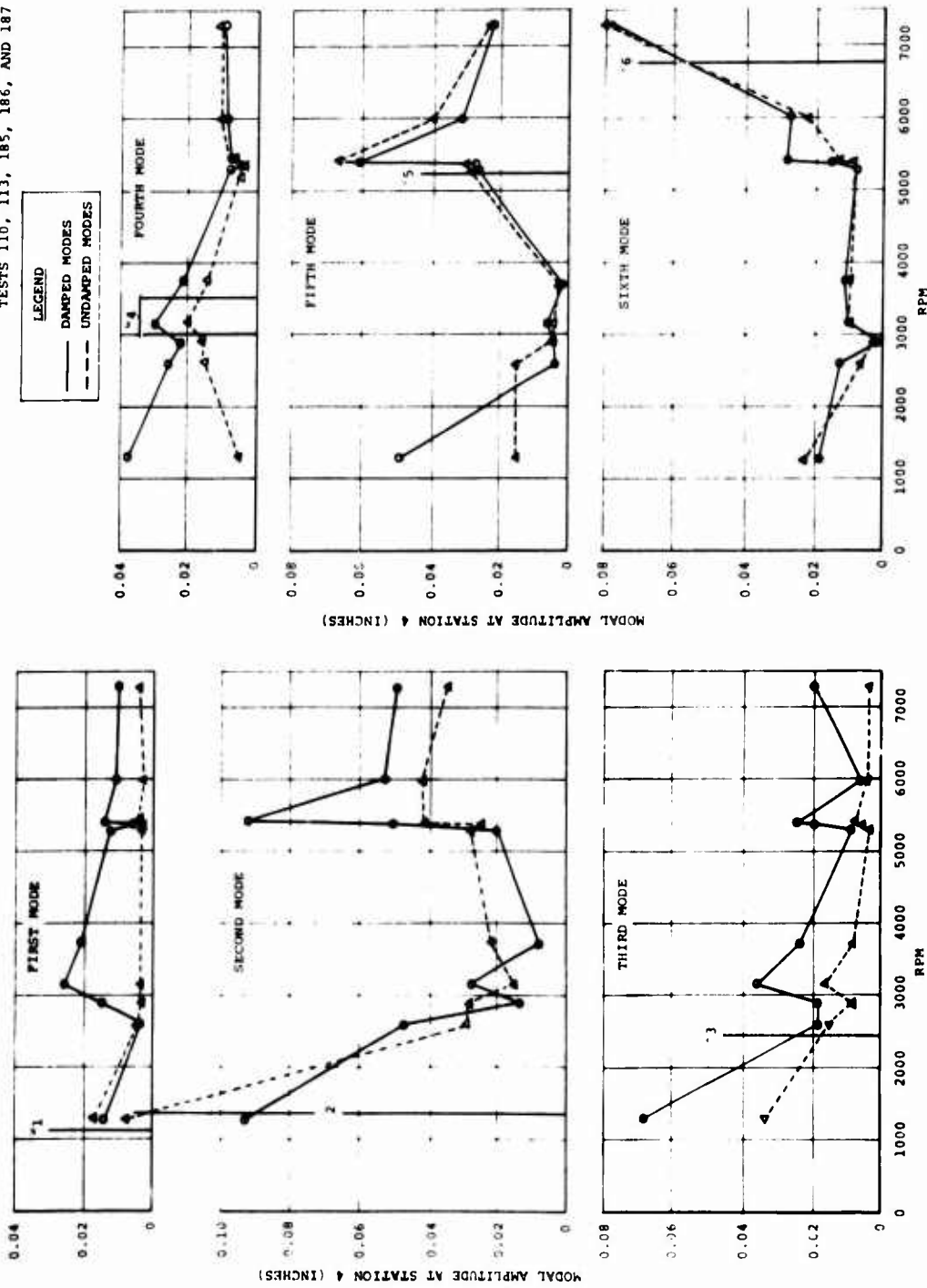


Figure 152. Generalized Coordinate Analysis of Unbalanced Shaft - Modal Amplitude.

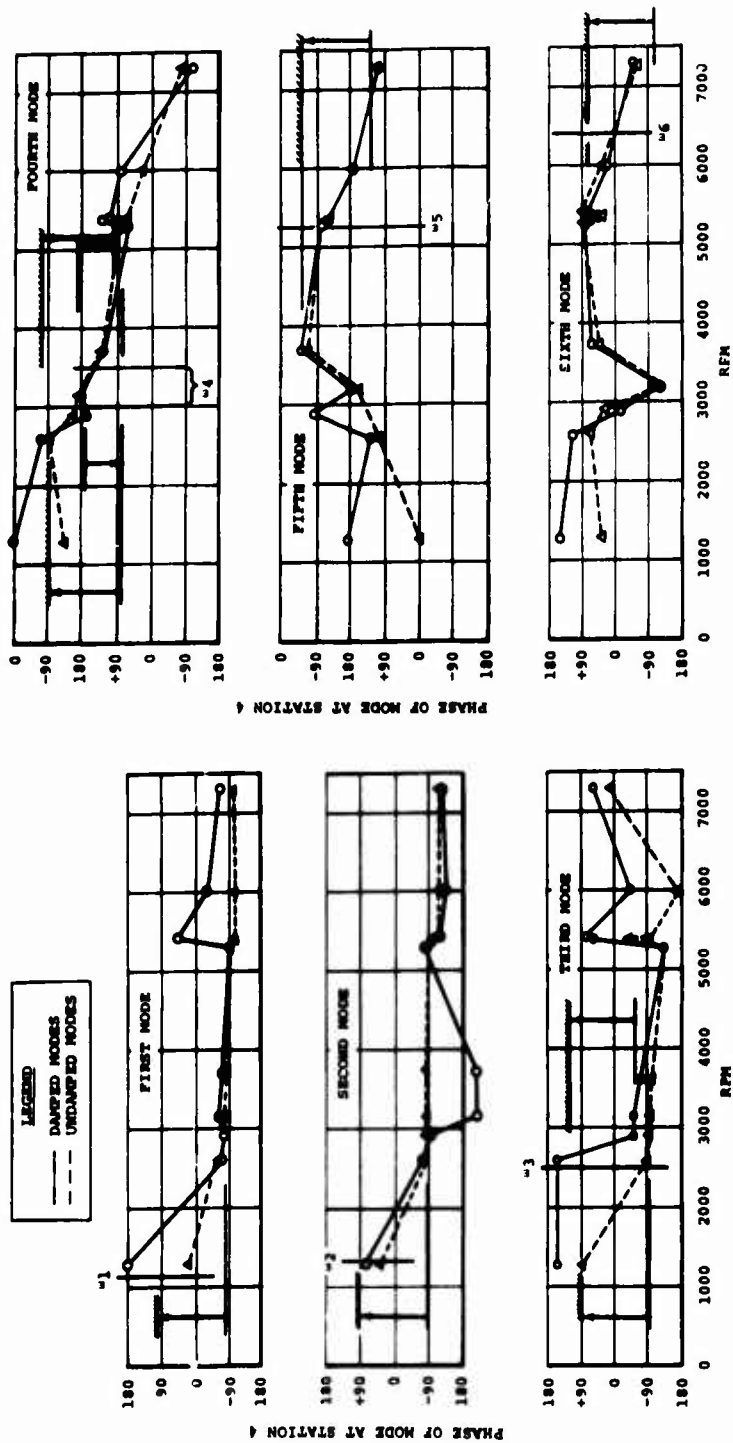


Figure 153. Generalized Coordinate Analysis of Unbalanced Shaft - Modal Phase.

TABLE VI. SUMMARY OF RESULTS; GENERALIZED COORDINATE ANALYSIS WITH UNDAMPED MODES						
Mode	Test rpm	Test Modes Corrected for Initial Bend		Final Test Balance Configuration		Phase to Balance Initial Bend (Initial Bend + 180°)
		Force*	Phase**	Force	Phase**	
1	1140 (est)	732	- 80°	96	- 125°	+ 2°
2	1350	108	- 85°	25	- 107°	+116°
3	2500	64	- 95°	47	- 107°	- 52°
4***	3000	70	+100°	32	- 42°	+124°
	3500	82	+ 60°	44	- 42°	
5	5250	16	+125°	13	+161°	+143°
6	6400	87	+110°	91	+ 97°	+ 83°
NOTE: * Force required to balance mode ** Phase of mode at station 4 *** Position of fourth shaft mode not certain						

TABLE VII. SUMMARY OF RESULTS: GENERALIZED COORDINATE ANALYSIS WITH DAMPED RESPONSE SHAPES					
Mode	Test rpm	Test Modes		Final Test	
		Corrected for Force*	Initial Bend Phase**	Balance Force	Configuration Phase**
1	1140 (est)	25	- 80°	36	- 115°
2	1350	19	- 85°	28	- 111°
3	2500	25	- 60°	14	- 103°
4***	3000	76	+ 80°	28	- 57°
	3500	90	+ 55°	39	- 57°
5	5250	8	+125°	11	+148°
6	6400	76	+110°	90	+ 90°
NOTES: * Force required to balance mode ** Phase of mode at station 4 *** Position of 4th shaft mode not certain					

At the n th critical speed

$$FX_n = C \left[H_n^2(y_1) + H_n^2(y_2) \right] \omega_n A_n(\omega_n)$$

$$FZ_n = C \left[H_n^2(y_1) + H_n^2(y_2) \right] \omega_n B_n(\omega_n)$$

where

FX_n and FZ_n are the generalized forces in the X and Z directions at the n th natural frequency.

$H_n(y_1)$ and $H_n(y_2)$ are the amplitudes of the n th coordinate at the damper locations.

$A_n(\omega_n)$ and $B_n(\omega_n)$ are the modal coefficients at the n th critical speed from the generalized coordinate analysis.

ω_n is the frequency at the n th critical speed.

C is the damping coefficient at the supports.

Likewise at the n th critical speed:

$$FX_n = \sum_{i=1}^h \epsilon M_i(x) H_n(y_i) \omega_n^2$$

$$FZ_n = \sum_{i=1}^h \epsilon M_i(z) H_n(y_i) \omega_n^2$$

where

$H_n(y_i)$ is the amplitude of the n th coordinate at i th balance station.

$M_i(x)$ and $M_i(z)$ are the components of the i th balance weight in the x and z directions.

ϵ is the radius at which balance weight is added.

h is the number of balance locations

Examination of Table VI, which summarizes the results obtained with the undamped mode coordinates, shows a fair degree of correlation with the test balance configuration. With the exception of the fourth mode, the phase angles from the generalized coordinate analysis are reasonably close to the test values. The generalized forces compare favorably for the third, fifth, and sixth modes; while the fourth mode is approximately twice the test value. The largest apparent error in the generalized forces occurs at the first and second modes. So far as the initial bend is concerned, only the fifth and sixth modes show any correlation with the test

balance configuration, which is difficult to understand since it is generally accepted that the initial bend contributes heavily to the lower mode unbalance. Note that the test balance configuration does not represent a fully balanced condition. The primary test effort was directed at the range above 5,000 rpm (fifth and sixth modes), and the response at the single low-frequency peak (coupled first and second modes) was reduced by only 60 percent. Considering these facts, good correlation should be anticipated for the fifth and sixth modes, while a 40- to 50-percent difference may be expected at the first and second modes.

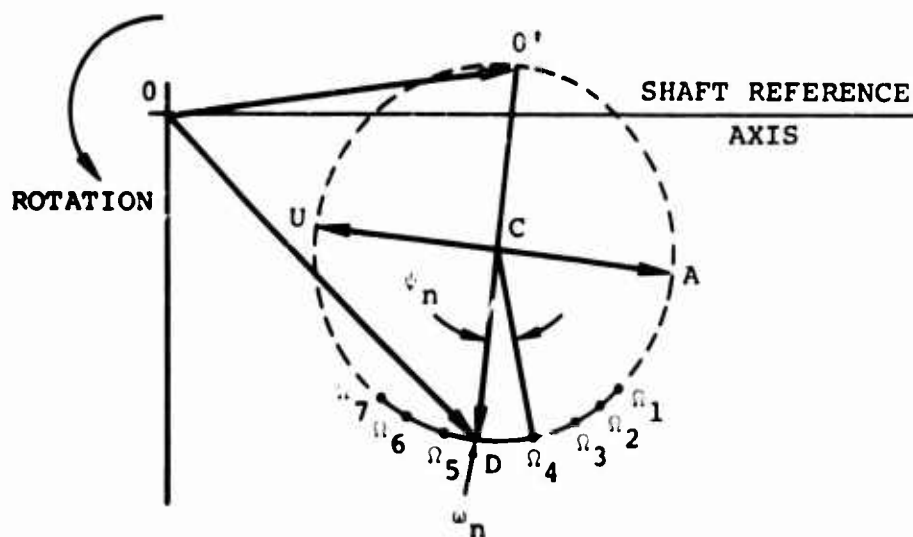
Summarized results presented in Table VII for the damped coordinates compare somewhat more favorably with the test balance configuration. Except for the third and fourth modes, the phase angles agree reasonably with the test values and do not significantly differ from the previous results with the undamped modes. Magnitude of the generalized forces at the third and fourth modes ranges from 2 to 2-1/2 times the test values, however, the remaining modes, including the first and second, compare quite favorably with the test values. The improved correlation of the first and second mode generalized forces appears to be the principal difference resulting from the use of the damped coordinates.

In conclusion, the generalized coordinate analysis of test-response shapes can be an effective method of obtaining both the phase and magnitude of the unbalance when the measured response is a superposition of several modes. However, a large number of test points near each critical speed are required to accurately define the phase response. Furthermore, once the phase response is defined, a great deal of judgment is involved in establishing the plane of the unbalance. Generally speaking, therefore, the process is rather time consuming and does not lend itself to an automated procedure.

GRAPHIC ISOLATION OF MODES

A graphic method for isolating the response of a particular mode, in the case where the shaft deflections are a superposition of modes, is presented. The method is best described as a modification of the Kennedy-Pancu method of resonance testing.⁹ For the purposes of this report, it will suffice to outline the procedure and explain the significance of the various diagrams which must be constructed.

1. At a series of frequencies Ω_i taken at constant speed increments, obtain the vector response $\eta(o)$ for the unbalanced shaft through the critical speed range. Construct a polar plot of $\eta(o)$, and fit a circle through the points with the maximum frequency spacing (see Figure 158).
2. Add a trial weight at any arbitrary angle β_n from the shaft reference axis, and measure the response $\eta(1)$ at the same frequencies used in step 1.
3. Compute the vectors $\eta_m(1) = \eta(1) - \eta(o)$. Construct a polar plot of $\eta_m(1)$ and fit a circle to the points as in step 1 (see Figure 155).
4. In Figure 154, draw the resonance diameter $O'D$ so that it makes a 90-degree angle ($\beta_n - 90$) with the reference axis. This locates the critical speed ω_n . Measure ψ_n from the reference frequency (in this case Ω_4), and use this information to construct the resonance



- where $\eta(0)$ = Vector response of the unbalanced shaft
- OD = Total response at the r th critical speed
- $O'D$ = Response in the mode of the r th critical
- OO' = Contribution of other modes at r th critical
- CA = Direction of the unbalance
- CU = Direction in which balance weight must be added
- ω_n = Critical speed
- Ω_i = Speeds at which data is obtained

Figure 154. Vector Response of Unbalanced Shaft at the n th Critical Speed.

diameter $O'D$ on Figure 155. The direction of the unbalance (vector CA) may now be located in Figure 154, 90 degrees ahead (in direction of rotation) of the resonance diameter $O'D$. It is also possible to obtain the approximate location of $O'D$ in both Figures 154 and 155 by inspection alone, since the critical speed occurs in the area where the test points display the maximum frequency spacing.

5. An estimate of the magnitude of the required balance weight is as follows:

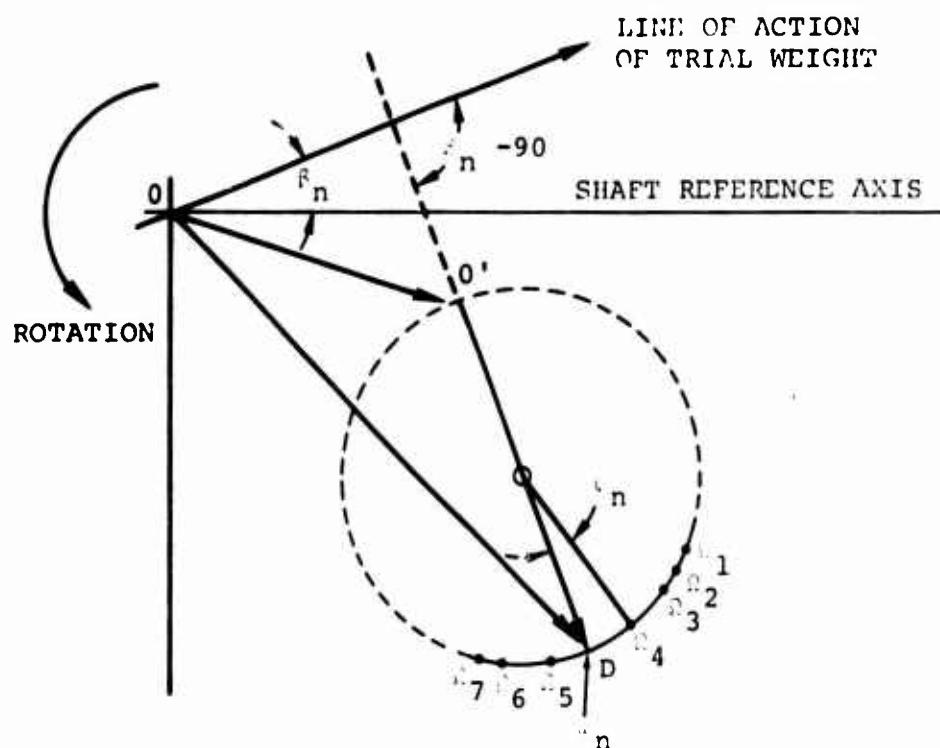
$$\text{Required Weight} = \frac{\text{Diameter of Circle Made Using } \eta(0)}{\text{Diameter of Circle Made Using } \eta_m(1)} \times (\text{Trial Weight})$$

In the situation where the response involves a significant superposition of modes, the experimental modal balancing procedure discussed in the previous report² cannot be used since it is necessary to observe the response of a single mode. However, application of the procedure described above should make it possible to observe the isolated response of the mode which is being balanced so that the experimental modal balancing procedure may again be followed. While a fair amount of graphic analysis is required, the method offers the advantage of determining, with one position of a trial weight, both the plane of the unbalance and the effective weight required to balance the mode. The principal disadvantage is that the modal method requires a knowledge of the basic mode shapes.

Validity of the modified Kennedy-Pancu method was investigated using available test data. Figure 156 shows a polar plot of the vector response for shaft station 4 in the vicinity of the combined first and second modes. The frequency spacing gives a reasonably good indication of a mode in the range from 1,275 to 1,400 rpm, which corresponds to the second mode. There is also some indication of the first mode in the range from 1,200 to 1,250 rpm; the presence of a second loop, illustrated in Figure 157, confirms this.

Response to a trial weight at station 5 is shown in Figure 158. As in the case of Figure 156, this plot fails to clearly show the presence of a lower mode; however, the cusp at 1,250 rpm indicates that a second loop is beginning to form. Based on previous analysis, a trial weight at the opposite end of the shaft would excite the first mode. Fitting a circle through the points of maximum frequency spacing and constructing the resonance diameter $O'D$ 90 degrees behind the line of action of the trial weight, indicates a resonant frequency at 1,350 rpm. Returning to Figure 156 and constructing the diameter $O'D$ indicates that the balance weight should be placed at -102 degrees or 90 degrees behind the response at resonance. Computing the balance weight as indicated in step 5, a weight of 62.5 grams at station 5 is required to balance the mode. Note from Figure 156 that balancing the second mode does not reduce the response to zero since the response $O'O' = 0.1$ inch due to other modes is still present. These results are in general agreement with the experimentally observed results.

Attempts to apply the method in the area of the other modes were inconclusive. Failure of the method in general is probably caused by the small amplitudes at resonance and the relatively heavy damping in these modes. Results for the fifth mode presented in Figures 159 and 160 are typical. The response of the unbalanced shaft, Figure 159, shows a loop between 5,100 and 5,450 rpm. The frequency spacing taken at face value indicates a possible resonance between 5,250 and 5,350 rpm within the loop in addition to a second resonance between 5,450 and 5,500 rpm. A circle fitted through the points at 5,450 and 5,500 rpm shows that a circle of



where $r_n(1)$ = Vector response of the shaft to the trial weight above

r_n = Angular location of trial weight

ϕ_n = Angular location of resonance diameter $0'D$ from reference speed ω_4

Figure 155. Vector Response to Trial Weight at the nth Critical Speed.

$$50.0 \left(\frac{0.275}{0.22} \right) = 62.5 \text{ GRAMS AT } -102^{\circ}$$

204

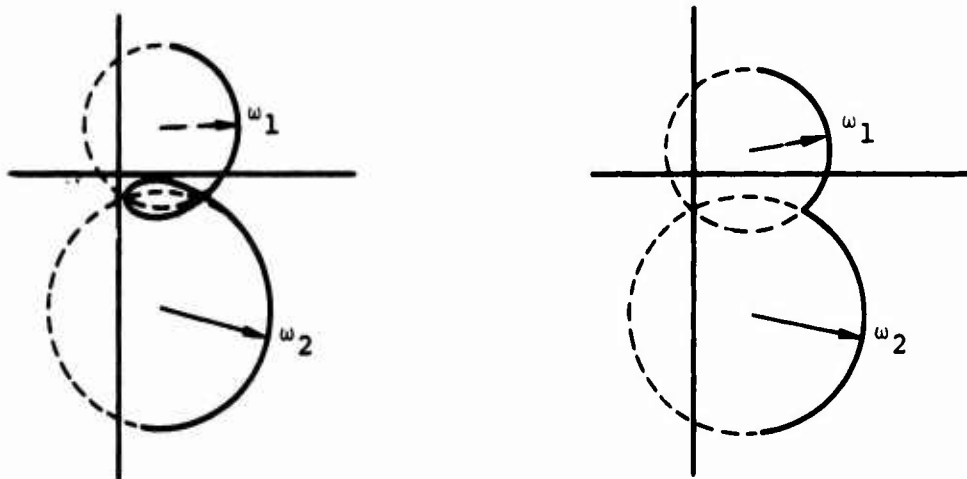
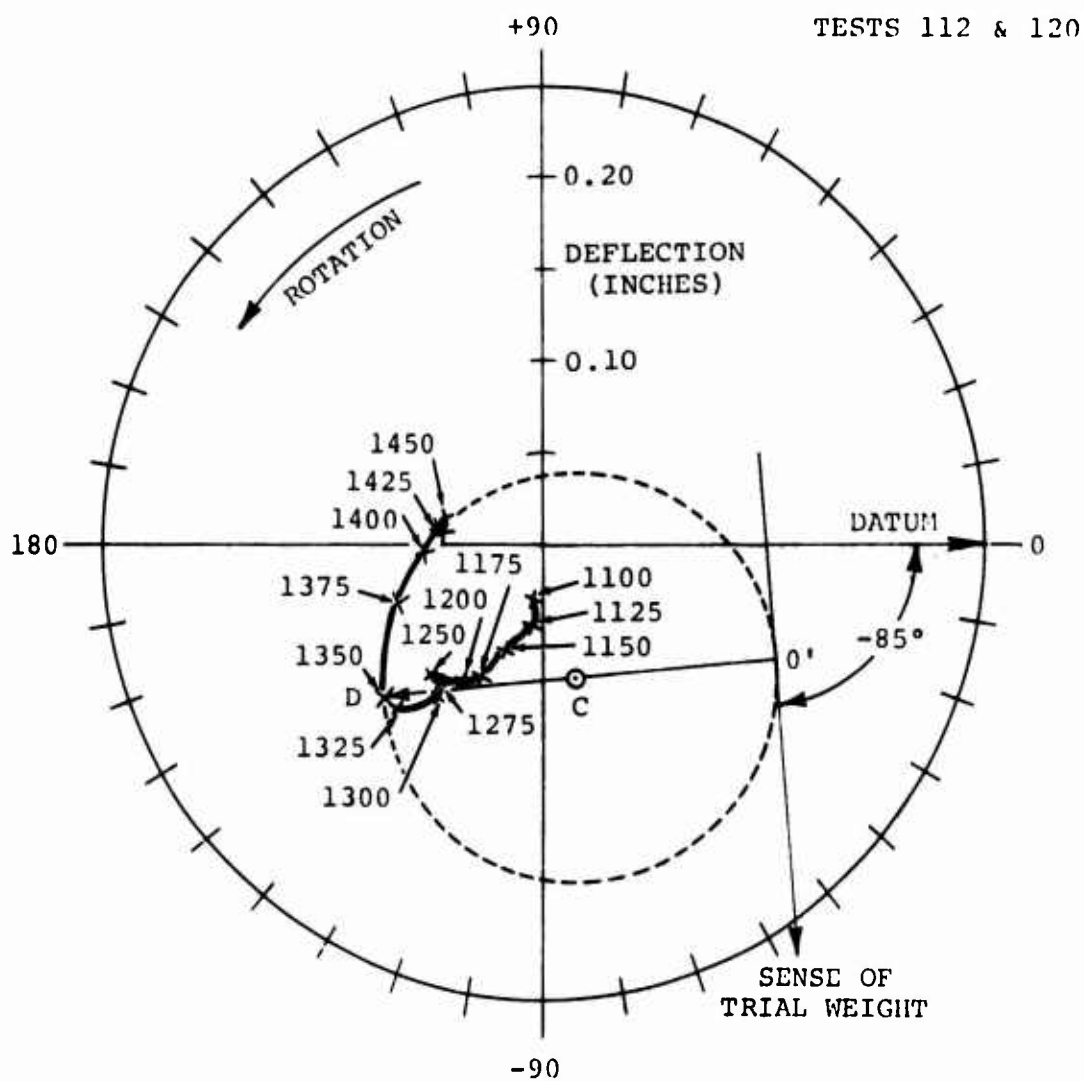


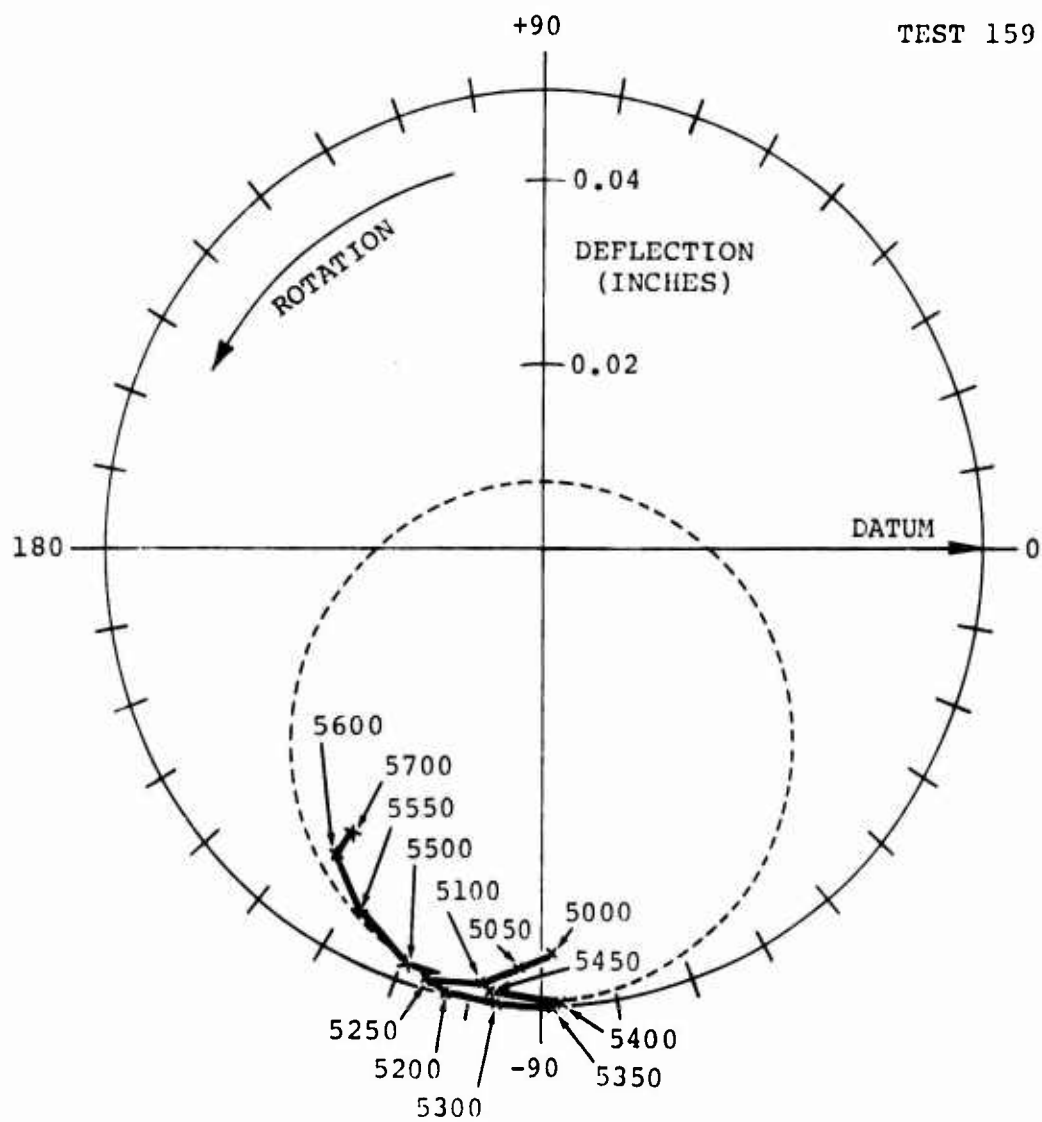
Figure 157. Typical Polar Plot Characteristics for Two Modes.



NOTE:

50 GRAM TRIAL WEIGHT AT -85° AT STATION 5

Figure 158. Response to Trial Weight at First and Second Modes.

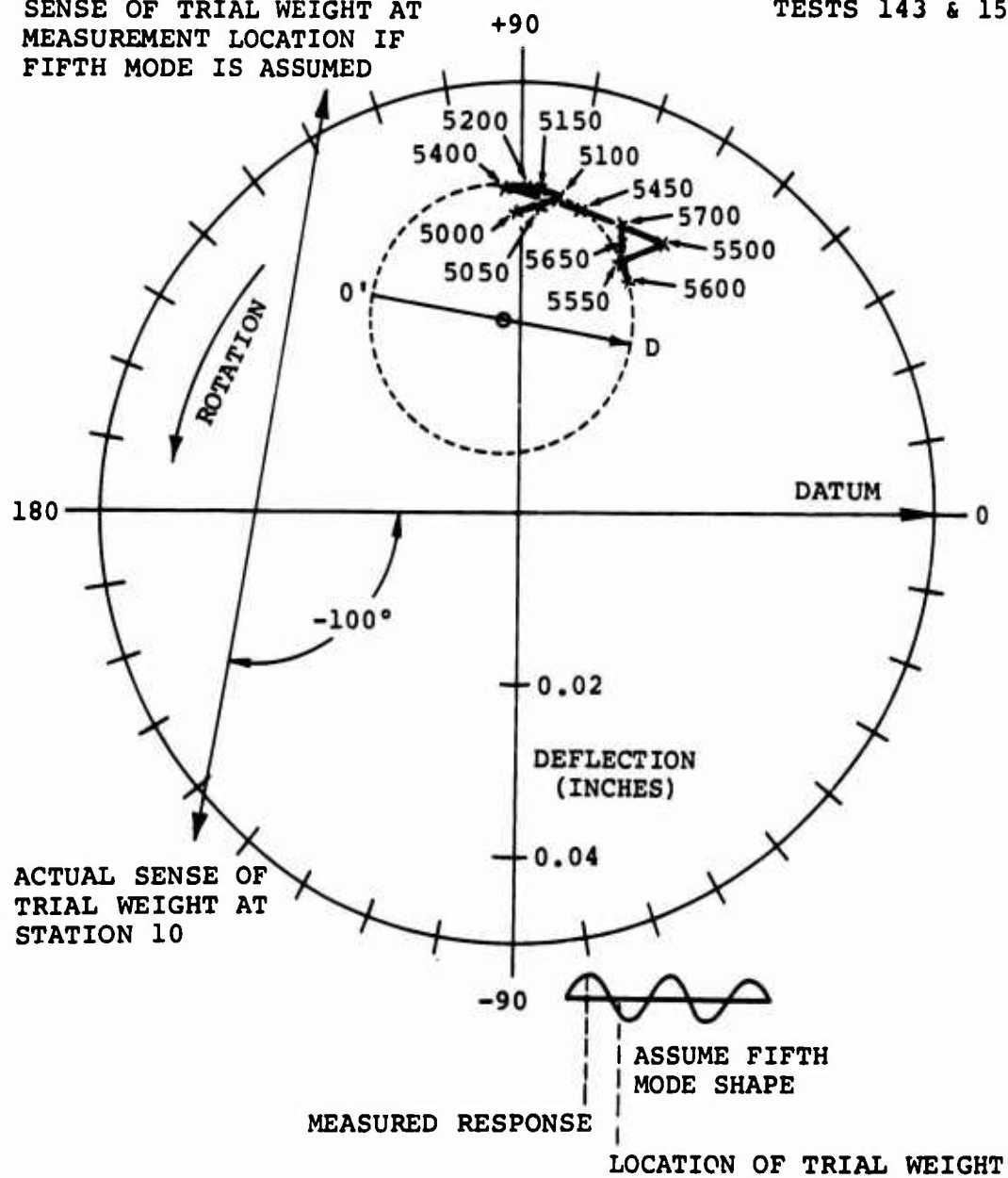


NOTE:
LOW-SPEED SHAFT REMOVED

Figure 159. Shaft Response at Fifth Mode.

SENSE OF TRIAL WEIGHT AT
MEASUREMENT LOCATION IF
FIFTH MODE IS ASSUMED

TESTS 143 & 159



NOTE:

25 GRAM TRIAL WEIGHT AT -100° AT STATION 10

Figure 160. Response to Trial Weight at Fifth Mode.

only slightly larger diameter would pass through the points between 5,250 and 5,350 rpm. Response to a trial weight at station 10 (deflections measured at station 4) is shown in Figure 160; here the frequency spacing indicates a resonance only in the 5,450- to 5,500-rpm range. If the modal circle is fitted through these points and the resonance diameter $O'D$ erected perpendicular to the line of action of the trial weight, a meaningless result is obtained since the resonance diameter does not intersect the locus of the test points.

INFLUENCE COEFFICIENT BALANCING METHOD

During the test program, a series of runs was made to determine the effectiveness of a trial weight at each available balancing station in reducing the deflections at the monitoring location (station 4). By varying the angular position of the trial weight, it was also possible to determine the most effective angle. While it was still necessary to resort to a trial-and-error procedure, this information was instrumental in finally obtaining an acceptable balance configuration. Since the trial weight effectiveness determined experimentally was in essence an influence coefficient, a procedure employing a formalized application of the influence coefficient principle may be used as a method of balancing. Such a procedure is outlined in Reference 8.

Reference 8 indicates a number of methods of applying the influence coefficient principle to a rotating shaft. In general, an n-point balance can be computed provided that

$$\Sigma (\text{Measurement Locations}) \times (\text{Test Speeds}) = n$$

For example, a six-point balance can be computed either from test measurements at two locations and three speeds or test measurements at a single location and six speeds. Data available from the test program fall into the latter category. The equations suitable to the existing data are presented in the following paragraph.

In computing an n-point balance, it is assumed that the distributed unbalance in the shaft can be represented by n discrete unbalanced masses located at the balancing stations. At a speed of ω_i , the displacement of the unbalanced shaft at the monitoring location is given by

$$W_{AO}(\omega_i) = \sum_{n=1}^h \alpha_{An}(\omega_i) U_n \quad (i=1 \text{ to } n)$$

where $W_{AO}(\omega_i)$ is displacement of the unbalanced shaft at station (A) at a shaft speed of ω_i

$\alpha_{An}(\omega_i)$ is dynamic influence coefficient at station (A) for an unbalanced mass at station (n) at a shaft speed of ω_i

U_n is the effective unbalanced mass at station (n)

h is the number of balance stations.

The dynamic influence coefficients are obtained experimentally. Displacement and phase of the unbalanced shaft are measured at station A for n different shaft speeds covering the operating range. Measurements close to each of the critical speeds are desirable. A trial weight T is then placed at one of the selected balance stations, and the response at station A is measured for the same shaft speeds. This procedure is repeated with the trial weight located in turn at each of the remaining balance stations. At the shaft speed ω_1 , the displacement of the unbalanced shaft $W_{A0}(\omega_1)$ and the displacement $W_{A1}(\omega_1)$ with the trial weight at balance station 1 are given by

$$W_{A0}(\omega_1) = \alpha_{A1}(\omega_1) U_1 + \alpha_{A2}(\omega_1) U_2 + \dots + \alpha_{An}(\omega_1) U_n$$

$$W_{A1}(\omega_1) = \alpha_{A1}(\omega_1) [U_1 + T] + \alpha_{A2}(\omega_1) U_2 + \dots + \alpha_{An}(\omega_1) U_n$$

Subtracting the first equation from the second yields

$$\alpha_{A1}(\omega_1) = \frac{W_{A1}(\omega_1) - W_{A0}(\omega_1)}{T}$$

and in general

$$\alpha_{An}(\omega_n) = \frac{W_{An}(\omega_n) - W_{A0}(\omega_n)}{T}$$

The complex deflection matrix for n balancing locations and shaft speeds is as follows:

$$\begin{Bmatrix} W_{A0}(\omega_1) \\ W_{A0}(\omega_2) \\ W_{A0}(\omega_3) \\ \vdots \\ W_{A0}(\omega_n) \end{Bmatrix} = \begin{Bmatrix} \alpha_{A1}(\omega_1) & \alpha_{A2}(\omega_1) & \alpha_{A3}(\omega_1) & \dots & \alpha_{An}(\omega_1) \\ \alpha_{A1}(\omega_2) & \alpha_{A2}(\omega_2) & \alpha_{A3}(\omega_2) & \dots & \alpha_{An}(\omega_2) \\ \alpha_{A1}(\omega_3) & \alpha_{A2}(\omega_3) & \alpha_{A3}(\omega_3) & \dots & \alpha_{An}(\omega_3) \\ \vdots & \vdots & \vdots & \ddots & \vdots \\ \alpha_{A1}(\omega_n) & \alpha_{A2}(\omega_n) & \alpha_{A3}(\omega_n) & \dots & \alpha_{An}(\omega_n) \end{Bmatrix} \begin{Bmatrix} U_1 \\ U_2 \\ U_3 \\ \vdots \\ U_n \end{Bmatrix}$$

In this expression, the $\{W_{A0}(\omega_i)\}$ and $\{\alpha_{An}(\omega_i)\}$ matrices are defined numerically from the test data as previously discussed. Using a conventional complex matrix routine such as Vertol's program D-73, the values of the *effective* unbalance U_n at each balance station can be obtained. The required balance is obtained by simply shifting the calculated unbalance 180 degrees.

An evaluation of the influence coefficient method was undertaken using available test data. Influence coefficients for 5,300, 6,250, 7,300 and 8,300 rpm were obtained from the data of test runs 210 through 233 (Figures 106 through 119). At 1,300 rpm, the influence coefficient

at station 11 was determined from test runs 115 and 116 (not shown), and values for the remaining balance stations were extrapolated on the basis of the measured mode at 1,300 rpm. The real and imaginary components of the influence coefficients thus obtained are tabulated in Table VIII for possible future use.

Using the influence coefficients of Table VIII and test data for the unbalanced shaft at corresponding speeds, a calculation was performed to obtain a five-point balance configuration. For comparison purposes, the required additional balance weights for a partially balanced configuration and the final test balance configuration were also computed. For each configuration, the total required balance weight and phase at each of the selected balance stations are summarized in Table IX. Provided the system is linear and there are no errors in either the influence coefficients or the measured shaft response, each of the calculated balance configurations should be the same. Examination of Table IX indicates that such is not the case. In particular, Configuration I based on the measured response of the unbalanced shaft shows a large disparity at stations 24 and 27 when compared with the other calculated results and the final test balance configuration. Configuration II, using measured response from a partially balanced shaft, displays very good correlation with the final test configuration and only slightly less agreement with Configuration III. Results for Configuration III, based on measured response with the final test balance configuration, indicate relatively small variations when compared to the test balance weights.

Table X presents a comparison between the initial weight distribution for the calculated balance configurations and the weight distribution on the shaft at the time the influence coefficients were determined. Initial weight distribution for calculated balance Configuration II shows the greatest similarity to the weight distribution present when the influence coefficients were determined, while Configuration I is least similar. Significantly, Configuration II displays the best correlation with the test balance configuration and Configuration I the least correlation. In itself, this observation suggests a nonlinearity in the shaft behavior since the baseline response for Configuration I was significantly higher than that for Configuration II, which was already partially balanced.

Considering the accuracy of the test measurements, the fact that shaft deflections were measured in only one plane, and the use of some extrapolated values for the influence coefficients at 1,300 rpm, the results obtained by the influence coefficient method are quite encouraging. Clearly, more accurate test data would improve the results. Of the various schemes examined, the influence coefficient method is the only method which appears to predict a reasonable balance weight distribution without resort to a great deal of engineering judgment. Unlike the other methods, a detailed knowledge of the mode shapes and the exact location of the critical speeds is not necessary; however, a general knowledge of the mode shapes is helpful in selecting the balance stations.

As indicated previously, there are a number of possible combinations of measurement locations and speeds which will permit the calculation of a balance weight distribution for a given shaft. In each case, the best combination is dependent on the shaft configuration and the operating conditions. For the present shaft, a six-point balance is desirable since all evidence indicates that there are six criticals in the total speed range. The following scheme, Table XI, which favors the steady operating condition, is suggested:

TABLE VIII. EXPERIMENTALLY DETERMINED INFLUENCE COEFFICIENTS AT STATION 4 WITH STIFFENED DAMPER SUPPORT STRUCTURE											
Shaft Speed (RPM)		Balance Location									
		α_1 Station 5		α_2 Station 11		α_3 Station 21+1 Inch		α_4 Station 24		α_5 Station 27	
		Real	Imaginary	Real	Imaginary	Real	Imaginary	Real	Imaginary	Real	Imaginary
ω_1	1300	-1.18×10^{-3}	-1.76×10^{-3}	-1.12×10^{-3}	-1.86×10^{-3}	-2.08×10^{-3}	-0.48×10^{-3}	-2.26×10^{-3}	-0.24×10^{-3}	-2.26×10^{-3}	-0.24×10^{-3}
ω_2	5300	0.16×10^{-3}	-0.25×10^{-3}	5.16×10^{-3}	1.44×10^{-3}	4.78×10^{-3}	0.87×10^{-3}	4.03×10^{-3}	1.35×10^{-3}	5.16×10^{-3}	-0.32×10^{-3}
ω_3	6250	0.21×10^{-3}	0.47×10^{-3}	2.91×10^{-3}	-0.50×10^{-3}	1.25×10^{-3}	-0.62×10^{-3}	2.39×10^{-3}	-0.50×10^{-3}	1.45×10^{-3}	-1.74×10^{-3}
ω_4	7300	-1.38×10^{-3}	3.23×10^{-3}	2.64×10^{-3}	-0.36×10^{-3}	0.51×10^{-3}	1.80×10^{-3}	1.40×10^{-3}	1.34×10^{-3}	0.55×10^{-3}	1.44×10^{-3}
ω_5	8300	1.25×10^{-3}	1.06×10^{-3}	2.03×10^{-3}	-2.55×10^{-3}	0.68×10^{-3}	-0.58×10^{-3}	2.26×10^{-3}	-0.43×10^{-3}	0.13×10^{-3}	-1.76×10^{-3}

TABLE IX. COMPARISON OF CALCULATED BALANCE CONFIGURATIONS OBTAINED BY INFLUENCE COEFFICIENT METHOD						
Shaft Station	Configuration I		Configuration II		Configuration III	
	Weight (Grams)	Phase	Weight (Grams)	Phase	Weight (Grams)	Phase
5	19.5	- 96	19.7	- 93	31.4	- 110
11	29.8	- 108	30.7	- 118	38.6	- 117
21+1"	13.2	+116	25.3	+ 81	30	+ 79
24	40	+ 59	31.7	- 35	32.8	- 47
27	1.3	+144	19.6	+111	34.9	+ 78
NOTE: <div> Configuration I --- Baseline response data from unbalanced (no weights) shaft Configuration II --- Baseline response data from partially balanced shaft Configuration III --- Baseline response data from final test balance configuration </div>						

TABLE X. COMPARISON OF INITIAL WEIGHT DISTRIBUTIONS FOR CALCULATED BALANCE CONFIGURATIONS										
Shaft Station	Initial Weight Distributions for Calculated Balance Configurations						Weight Distribution During Influence Coefficient Tests			
	Configuration I		Configuration II		Configuration III		Station 21 + 1 Inch		Stations 5, 11, 24, 27	
	Weight (Grams)	Phase	Weight (Grams)	Phase	Weight (Grams)	Phase	Weight (Grams)	Phase	Weight (Grams)	Phase
5	0	0	21.2	- 90	27.6	- 105	21.2	- 90	21.2	- 90
11	0	0	23.1	- 90	30	- 105	23.1	- 90	23.1	- 90
21+1"	0	0	19	+ 90	26	+ 68	19	+ 90	15.2	+ 66
24	0	0	0	0	21.9	- 80	0	0	0	0
27	0	0	22.2	+ 90	28.8	+ 75	22.2	+ 90	22.2	+ 90

TABLE XI. SUGGESTED BALANCE ARRANGEMENT	
Measurement Location	Speed
Station 5	1,300 rpm
Station 5	3,000 (Idle Range)
Station 5	5,300
Stations 5 and 27	7,000 (Normal Operation)
Station 5	8,300 (Maximum Operating)
Balance at Stations: 5, 11, 15, 21, 27, 33	

Balance stations are selected to place one balance station near each antinode of the sixth mode, which is the mode nearest the operating speed. This balance arrangement should provide a smooth-running flexible shaft throughout the entire speed range.

The problem of unbalance at the ends of the shaft could be combined with the balance of the flexible system if the measurement data are obtained at the ends, or this problem could be handled separately.

ANALYTICAL SIMULATION OF A ROTATING SYSTEM

The basic design of a supercritical-shaft system can be established by conventional methods from an analysis of a nonrotating system. However, in order to adequately predict the performance and assess the effect of such items as shaft straightness, bearing misalignment, and nonisotropic-support-point stiffness, an analysis of the rotating system is required.

For the most part, studies of the behavior of rotating shafts on flexible supports have been restricted to simplified isotropic systems.^{10,11} A more general analysis using numerical methods is presented in Reference 12; however, this method is also restricted to isotropic systems.

Consideration of nonisotropic support conditions results in a set of linear differential equations with periodic coefficients which are most readily evaluated on a digital computer using available numerical integration techniques. Development of an analysis for a rotating shaft with nonisotropic structural supports (program C-58) is presented in Appendix I.

ANALYTICAL MODEL AND CASES ANALYZED

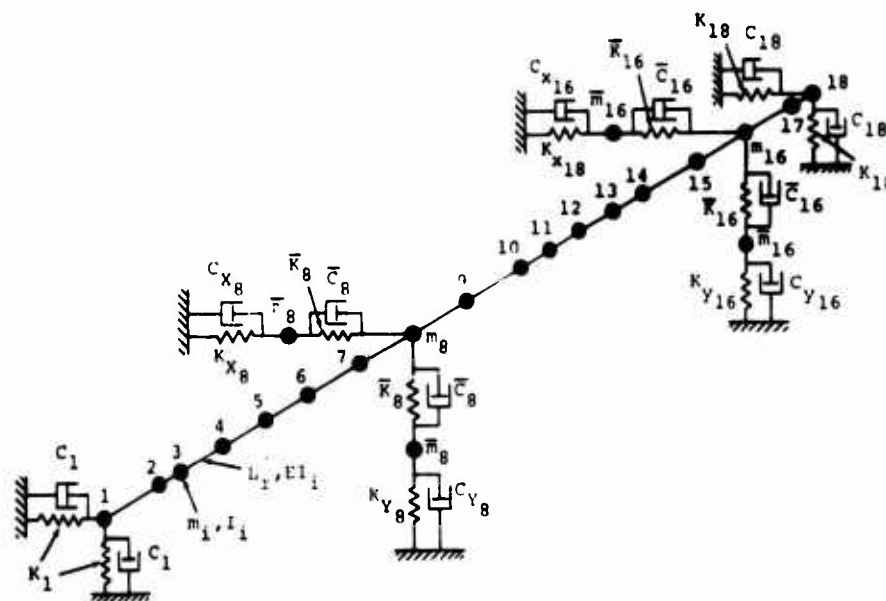
An analytical model generally representative of the present test configuration is shown in Figure 161. The nonuniform axial distribution of the shaft mass was necessary to place mass stations at locations corresponding to the shaft balance stations. Exact support conditions are difficult to define without an extensive analysis of the support structure. Calculated stiffness of the orbiting-end-load fitting indicates that the ends are effectively rigid; therefore, an isotropic condition has been assumed for convenience. At the intermediate supports, a nonisotropic condition prevails, and the calculated local stiffnesses are used in conjunction with the weight of the nonrotating portion of the damper assembly. Structural damping at the supports has been taken as 2 percent of critical based on the local mass and stiffness.

Static stiffness matrices obtained from an existing program (Vertol program D-46) are used as an input to the C-58 shaft-analysis program, and it is possible to analyze a system with nonisotropic shaft stiffness as well as axial variations in shaft stiffness. These items do not appear to be of any significance in the case of the present shaft; consequently, an isotropic shaft with a constant EI has been assumed.

Specific questions arose during the test phase of the program. The analytical configurations believed necessary to obtain insight into these questions as well as to evaluate the principal characteristics of the system are as follows:

Rigid Support Structure (Isotropic System)

- A coplanar third-order initial bend
- A coplanar third-order mass unbalance with a distributed unbalance equivalent to the coplanar third-order initial bend
- A coplanar second-order bend which produces an initial deflection at the aft damper



SHAFT PROPERTIES

i	m_i (lb-sec ² /lb)	I_i (lb-in-sec ²)	l_i (in)	EI_i (lb-in ²)
1	0.04	0	29.868	4.18×10^7
2	0.0032	0.985	9.956	4.18×10^7
3	0.008542	0.304	19.912	4.18×10^7
4	0.008542	0.304	19.912	4.18×10^7
5	0.008542	0.304	19.912	4.18×10^7
6	0.008542	0.304	24.89	4.18×10^7
7	0.013813	0.985	24.89	4.18×10^7
8	0.0448	0.444	26.1345	4.18×10^7
9	0.013881	1.246	23.6455	4.18×10^7
10	0.006406	0.135	14.934	4.18×10^7
11	0.006406	0.135	14.934	4.18×10^7
12	0.006406	0.135	14.934	4.18×10^7
13	0.006406	0.135	14.934	4.18×10^7
14	0.006406	0.135	23.6455	4.18×10^7
15	0.13001	1.246	26.1345	4.18×10^7
16	0.0448	0.444	19.912	4.18×10^7
17	0.008542	0.304	9.956	4.18×10^7
18	0.04	0		

SUPPORT STRUCTURE

K_1	=	K_{18}	=	4×10^6 lb/in.
C_1	=	C_{18}	=	16.5 lb-sec/in.
m_8	=	m_{16}	=	0.01036 lb-sec ² /in.
K_8	=	K_{16}	=	2000 lb/in.
C_8	=	C_{16}	=	21.3 lb-sec/in.
K_{x8}	=	K_{x16}	=	2300 lb/in.
K_{y8}	=	K_{y16}	=	6.8×10^5 lb/in.
C_{x8}	=	C_{x16}	=	0.2 lb-sec/in.
C_{y8}	=	C_{y16}	=	3.4 lb-sec/in.

Figure 161. Analytical Model for Test Configuration.

- A noncoplanar mass unbalance which is the reverse of the final test balance configuration

Flexible Support Structure (Nonisotropic System)

- A noncoplanar mass unbalance which is the reverse of the final test balance configuration

Plots illustrating the initial deflection and mass unbalance versus shaft span for the above configurations are presented in Figure 162.

RESULTS OF ANALYSIS

Within the time frame of the present program, it was not possible to complete all of the desired analyses. Figure 162 shows that the unbalance for coplanar configurations is at either +90 or -90 degrees. Typical results with rigid support structure obtained at 1.350 rpm are shown in Figure 163. The predominant response for the coplanar configurations is essentially a second mode which lags the unbalance by 90 degrees. This indicates a near resonant condition. Response in the plane of the unbalance strongly resembles the undamped first mode obtained in the initial design analysis. The second mode shape of the predominant response and the frequency agree with the previous analytical results which predicted a second mode at this speed.

As anticipated, identical results were obtained for the coplanar third-order initial bend and the equivalent third-order mass unbalance. Characteristics of the two types of unbalance with balance weights installed were not investigated; however, the analysis in **VIBRATION AND BALANCE OF AN UNBALANCED FLEXIBLE ROTOR**¹⁰ indicates that the initial bend can be removed only at the critical speed. Response to the second-order initial bend varies only slightly from the results obtained for the third-order bend, which is not unexpected since the second-mode component of the unbalance in both cases is very nearly the same. Principal interest in the second-order bend is the effect on damper load at the higher speeds, which have not been analyzed.

Results for the noncoplanar mass unbalance generally resemble those obtained for the coplanar configurations. The increase in amplitude is due to the increased magnitude of the unbalance as shown in Figure 162. Distortion of the response in the 0/180-degree plane is due to the fact that strong components of other modes are present in the unbalance distribution.

Generally speaking, the results obtained display many of the characteristics of the test data. Of particular interest is the mixed modal response, with a second mode predominant in one plane and a first mode predominant in a plane 90 degrees away. This superposition of modes which is present even with a coplanar unbalance produces a static noncoplanar deflection of the shaft.

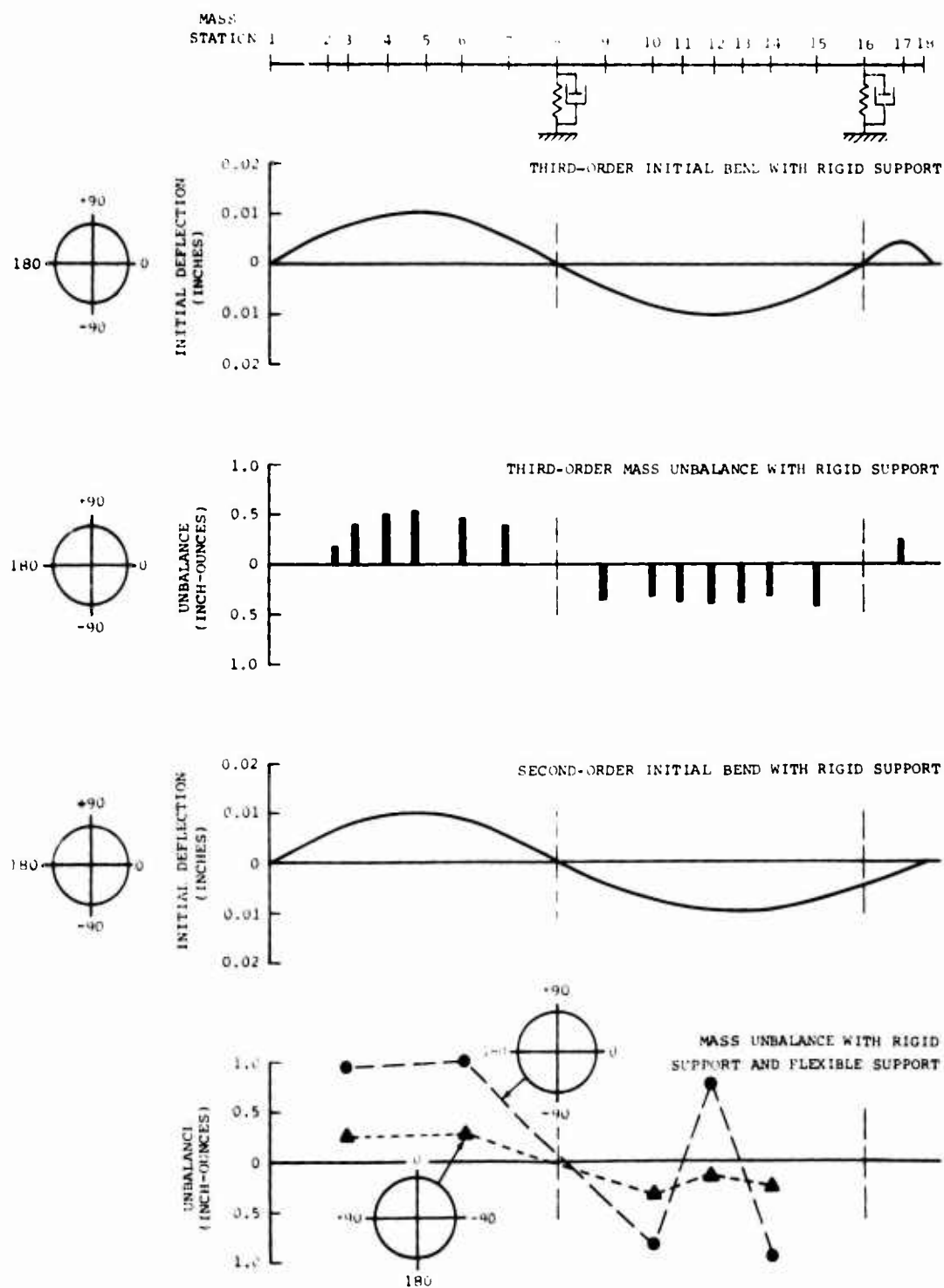


Figure 162. Unbalance Distribution - Analytical Cases.

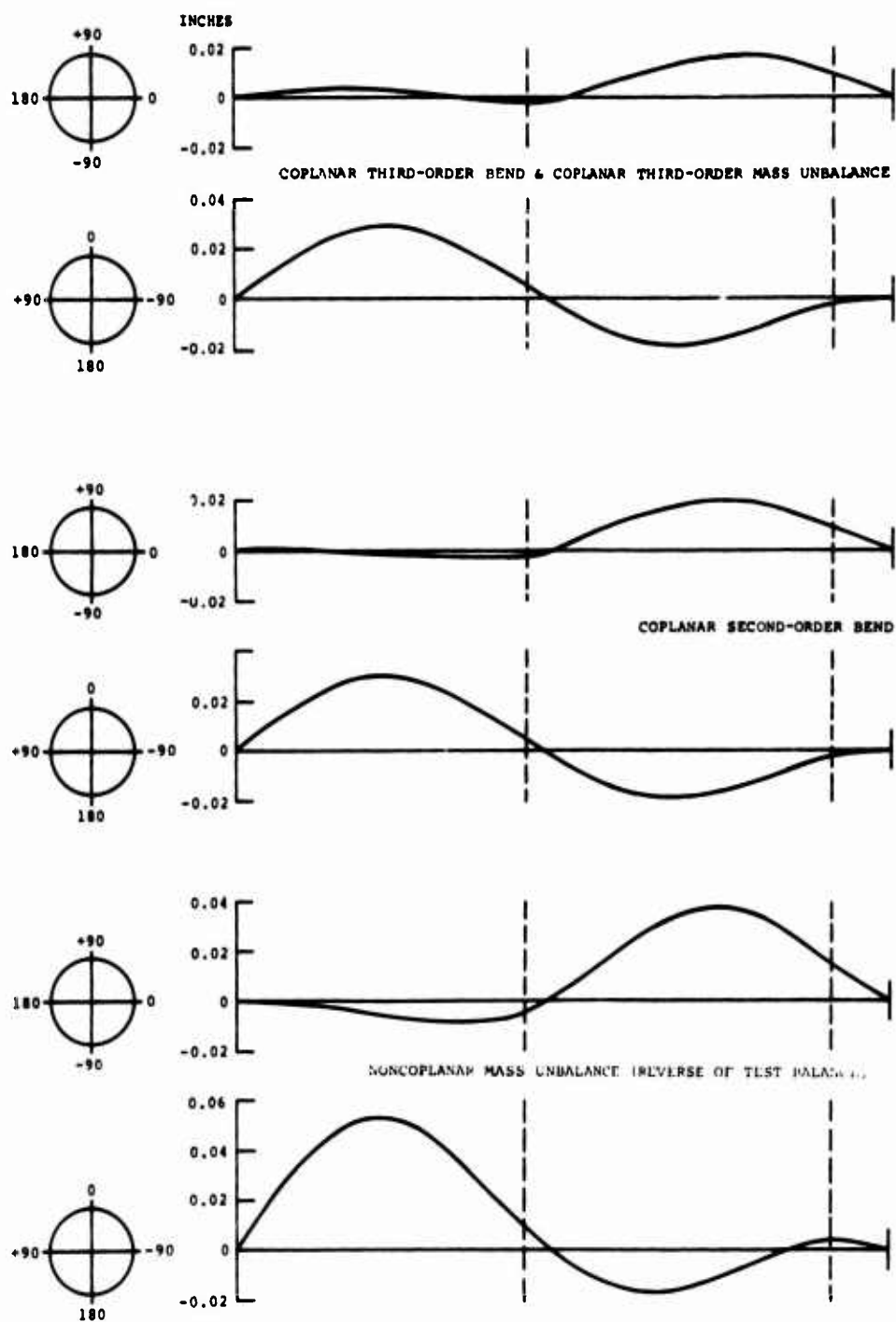


Figure 163. Calculated Response - Rotating Analysis.

CONCLUSIONS

The information presented in this report makes it possible to design supercritical-speed shafts that can efficiently transfer propulsive power over long shaft lengths. Three general areas were investigated:

Strength Properties—The structural integrity of the supercritical-speed shaft was substantiated analytically by conventional methods. Loading conditions and allowable stresses are similar for both subcritical- and supercritical-speed shaft systems.

Dynamic Properties—The dynamic properties for the initial design of a supercritical shaft were determined from an analysis of the nonrotating system using established methods. In the early stages, the nonrotating analysis was preferred since it permitted a rapid evaluation of the important parameters. Critical speeds, required damping, and isotropic-support-structure effects were determined by this type of analysis. Undamped modes or forced shapes with damping obtained from a nonrotating analysis were useful guides in establishing spanwise location of balance weights. Once the system parameters were established from the nonrotating analysis, performance of the design was verified using a Boeing-developed computer program (C-58) for a rotating system.

In addition to the effects of nonisotropic support structure, the response for various degrees of shaft straightness and bearing misalignment was examined. Effects of balance weight locations were evaluated along with the investigation of balancing methods. The development of an analytical simulation of a rotating system has been demonstrated. This analytical simulation is the *basic tool* that will serve as an analytical test stand for supercritical-shaft systems of the future.

Balance Requirements—Once the system was designed and built, the reactions through the dampers and at the ends of the shaft were reduced to acceptable levels by dynamic balancing. A number of balancing procedures were available. The most promising was the COMPUTER PROGRAM FOR BALANCING OF FLEXIBLE ROTORS.⁸ The experimentally balanced shaft was compared with the computer balancing program, and excellent correlation between the two methods was evidenced (see Table IX).

It is anticipated that between 9 and 22 test runs would be required to balance a typical test shaft. The computer program and balance procedure could be refined so that no more than two or three runs would be necessary to balance a production shaft.

The end loads developed by the flexible shaft after dynamic balancing were less than the end loads developed by a standard drive shaft in flight. This indicates that installation of the supercritical-speed shaft in the CH-47 would reduce vibration.

LITERATURE CITED

1. DESIGN CRITERIA FOR HIGH SPEED POWER TRANSMISSION SHAFTS, PART I and PART II. ASD-TDR-62-728. Battelle Memorial Institute, Columbus, Ohio.
2. Baier, R.J., and J. Mack. DESIGN AND TEST EVALUATION OF A SUPERCRITICAL-SPEED SHAFT. The Boeing Company, Vertol Division, USAAVLABS Technical Report 66-49, U.S. Army Aviation Materiel Laboratories, Fort Eustis, Virginia, June 1966.
3. Ko, P.L., SUPERCRITICAL SPEED SHAFT SYSTEM ANALYSIS BOEING-VERTOL MODEL CH-47A & B, D8-0939, The Boeing Company, Vertol Division, Philadelphia, Pennsylvania, December 1967.
4. METALLIC MATERIALS AND ELEMENTS FOR AEROSPACE VEHICLE STRUCTURES, MIL-HDBK-5A, Department of Defense, Washington, D.C., February 1966.
5. VERTOL STRUCTURES DESIGN BOOK 86LI OF THE BOEING COMPANY ENGINEERING DESIGN MANUAL, D-5000, The Boeing Company, Seattle, Washington, 1967.
6. STRUCTURAL DESIGN CRITERIA CH-47B AND C, 114-SS-603 Revision B, The Boeing Company, Vertol Division, Philadelphia, Pennsylvania, September 1967.
7. Liu, Yuan-Ning, A COMPUTER PROGRAM (D-10) FOR BALANCING FLEXIBLE SHAFTS WITH DISTRIBUTED MASS, The Boeing Company, Vertol Division, 114-DY-014, Philadelphia, Pa., October 1967.
8. Reiger, N.F., COMPUTER PROGRAM FOR BALANCING OF FLEXIBLE ROTORS, Mechanical Technology Incorporated, Report MTI-67RD68, September 1967.
9. Bishop, R.E.D., and A.G. Parkinson, ON THE ISOLATION OF MODES IN THE BALANCING OF FLEXIBLE SHAFTS, Proceedings of the Institution of Mechanical Engineers, Vol. 177, No. 16, 1963.
10. Bishop, R.E.D., and G.M.L. Glaswell, THE VIBRATION AND BALANCING OF AN UNBALANCED FLEXIBLE ROTOR, Journal of Mechanical Engineering Science, Vol. 1, No. 1, 1959, pp. 66-77.
11. Bishop, R.E.D., THE VIBRATION OF ROTATING SHAFTS, Journal of Mechanical Engineering Science, Vol. 1, No. 1, 1959, pp. 50-65.
12. Koenig, E.C., ANALYSIS FOR CALCULATING LATERAL VIBRATION CHARACTERISTICS OF ROTATING SYSTEMS WITH ANY NUMBER OF FLEXIBLE SUPPORTS, Journal of Applied Mechanics, December 1961.
13. Sciarras, J.J., DYNAMIC UNIFIED STRUCTURAL ANALYSIS METHOD USING STIFFNESS MATRICES, AIAA/ASME 7th Structures and Materials Conference, April 1966.
14. Sciarras, J.J., APPLICATION OF A COMBINED DIRECT STIFFNESS AND MOBILITY METHOD TO VIBRATION ABSORBER STUDIES, 67-VIBR-65, ASME/MDD Vibrations Conference, March 1967.

SELECTED BIBLIOGRAPHY

1. Den Hartog, J.P., MECHANICAL VIBRATIONS, 4th Edition, New York, McGraw Hill Book Co., Inc., 1956.
2. Timoshenko, S., STRENGTH OF MATERIALS PART II, ADVANCED THEORY AND PROBLEMS, 3rd Edition, New Jersey, D. Van Nostrand Co., March 1956.
3. Parkinson, A.G., K. L. Jackson, R.E.D. Bishop, SOME EXPERIMENTS ON BALANCING OF SMALL FLEXIBLE ROTORS: PART I – THEORY, Journal of Mechanical Engineering Science, Volume 5, No. 2, 1963, pp 133-145.
4. SELECTING TRANSMISSION SYSTEMS FOR HIGH-SPEED LIGHTWEIGHT APPLICATIONS, Document Number ASME 66-MD-71, 1966.
5. DRIVE SYSTEM ANALYSIS, BOEING-VERTOL MODEL CH-47A, Boeing-Vertol Document Number 114-S-409.1.3, February 15, 1965.
6. DRIVE SYSTEM ANALYSIS, BOEING-VERTOL MODELS YHC-1B and HC-1B, Boeing-Vertol Document Number 114-S-09.1.3, March 23, 1961.
7. FINAL REPORT OF FATIGUE TESTING OF DRIVE SYSTEM COMPONENTS FOR THE CH-47A HELICOPTER, Boeing-Vertol Document Number 114-T-40, October 16, 1964.
8. CH-47A DYNAMIC COMPONENT FATIGUE LIFE EVALUATION, Boeing-Vertol Document Number 114-T-112.2, July 9, 1965.
9. STRUCTURAL DESIGN REQUIREMENTS, HELICOPTERS, Military Specification MIL-S-8698, July 1, 1954.
10. STRUCTURAL DESIGN CRITERIA, Boeing-Vertol Document Number 114-SS-603, Revision B, September 1, 1967.

APPENDIX I. DEVELOPMENT OF AN ANALYSIS FOR A ROTATING SHAFT, PROGRAM C-58

The purpose of this analysis is to adequately predict the performance of a rotating supercritical-speed-shaft system and to assess the effect items such as shaft straightness, bearing misalignment, and nonisotropic-support-point stiffness will have on such a system.

The shaft was idealized by using a lumped-mass representation in which the distributed shaft mass was replaced by a finite number of concentrated masses. Figure 164 shows the analytical model which included two intermediate flexible supports as well as flexible end supports with damping at all support locations. In order to simulate a rotating system, each of the masses must be free to move in two directions. If the moment of inertia is neglected and only the linear motion of the masses considered, the twenty-mass representation (see Figure 164) requires that solutions be obtained to 40 simultaneous second-order differential equations; i.e., a 40-degree-of-freedom problem. The effect of the moment of inertia was investigated by analyzing this configuration as a nonrotating system. Maximum error in the natural frequencies of the first seven modes was 5 percent when the moment of inertia was not considered. This was felt to be within acceptable limits (a crucial point since consideration of the shaft moment of inertia would introduce an additional 36 degrees of freedom).

A matrix approach employing the direct stiffness method^{13,14} is used since it appeared to require the minimum programming effort. In order to facilitate programming, the analysis is restricted to that of Figure 164. With the exception of the 40-degree-of-freedom limitation, the geometric limitations can easily be generalized. However, the 40-degree-of-freedom representation approaches the limit of the computer core storage, and a more complicated system would require more sophisticated programming techniques such as overlaying and external tape storage.

The local idealization of the system elements at the intermediate support are illustrated in Figure 165. The central mass is permitted to move in both the X and Y directions with the motion restrained by the flexibility of the shaft, the spring of the fixed system shaft damper, and the stiffness of the supports. Also shown is the support mass which is connected to ground through a damper and nonisotropic springs acting in the fixed system X and Y directions. For convenience, solutions are desired in the ξ and η freedoms of the rotating coordinate system which rotates at the shaft speed Ω . Unbalance masses which act at a distance a from the central mass are located in the $\xi - \eta$ plane by the angle ϕ_{ai} . Balance weights at each central mass are located in a similar manner.

To develop the system equations, the motions of the elemental masses at the intermediate support locations are considered as shown in Figure 166. Displacements of these masses in the fixed x-y coordinate system are:

$$X_{m_s} = \xi_s \cos \Omega t - \eta_s \sin \Omega t$$

$$Y_{m_s} = \xi_s \sin \Omega t + \eta_s \cos \Omega t$$

$$X_{m_i} = \xi_i \cos \Omega t - \eta_i \sin \Omega t$$

NOTE:

THIS ANALYSIS ASSUMES THE FOLLOWING SYMMETRY:

$$\begin{aligned}
 K_{x_1} &= K_{y_1} = K_1 & C_{x_1} &= C_{y_1} = C_1 \\
 K_{x_{18}} &= K_{y_{18}} = K_{18} & C_{x_{18}} &= C_{y_{18}} = C_{18}
 \end{aligned}$$

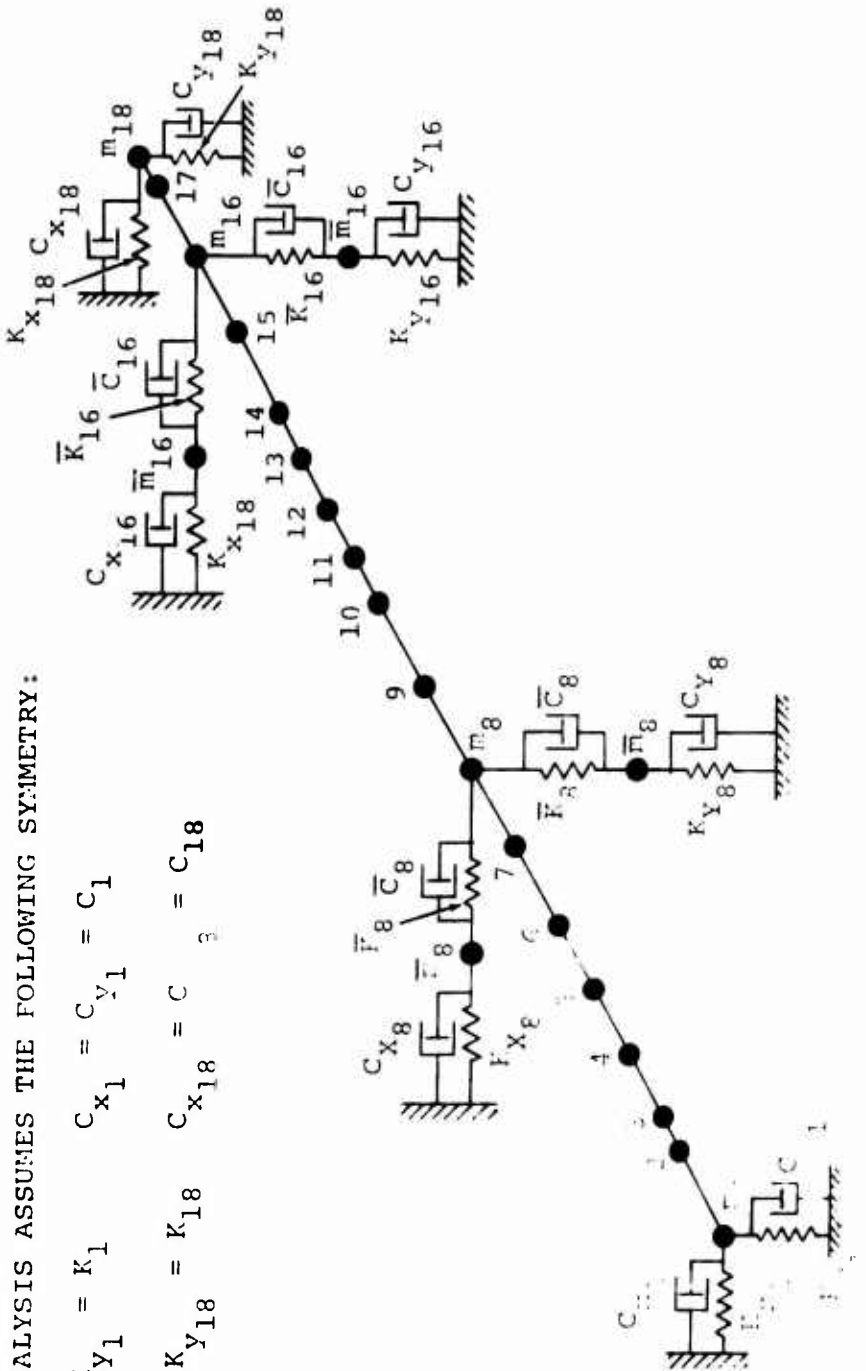


Figure 164. Analytical Model for Rotating System.

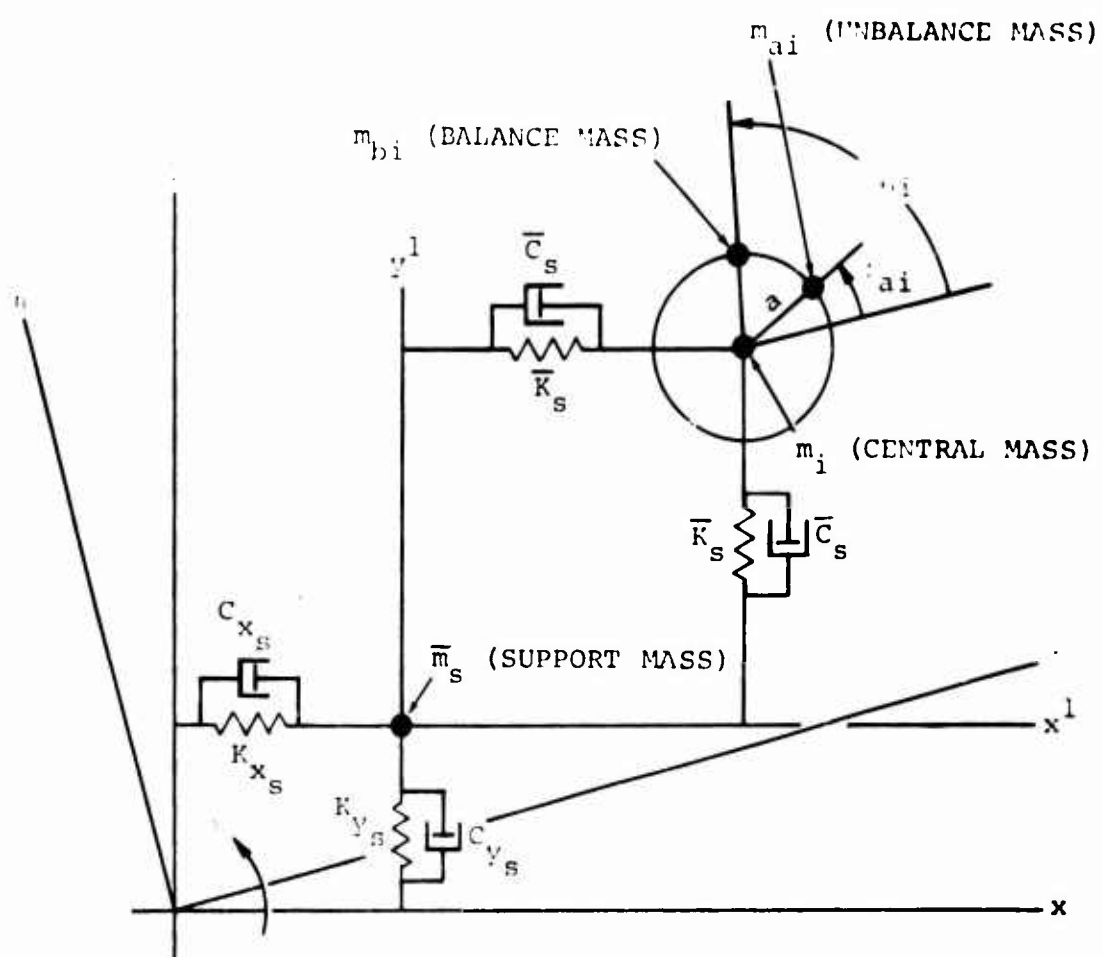
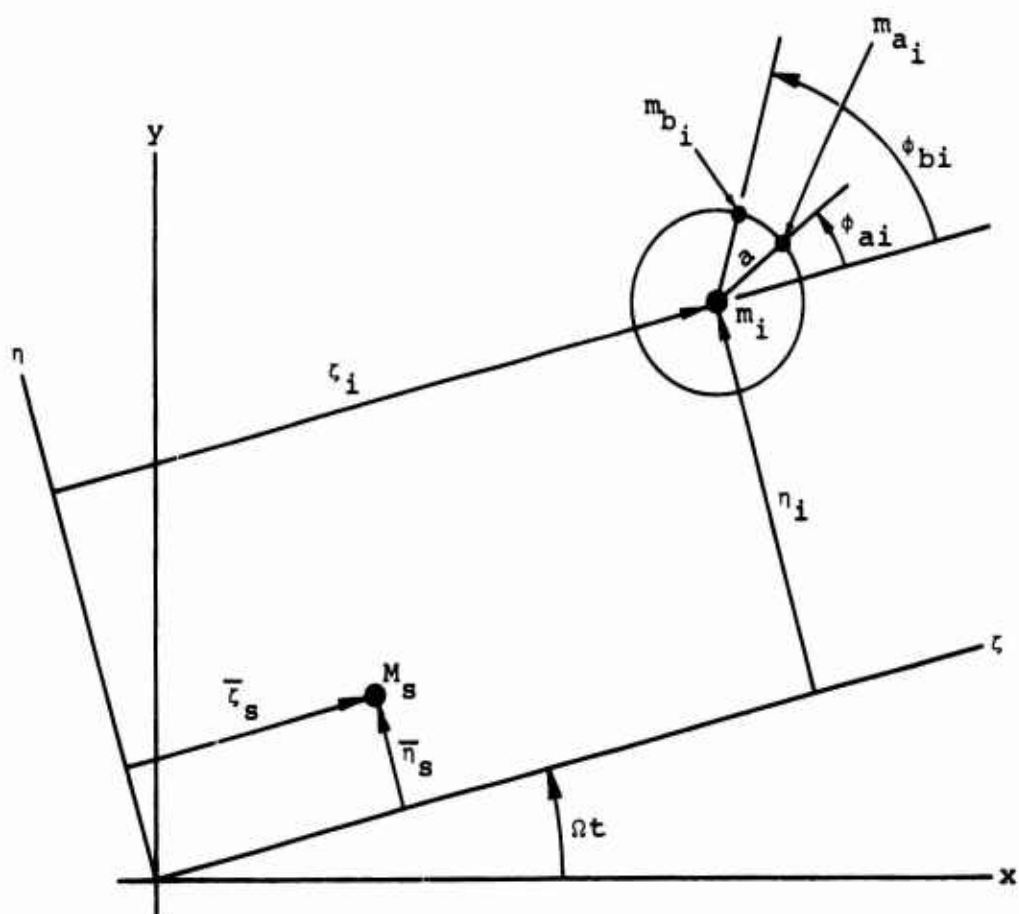


Figure 165. Idealization at Intermediate Support.



NOTE:

$$\eta_i = \eta_{oi} + \eta_i(\Omega) = \text{INITIAL} + \text{DYNAMIC}$$

$$\zeta_i = \zeta_{oi} + \zeta_i(\Omega)$$

Figure 166. Mass Motions at Intermediate Support.

$$\begin{aligned}
Y_{m_i} &= \zeta_i \sin \Omega t + \eta_i \cos \Omega t \\
X_{m_{ai}} &= \zeta_i \cos \Omega t - \eta_i \sin \Omega t + a \cos (\phi_{ai} + \Omega t) \\
Y_{m_{ai}} &= \zeta_i \sin \Omega t + \eta_i \cos \Omega t + a \sin (\phi_{ai} + \Omega t) \\
X_{m_{bi}} &= \zeta_i \cos \Omega t - \eta_i \sin \Omega t + a \cos (\phi_{bi} + \Omega t) \\
Y_{m_{bi}} &= \zeta_i \sin \Omega t + \eta_i \cos \Omega t + a \sin (\phi_{bi} + \Omega t)
\end{aligned}$$

The kinetic energy and the dissipation functions of the system are defined as follows:

$$\begin{aligned}
T &= \frac{1}{2} \sum_{i=1}^{18} m_i (X_{m_i}^2 + Y_{m_i}^2) + m_{ai} (X_{m_{ai}}^2 + Y_{m_{ai}}^2) + m_{bi} (X_{m_{bi}}^2 + Y_{m_{bi}}^2) \\
&\quad + \frac{1}{2} [m_8 (X_{m_8}^2 + Y_{m_8}^2) + m_{16} (X_{m_{16}}^2 + Y_{m_{16}}^2)] \\
D &= \frac{1}{2} [C_1 (X_{m_1}^2 + Y_{m_1}^2) + C_{18} (X_{m_{18}}^2 + Y_{m_{18}}^2) + c_{x8} X_{m_8}^2 + c_{y8} Y_{m_8}^2 \\
&\quad + C_{x16} X_{m_{16}}^2 + C_{y16} Y_{m_{16}}^2 + C_8 [(X_{m_8} - X_{m_8})^2 + (Y_{m_8} - Y_{m_8})^2] \\
&\quad + C_{16} [(X_{m_{16}} - X_{m_{16}})^2 + (Y_{m_{16}} - Y_{m_{16}})^2]]
\end{aligned}$$

Because of the flexibility of the beam, the potential energy of the system is quite complex in that it involves the interaction of each mass point with all the other mass points. The general form of the expression is

$$\begin{aligned}
V &= \frac{1}{2} \sum_{i=1}^{18} \sum_{j=1}^{18} K_{\eta_{ij}} \eta_i \eta_j + K_{\zeta_{ij}} \zeta_i \zeta_j \\
&\quad + \frac{1}{2} [K_1 (X_{m_1}^2 + Y_{m_1}^2) + K_{18} (X_{m_{18}}^2 + Y_{m_{18}}^2) + K_{x8} X_{m_8}^2 + K_{y8} Y_{m_8}^2 \\
&\quad + K_{x16} X_{m_{16}}^2 + K_{y16} Y_{m_{16}}^2 + K_8 [(X_{m_8} - X_{m_8})^2 + (Y_{m_8} - Y_{m_8})^2] \\
&\quad + K_{16} [(X_{m_{16}} - X_{m_{16}})^2 + (Y_{m_{16}} - Y_{m_{16}})^2]]
\end{aligned}$$

where $K_{\eta_{ij}}$ and $K_{\zeta_{ij}}$ are the shaft stiffnesses at mass point (i) relative to mass point (j).

In the matrix notation, the equation for the forces response of the system is of the form

$$[M] \ddot{q} + [C] \dot{q} + ([K]_{\text{static}} + [K]_{\text{dynamic}}) q = F$$

All of the coefficients in the above equation can be obtained by applying the Lagrange equation $\frac{\delta T}{\delta q} - \frac{d}{dt} \frac{\delta T}{\delta \dot{q}} + \frac{\delta D}{\delta \dot{q}} + \frac{\delta V}{\delta q} = 0$.

Carrying out the operations indicated by the Lagrange equation, the mass, stiffness, damping, and forcing matrices for the 40-degree-of-freedom shaft configuration of Figure 164 are obtained. The matrices in compressed form showing only the nonzero values are presented in Figures 167 through 170. In the case of the stiffness, only the dynamic matrix is shown. Computation of the static stiffness for the entire shaft is quite complex, and the numeric static stiffness matrix is obtained from an existing program (Vertol program D-46).

An IBM 360-65 computer program was set up according to the flow diagram of Figure 171. With nonisotropic supports there are terms in the dynamic stiffness matrix and the damping matrix which are functions of time, and the only readily available method of solution is by numerical integration.

		$\ddot{\eta}_1$	$\ddot{\zeta}_1$			$\ddot{\eta}_8$	$\ddot{\zeta}_8$	$\ddot{\eta}_8$
ROW	COLUMN	1	2			15	16	17
		$m_1 + m_{a_1} + m_{b_1}$						
1								
2			$m_1 + m_{a_1} + m_{b_1}$					
				SEE NOTE				
15						$m_8 + m_{a_8} + m_{b_8}$		
16							$m_1 + m_{a_8} + m_{b_8}$	
17								\overline{m}_8
18								
33								
34								
35								
36								
39								
40								

NOTE: DIAGONAL TERM = $m_i + m_{a_i} + m_{b_i}$ EXCEPT AS SHOWN

Figure 167. Mass Matrix.

13

\ddot{c}_8	\ddot{n}_{16}	\ddot{z}_{16}	$\ddot{\bar{n}}_{16}$	$\ddot{\bar{z}}_{16}$	\ddot{n}_{18}	\ddot{z}_{18}
18	33	34	35	36	39	40
\bar{m}_8						
SEE NOTE						
	$m_{16} + m_{a_{16}} + m_{b_{16}}$					
		$m_{16} + m_{a_{16}} + m_{b_{16}}$				
			\bar{m}_{16}			
				\bar{m}_{16}		
SEE NOTE						
					$m_{18} + m_{a_{18}} + m_{b_{18}}$	
						$m_{18} + m_{a_{18}} + m_{b_{18}}$

R

		$\dot{\eta}_1$	$\dot{\zeta}_1$				
ROW	COLUMN	1	2	$\dot{\eta}_8$	$\dot{\zeta}_8$	$\dot{\eta}_8$	$\dot{\zeta}_8$
		1	2	15	16	17	18
1		C_1	$2\Omega (\bar{m}_1 + m_{a1} + m_{b1})$				
2		$-2\Omega (\bar{m}_1 + m_{a1} + m_{b1})$	C_1				
				SEE NOTE			
15				\bar{C}_8	$2\Omega (\bar{m}_8 + m_{a8} + m_{b8})$	$-\bar{C}_8$	
16				$-2\Omega (\bar{m}_8 + m_{a8} + m_{b8})$	\bar{C}_8		$-\bar{C}_8$
17				$-\bar{C}_8$		17,17	17,18
18					$-\bar{C}_8$	18,17	18,18
				SEE NOTE			
33							
34							
35							
36							
NOTE:							
DIAGONAL TERM (C_i) = 0 EXCEPT AS SHOWN							
OFF DIAGONAL TERM = $2\Omega (\bar{m}_i + m_{a_i} + m_{b_i})$ EXCEPT AS SHOWN							
39							
40							

$$17,17 = \bar{C}_8 + C_{x8} \sin^2 \Omega t + C_{y8} \cos^2 \Omega t$$

$$18,17 = -2\Omega \bar{m}_8 - (C_{x8} - C_{y8}) \sin \Omega t \cos \Omega t$$

$$17,18 = 2\Omega \bar{m}_8 - (C_{x8} - C_{y8}) \sin \Omega t \cos \Omega t$$

$$18,18 = \bar{C}_8 + C_{x8} \cos^2 \Omega t + C_{y8} \sin^2 \Omega t$$

$$35,35 = \bar{C}_{16} + C_{x16} \sin^2 \Omega t + C_{y16} \cos^2 \Omega t$$

$$36,35 = -2\Omega \bar{m}_{16} - (C_{x16} - C_{y16}) \sin \Omega t \cos \Omega t$$

$$35,36 = 2\Omega \bar{m}_{16} - (C_{x16} - C_{y16}) \sin \Omega t \cos \Omega t$$

$$36,36 = \bar{C}_{16} + C_{x16} \cos^2 \Omega t + C_{y16} \sin^2 \Omega t$$

Figure 168. Damping Matrix.

17

		η_1	ζ_1					η_8	ζ_8	$\bar{\eta}_8$	$\bar{\zeta}_8$
COLUMN	ROW	1	2					15	16	17	18
		$-\dot{\eta}_1^2 (m_1 + m_{a_1} + m_{b_1})$	$C_1 \dot{\eta}_1$								
	1										
	2	$-C_1 \dot{\eta}_1$	$-\dot{\eta}_1^2 (m_1 + m_{a_1} + m_{b_1})$								
				SEE NOTE							
	15			$-\dot{\eta}_8^2 (m_8 + m_{a_8} + m_{b_8})$	$\bar{C}_8 \dot{\eta}_8$						$-\bar{C}_8 \dot{\eta}_8$
	16			$-\bar{C}_8 \dot{\eta}_8$	$-\dot{\eta}_8^2 (m_8 + m_{a_8} + m_{b_8})$	$\bar{C}_8 \dot{\eta}_8$					
	17				$-\bar{C}_8 \dot{\eta}_8$	17,17	17,18				
	18			$\bar{C}_8 \dot{\eta}_8$		18,17	18,18				
				SEE NOTE							
	33										
	34										
	35										
	36										
NOTE:											
DIAGONAL TERMS = $-\dot{\eta}_1^2 (m_1 + m_{a_1} + m_{b_1})$ EXCEPT AS SHOWN											
	39										
	40										

$17,17 = -m_8 \dot{\eta}_8^2 + K_{x_8} \sin^2 \eta t + K_{y_8} \cos^2 \eta t + \eta (C_{x_8} - C_{y_8}) \sin \eta t \cos \eta t + \bar{K}_8$
35,35 =

$18,17 = -C_{x_8} \dot{\eta}_8 \cos^2 \eta t - C_{y_8} \dot{\eta}_8 \sin^2 \eta t - (K_{x_8} - K_{y_8}) \sin \eta t \cos \eta t + \bar{C}_8 \dot{\eta}_8$
36,35 =

$17,18 = C_{x_8} \dot{\eta}_8 \sin^2 \eta t + C_{y_8} \dot{\eta}_8 \cos^2 \eta t - (K_{x_8} - K_{y_8}) \sin \eta t \cos \eta t + \bar{C}_8 \dot{\eta}_8$
35,36 =

$18,18 = -\bar{m}_8 \dot{\eta}_8^2 + K_{x_8} \cos^2 \eta t + K_{y_8} \sin^2 \eta t - \eta (C_{x_8} - C_{y_8}) \sin \eta t \cos \eta t + \bar{K}_8$
36,36 =

Figure 169. Dynamic Stiffness Matrix.

B

\bar{c}_8	η_{16}	ζ_{16}	$\bar{\eta}_{16}$	$\bar{\zeta}_{16}$	η_{18}	ζ_{18}
18	33		35	36	39	40
$-\bar{c}_8 n$						
17,18						
18,18						
SEE NOTE						
	$-\dot{n}^2 (m_{16} + m_{a16} + m_{b16})$	$\bar{c}_{16} n$		$-\bar{c}_{16} n$		
	$-\bar{c}_{16} n$	$-\dot{n}^2 (m_{16} + m_{a16} + m_{b16})$	$\bar{c}_{16} n$			
		$-\bar{c}_{16} n$	35,35	35,36		
	$\bar{c}_{16} n$		36,35	36,36		
					$-\dot{n}^2 (m_{18} + m_{a18} + m_{b18})$	$c_{18} n$
					$-c_{18} n$	$-\dot{n}^2 (m_{18} + m_{a18} + m_{b18})$

$$\begin{aligned}
 35,35 &= \bar{m}_{16} \dot{n}^2 + K_{x16} \sin^2 nt + K_{y16} \cos^2 nt + n (C_{x16} - C_{y16}) \sin nt \cos nt + \bar{K}_{16} \\
 36,35 &= -C_{x16} n \cos^2 nt - C_{y16} n \sin^2 nt - (K_{x16} - K_{y16}) \sin nt \cos nt - \bar{c}_{16} n \\
 35,36 &= C_{x16} n \sin^2 nt + C_{y16} n \cos^2 nt - (K_{x16} - K_{y16}) \sin nt \cos nt + \bar{c}_{16} n \\
 36,36 &= \bar{m}_{16} \dot{n}^2 + K_{x16} \cos^2 nt + K_{y16} \sin^2 nt - n (C_{x16} - C_{y16}) \sin nt \cos nt + \bar{K}_{16}
 \end{aligned}$$

$$\{F\} = \left\{ \begin{array}{l}
\Omega^2 [\eta_{01} (m_1 + m_{a1} + m_{b1})] + a\Omega^2 [m_{a1} \sin \phi_{a1} + m_{b1} \sin \phi_{b1}] \\
\Omega^2 [\xi_{01} (m_1 + m_{a1} + m_{b1})] + a\Omega^2 [m_{a1} \cos \phi_{a1} + m_{b1} \cos \phi_{b1}] \\
\bullet \\
\bullet \\
\bullet \\
\bullet \\
\bullet \\
\Omega^2 [\eta_{08} (m_8 + m_{a8} + m_{b8})] + a\Omega^2 [m_{a8} \sin \phi_{a8} + m_{b8} \sin \phi_{b8}] \\
\Omega^2 [\xi_{08} (m_8 + m_{a8} + m_{b8})] + a\Omega^2 [m_{a8} \cos \phi_{a8} + m_{b8} \cos \phi_{b8}] \\
0 \\
0 \\
\Omega^2 [\eta_{09} (m_9 + m_{a9} + m_{b9})] + a\Omega^2 [m_{a9} \sin \phi_{a9} + m_{b9} \sin \phi_{b9}] \\
\Omega^2 [\xi_{09} (m_9 + m_{a9} + m_{b9})] + a\Omega^2 [m_{a9} \cos \phi_{a9} + m_{b9} \cos \phi_{b9}] \\
\bullet \\
\bullet \\
\bullet \\
\bullet \\
\bullet \\
\bullet \\
\Omega^2 [\eta_{015} (m_{15} + m_{a15} + m_{b15})] + a\Omega^2 [m_{a15} \sin \phi_{a15} + m_{b15} \sin \phi_{b15}] \\
\Omega^2 [\xi_{015} (m_{15} + m_{a15} + m_{b15})] + a\Omega^2 [m_{a15} \cos \phi_{a15} + m_{b15} \cos \phi_{b15}] \\
0 \\
0 \\
\Omega^2 [\eta_{017} (m_{17} + m_{a17} + m_{b17})] + a\Omega^2 [m_{a17} \sin \phi_{a17} + m_{b17} \sin \phi_{b17}] \\
\Omega^2 [\xi_{017} (m_{17} + m_{a17} + m_{b17})] + a\Omega^2 [m_{a17} \cos \phi_{a17} + m_{b17} \cos \phi_{b17}] \\
\Omega^2 [\eta_{018} (m_{18} + m_{a18} + m_{b18})] + a\Omega^2 [m_{a18} \sin \phi_{a18} + m_{b18} \sin \phi_{b18}] \\
\Omega^2 [\xi_{018} (m_{18} + m_{a18} + m_{b18})] + a\Omega^2 [m_{a18} \cos \phi_{a18} + m_{b18} \cos \phi_{b18}]
\end{array} \right\}$$

Figure 170. Forcing Function Matrix.

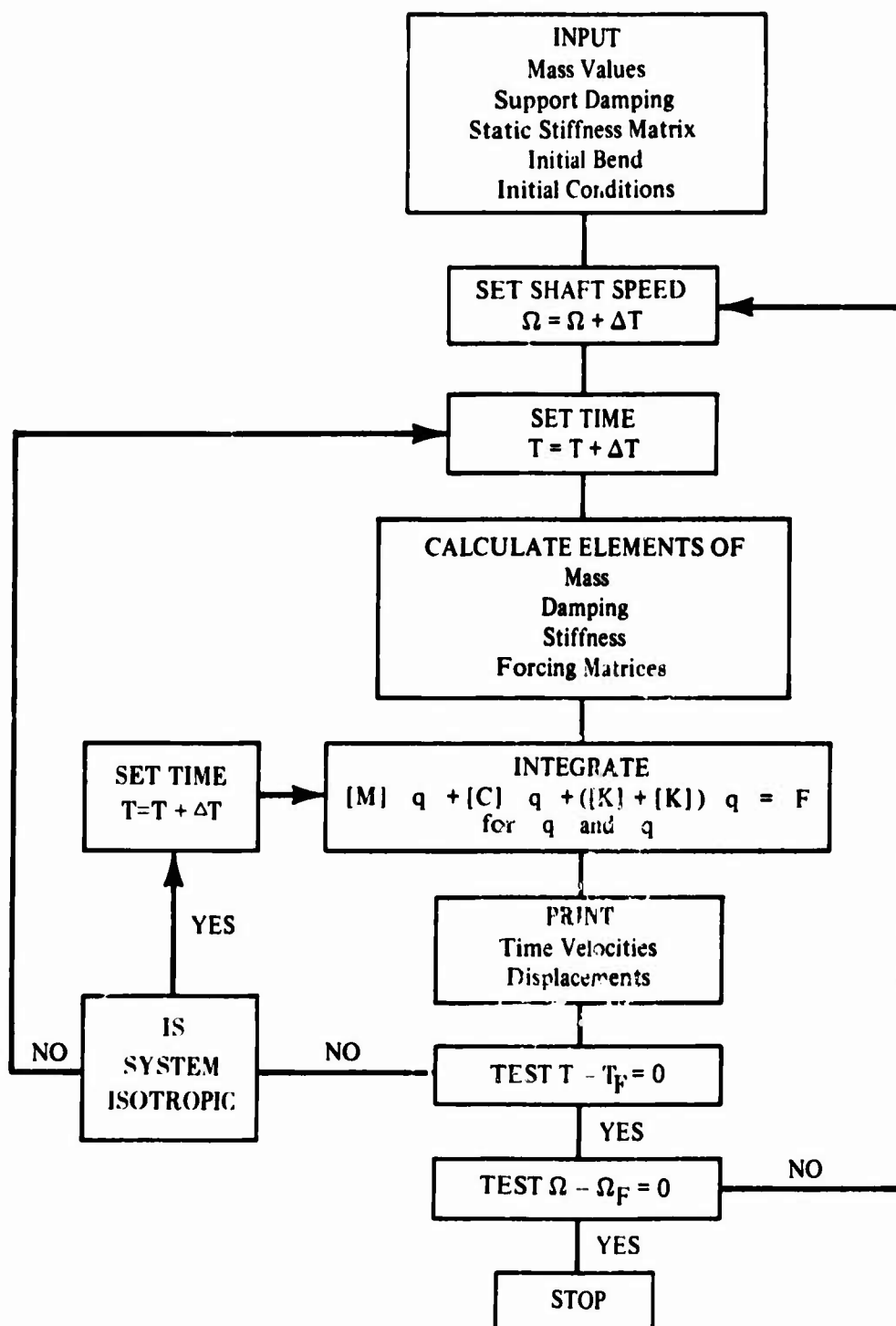
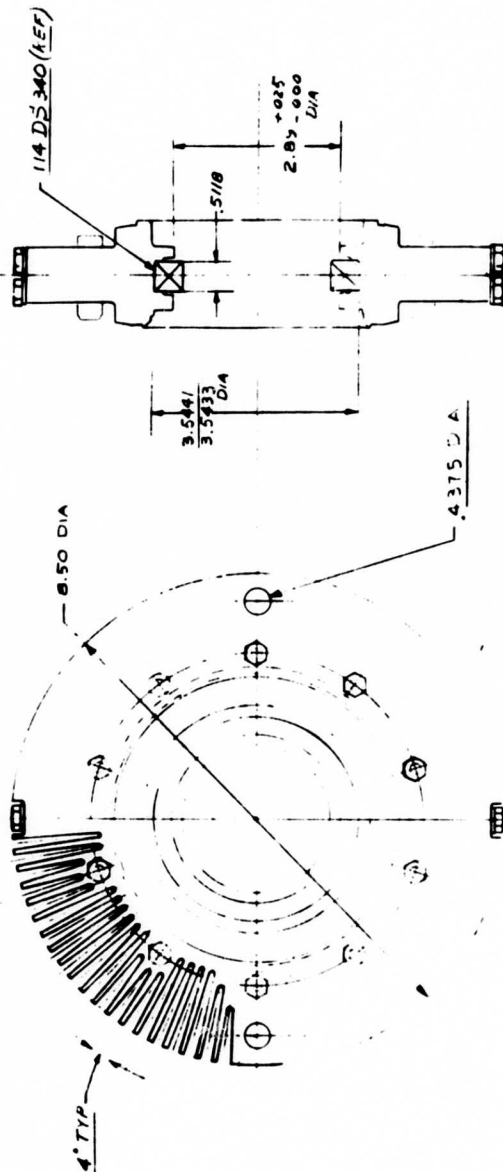
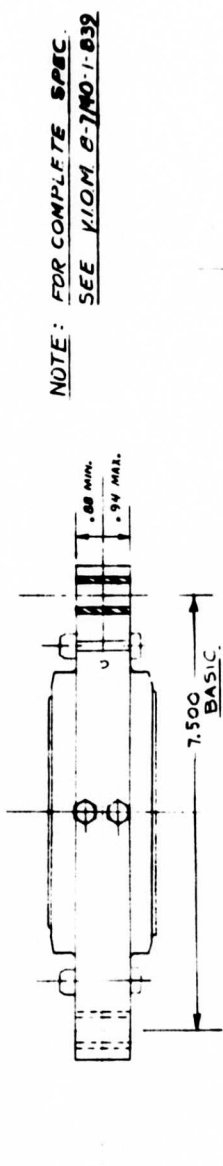


Figure 171. Program Flow Diagram.

TABLE XII. LIST OF SYMBOLS FOR APPENDIX I	
m_i	shaft control mass
m_{ai}	unbalance mass
m_{bi}	balance mass
m_s	support mass
ζ, η	rotating system coordinates
X, Y	fixed system coordinates
C	fixed system damping coefficient of shaft damper
C_X, C_Y	fixed system (supports) damping coefficient in X and Y directions
K	fixed system spring rate of shaft damper
K_X, K_Y	fixed system (support) spring rates in X and Y directions
$K_{\zeta ij}, K_{\eta ij}$	shaft stiffness at point (i) relative to point j in ζ and η directions.
ϕ_{ai}	angular position of unbalance mass
ϕ_{bi}	angular position of balance mass
a	radial offset of unbalance and balance masses
Ω	shaft speed

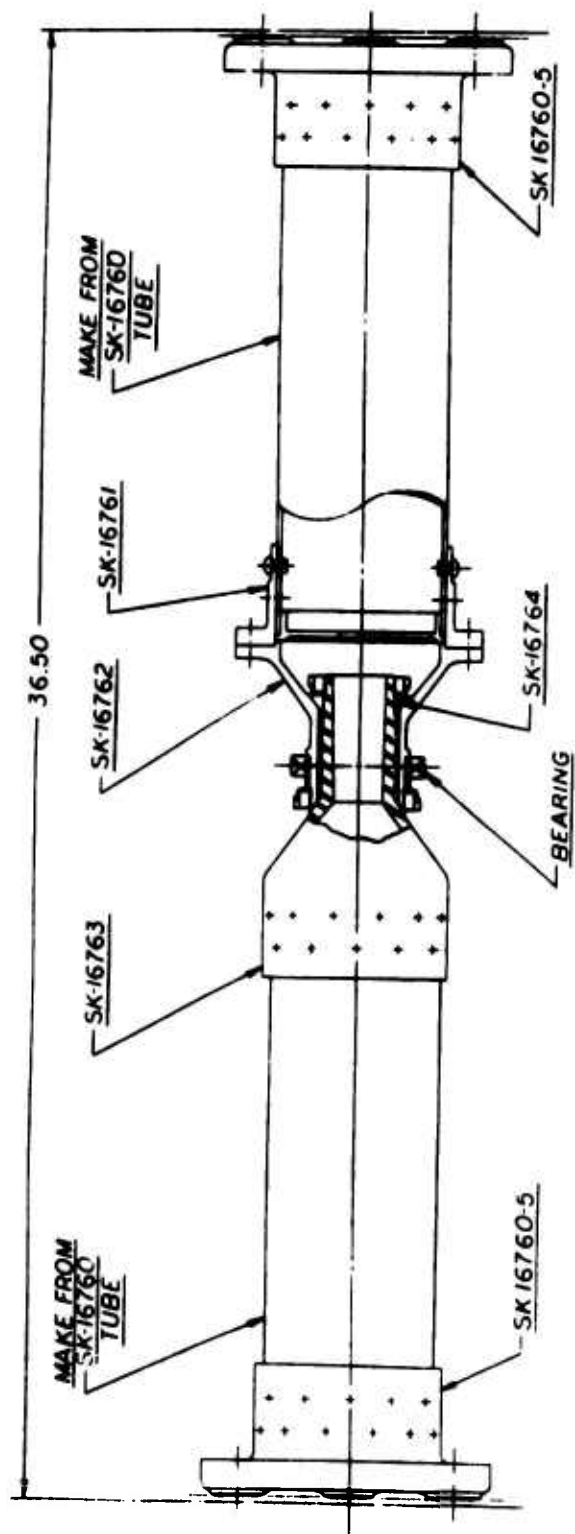
APPENDIX II. ASSEMBLY DRAWINGS

SK-16381	Specification Control Drawing -- Damper
J-12331-5	Damper Drawing - Lord Manufacturing Company
ST-10220	Torsion Fatigue Test Specimen
SK-16760	Shaft Assembly Drawing



THE BEND COMPANY		DATE	
DAMPER		JUL 1967	
SPECIFICATION CONTROL		BY	
SUPERCRITICAL SPEED SHAFT		CHECKED	
C 81208		SK-16381	
SCALE 1/8" = 1"		BY 1 OF 1	

REVISIONS	DATE	BY	REASON
1			
2			
3			
4			
5			
6			
7			
8			
9			
10			
11			
12			
13			
14			
15			
16			
17			
18			
19			
20			
21			
22			
23			
24			
25			
26			
27			
28			
29			
30			
31			
32			
33			
34			
35			
36			
37			
38			
39			
40			
41			
42			
43			
44			
45			
46			
47			
48			
49			
50			
51			
52			
53			
54			
55			
56			
57			
58			
59			
60			
61			
62			
63			
64			
65			
66			
67			
68			
69			
70			
71			
72			
73			
74			
75			
76			
77			
78			
79			
80			
81			
82			
83			
84			
85			
86			
87			
88			
89			
90			
91			
92			
93			
94			
95			
96			
97			
98			
99			
100			



THE BEING COMPANY		VERTOL DIVISION PHILADELPHIA, PA.	
DATE	BY	DATE	BY
1-1-55	J. J. J.	1-1-55	J. J. J.
CHK	SYNCT	WTS	GR
PROJ	TORSIONAL FATIGUE TEST OF SHAFT COUPLING - SUPERCRITICAL SHAFT TEST		
SIZE	CODE	NO	ST-10220
D	mm		
SCALE: 1/2"		SH / OF /	

UNCLASSIFIED
Security Classification

DOCUMENT CONTROL DATA - R & D		
(Security classification of title, body of abstract and indexing annotation must be entered when the overall report is classified)		
1. ORIGINATING ACTIVITY (Corporate author) The Boeing Company, Vertol Division Boeing Center Philadelphia, Pennsylvania 19142		2a. REPORT SECURITY CLASSIFICATION Unclassified
		2b. GROUP
3. REPORT TITLE FLIGHT TEST EVALUATION OF A SUPERCRITICAL-SPEED SHAFT		
4. DESCRIPTIVE NOTES (Type of report and inclusive dates) Final Report		
5. AUTHOR(S) (First name, middle initial, last name) Robert J. Baier		
6. REPORT DATE September 1970	7a. TOTAL NO. OF PAGES 262	7b. NO. OF REFS 24
8. CONTRACT OR GRANT NO. DA 44-177-AMC-353(T) a. PROJECT NO. Task 1G162203D14414 c. d.		9a. ORIGINATOR'S REPORT NUMBER(S) USAAVLABS Technical Report 70-50 9b. OTHER REPORT NO(S) (Any other numbers that may be assigned this report) D210-10082-1
10. DISTRIBUTION STATEMENT This document is subject to special export controls, and each transmittal to foreign governments or foreign nationals may be made only with prior approval of US Army Aviation Materiel Laboratories, Fort Eustis, Virginia 23604.		
11. SUPPLEMENTARY NOTES		12. SPONSORING MILITARY ACTIVITY US Army Aviation Materiel Laboratories Fort Eustis, Virginia
13. ABSTRACT This report presents the effort by The Boeing Company, Vertol Division on the bench testing and analytical description of a full-size supercritical-speed shaft designed for installation in the CH-47 helicopter. A full-size shaft was built, and shaft damper was developed to meet the requirements of the system as installed in an aircraft. The bench test program included tests of the damper, torsional fatigue tests of the redesigned adapter fittings, and dynamic tests of the full-size supercritical-speed shaft. Previous balance methods proved to be unsatisfactory for a shaft of this size because of the noncoplanar nature of the shaft deflection at higher speeds. A new technique was developed to successfully balance the shaft throughout the desired six critical speeds. The ground and flight test portion of the program has been replaced by an analytical description of the phenomena of multiple-mode bending identified during the bench test program. This analytical description includes variables anticipated in future supercritical shaft system designs. The relative weight, reliability, safety, and economics of supercritical-speed drive systems can be compared with more conventional drives since the unknowns have been identified.		

DD FORM 1473

REPLACES DD FORM 1473, 1 JAN 64, WHICH IS OBSOLETE FOR ARMY USE.

UNCLASSIFIED

Security Classification

14.	KEY WORDS	LINK A		LINK B		LINK C	
		ROLE	WT	ROLE	WT	ROLE	WT
	Critical Speed Supercritical Speed Damper Torsion Test Multiple Mode Shape Superimposed Modes Noncircular Whirling Motion Influence Coefficient Balancing Method Computer Balancing Program						